PREDICTIVE CONTROL OF POWER GRID-CONNECTED ENERGY SYSTEMS BASED ON ENERGY AND EXERGY METRICS

By

Meysam Razmara

A DISSERTATION

Submitted in partial fulfillment of the requirements for the degree of

DOCTOR OF PHILOSOPHY

In Mechanical Engineering-Engineering Mechanics

MICHIGAN TECHNOLOGICAL UNIVERSITY

2016

This dissertation has been approved in partial fulfillment of the requirements for the Degree of DOCTOR OF PHILOSOPHY in Mechanical Engineering-Engineering Mechanics.

Department of Mechanical Engineering-Engineering Mechanics

Dissertation Co-advisor: *Dr. Mahdi Shahbakhti*

Dissertation Co-advisor: *Dr. Rush D. Robinett III*

Committee Member: *Dr. Gordon G. Parker*

Committee Member: *Dr. Sumit Paudyal*

Committee Member: *Dr. Scott A. Miers*

Department Chair: *Dr. William W. Predebon*

Dedication

To my mother Pari and my father Nadali

for their continual support, and unconditional love without which I would have not been able to succeed.

Contents

List of Figures

List of Tables

Preface

The manuscript and the Results of this dissertation are mainly based on five journal and peer-reviewed conference papers. Publishers of these papers have granted the permissions found in Appendix E. The contribution of the author of this dissertation as well as the contributions of the co-authors for each of the papers are as follows:

- Contribution for Chapter 2 ([1]): Data collection, analysis of the experimental data, thermal modeling, validation of the building model and writing these sections have been done by the author of this dissertation, M. Razmara. Design of Kalman Filter including EKF and UKF, Control design including MPC and RMPC, and evaluation of the controllers have been done by my colleague, Dr. M. Maasoumy. Dr. M. Shahbakhti and Dr. A. Sangiovanni-Vincentelli provided technical comments and manuscript editing during the course of this paper.

- Contribution for Chapter 3 ([2]): Thermal modeling and validation, exergy modeling, control design and evaluation, and writing the paper were done by the author, M. Razmara. Dr. M. Maassoumy has provided technical comments on predictive controller design, Linear Parameter Varying (LPV) and helped the authors writing the paper. Dr. M. Shahbakhti and Dr. R.D. Robinett IIIanalyzed the results, provided technical comments and edited the manuscript.

- Contribution for Chapter 4 ([3, 4]): Analysis of the experimental data, creating energy and exergy models for an Internal Combustion Engine (ICE), designing predictive controller, creating the exergy/energy maps and writing the paper were done by the author, M. Razmara. Control algorithm design, evaluation of the controller in simulation, and writing of these sections have been done by the co-author, Dr. M. Bidarvatan. Dr. M. Shahbakhti and Dr. R.D. Robinett III analyzed the results and provided technical comments and edited the manuscript.

- Contribution for Chapter 5 ([5]): Building energy modeling, optimization model for demand side, building to grid index and writing the paper were done by the author, M. Razmara under supervision of Dr. M. Shahbakhti. Distribution power grid modeling, supply side optimization including load factor and load penetration maximization and writing of these sections were done by our colleagues in Department of Electrical Engineering at MTU, G.R. Bharati and Dr. S. Paudyal. Dr. R.D. Robinett III has supervised this research and provided technical comments, and edited the manuscript.

Acknowledgments

I gratefully thank many wonderful individuals who supported me in successful completion of my doctoral dissertation during years of studying at Michigan Tech.

My principal gratitude goes to my PhD advisors, Drs. Mahdi Shahbakhti and Rush D. Robinett III. My advisors provided me with the encouragement, guidance, and mentorship and gave me the opportunity to develop my research background in the field of controls and optimization of energy systems. Mahdi's enthusiasm for research have motivated me to publish the research results in journal and conference articles. Dr. Rush D. Robinett facilitated my study by providing financial support during the course of my studies in the wonderful Upper Peninsula of Michigan. I thank Rush for his vision, and perpetual exergy for research which motivated me to explore new ideas.

Special thanks to Dr. Gordon Parker, Dr. Sumit Paudyal and Dr. Scott Miers who agreed to serve on my Dissertation Committee.

My colleague and my friend, Dr. Mehdi Maasoumy from UC-Berkley, was an important figure in shaping my background in controls theory, and applying control techniques to energy efficient buildings. Although Mehdi was not at MTU campus, I had the opportunity to receive his solid comments and discussions through email

communications, and online meetings.

I graciously acknowledge Dr. Sumit Paudyal and his PhD student, Guna R. Bharati, from Department of Electrical and Computer Engineering at MTU for a long-term collaboration in the field of building to grid. They helped me to build up the required background for power grid systems and write up the technical articles.

I would never forget the twists and turns at Mont Ripley ski slopes where I hit the ground face down multiple times, but kept going along my tortuous journey as a PhD student at MTU.

I would like to thank my colleague Dr. Mehran Bidarvatan, Mohammadreza Nazemi, and Mohammad Reza Mamini for their technical help during my PhD.

I am grateful to Mr. Gregory Kaurala (MTU Energy Management Assistant) for his valuable assistance and technical comments in collecting the building experimental data.

I would also like to thank many people who provided comments and suggestions on my research: Dr. Seyed, Dr. Ehsan Taheri, Amir Rezaei, Nastaran Alinezhad and Ali Soloukmofrad. I gratefully acknowledge Professor Bob Koch from the University of Alberta for providing the experimental data for Chapter 4 of this dissertation.

I acknowledge the help I received from my friend, Dr. Ali Mirchi and his beloved wife,

Sara Alian whose friendship and guidance made living pleasant up here! I would like to acknowledge my dear friends back home and around the globe: Ali Babalhavaeji, Dr. Hamidreza Bedri, Mohammad Rahbar, Mohammadali Mortazavi, Dr. Aref Bozorgavar Majdara, Amir Zandnia, Saeid Dini, Farzad Fatemipanah, Kenny Peterson, Lucia Li, Shayan Shafiee.

I owe deep gratitude to my parents, Pari Akbari and Nadali Razmara, to my supportive brothers Dr. Majid Razmara and Mahyar Razmara; my sacrificing sisters Pariva Razmara, and Dr. Parisa Razmara, my sister in law Dr. Maryam Sadeghi and my brother in law, Dr. Saeed Saeedijam.

List of Abbreviations

Parameters/ Variables	Chapter	Description and Unit
$\alpha_{i,j}$	2	Absorption coefficient of the wall between room i & j (-)
α	2	Fan power constant (kW.s^3/kg^3)
$A_{w_{i,j}}$	2	Area between room i^{th} & room j^{th} (m^2)
A_{win_i}	2	Total area of window on walls surrounding i^{th} room (m^2)
C	2	Cloud coverage constant (-)
clo	2	Clothing thermal resistance (m^2.C/W)
C_i^r	2	Heat capacity of the i^{th} room
$C_{i,j}^w$	2	Heat capacity of wall between room i & j (kJ/K)
c_a	2	Specific heat capacity of air (kJ/kg.K)
c_w	2	Specific heat capacity of wall material (kJ/kg.K)
d	2	Disturbance realization vector (-)
δ	2	Model uncertainty (-)
ϵ	2	Emissivity coefficient (-)
h_{in}	2	Inside convection heat coefficient (W/m^2.K)
h_{out}	2	Outside convection heat coefficient (W/m^2.K)
i	2	Number of room (-)

I_d	2	Discomfort index (°Ch)
I_e	2	Energy index (kWh)
I_{OP}	2	Overall performance index (-)
K	2	Cloud height coefficient (-)
k_w	2	Conductive heat transfer coefficient (kW/m.K)
L_w	2	Thickness of walls (m)
λ	2	The ℓ_∞ norm bound of the uncertainty (-)
met	2	The metabolic rate (1met = 58.2 W/m^2) (W/m^2)
$\dot{m}_c$	2	Cooling air mass flow rate (kg/s)
$\dot{m}_h$	2	Heating air mass flow rate (kg/s)
$\dot{m}_{r_i}$	2	Air mass flow rate into the i$^{\text{th}}$ room (kg/s)
$\mathcal{N}_{w_{i,j}}$	2	Set of all of neighboring nodes to node $w_{i,j}$ (-)
$\mathcal{N}_{r_i}$	2	Set of all of neighboring nodes to node i (-)
P_c	2	Cooling power (kW)
P_f	2	Fan power (kW)
P_h	2	Heating power (kW)
$Q_{\text{rad}_{i,j}}$	2	Radiative heat flux density on wall (i, j) (W/m^2)
Q_{bldg}	2	Heat flow from the building to the environment (W/m^2)
Q_{sky}	2	Heat flow from the sky to the building (W/m^2)
Q_{solar}	2	Solar heat flow to the building (W/m^2)
$\dot{Q}_{\text{int}_i}$	2	Internal heat generation in room i (W)

$r_{i,j}$	2	Wall identifier (-)
R_{i,j_k}	2	Total resistance between wall i & j & the side of wall (K/W)
$R_{i,j}^{\text{win}}$	2	Thermal resistance of window between room i & j (K/W)
RH	2	Relative humidity (-)
ψ	2	CO_2 concentration in the room (ppm)
σ	2	Stefan-Boltzmann law constant ($W/m^2.K^4$)
τ_{w_i}	2	Transmissivity of glass of window i (-)
T_{bldg}	2	Average temperature of the building (°C)
T_{r_i}	2	Temperature of the i^{th} room (°C)
T_{out}	2	Outside air temperature (°C)
$T_{w_{i,j}}$	2	Temperature of the wall between room i & j (°C)
T_{s_i}	2	Supply air temperature of the i^{th} room (°C)
$\underline{T}$	2	Lower limit on the room air temperature (°C)
$\overline{T}$	2	Upper limit on the room air temperature (°C)
v	2	Measurement noise (-)
w_i	2	Window identifier (-)
w_k	2	Model uncertainty (-)

Parameters/ Variables	Chapter	Description and Unit
$\alpha_{i,j}$	3	Absorption coefficient of the wall between room i & j (-)
$A^{w}_{i,j}$	3	Area between room i^{th} & room j^{th} (m^2)
A^{win}_{k}	3	Total area of window between room i and room k (m^2)
$c_{p_{avg}}$	3	Specific heat capacity at constant pressure (kJ/kg.K)
$c_{v_{avg}}$	3	Specific heat capacity at constant volume (kJ/kg.K)
COP	3	Coefficient of Performance $(-)$
C^{r}_{i}	3	Heat capacity of the i^{th} room (kJ/K)
$C^{w}_{i,j}$	3	Heat capacity of wall between room i & j (kJ/K)
$\underline{\epsilon}$	3	Lower slack variables vector (K)
$\overline{\epsilon}$	3	Upper slack variables vector (K)
gz	3	Specific gravitational potential energy (kJ/kg)
h	3	Enthalpy of the fluid (kJ/kg.K)
h_0	3	Dead-state enthalpy of the fluid (kJ/kg.K)
I_e	3	Energy index (kWh)
κ	3	fan coefficient ($W.s^3.kg^{-}3$)
m^{room}_{i}	3	mass of the air inside room i (kJ)
$\dot{m}^{r}_{i}$	3	Air mass flow into or out to the room i (kg/s)
N	3	Prediction time horizon (-)
$\mathcal{N}^{r}_{i}$	3	Set of all nodes surrounding room i (-)

$\mathcal{N}_{i,j}^{w}$	3	Set of all neighboring nodes to node $w_{i,j}$ (-)
$\pi_{i,j}$	3	Window identifier (-)
P_c	3	Cooling power (W)
P_h	3	Heating power (W)
P_f	3	Fan power (W)
Q_i^{rad}	3	Radiative heat flux density on wall (i,j) (W/m^2)
$\dot{Q}_i^{int}$	3	Internal heat generation in room i (W)
$\dot{Q}_i^{H.T.,k}$	3	Rate of heat transfer to room i (W)
ρ_{en}	3	Comfort Penalty for EMPC (kWh/K)
ρ_{ex}	3	Comfort Penalty for XMPC (kWh/K)
$r_{i,j}$	3	Wall identifier (-)
R	3	Gas constant (kJ/kg.K)
$R_{i,j}^{w}$	3	Thermal resistance of the centerline and the side of the wall (K/W)
$R_{i,j}^{win}$	3	Thermal resistance of window of room i & j (K/W)
ψ	3	Specific flow exergy (kJ/kg)
s	3	Entropy of the fluid (kJ/kg.K)
s_0	3	Dead-state entropy of the fluid (kJ/kg.K)
T_c	3	Cooling temperature (°C)
T_h	3	Heating temperature (°C)
T_0	3	Reference air temperature (°C)

T_i^s	3	Supply air temperature of the i$^{\text{th}}$ room (°C)
T_i^r	3	Temperature of i^{th} room ($°C$)
T_j^r	3	Temperature of j^{th} room neighboring room i ($°C$)
$T_{i,j}^w$	3	Temperature of the wall between room i and j ($°C$)
U_t	3	Vector of control inputs ($°C$)
$\underline{\mathcal{U}}$	3	Minimum value for control input ($°C$)
$\overline{\mathcal{U}}$	3	Maximum value for control input ($°C$)
$\delta\underline{\mathcal{U}}$	3	Lower limit on rate of change of supply air temperature ($°C$)
$\delta\overline{\mathcal{U}}$	3	Upper limit on rate of change of supply air temperature ($°C$)
v	3	Specific volume (-)
$\frac{V^2}{2}$	3	Specific kinetic energy of the fluid (kJ/kg)
$\dot{W}_i^r$	3	Rate of exergy transfer by work (W)
$\dot{X}_{dest_i}^r$	3	Rate of exergy destruction in i^{th} room (W)
$\dot{X}_i^{H.T.,r}$	3	Total exergy transfer by the heat transfer (W)

Parameters/ Variables	Chapter	Description and Unit
$CA50$	4	Crank-angle for 50% burnt fuel ($CADaTDC$)
$CA50_{OPT}$	4	Optimum CA50 ($CADaTDC$)
c_p	4	Specific heat at constant pressure ($J/kg.K$)
$\underline{\delta}^{\circ}$	4	Lower limitation on rate of change of CA50 ($CAD/Cycle$)
$\overline{\delta}^{\circ}$	4	Upper limitation on rate of change of CA50 ($CAD/Cycle$)
EOC	4	End of combustion ($CADaTDC$)
EGR	4	Exhaust gas recirculation rate (%)
$\eta_{II,CPEX}$	4	2^{nd} law efficiency for CPEX applications (%)
$\eta_{II,W}$	4	Second law efficiency for work (%)
$FMEP$	4	Friction mean effective pressure (Pa)
ϕ	4	Fuel-air equivalence ratio ($-$)
h	4	Specific enthalpy (J/kg)
H	4	Enthalpy (J)
$IMEP$	4	Indicated Mean Effective Pressure (bar)
LHV	4	Fuel lower heating value (J/kg)
m_{Fuel}	4	Fuel mass (kg)
m_{Air}	4	Air mass (kg)

MW_a	4	Molecular weight of air $(kg/mole)$
MW_{n-Hep}	4	Molecular weight of n-Heptane $(kg/mole)$
$MW_{iso-Oct}$	4	Molecular weight of iso-Octane $(kg/mole)$
μ	4	Specific chemical potential (J/kg)
N	4	Engine speed (RPM)
ON	4	Octane number $(-)$
P_{max}	4	In-cylinder maximum pressure (Pa)
P	4	In-cylinder pressure (Pa)
P_{man}	4	Intake manifold pressure (Pa)
Q_L	4	Heat-loss energy (J)
R_u	4	Universal gas constant $(J/mole.K)$
SOC	4	Start of combustion $(CADaTDC)$
s	4	Specific entropy $(J/kg.K)$
S	4	Entropy (J/K)
T	4	Temperature (K)
T_{man}	4	Intake manifold temperature (K)
U_p	4	Mean piston speed (m/s)
u	4	Specific internal energy (J/kg)
v	4	Specific volume (m^3/kg)
V_d	4	Displacement volume (m^3)

X_W	4	Exergy transfer by work (J)
X_{Exh}	4	Exhaust physical exergy (J)
$X_{d,Fric}$	4	Exergy destruction due to friction (J)
$X_{d,Comb}$	4	Exergy destruction due to combustion (J)
$X_{d,Mix}$	4	Exergy destruction due to mixing (J)
X_{Others}	4	Exergy loss/destruction due to $X_{d,Mix}$, $X_{Blow-by}$, X_{UHC} and etc. (J)
X_d	4	Total exergy destruction due to $X_{d,Fric}$, $X_{d,Comb}$ and X_{HT} (J)
$X_{Blow-by}$	4	Exergy loss corresponding to the blow-by gases (J)
X_{UHC}	4	Exergy loss due to UHC (J)
X_{HT}	4	Exergy destruction due to heat-loss (J)
$X_{Phys,in}$	4	Physical exergy of the mixture at IVC (J)
X_{Fuel}	4	Fuel exergy (J)
x_{total}	4	Total specific exergy (J/kg)
x_{Phys}	4	Specific physical exergy (J/kg)
x_{Chem}	4	Specific chemical exergy (J/kg)
$\mathcal{X}$	4	Engine model states vector
$\mathcal{Y}$	4	Engine model output vector
$\mathcal{U}$	4	Engine model input vector
$\mathcal{V}$	4	Engine model disturbance vector

Acronyms		
$aBDC$	4	After Bottom Dead Center
$aTDC$	4	After Top Dead Center
$CPEX$	4	Combined Power and Exhaust Exergy
CAD	4	Crank-Angle Degree
CHP	4	Combined Heat and Power
CI	4	Compression Ignition
CR	4	Compression Ratio
EVO	4	Exhaust Valve Opening
EVC	4	Exhaust Valve Closing
FLT	4	First Law of Thermodynamics
$HCCI$	4	Homogeneous Charge Compression Ignition
$HVAC$	4	Heating, Ventilation and Air-Conditioning
ICE	4	Internal Combustion Engines
IVO	4	Intake Valve Opening
IVC	4	Intake Valve Closing
LTC	4	Low Temperature Combustion
PRF	4	Primary Reference Fuel
SLT	4	Second Law of Thermodynamics
SI	4	Spark Ignition

Acronyms		
TEG	4	Thermo-Electric Generator
UHC	4	Unburnt Hydrocarbon
VVA	4	Variable Valve Actuation
$XCICE$	4	Exergy-based Control of Internal Combustion Engine
$XOCP$	4	Exergy-Based Optimal Combustion Phasing

Parameters/

Variables	Chapter	Description and Unit
$A^{w}_{i,j}$	5	Area of wall between room i and j (m^2)
$A^{win}_{i,j}$	5	Total area of window between room i and surrounding room j (m^2)
C	5	Output matrix with proper dimension to return output (-)
$C^{w}_{i,j}$	5	Heat capacity of the wall between room i and j (J/K)
C^{r}_{i}	5	Heat capacity of the room i (J/K)
$c_{p_{avg}}$	5	Average specific heat capacity of air $(J/kg.K)$
$c_{p_{avg}}$	5	Average specific heat capacity of air $(J/kg.K)$
$Ctap^{n}_{t}$	5	Number of capacitor banks switched on (-)
Δs	5	Voltage change (p.u.) (%)
ϵ	5	Deviation from comfort temperature bound (K)
ϕ	5	Power factor angle of the building load (-)
$\gamma_{i,j}$	5	Radiation heat absorption coefficient (W/m^2)
$I^{res,m-1}_{t}$	5	Receiving end currents on branch $m-1$ and m (A)
$I^{sen,m}_{t}$	5	Sending end currents on branch $m-1$ and m (A)
$I^{P,n}_{t}$	5	Currents from the constant power at node n (A)
$I^{I,n}_{t}$	5	Currents from the constant current at node n (A)
$I^{Z,n}_{t}$	5	Currents from the constant impedance at node n (A)
$I^{C,n}_{t}$	5	Currents from the capacitor banks at node n (A)
I^{F}_{t}	5	Fairness index (-)

I_{B2G}	5	Building-to-Grid (B2G) integration index (-)
L_f	5	Nodal load factor (-)
l	5	Number of inputs to each thermal zone (-)
λ	5	Fan power coefficient ($W.s^3/kg^3$)
m	5	Feeder branche (-)
$\dot{m}_i^r$	5	Air mass flow into or out of the room i (kg/s)
N	5	Prediction horizon (-)
n	5	Distribution grid node (-)
nb	5	Grid nodes where buildings are connected (-)
$\mathcal{N}_{i,j}^w$	5	Set of all neighboring nodes to node $w_{i,j}$ (-)
$\mathcal{N}_i^r$	5	Set of all nodes surrounding room i (-)
Ω	5	dynamic pricing of electricity ($/$Whr$)
P_t^B	5	Active power consumption of building (W)
P^h	5	Heating consumption of building (W)
P^c	5	Cooling power consumption of building (W)
P_t^{var}	5	Maximum allowable building active power penetration in the distribution grid (W)
P^o	5	Building's lighting and appliances loads (W)
$P_t^{E,nb}$	5	Base load in nodes nb (W)
P_t	5	Total active power load connected to the distribution grid at hour t (W)
P^f	5	Building's fan load (W)
p	5	Number of nodes (-)

$\pi_{i,j}$	5	Window identifier (-)
$Q_{i,j}^{rad}$	5	Radiative heat flux density on wall (i,j) (W/m^2)
Q_i^{rad}	5	Radiative heat flux density per unit area radiated to room i (W/m^2)
$\dot{Q}_i^{int}$	5	Internal heat generation in room i (W)
q	5	Number of nodes (-)
$R_k^{w_{i,j}}$	5	Thermal resistance between the node $w_{i,j}$ and node k (K/W)
$r_{i,j}$	5	Wall identifier (-)
ρ	5	Penalty for optimization's slack variables (-)
$T_{i,j}^w$	3	Temperature of the wall between room i and room j (K)
T_i^s	5	Temperature of the supply air to room i (K)
T_k^r	5	Temperature of adjacent rooms to wall $w_{i,j}$ (K)
T_k	5	Temperature of surrounding node k to room i (K)
T^h	5	Supply air temperatures in the heating mode (K)
T^c	5	supply air temperatures in the cooling mode (K)
$Ttap_t^m$	5	LTC tap positions (-)
$\tau_{i,j}^w$	5	Transmissivity of glass of window between room i and j (-)
$u(t)$	5	Control input vector (-)
V_t^n	5	Nodal voltage (V)
$w(t)$	5	The disturbance to the model (-)
$x(t)$	5	State vector of the system (-)
$y(t)$	5	Output vector of the system (-)
Z^n	5	Impedance of single capacitor in a bank at nominal power and voltage (Ω)

Abstract

Building and transportation sectors account for 41% and 27% of total energy consumption in the US, respectively. Designing smart controllers for Heating, Ventilation and Air-Conditioning (HVAC) systems and Internal Combustion Engines (ICEs) can play a key role in reducing energy consumption. Exergy or availability is based on the First and Second Laws of Thermodynamics and is a more precise metric to evaluate energy systems including HVAC and ICE systems. This dissertation centers on development of exergy models and design of model-based controllers based on exergy and energy metrics for grid-connected energy systems including HVAC and ICEs.

In this PhD dissertation, effectiveness of smart controllers such as Model Predictive Controller (MPC) for HVAC system in reducing energy consumption in buildings has been shown. Given the unknown and varying behavior of buildings parameters, this dissertation proposes a modeling framework for online estimation of states and unknown parameters. This method leads to a Parameter Adaptive Building (PAB) model which is used for MPC.

Exergy destruction/loss in a system or process indicates the loss of work potential. In this dissertation, exergy destruction is formulated as the cost function for MPC problem. Compared to RBC, exergy-based MPC achieve 22% reduction in exergy

destruction and 36% reduction in electrical energy consumption by HVAC system. In addition, the results show that exergy-based MPC outperforms energy-based MPC by 12% less energy consumption.

Furthermore, the similar exergy-based approach for building is developed to control ICE operation. A detailed ICE exergy model is developed for a single cylinder engine. Then, an optimal control method based on the exergy model of the ICE is introduced for transient and steady state operations of the ICE. The proposed exergy-based controller can be applied for two applications including (i) automotive (ii) Combined Heat and Power (CHP) systems to produce electric power and thermal energy for heating purposes in buildings. The results show that using the exergy-based optimal control strategy leads to an average of 6.7% fuel saving and 8.3% exergy saving compared to commonly used FLT based combustion control.

After developing thermal and exergy models for building and ICE testbeds, a framework is proposed for bilevel optimization in a system of commercial buildings integrated to smart distribution grid. The proposed framework optimizes the operation of both entities involved in the building-to-grid (B2G) integration. The framework achieves two objectives: (i) increases load penetration by maximizing the distribution system load factor and (ii) reduces energy cost for the buildings. The results show that this framework reduces commercial buildingsâĂŹ electricity cost by 25% compared to the unoptimized case, while improving the system load factor up to 17%.

Chapter 1

Introduction

The US building sector contributed 72% of total electricity consumption in 2006, which is projected to increase to 75% by 2025 [10]. The electricity consumption in the building sector is almost evenly distributed to commercial and residential buildings [10].

According to Energy Information Administration of DOE (EIA/DOE) [11], buildings account for 39% of the US total CO_2, a primary Greenhouse Gas (GHG), emissions. Of that total, 21% goes to the residential sector and 18% to the commercial sector.

In the US, buildings sector accounted for 41% of primary energy consumption and of that total, HVAC contributed 20% of energy consumption in 2010 [12]. According to the U.S. Environmental Protection Agency (EPA), 30% of the energy in commercial

buildings is wasted. Given the energy waste/consumption trend in the buildings sector, energy efficiency is one of the major ways to reduce GHG emissions, and energy consumption. Building Technology Office (BTO) has set a long-term goal for energy efficiency by 2025. BTO aims for reduction of residential energy consumption by 40% and commercial buildings by at least 35% compared to typical commercial buildings in 2010 [13].

The considerable amount of energy consumption and GHG emissions in building sector make HVAC systems a very attractive candidate for energy efficiency programs and policies. It has been proven that one of the most effective ways to reduce energy consumption is to design advanced controllers such as model-based controllers for buildings [1]. Figure 1.1 shows a cluster of smart buildings connected to a smart grid. Robustness, tunability, and flexibility of Model Predictive Control (MPC) make them a promising model-based control strategy for buildings. MPC has shown results for achieving higher energy efficiency in buildings. However, to design MPC, having an accurate model to predict system dynamics of the plant (i.e., building) is crucial. Such model should be able to provide an accurate temperature prediction of the building by capturing the interaction between the thermal behavior of the building's components, temperature schedules, and constraints [1]. Given the uncertain and time-varying physical, occupancy characteristics and also unmodeled dynamics, the parameters of the mathematical model need to constantly adapt to this change over time. In Chapter 2, a Parameter Adaptive Building (PAB) technique will be presented. In the

proposed method, PAB model learns and updates building time-varying parameters. Then, a comparative method is introduced to choose building controller among MPC, Robust MPC (RMPC) and conventional Rule Based Controller (RBC) based on model uncertainty. Chapter 2 builds the block of mathematical building model and MPC formulation required for integration of buildings-to-grid (B2G) framework.

To evaluate efficiency of HVAC systems, First Law of Thermodynamics (FLT) is always used as a metric in the context of building HVAC control. The FLT deals with energy conservation whereas Second Law of Thermodynamics (SLT) concerns entropy production and irreversibilities in processes which cause deficiency and energy waste. SLT states that energy has quality in addition to its quantity. Exergy or availability is the portion of energy that can do work in a specific environment. HVAC processes occur close to the environment temperature (25^oC) and therefore are considered as low quality energy demands. However, these demands are mostly granted with high quality energy (high exergy) sources such as electricity from grid which themselves are mainly obtained from high exergy sources such as fossil fuels.

HVAC systems can be operated in low exergy fashion by applying exergy-aware control algorithm which reduces irreversibilities. In other words, systems can be operated with less irreversibility and as a result, system operation will be more energy efficient and more sustainable.

Given the unprecedented focus on energy efficiency due to aforementioned facts, and

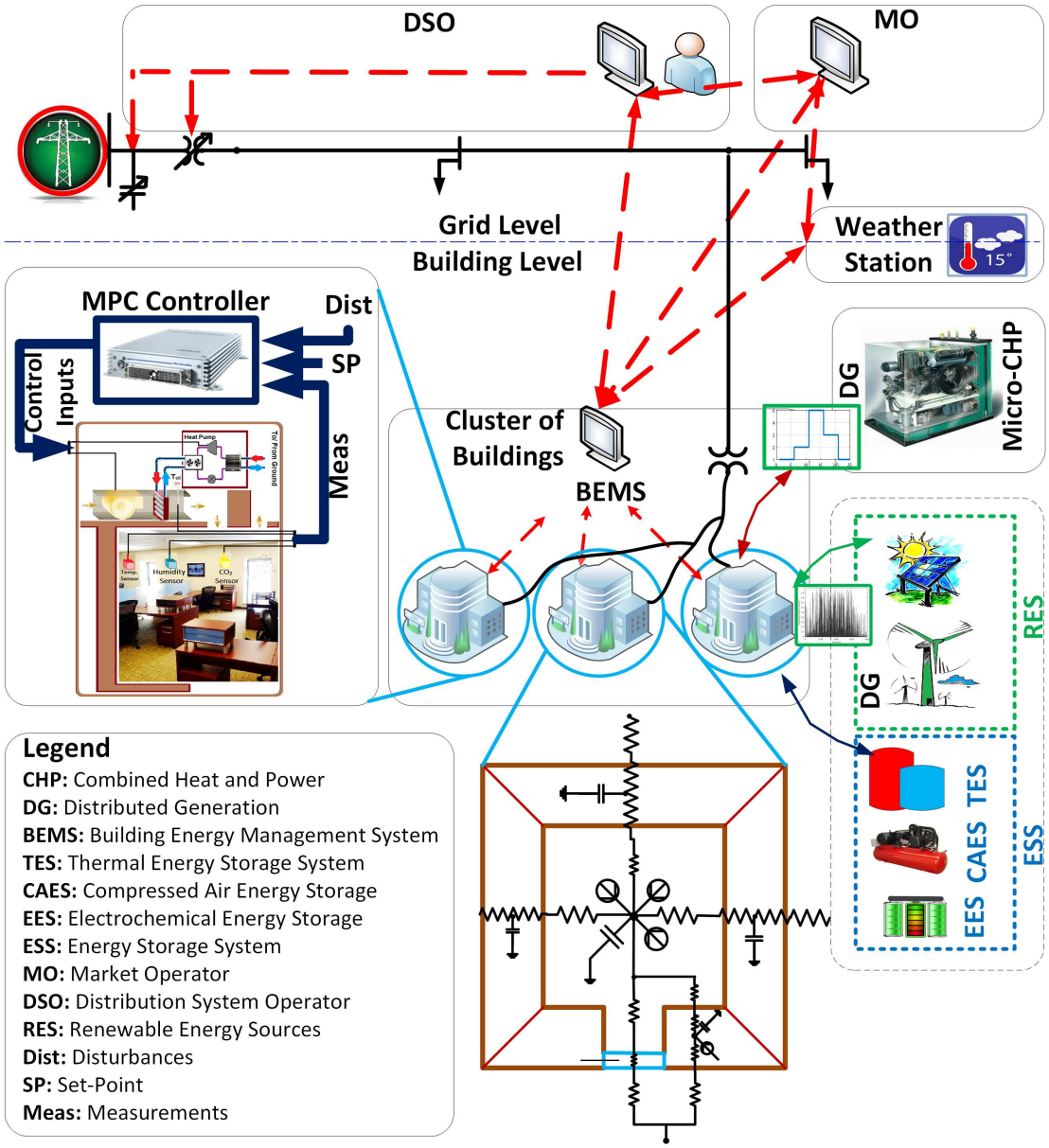

Figure 1.1: Concept summary of grid-connected energy systems and model-based predictive control.

at the same time, increasing penetration of Renewable Energy Sources (RES), controller design algorithms for building HVAC systems with exergy considerations is crucial. A comparison between exergy objective function with the price and the carbon emission objective functions has been made in [14] that shows economical benefits

of carefully managing exergy.

In Chapter 3, exergy is introduced as an appropriate metric to assess performance of an HVAC system. An exergy model of a testbed building and an MPC strategy based on the minimization of exergy destruction are developed. The Exergy-based MPC (XMPC) reduces irreversible entropy generation of an HVAC system by minimizing exergy destruction. It also addresses not only energy saving but also environmental concerns by saving exergy. Chapter 3 provides exergy model for buildings as one of the major components of the demand side connected to power grid (Figure 1.1).

Internal Combustion Engines (ICEs) are energy system devices that are widely used in Combined Heat and Power (CHP) systems, transportation and service/utility industries. ICEs account for over 22% of US total energy consumption [15, 16] and produce the largest portion of CO2 GHG emissions in urban areas [16, 17]. In 2011, a new standard for vehicles fuel economy model years 2017 to 2025 was announced by EPA [18]. According to this standard, fuel economy is required a 5% and 3.5% annual rise for passenger cars and light trucks, respectively. In 2010, transportation sector accounted for 23% global GHG emissions [19] and it is anticipated that the Production of GHG will rise by 29% from 2015 to 2030 [20]. Considering the fact that energy and GHG emission are not limited to building's sector, we designed an exergy-based control method for ICE which is also used in Combined Heat and Power (CHP) systems.

Recently, due to their high thermal efficiency, CHP systems as one of the emerging Distributed Generation (DG) are of interest for commercial and residential buildings. A grid-connected DG can operate in parallel to the grid or can operate in island as an Uninterruptible Power Supply (UPS) services [21]. Unlike renewables (e.g., wind and solar energy) which are intermittent in nature and considered as negative load, CHPs are considered as dispatchable supplies as shown in Figure 1.1. CHPs enable smart buildings' to reduce energy cost by supplying required power to buildings at peak price hours and benefit the distribution power grid.

CHP systems have three main parts: (i) ICE, (ii) heat exchanger, and (iii) Thermal Energy Storage System (TES). In ICEs, exergy can be destroyed through irreversible processes including combustion, heat transfer, friction and mixing. Exergy destruction in ICEs leads to the loss of work potential during operation. For instance, exergy destruction of the combustion process reduces the fuel potential to do mechanical work. Thus, identification of sources of exergy destruction in an ICE is crucial to enhance the engine performance and efficiency. SLT characterizes and quantifies the sources of irreversibility and exergy loss in ICEs. In Chapter 4, an Exergy-based control of ICE (XCICE) algorithm is introduced. XCICE optimizes the steady-state and transient operation of ICEs applicable for CHP systems and vehicles.

XCICE minimizes exergy losses and therefore maximizes SLT efficiency. Depending on the application, the desired output of an ICE can be power or Combined Power and

Exhaust Exergy (CPEX). Exhaust exergy can be used in both stationary and mobile applications of energy systems. For example, exhaust exergy is used in turbochargers to boost the intake pressure that leads to ICE fuel economy improvement and also exhaust exergy is recovered in CHP systems. CHP is an efficient method to produce thermal energy and shaft power simultaneously. The thermal energy of CHP is used or stored for domestic and commercial heating applications and generators convert shaft power to electric power. Chapter 4 builds the block of micro-CHP as a DG in power grid-connected energy systems shown in Figure 1.1.

Smart buildings can play a key-role in energy efficiency, comfort and ancillary service for distribution power grids. Smart buildings are a new generation of energy systems that provide comfort climate and services to the occupants by consuming optimum energy at optimum time of the day. As shown in Figure 1.1, Building Energy Management System (BEMS) in smart buildings communicates with occupants as the main clients, as well as weather stations, Market Operators (MO), and Distribution System Operators (DSO) to adjust and optimize their operations in both cost and energy effective ways. The smart building operation can provide services needed by distribution power grid system. These services include ancillary service e.g., voltage and frequency regulations, and Demand Response (DR). Unlike conventional buildings, smart buildings can provide Energy Storage Systems (ESS) and DG. Building's ESS offers flexibility to participate in DR and reduces the cost of energy by load shifting.

In Chapter 5 a B2G framework is proposed based on information exchange between the two levels, i.e, the BEMS and DSO control center. For the demand response applications discussed in this chapter, a bidirectional communication infrastructure is required between the BEMSs and the DSO. The proposed B2G optimization framework minimizes building's energy cost and provides DR service for grid and in particular maximizes distribution system load factor. The inputs to the algorithm are maximum demand limit, energy price, weather forecast, and the occupancy schedule. The contribution of Chapter 5 is on the development of generic hierarchical optimization framework for B2G system. Such development is essential for coordinated control of multiple BEMSs connected to distribution grid for large scale demand response and other grid level services. Chapter 5 constructs the framework for smart B2G connection shown in Figure 1.1.

Figure 1.2 summarizes the organization of chapters in this dissertation.

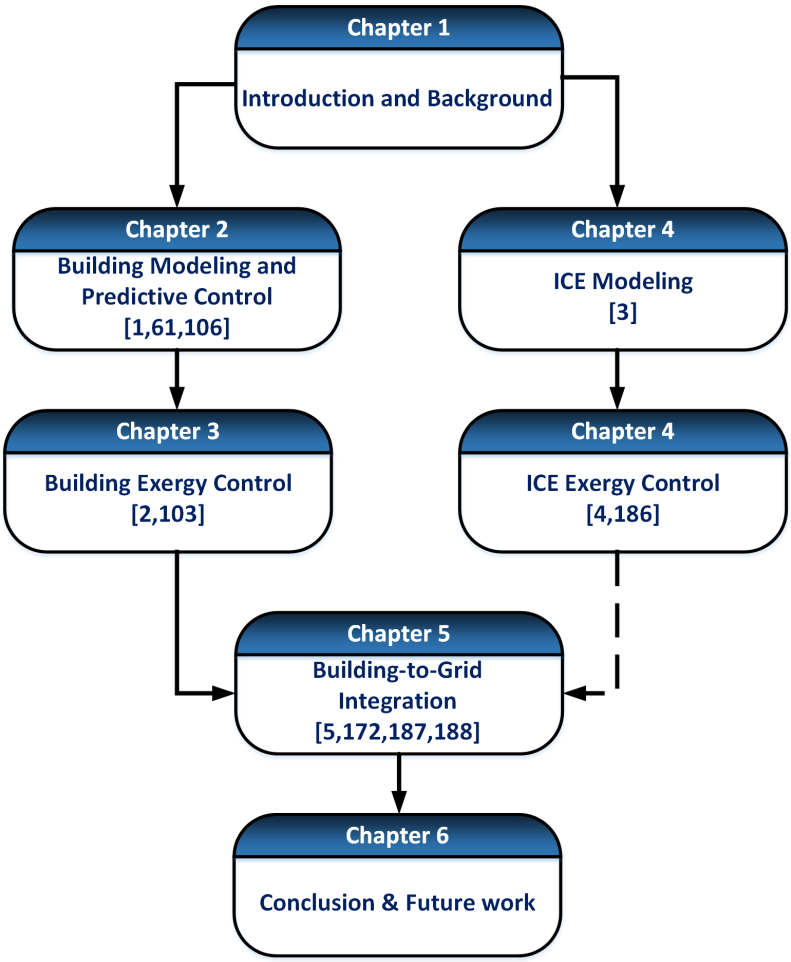

Figure 1.2: Organization of this dissertation.

Chapter 2

Handling Model Uncertainty in Model Predictive Control for Energy Efficient Buildings[1]

Model uncertainty is a significant challenge to more widespread use of model predictive controllers (MPC) for optimizing building energy consumption. This dissertation presents two methodologies to handle model uncertainty for building MPC. First, we propose a modeling framework for online estimation of states and unknown parameters leading to a parameter-adaptive building (PAB) model. Second, we propose a robust model predictive control (RMPC) formulation to make a building controller

[1]This chapter has been published in Journal of Energy and Buildings [1] (doi:10.1016/j.enbuild.2014.03.057) with permissions from Elsevier as shown in Appendix E

robust to model uncertainties. The results from these two approaches are compared with those from a nominal MPC and a common building rule based control (RBC). The results are then used to develop a methodology for selecting a controller type (i.e. RMPC, MPC, or RBC) as a function of building model uncertainty. RMPC is found to be the superior controller for the cases with an intermediate level of model uncertainty (30âĂŞ67%), while the nominal MPC is preferred for the cases with a low level of model uncertainty (0âĂŞ30%). Further, a common RBC outperforms MPC or RMPC if the model uncertainty goes beyond a certain threshold (e.g. 67%).

2.1 Introduction

Reducing the energy consumption of buildings by designing smart controllers for operating the HVAC system in a more efficient way is critically important to address energy and environmental concerns [12]. Advanced control algorithms are considered major enablers to achieve higher energy efficiency in commercial buildings. Entire sections of the ASHRAE 90.1 standard [22] are dedicated to the specification of control requirements. Although the optimal control of an HVAC system is a complex multi-variable problem, it is standard practice to rely on simple control strategies that include on-off controllers with hysteresis, and PID controllers.

For optimal control design a thermal model of the building is needed. To achieve

building-level energy-optimality, building model should be able to capture the interaction between physically connected spaces in the building, heat storage in walls, and provide an accurate prediction of temperature in the building. Control algorithm on the other hand, should be able to minimize energy consumption and optimize thermal comfort by exploiting occupancy schedules, weather forecast, and system dynamics (i.e. a model to predict temperature evolution of indoor air), and satisfy state (i.e. room air temperature and wall temperatures) and inputs (i.e. discharge air temperature and air mass flow rate) constraints and operate the HVAC system of the building in an optimal fashion within the range of operation of the components.

Model Predictive Control (MPC) is a promising control strategy that is capable of addressing all the aforementioned criteria and has shown results for achieving higher energy efficiency in buildings [23, 24, 25, 26, 27]. MPC can provide a potential building energy saving of 16%-41% compared to the commonly used rule-based building HVAC controllers [23, 28, 29]. Other advantages of MPC for building HVAC systems include robustness, tunability, and flexibility [23]. Application of MPC for building energy control has been reported in the literature [23, 27, 28, 30, 31, 32, 33, 34]. There are different variations of nominal MPC such as distributed [33, 35], robust [30, 36] and stochastic [24, 27] MPC strategies to systematically address various challenges in building energy control. In [37] the authors propose a computationally tractable approximation of the nonlinear optimal control problem by which they optimize the

predicted mean vote (PMV) index, as opposed to the static temperature range. A robust control strategy based on static pressure and supply air temperature reset control is presented in [38] for variable air volume (VAV) system. [39] proposes a controller based on a three mode robust control strategy where each mode addresses different control objectives and conditions; this proposed controller is robust in different load conditions. Authors of [40] showed that in presence of model uncertainty an H_∞-robust controller achieves not only a robust performance on set-point tracking of the air-handling unit but also less energy consumption compared to the pole-placement controller. Authors in [41] observed that indoor zone volume acts as system's bifurcation parameter. A multi-variable regulation strategy based on feedback linearization is used to prevent secondary Hopf bifurcation. The designed control improves the limit cycle behavior and decreases indoor temperature variation.

However, these control techniques rely heavily on a perfect (or almost perfect) mathematical model of the building and a perfect estimation of the unmodeled dynamics of the system [23] to achieve considerable energy saving. In [28] the authors argue that, based on industrial experience, modeling is the most time-demanding and costly part of the automation process. Recently, numerous mathematical models of building thermal dynamics have been proposed in the literature. Resistor-capacitor (RC) models with disturbances to capture unmodeled dynamics have been proposed in [23, 29, 42]. A bilinear version of an RC model is presented in [27] that takes into account weather predictions to increase building energy efficiency. In [43], the authors found that time

varying properties such as occupancy can significantly change the dynamic thermal model and influence how building models are identified. While modeling a multi-zone building, the authors of [43] observed that the experimental data often did not have sufficient quality for system identification and hence, proposed a closed-loop architecture for active system identification using prediction-error identification method (PEM). Although a great deal of progress has been made in modeling the thermal behavior of building envelope and HVAC system [23, 25, 26, 29, 42, 44], the random nature of some components of these systems makes it very hard to predict, with high fidelity, the temperature evolution of the building using mathematical models.

Buildings are dynamical systems with uncertain and time-varying physical and occupancy characteristics. The heat transfer characteristics of a building are highly dependent on the ambient conditions. For instance, heat transfer properties such as convective heat transfer coefficient h, of peripheral walls is dependent on outside temperature, wind speed and direction. Also, unmodeled dynamics of a building [23] is function of 1) *external factors*: ambient weather conditions such as radiative heat flux into the walls and windows, and cloudiness of the sky, and 2) *internal factors:* such as occupancy level, internal heat generation from lighting, and computers. These quantities are highly time-varying and therefore the dynamics of the building and, consequently, parameters of the mathematical model need to constantly adapt to this change over time.

One approach to increase the accuracy of the linear building models is to use an adaptive parameter estimation technique such that the building parameters are updated as the environment changes which leads to an adaptive modeling framework. Although this technique has been used for joint state-parameter estimation in other applications [45, 46, 47], to the best of the authors' knowledge, this dissertation is the first study on developing adaptive modeling framework for simultaneous estimation of building *parameters*, *states* and *unmodeled dynamics*.

Four approaches can be taken to model dynamic behavior of buildings and overcome model uncertainty for building controls:

1. Develop detailed nonlinear physical models for building [48, 49], and infer time-varying factors such as weather conditions, occupancy level, etc [50].

2. Incorporate sensors to measure time-varying factors [51, 52].

3. Develop an adaptive computationally efficient model which learns and updates building time-varying parameters.

4. Design building controllers which are robust to model uncertainties.

The first approach is typically computationally expensive. Consequently, its application for real-time building controls is limited. The second approach provides accurate information about time-variation of influential factors on building performance but

this approach is not cost-efficient and can be limited by the possibility of adding new sensors to a building. The third and fourth approaches are promising and they are the focus of this Chapter. In particular, we develop a parameter adaptive building (PAB) model and design a robust MPC for buildings. In this Chapter we build upon our previous work reported in [23, 29, 36, 42, 53].

The overall contribution of this Dissertation is putting together modeling, control and co-design in a coherent framework to develop a methodology for selecting a controller type (i.e. RMPC, MPC, or RBC) as a function of building model uncertainty. Particular contributions are:

1. A novel adaptive modeling framework for building predictive control is presented. The modeling framework also illustrates the application of unscented Kalman filter (UKF) technique for building online parameter identification and state estimation

2. Impact of model uncertainty on HVAC predictive controllers is characterized.

3. A new RMPC structure that uses disturbance feedback parameterization of the input is introduced. We show that this parameterization reduces the number of decision variables of the optimization problem and hence results in a faster alternative to the existing parameterizations in the literature, while maintaining the performance level of the RMPC.

4. A guideline for choosing an MPC versus an RMPC, versus a rule-based control based on the level of model uncertainty is proposed.

The rest of this Chapter is organized as follows. Section 2 explains the experimental setup used to collect data for this Thesis. We present the proposed parameter adaptive building (PAB) model and the developed parameter/state estimation technique in Section 3. Controller design and performance results for MPC and RMPC, as well as the indices based on which we assess the performances of the introduced controllers are presented in Section 4. Conclusions are drawn in Section 5.

2.2 Test-Bed and Historical Data

The model studied in this chapter is a model for an office room in Lakeshore building at Michigan Technological University. This room is surrounded by two rooms and a corridor in the building and connected to the outdoor area with a thick concrete wall and two south-oriented double-layered windows. Each room is equipped with temperature and humidity sensors (Uni-curve Type II) with the temperature accuracy of $\pm 0.2°C$ as part of the Building Management System (BMS). We have used a different sensing device, (temperature data logger with accuracy of $\pm 0.8°C$) to account for spatial temperature variation in the room and sensing accuracies of individual sensors. Location of the zone sensors are shown in Fig. 2.1. Temperature readings

from these two sensors are shown in Fig. 2.2. We follow the methodology proposed in [53] to find the temperature measurement accuracy, which is obtained to be $\pm 0.8°C$, and is used in the state estimation algorithm which is described in section 2.3.3. Outdoor temperature is also measured by the BMS system.

Figure 2.1: Location of the temperature sensors in the test-bed. The sensor 1-a is the room temperature sensor and the sensor 1-b is a temperature data logger installed to calculate measurement errors.

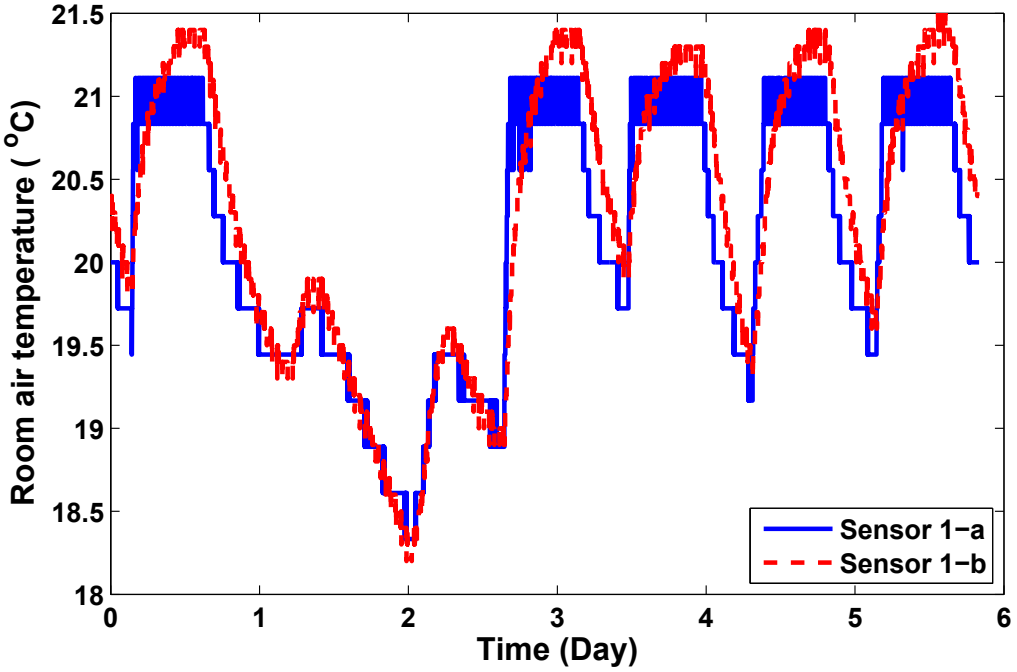

Figure 2.2: Data logger and BMS sensor temperature readings in Fig. 2.1.

The HVAC system in the building uses Ground-Source Heat-Pumps (GSHP) to obtain required energy for heating purposes. Each unit in this system provides heating for an individual zone. Therefore, a unit operates when heating is required for its zone: the setpoint can be defined independently based on the functionality of each zone. The HVAC system uses an on-off controller to provide a desired temperature for each zone. Zone temperatures are measured with a sampling period of 60 seconds.

2.3 Parameter Adaptive Building (PAB) Model

Building models proposed in the literature depend on many parameters. The reason is that buildings are composed of many sub-systems and a variety of thermal mechanisms takes place in the building such as heat conduction through walls, forced convection due to air conditioning systems, and thermal radiation from outside. A mathematical model that is descriptive enough to accurately explain these phenomena will end up with many time-varying parameters. Finding the best parameters at each time step is shown to be cumbersome [43]. In this section *we propose and develop a novel parameter adaptive building (PAB) model that facilitates this parameter tuning process in an online and automatic fashion*. The architecture of the proposed PAB model is shown in Fig. 2.3. Measurement data from various sensors such as temperature and airflow are stored in a data repository. The PAB model has a parameter update module which takes care of automatic parameter tuning on the fly, and is explained in detail later in this section. The PAB model works as follows: Historical data is used to perform off-line, one-step model calibration. The obtained parameters from model calibration is used in the parameter update module (exploiting Kalman filtering algorithm) as an initial set of parameters. Kalman filter updates the parameters of the building model, as the new measurements arrive. The control module then uses the new updated set of parameters for the next time step.

Here we first review fundamental heat transfer mechanisms in buildings, leading to a mathematical model of building climate, on top of which we develop the PAB model in the rest of this section.

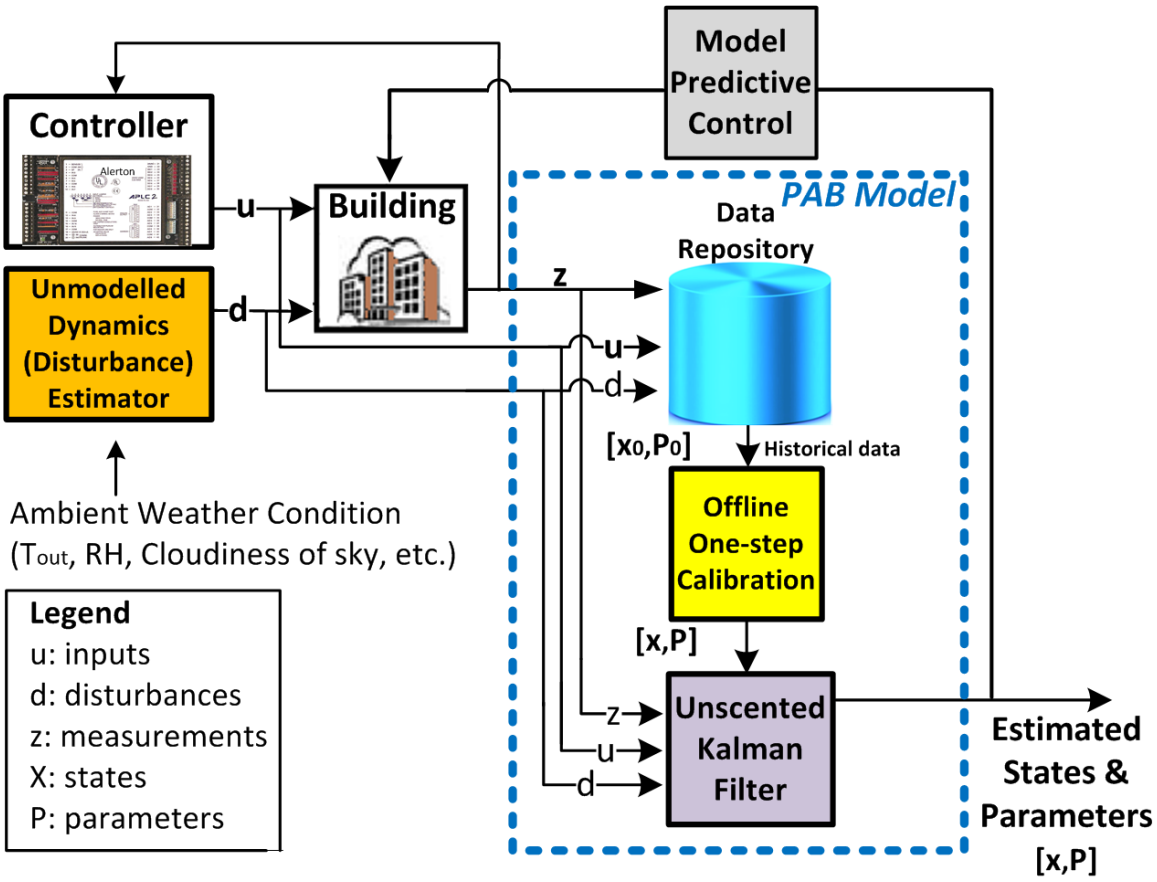

Figure 2.3: Architecture of the building control based on the proposed PAB model with its components.

2.3.1 Mathematical Modeling

Fig. 2.4 depicts the schematic of a typical room studied in this chapter. We use lumped model analysis [54] to reduce the complexity of the model, and obtain a low

order model, suitable for control purposes. As a simplifying assumption, temperature is considered uniform inside the room. We use RC model from [42] in which the building is considered as a network of nodes. We account for *time varying* parameters by updating the parameters on the fly. More details on online parameter estimation is presented in Section 2.3.2.

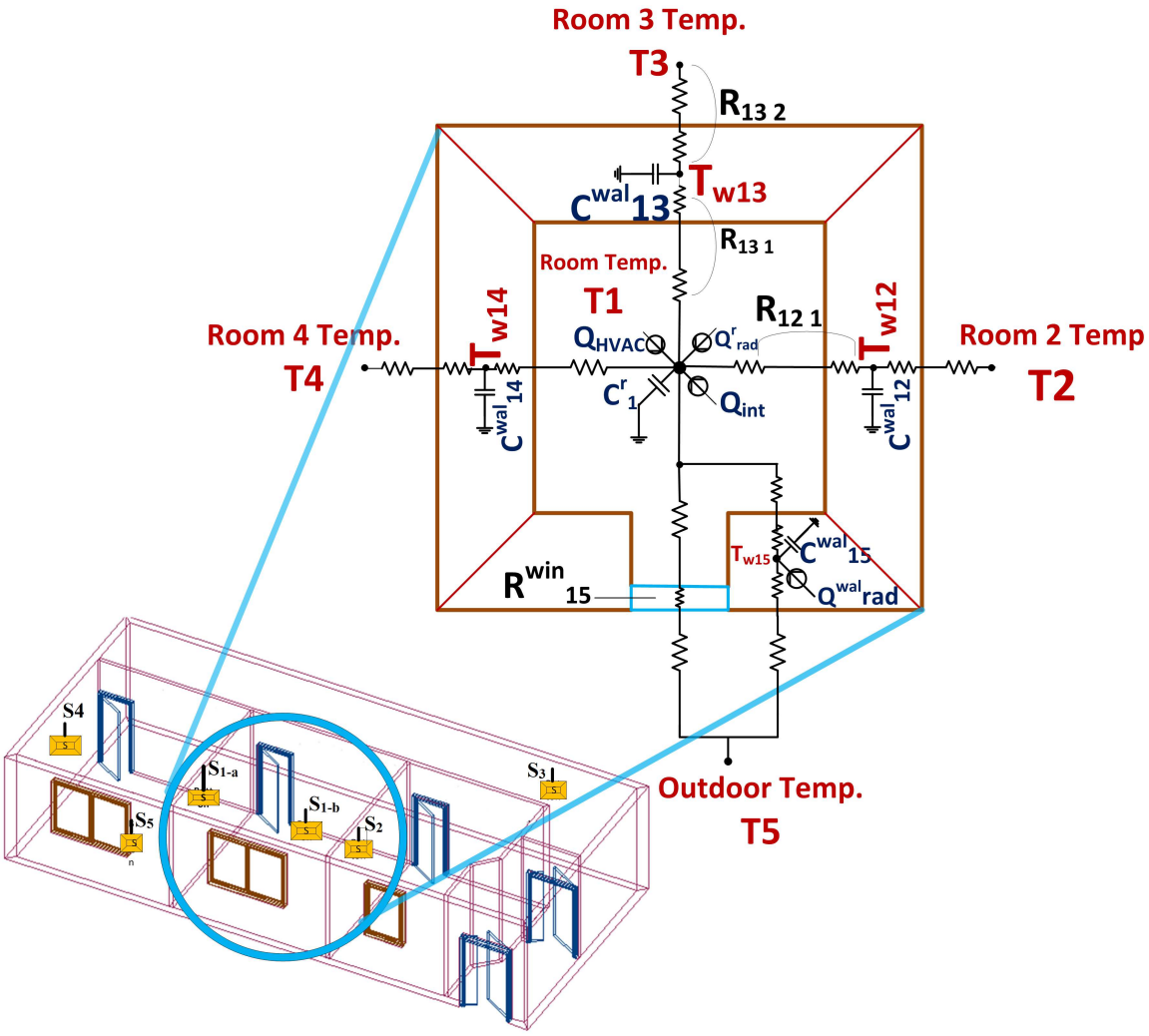

Figure 2.4: Schematic of a typical room with a window. Temperature sensors are denoted by "S" in this figure.

2.3.1.1 Heat Transfer

There are two types of nodes in the building network: walls and rooms. Consider in total n nodes, m of which represent rooms and the remaining $n-m$ nodes represent walls. We denote the temperature of room i with T_{r_i}. The wall node and temperature of the wall between room i and j are denoted by (i,j) and $T_{w_{i,j}}$, respectively, thermal dynamics of which is governed by the following equation:

$$C^w_{i,j}\frac{dT_{w_{i,j}}}{dt} = \sum_{k\in\mathcal{N}_{w_{i,j}}} \frac{T_{r_k} - T_{w_{i,j}}}{R_{i,j_k}} + r_{i,j}\alpha_{i,j}A_{w_{i,j}}Q_{\mathrm{rad}_{i,j}} \tag{2.1}$$

where $C^w_{i,j}$, $\alpha_{i,j}$ and $A_{w_{i,j}}$ are heat capacity, radiative heat absorption coefficient and area of wall between room i and j, respectively. R_{i,j_k} is the total thermal resistance between the centerline of wall (i,j) and the side of the wall where node k is located. $Q_{\mathrm{rad}_{i,j}}$ is the radiative heat flux density on wall (i,j). $\mathcal{N}_{w_{i,j}}$ is the set of all of neighboring nodes to node $w_{i,j}$. $r_{i,j}$ is wall identifier which is equal to 0 for internal walls, and equal to 1 for peripheral walls (*i.e.* either i or j is an outside node). In equation (2.1) the left term denotes the rate of change of stored heat in the wall between room i and room j. The first term of the right hand side of this equation represents the flow of heat between room k and wall (i,j) due to temperature difference and the second term shows the heat flow to the wall, due to solar radiation. Temperature

dynamics of the i^{th} room is modeled by the following equation:

$$C_i^r \frac{dT_{r_i}}{dt} = \sum_{k \in \mathcal{N}_{r_i}} \frac{T_k - T_{r_i}}{R_{i,k_i}} + \dot{m}_{r_i} c_a (T_{s_i} - T_{r_i}) + w_i \tau_{w_i} A_{\text{win}_i} Q_{\text{rad}_i} + \dot{Q}_{\text{int}_i} \tag{2.2}$$

where T_{r_i}, C_i^r and $\dot{m}_{r_i}$ are the temperature, heat capacity and air mass flow into room i, respectively. c_a is the specific heat capacity of air, and T_{s_i} is the temperature of the supply air to room i. π_i is window identifier which is equal to 0 if none of the walls surrounding room i have a window, and is equal to 1 if at least one of them has a window. τ_{w_i} is the transmissivity of glass of window i, A_{win_i} is the total area of windows on walls surrounding room i, Q_{rad_i} is the radiative heat flux density per unit area radiated to room i, and $\dot{Q}_{\text{int}_i}$ is the internal heat generation in room i. $\mathcal{N}_{r_i}$ is the set of all of the neighboring *room* nodes to room i. In equation (2.2) the left term denotes the rate of change of stored heat in the air in room i. The first term of the right hand side of this equation represents the flow of heat between node k and room i due to temperature difference, the second term shows the heat flow delivered by the heating system, the third term represents the total radiative heat passing through the windows and the fourth term is the internal heat generation inside room i. More details of building thermal modeling and estimation of the unmodeled dynamics is available in [23, 29, 42]. Note that we approximate the values of $Q_{\text{rad}_i}(t)$ and $\dot{Q}_{\text{int}}(t)$

based on the following equations:

$$Q_{\mathrm{rad}_i}(t) = \tau T_{\mathrm{out}}(t) + \zeta \tag{2.3}$$

$$\dot{Q}_{\mathrm{int}}(t) = \mu \Psi(t) + \nu \tag{2.4}$$

where T_{out} and Ψ are the outside air temperature and CO_2 concentration in the room, respectively [55]. Air ventilation is considered constant as a simplifying assumption. A more sophisticated model for gas transport process in buildings can be found in [56]. Parameters τ, ζ, μ and ν are obtained by the parameter estimation algorithm detailed in Section 2.3.3.

We model the radiative heat transfer between building and ambient environment as proposed in [57]. The amount of heat transferred from the building to the environment is given by the Stefan-Boltzmann law:

$$Q_{\mathrm{bldg}} = \epsilon \sigma T_{\mathrm{bldg}}^4 \tag{2.5}$$

where T_{bldg} is the average temperature of the building. We also consider solar radiation heat transfer, Q_{solar} absorbed by the walls, and the room through the windows. The data used in this chapter is based on the past 30 years monthly average of solar

radiation for flat-plate collectors facing south (resembling the south facing flat vertical walls of the building), and is obtained from NREL (National Renewable Energy Laboratory) [58] database for Houghton, MI in January. Furthermore, we take into account the radiation cooling at night (*i.e.* sky thermal radiation to the building) based on the proposed relation in [57]:

$$Q_{\text{sky}} = (1 + KC^2)8.78 \times 10^{-13} T_{\text{out}}^{5.852} RH^{0.07195} \tag{2.6}$$

where K is the coefficient related to the cloud height and C is a function of cloud coverage. We use $K = 0.34$ and $C = 0.8$ for simulations, based on the results in [57]. T_{out} is the outside air temperature, and RH is the air relative humidity percentage.

The total radiation exchange between building and ambient environment is then given by:

$$Q_{\text{rad}} = Q_{\text{sky}} + Q_{\text{solar}} - Q_{\text{bldg}} \tag{2.7}$$

Note that Q_{sky} and Q_{solar} are heat flow *into* the building, and Q_{bldg}, is the heat flow *from* the building *to* the environment.

2.3.1.2 System Dynamics

Heat transfer equations for walls and rooms yield the following system dynamics:

$$\dot{x}_t = f(x_t, u_t, d_t, t)$$
$$y_t = Cx_t \tag{2.8}$$

where $x_t \in \mathbb{R}^n$ is the state vector representing the temperature of the nodes in the thermal network, $u_t \in \mathbb{R}^{lm}$ is the input vector representing the air mass flow rate and discharge air temperature of conditioned air into each thermal zone, and $y_t \in \mathbb{R}^m$ is the output vector of the system which represents the temperature of the thermal zones. l is the number of inputs to each thermal zone (e.g., two for air mass flow and supply air temperature). C is a matrix of proper dimension and the disturbance vector is given by $d_t = g(Q_{\text{rad}_i}(t), \dot{Q}_{\text{int}}(t), T_{\text{out}}(t))$.

2.3.1.3 Disturbance

Following the intuitive linear relation between outside temperature T_{out}, internal heat generation $\dot{Q}_{\text{int}}$, and solar radiation Q_{rad}, with the building internal temperature rise

we approximate g with an affine function of these quantities, leading to:

$$d_t = aQ_{\text{rad}_i}(t) + b\dot{Q}_{\text{int}}(t) + cT_{\text{out}}(t) + e \tag{2.9}$$

where a, b, c, e are constants to be estimated. By substituting (2.3) and (2.4) into (2.9) and rearranging the terms, we get:

$$\begin{aligned} d_t &= (a\tau + c)T_{\text{out}}(t) + b\mu\Psi(t) + a\zeta + b\nu + e \\ &= \bar{a}T_{\text{out}}(t) + \bar{b}\Psi(t) + \bar{e} \end{aligned} \tag{2.10}$$

where $\bar{a} = a\tau + c$, $\bar{b} = b\mu$, and $\bar{e} = a\zeta + b\nu + e$. Therefore, only measurements of outside air temperature and CO_2 concentration levels are needed to determine the disturbance to the model. The values of $\bar{a}$, $\bar{b}$, and $\bar{e}$ are estimated along with other parameters of the model.

2.3.1.4 Additive uncertainty

We linearize the original nonlinear dynamic system and use Euler's discretization method to obtain a linear discrete-time system. We also add an additive uncertainty to the state update equation to account for model uncertainties, leading to:

$$x_{k+1} = Ax_k + Bu_k + E(d_k + w_k) \tag{2.11}$$

where the uncertainty $w_k \in \mathbb{R}^r$ is a stochastic additive disturbance. $t \in \mathbb{R}$ refers to time in continuous-time domain and $k \in \mathbb{Z}$ refers to time in discrete-time domain. The set of possible disturbance uncertainties is denoted by $\mathcal{W}$ and $w_k \in \mathcal{W} \ \ \forall k = 0, 1, ..., N-1$. For this study, we consider box-constrained disturbance uncertainties given by

$$\mathcal{W}_\lambda = \{w : ||w||_\infty \leq \lambda\} \tag{2.12}$$

2.3.2 State-Parameter Estimation

Using (2.1) for each wall and (2.2) for each room node in the building network, system dynamics is given by:

$$\begin{aligned}\dot{x}_1 = \frac{1}{C_1^r} \cdot \Bigg(\Bigg(&\frac{1}{R_{12_1}} - \frac{1}{R_{13_1}} - \frac{1}{R_{14_1}} - \frac{1}{R_{15_1}} - \frac{1}{R_{15}^{\text{win}}} - \dot{m}_{r1} c_a \Bigg) x_1 \\ &+ \frac{x_2}{R_{12_1}} + \frac{x_3}{R_{13_1}} + \frac{x_4}{R_{14_1}} + \frac{x_5}{R_{15_1}} + c_a T_{s1} \dot{m}_{r1} + \frac{T_5}{R_{15}^{\text{win}}} + A_{\text{win}} \tau Q_{\text{rad}} + \dot{Q}_{\text{int}_1} \Bigg)\end{aligned} \tag{2.13a}$$

$$\dot{x}_2 = \frac{1}{C_{21}^w} . \left(\frac{x_1}{R_{21_1}} - \left(\frac{1}{R_{21_1}} + \frac{1}{R_{21_2}} \right) x_2 + \frac{T_2}{R_{21_2}} \right) \tag{2.13b}$$

$$\dot{x}_3 = \frac{1}{C_{31}^w} . \left(\frac{x_1}{R_{31_1}} - \left(\frac{1}{R_{31_1}} + \frac{1}{R_{31_3}} \right) x_3 + \frac{T_3}{R_{31_3}} \right) \tag{2.13c}$$

$$\dot{x}_4 = \frac{1}{C_{41}^w} . \left(\frac{x_1}{R_{41_1}} - \left(\frac{1}{R_{41_1}} + \frac{1}{R_{41_4}} \right) x_4 + \frac{T_4}{R_{41_4}} \right) \tag{2.13d}$$

$$\dot{x}_5 = \frac{1}{C_{51}^w} . \left(\frac{x_1}{R_{51_1}} - \left(\frac{1}{R_{51_1}} + \frac{1}{R_{51_5}} \right) x_5 + \frac{T_5}{R_{51_5}} + A_{w_{51}} \alpha Q_{\text{rad}} \right) \tag{2.13e}$$

where x_1 is the room temperature (T_{r_1}), and x_2, x_3, x_4, x_5 are the peripheral walls' temperature (i.e. T_{w12}, T_{w13}, T_{w14}, T_{w15}). T_2, T_3, T_4, T_5 are the temperatures of the surrounding zones, as shown in Fig. 2.4 and Fig. 2.5. These temperatures act as disturbance to the system dynamics for a single zone thermal model, and x is the state vector:

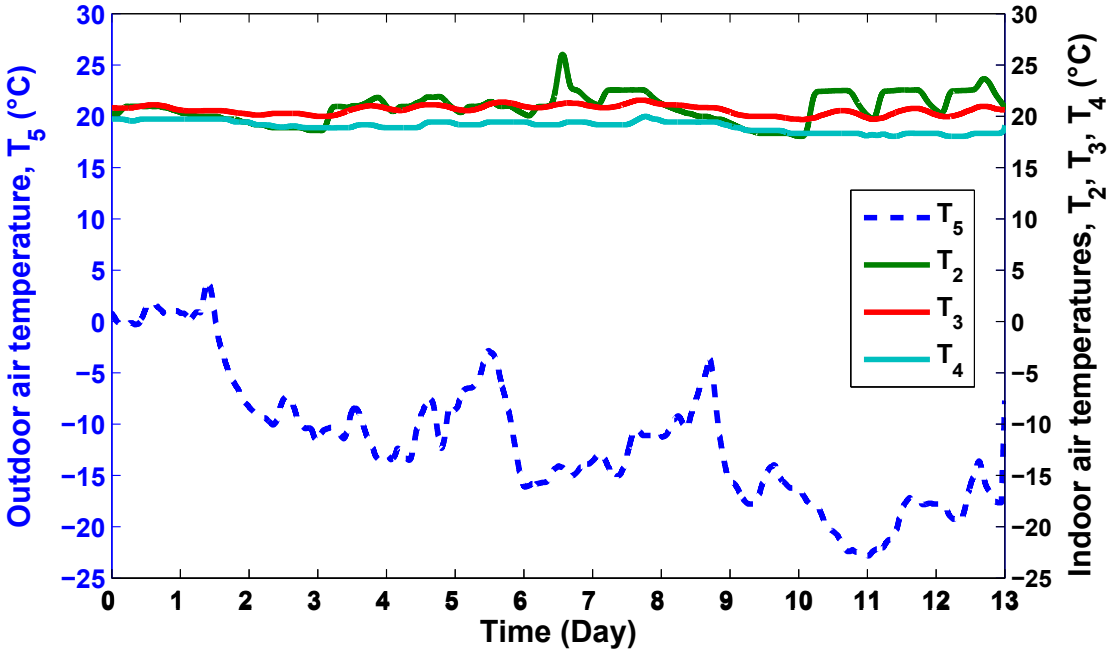

Figure 2.5: Temperatures of neighboring zones acting as disturbance to the PAB model.

$$x = \left[T_{r1}, T_{w12}, T_{w13}, T_{w14}, T_{w15}\right]^T \tag{2.14}$$

One way to adapt the model to account for time varying parameters is to assume

that all the parameters of the model are independent, and hence define a state corresponding to each parameter. However, this would lead to excessive number of states (e.g. 18 states for a room shown in Fig. 2.4). To overcome this problem, we take a different approach. We reduce the number of states by exploiting the redundancies in the resulting model. For instance, thermal properties of wall material (e.g. specific heat capacity and conductive heat transfer coefficient) are the same across the building, as these are functions of the materials used as the building walls. In addition, the thickness of internal walls and thickness of peripheral walls are the same throughout the building. Following this approach, we are able to reduce the number of independent parameters from 18 to 10. Hence we re-write the thermal equations of the walls, *i.e.* (2.13b)-(2.13e) as follows:

$$\dot{x}_2 = \frac{x_1}{C^w R^w} - \frac{2}{C^w R^w} x_2 + \frac{T_2}{C^w R^w} \tag{2.15}$$

$$\dot{x}_3 = \frac{x_1}{C^w R^w} - \frac{2}{C^w R^w} x_3 + \frac{T_3}{C^w R^w} \tag{2.16}$$

$$\dot{x}_4 = \frac{x_1}{C^w R^w} - \frac{2}{C^w R^w} x_4 + \frac{T_4}{C^w R^w} \tag{2.17}$$

$$\dot{x}_5 = \frac{x_1}{C^w_{51} R_{51_1}} - \left(\frac{1}{C^w_{51} R_{51_1}} + \frac{1}{C^w_{51} R_{51_5}} \right) x_5 + \frac{T_5}{C^w_{51} R_{51_5}} + \frac{A_{w_{51}} \alpha Q_{\text{rad}}}{C^w_{51}} \tag{2.18}$$

As shown in (2.19), $C_w R_w$ is not a function of the area of wall:

$$C^w R_w = (c_w A_w L_w)(\frac{L_w/2}{k_w A_w} + \frac{1}{h_{in} A_w}) = \frac{c_w L_w^2}{2k_w} + \frac{c_w L_w}{h_{\text{in}}} \tag{2.19}$$

where c_w, k_w, A_w and L_w are the specific heat capacity, conductive heat transfer coefficient of wall material, area and thickness of wall, respectively, and h_{in} is the indoor convective heat transfer coefficient. Hence, we can use one common term to express thermal capacitance-resistance between centerline of each wall and the node on each side of the wall for the equations of walls in the building.

We designate a state variable to all the independent time-varying parameters of the system as follows:

$$x_6 = \frac{1}{C_1^r R_{12_1}} \qquad x_7 = \frac{1}{C_1^r R_{13_1}} \tag{2.20}$$

$$x_8 = \frac{1}{C_1^r R_{14_1}} \qquad x_9 = \frac{1}{C_1^r R_{15_1}} \tag{2.21}$$

$$x_{10} = \frac{1}{C_1^r} \qquad x_{11} = \frac{1}{C_w R_w} \tag{2.22}$$

$$x_{12} = \frac{1}{C_{51}^w R_{51_1}} \qquad x_{13} = \frac{1}{C_{51}^w R_{51_5}} \tag{2.23}$$

$$x_{14} = \frac{\alpha}{C_{51}^w} \qquad x_{15} = \frac{1}{R_{15}^{\text{win}}} \tag{2.24}$$

Rate of change of these states is equal to zero, as shown in the corresponding state update equation (2.30). We then add a low-magnitude *fictitious noise* to the dynamics

of parameters to allow slow changes in their values over time.

$$\dot{x}_1 = (x_6 - x_7 - x_8 - x_9 - x_{10}x_{15} - x_{10}u_2c_a)x_1 + x_6x_2 + x_7x_3$$
$$+ x_8x_4 + x_9x_5 + (c_au_1u_2 + T_5x_{15} + A_{\text{win}}\tau Q_{\text{rad}} + \dot{Q}_{\text{int}}).x_{10} \tag{2.25}$$

$$\dot{x}_2 = (x_1 - 2x_2 + T_2).x_{11} \tag{2.26}$$

$$\dot{x}_3 = (x_1 - 2x_3 + T_3).x_{11} \tag{2.27}$$

$$\dot{x}_4 = (x_1 - 2x_4 + T_4).x_{11} \tag{2.28}$$

$$\dot{x}_5 = x_1x_{12} - (x_{12} + x_{13})x_5 + T_5x_{13} + A^{w_{51}}x_{14}Q_{\text{rad}} \tag{2.29}$$

$$\dot{x}_i = 0 \qquad \forall i = 6, 7, ...15. \tag{2.30}$$

u is the input vector given by:

$$u = \begin{bmatrix} T_{s1} \\ \\ \dot{m}_{r1} \end{bmatrix} \tag{2.31}$$

In summary, we express the dynamics of the system using following state update model:

$$x_k = f(x_{k-1}, u_{k-1}, d_{k-1}, w_{k-1})$$
$$z_k = h(x_k) + v_k \tag{2.32}$$

where w_k and v_k are the process and measurement noise and are assumed to be zero

mean multivariate Gaussian process with variance W_k and V_k, (i.e. $w_k \sim \mathcal{N}(0, W_k)$ and $v_k \sim \mathcal{N}(0, V_k)$), respectively.

2.3.3 Estimation Algorithm

In order to estimate the unknown parameters of the system we augment the states of the system with a vector p_k which stores the parameters of the system, with a time evolution dynamics of $p_{k+1} = p_k$, as will be detailed in Appendix B. Due to the multiplication of states and parameters the resulting dynamic system is nonlinear. Nonlinear estimation algorithms such as Extended Kalman Filtering (EKF) or Unscented Kalman Filtering (UKF) can then be exploited to simultaneously estimate the states and the parameters of the system.

An alternative to using a Kalman filter would be a simple observer. However, given the random variations, inaccuracies and uncertainties in the system dynamics, as described earlier in the chapter, using a Kalman filter is suggested in order to get a statistically optimal estimate of system states [59, 60].

In our previous work [61] we showed that UKF outperforms EKF for building parameter estimation. Thus, we only focus on UKF in this study. We present an algorithmic description of the UKF in Appendix B, omitting some theoretical considerations.

2.3.3.1 Estimation Results

The test-bed from section 2.2 was used to collect measurements from January 11 to January 24, 2013. To remove noise from the temperature measurements, a second order Butterworth lowpass filter with cutoff frequency of 0.001 (Hz) was used. Fig. 2.5 shows the temperatures of the neighboring zones and the outside temperature which act as disturbance to the PAB model. Fig. 2.6 depicts the model inputs including the air mass flow rate and the supply air temperature. In order to obtain the best initial parameter values for the Kalman filter algorithm, we first perform a (static) parameter identification on the historical data. We consider the first part of the data as *training set* (shown in red in Fig. 2.7), and obtain the best parameters that minimize the least square error between the simulation and the measurement data. The result of this step is used to simulate the temperature evolution of the room air for the next three days (shown in black in Fig. 2.7). Due to time-varying parameters and disturbance to the model, it is difficult to find a set of parameters for the model which results in good temperature tracking for all days including weekdays and weekends, and hence, as shown in Fig. 2.7, the results of simulations for the following days in the *testing data* set is even worse.

The obtained initial parameters from the off-line calibration step is used as initial value for the UKF algorithm.

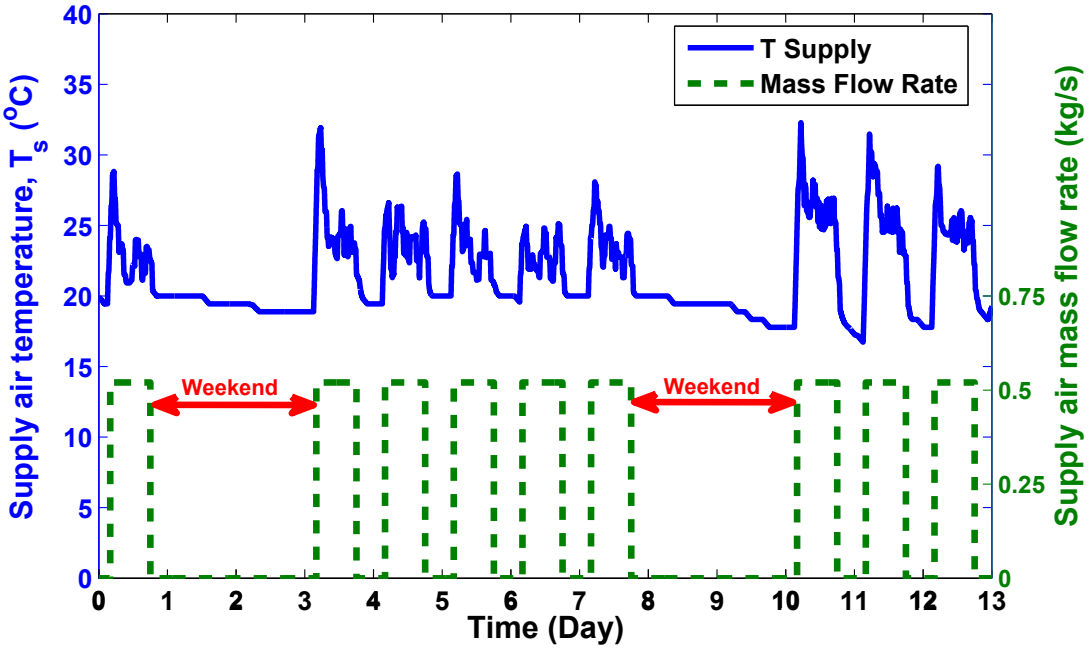

Figure 2.6: Inputs to the PAB model.

For the off-line parameter calibration practice, we used the historical data of two weeks where the first 60% of the data was used for training (calibration) and the remaining 40% of data was used for testing. The temperature estimation of room and walls, using UKF are depicted in Fig. 2.8 and Fig. 2.9. The evolution of parameters over time is shown in Fig. 2.10. The parameters evolve over time and the steady state values are not necessarily close to the initial points as expected, due to the changing environment. Note that the first part of the estimation of wall temperature by UKF leads to overshoot in the wall temperature, however, this overshoot is quickly recovered as UKF uses more data to tune the parameters more accurately.

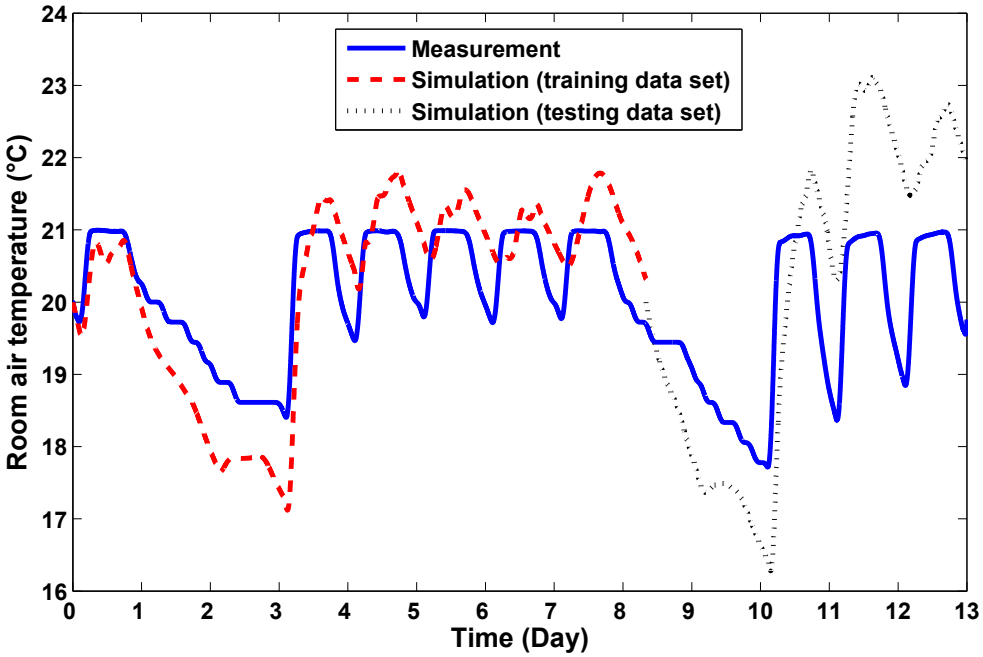

Figure 2.7: Off-line parameter calibration of the PAB model using room temperature measurements. The first set of data (shown in red) is the training data. We identify the parameters in one shot optimization by minimizing the ℓ_2 norm of the error between simulation and measurement data. Then we used the obtained parameters from the training data set (off-line calibration results) to predict the temperature evolution for the next days (shown in black).

UKF is also tested to estimate the temperature in the presence of process and measurement noise (w and v, respectively) as shown in Fig. 2.11. We add process and measurement noise to the model and use UKF to estimate the temperatures. UKF is used to estimate the temperature from the measurements. Performance of UKF is shown with model uncertainty w, and measurement noise v, given by $w_k \sim N(0, 0.2)$ and $v_k \sim N(0, 1.4)$, respectively. As seen in Fig. 2.11, UKF is able to cancel out the effect of noise very effectively.

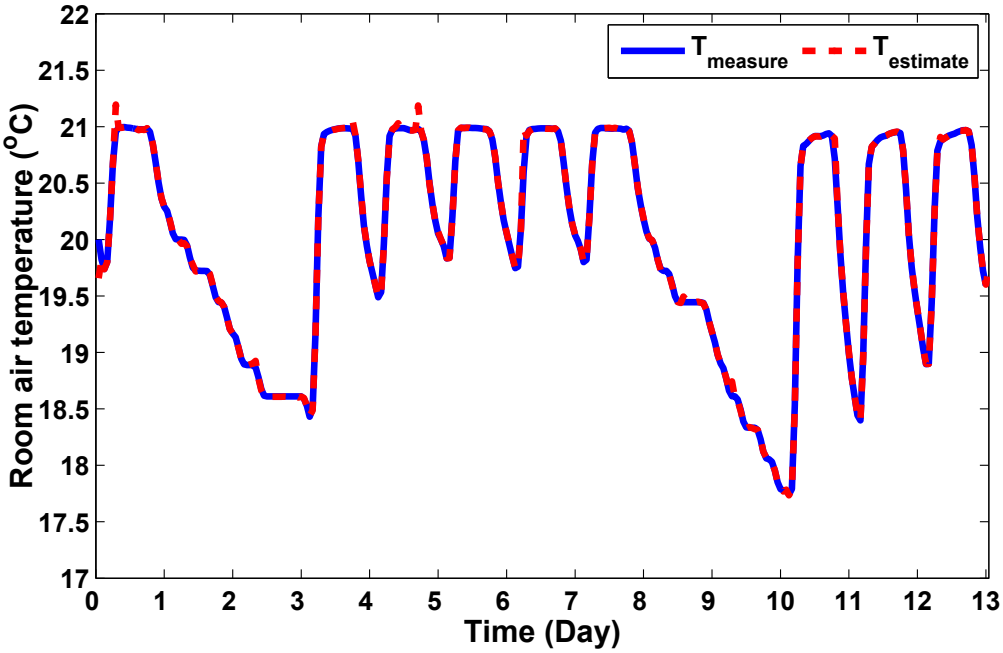

Figure 2.8: Estimated and measured room temperature using the designed UKF.

2.4 Controller Design

In this section we study *the impact of the use of the PAB model in a model-based control design framework*. State-of-the-art is to use a fixed-parameter model to design MPC for buildings. We propose using the updated parameter model obtained using the Kalman filter estimation process at each time step as shown in Fig. 2.3, which results in a more accurate model and hence lower model uncertainty. The underlying assumption here is that the parameters of the system do not change from time t to $t+1$. At the next time step, MPC uses the model with updated parameters, to derive the optimal inputs. Inputs are implemented on the system and at the next sampling

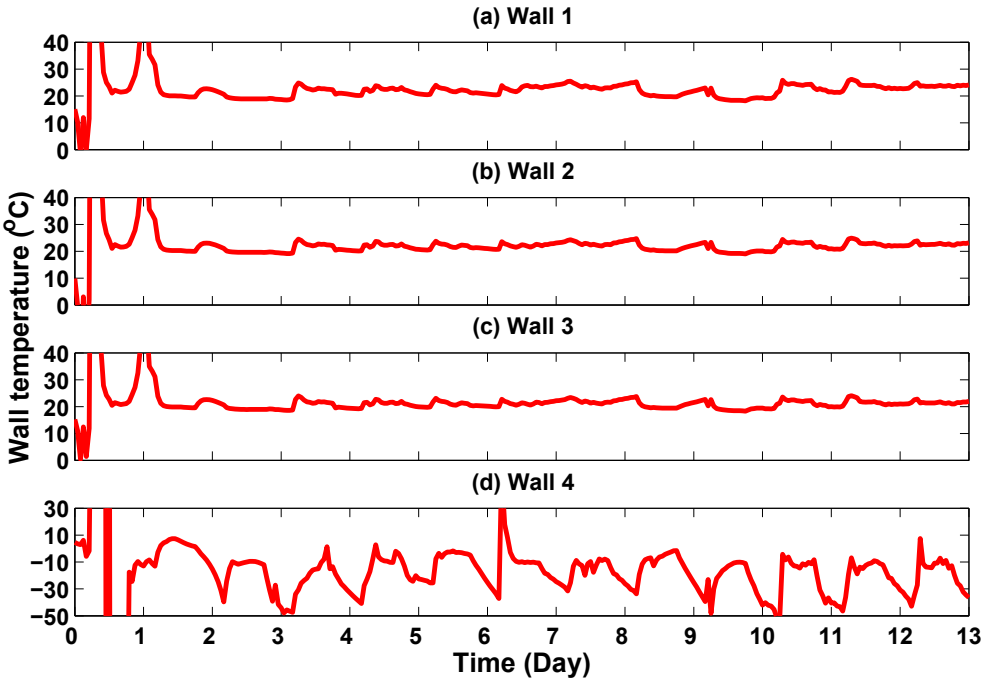

Figure 2.9: Estimated temperature of walls using UKF. We have zoomed the figures to focus on the more steady estimates of the walls rather than the first part transient behavior.

time new states (temperatures) are measured and sent to the PAB model, and this process repeats.

We also formulate a nominal MPC and a robust model predictive control (RMPC), and study their performances for various model uncertainty levels. MPC assumes that the model is perfect (no uncertainty), and the RMPC assumes that the model is uncertain and designs a robust control policy for a specific class of uncertainty. The results from MPC and RMPC are compared to a conventional rule-based control (RBC) for a typical building. *Novel performance indices are proposed* to compare the performance of these controllers. We also present *a methodology to select the best*

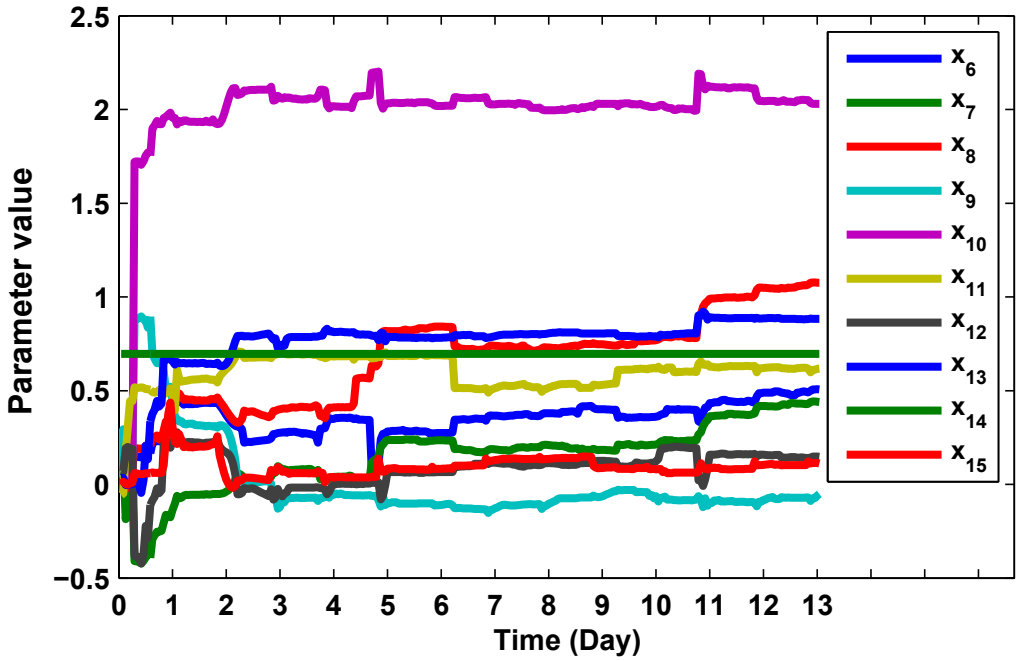

Figure 2.10: Estimated parameters of the PAB model using the designed UKF.

controller among the ones studied in this section for any given model uncertainty, which leads to optimum trade-off between energy consumption and comfort level.

2.4.1 ASHRAE requirements for Building Climate Control

ASHRAE's Standard 55 [62], *Thermal Environmental Conditions for Human Occupancy*, suggests the condition which is acceptable to at least 80% of occupants. According to this standard, the ideal temperature in typical clothing in summer (0.35-0.6 clo) is in the range of 22.5 °C to 26 °C. The operative temperature for occupants in normal clothing insulation in winter which is between 0.8 to 1.2 clo should be in range

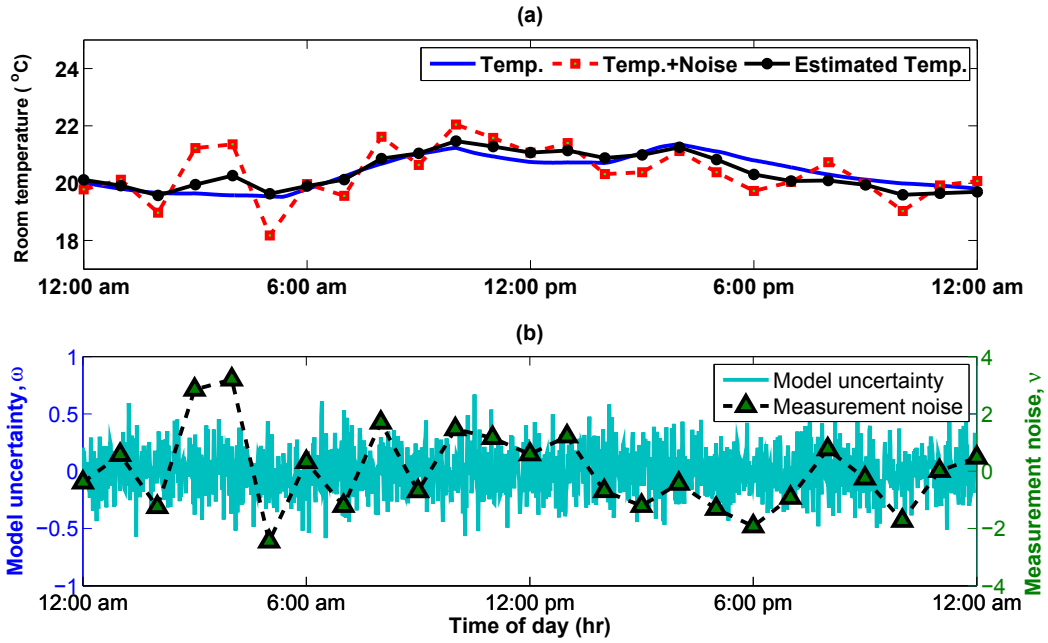

Figure 2.11: Performance of the designed UKF in the presence of model uncertainty and measurement noise.

of 20 °C to 23.5 °C. This temperature range is based on a metabolic rate of 1.2 *met* (70 W/m^2) and 60% RH. More details can be found in [63, 64, 65]. ASHRAE's Standard 62.1 [66], *Ventilation for Acceptable Indoor Air Quality*, explains outdoor air ventilation requirements for different types of indoor spaces. When the major contamination source is proportional to number of occupants, the *minimum ventilation rate* is enforced in CFM (L/s) and when other factors play the main role in contamination, the *minimum ventilation rate* is enforced in CFM/ft^2 $(L/s.m^2)$ [65]. We use this as a guideline for control design in this section.

2.4.2 Rule-Based Control (RBC)

The rule-based controller in this study is a conventional on-off HVAC controller. The time constant of the control action implementation is Δt. The controller opens the dampers of conditioned air flow to the thermal zones when heating is required and keeps it fully open for the duration of Δt. In the next time step the controller checks the temperature again and adjusts the damper position if the room temperature is within the comfort zone, or keeps it open if the room air temperature is still outside the comfort zone. In on-off control, position of the dampers can be either the *min* value or the *max* value. When system goes to the cooling mode, supply air temperature changes accordingly. The experimental data presented here is for the heating mode only. To be consistent and to perform a fair comparison, we use the same time constants Δt for all controllers.

2.4.3 Model Predictive Control (MPC)

A model predictive control problem is formulated with the objective of minimizing a linear combination of the total and the peak airflow. We implement the control inputs obtained from the MPC with the linearized system dynamics of the model on the original nonlinear model for forward simulation.

Fan energy consumption is proportional to the *cubic* of the airflow. Hence minimizing the peak airflow would dramatically reduce fan energy consumption. We have considered a cost function for the MPC which comprises linear combination of the total input airflow (ℓ_1 norm of input) and the peak of airflow (ℓ_∞ norm of input). The alternative would be to use the actual nonlinear function of fan energy consumption. However, it would lead to nonlinear MPC which is much slower than linear MPC. We use the proposed cost function to achieve better computational properties. Also in order to guarantee feasibility (constraint satisfaction) at all times, we implement soft constraints. The predictive controller solves at each time step the following optimization problem:

$$\min_{U_t,\bar{\epsilon},\underline{\epsilon}} \quad \{|U_t|_1 + \kappa|U_t|_\infty + \rho(|\bar{\epsilon}_t|_1 + |\underline{\epsilon}_t|_1)\} = \tag{2.33a}$$

$$\min_{U_t,\bar{\varepsilon},\underline{\varepsilon}} \quad \{\sum_{k=0}^{N-1} |u_{t+k|t}| + \kappa \max(|u_{t|t}|, \cdots, |u_{t+N-1|t}|) + \rho \sum_{k=1}^{N} (|\bar{\varepsilon}_{t+k|t}| + |\underline{\varepsilon}_{t+k|t}|)\} \tag{2.33b}$$

$$\text{s.t.} \quad x_{t+k+1|t} = Ax_{t+k|t} + Bu_{t+k|t} + Ed_{t+k|t}, \qquad k = 0, ..., N-1 \tag{2.33c}$$

$$y_{t+k|t} = Cx_{t+k|t}, \qquad k = 1, ..., N \tag{2.33d}$$

$$\underline{\mathcal{U}}_{t+k|t} \leq u_{t+k|t} \leq \overline{\mathcal{U}}_{t+k|t}, \qquad k = 0, ..., N-1 \tag{2.33e}$$

$$\underline{T}_{t+k|t} - \underline{\varepsilon}_{t+k|t} \leq y_{t+k|t} \leq \overline{T}_{t+k|t} + \bar{\varepsilon}_{t+k|t}, \qquad k = 1, ..., N \tag{2.33f}$$

$$\underline{\varepsilon}_{t+k|t}, \bar{\varepsilon}_{t+k|t} \geq 0, \qquad k = 1, ..., N \tag{2.33g}$$

where $U_t = [u_{t|t}, u_{t+1|t}, \cdots, u_{t+N-1|t}]$ is vector of control inputs, and $\underline{\epsilon} =$

$[\underline{\varepsilon}_{t+1|t}, \cdots, \underline{\varepsilon}_{t+N|t}]$ and $\overline{\epsilon} = [\overline{\varepsilon}_{t+1|t}, \cdots, \overline{\varepsilon}_{t+N|t}]$ are the slack variables used to utilize soft constraints on room temperature. $y_{t+k|t}$ is the room temperature vector, $d_{t+k|t}$ is the disturbance load prediction, and $\underline{T}_{t+k|t}$ and $\overline{T}_{t+k|t}$ for $k = 1, \cdots, N$ are the lower and upper limits on the room temperature, respectively. $\underline{\mathcal{U}}_{t+k|t}$ and $\overline{\mathcal{U}}_{t+k|t}$ are the lower and upper limits on the airflow input by the variable air volume (VAV) damper, respectively. Note that based on the ASHRAE Standard 62.1- Section 6.2.6.1, during unoccupied hours, ventilation systems should be able to maintain the required non-zero ventilation rates ($\underline{\mathcal{U}}_{t+k|t} > 0$) in the breathing zone [66]. ρ is the penalty on the comfort constraint violations, and κ is the penalty on peak power consumption.

At each time step only the first entry of U_t is implemented on the model. At the next time step the prediction horizon N is shifted leading to a new optimization problem. The prediction horizon is $N = 24$, and at each time step only the first entry of the input vector U_t is implemented on the model. This process is repeated over and over until the total time span of interest is covered. We use YALMIP [67] to set up the MPC problem in MATLAB.

2.4.4 Robust Model Predictive Control (RMPC)

We consider additive uncertainty to the system model as previously described in (2.11). A schematic of the robust optimal control implementation on the non-linear building model is shown in Fig. 2.12. In RMPC algorithm, the cost function is the same as in the one in MPC case:

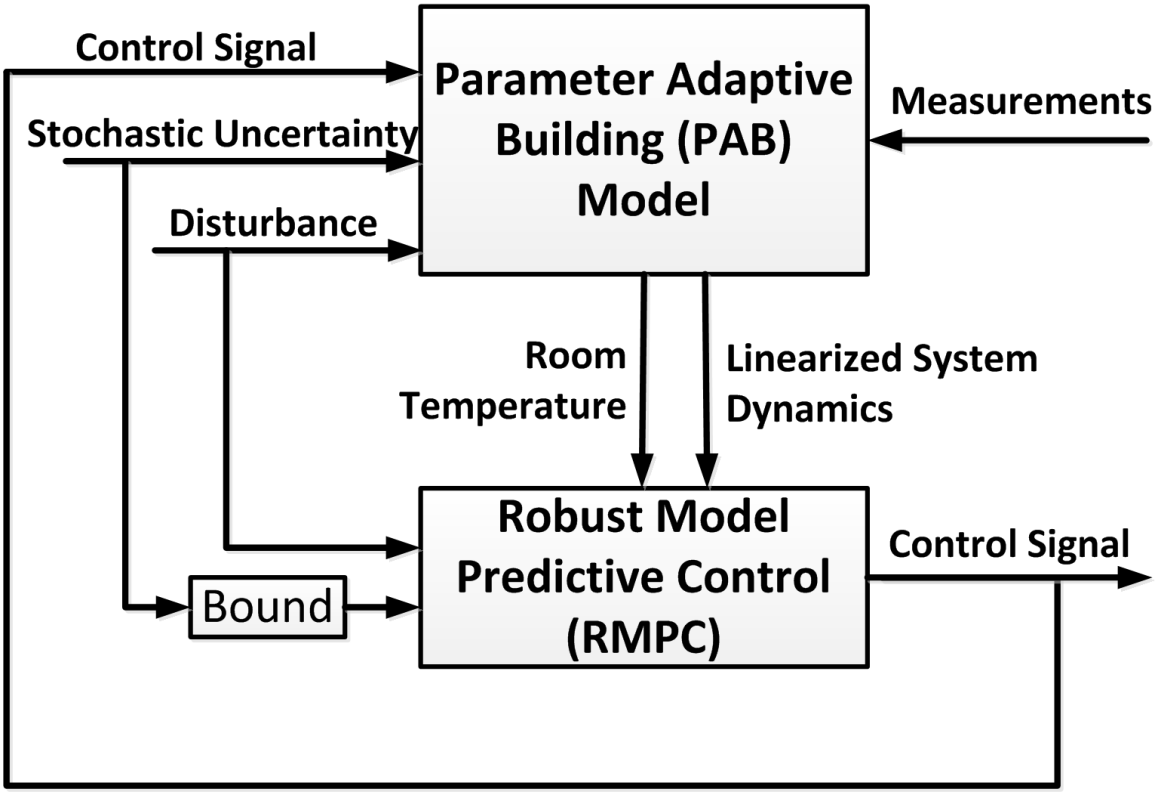

Figure 2.12: Schematic of the robust model predictive control implementation.

$$\min_{U_t,\bar{\varepsilon},\underline{\varepsilon}} \quad \{||\mathbf{U_t}||_1 + \kappa||\mathbf{U_t}||_\infty + \rho(||\bar{\epsilon}_\mathbf{t}||_1 + ||\underline{\epsilon}_\mathbf{t}||_1)\} \tag{2.34}$$

However, state and input constraints are as follows:

$$x_{t+k+1|t} = Ax_{t+k|t} + Bu_{t+k|t} + E(d_{t+k|t} + w_{t+k|t}) \qquad k = 0, 1, ..., N-1 \tag{2.35a}$$

$$y_{t+k|t} = Cx_{t+k|t} \qquad k = 1, 2, ..., N \tag{2.35b}$$

$$\underline{T}_{t+k|t} - \underline{\varepsilon}_{t+k|t} \leq y_{t+k|t} \leq \overline{T}_{t+k|t} + \overline{\varepsilon}_{t+k|t} \qquad k = 1, 2, ..., N \tag{2.35c}$$

$$\underline{\mathcal{U}}_{t+k|t} \leq u_{t+k|t} \leq \overline{\mathcal{U}}_{t+k|t} \qquad k = 0, 1, ..., N-1 \tag{2.35d}$$

$$\underline{\varepsilon}_{t+k|t}, \ \ \overline{\varepsilon}_{t+k|t} \geq 0 \qquad k = 1, 2, ..., N \tag{2.35e}$$

$$\forall \ w_{t+k|t} \in \mathcal{W} \qquad k = 0, 1, ..., N-1 \tag{2.35f}$$

The only difference with respect to MPC algorithm is the introduction of additive uncertainty term w in the state update equation.

Using this formulation, we derive a robust counterpart of an uncertain optimization problem in which constraints are satisfied for all possible uncertainties, and worst-case objective is calculated.

It is shown in [36] that the open-loop constrained robust optimal control (OL-CROC)

is conservative. . The closed-loop constrained robust optimal control (CL-CROC) formulation overcomes this issue but it can quickly lead to an intractable problem [68]. Next, we review the feedback prediction concept followed by our proposed formulation to improve upon the feedback prediction scheme.

2.4.4.1 Feedback predictions

The idea in feedback prediction, is to introduce new decision variables and parameterize the future control sequences using the future disturbances and an additive independent decision variable.

Define an affine disturbance feedback as:

$$u_i := \sum_{j=0}^{i-1} m_{i,j} w_j + n_i \qquad \forall i = 1, 2, ..., N-1 \tag{2.36}$$

Therefore the input vector can be written as $U = \mathbf{M}\mathbf{w} + \mathbf{n}$, where $\mathbf{M}$ and $\mathbf{n}$ are given by

$$\mathbf{M} := \begin{bmatrix} 0 & \cdots & \cdots & 0 \\ m_{1,0} & 0 & \ddots & 0 \\ \vdots & \ddots & \ddots & \vdots \\ m_{N-1,0} & \cdots & m_{N-1,N-2} & 0 \end{bmatrix}, \quad \mathbf{n} := \begin{bmatrix} n_0 \\ \vdots \\ \vdots \\ n_{N-1} \end{bmatrix} \tag{2.37}$$

and the vector of disturbances is given by $\mathbf{w} = [w_0 \quad w_1 \quad \cdots \quad w_{N-1}]'$.

The control sequence is parameterized directly in the uncertainty. What we have here is basically a sub-optimal version of the closed-loop min-max solution [68].

2.4.4.2 Two-Lower-Diagonal Structure (TLDS):

The main problem with the min-max formulation based on LTS parameterization is the excessive number of decision variables and constraints. The reason is the high-dimensional parameterization of matrix $\mathbf{M}$. To resolve the issue of high-dimensional parameterization of matrix $\mathbf{M}$, we propose the following new parameterizations.

By analyzing the structure of the optimal matrix $\mathbf{M}$, it was observed that the parameterization of the input does not need to consider feedback of more than past two values of $\mathbf{w}$ at each time, hence we propose the following disturbance feedback.

$$\begin{aligned} u_i &:= m_{i,i-2} w_{i-2} + m_{i,i-1} w_{i-1} + n_i \\ &= \sum_{j=i-2}^{i-1} m_{i,j} \omega_j + n_i \qquad \forall i = 1, 2, ..., N-1 \end{aligned} \tag{2.38}$$

and the corresponding parameterization matrix $\mathbf{M}$ is an $N \times N$ matrix that has the

entries on the first and second diagonal of $\mathbf{M}$ below its main diagonal as decision variables and 0 elsewhere.

$\mathbf{n}$ remains as in (2.37). With this structure we exploit the sparsity of the feedback gain matrix to enhance the computational characteristics of the controller.

2.4.5 Performance Indices

To compare the overall performance of the proposed controllers we define indices to measure the energy consumption and comfort level provided by each controller. In addition, we define a new index to evaluate the overall performance of each controller considering both the energy and comfort indices.

† The energy index I_e in (kWh) is defined:

$$I_e = \int_{t=0}^{24} [P_c(t) + P_h(t) + P_f(t)]\, dt \tag{2.39}$$

where cooling power P_c, heating power P_h and fan power P_f are determined by:

$$P_c(t) = \dot{m}_c(t) c_p [T_{out}(t) - T_c(t)] \tag{2.40a}$$

$$P_h(t) = \dot{m}_h(t) c_p [T_h(t) - T_{out}(t)] \tag{2.40b}$$

$$P_f(t) = \alpha \dot{m}^3(t) \tag{2.40c}$$

$c_p = 1.012(\text{kJ/kg.}^\circ\text{C})$ is the specific heat capacity of air and $\alpha = 0.5(\text{kW.s}^3/\text{kg}^3)$ is the fan power constant [25]. Using these constants, the fan power values, in (kW), can be calculated.

† The discomfort index I_d in degree Celsius hour ($^\circ$Ch) is defined as the sum of all the temperature violations in the course of a day.

$$I_d = \int_{t=0}^{24} \left[\min \left\{ \left| T(t) - \overline{T}(t) \right|, |T(t) - \underline{T}(t)| \right\} . \mathbf{1}_{\mathcal{B}(t)^c}(T(t)) \right] dt \tag{2.41}$$

where $\mathcal{B}(t) = [\underline{T}(t), \overline{T}(t)]$ is the comfort zone at time t and $\mathbf{1}$ is the indicator function.

† A good control performance means not only low energy consumption, but also low resulting discomfort. To assess the overall performance of the controllers, we need to examine both I_e and I_d at the same time. Using the two indices defined above we define a third index called Overall Performance Index (I_{OP}). The intuition behind this new index is to take into account the energy and

discomfort index in one single term. I_{OP} is defined as:

$$I_{OP} = \frac{(I_d^* - I_d)/||I_d||_\infty}{I_e/||I_e||_\infty} \tag{2.42}$$

where I_d^* is the maximum allowed discomfort and $||.||_\infty$ denotes infinity norm or the maximum value of energy indices among all three controllers. Negative value of I_{OP} means that the discomfort index is not within the preferred range. The lower the I_d and I_e are, the higher the I_{OP} will be. Therefore, the higher the I_{OP}, the better the overall performance. In this study, the limit on the allowed discomfort index is heuristically chosen to be $I_d^* = 0.5(^\circ\text{Ch})$ to ensure adequate comfort level.

2.4.6 Control Results

To illustrate the effectiveness of the controllers proposed in subsections 2.4.3 and 2.4.4, we assess their performances for different *model uncertainty* values denoted by δ and defined as

$$\delta = \frac{\lambda}{||\mathbf{d}||_\infty} \times 100\ [\%] \tag{2.43}$$

where λ is the ℓ_∞ norm bound of the uncertainty as given by (2.12) and $\mathbf{d} = [d_1', d_2', ..., d_N']'$ is the disturbance realization vector. d' represents transpose of vector

d.

A time constant of $\Delta t = 1$ (hr) is used for all controllers. We implement the introduced model predictive controllers with a prediction horizon of $N = 24$. The choice of $N = 24$ is to provide a good balance between performance and computational cost for the MPC framework in this study.

We use the following numerical values for parameters in (2.33) and (2.35). $\overline{\mathcal{U}} = 63$ cfm (0.03 m^3/s) is the higher limit on air mass flow, $[\underline{T}_{.|t} \ \overline{T}_{.|t}] = [20 \ 22]^{\circ}$C during occupied hours, and $[\underline{T}_{.|t} \ \overline{T}_{.|t}] = [19 \ 23]^{\circ}$C is used during unoccupied hours. For the simulations we use $\kappa = 0.75$ and $\rho = 50$. $\underline{\varepsilon}$ and $\overline{\varepsilon}$ are the slack variables used to avoid feasibility problem, where $\underline{\epsilon}$ and $\overline{\epsilon}$ are the vectors storing slack variables.

Optimal controller and the resulting room temperature with the presence of a box-constrained uncertainty in four cases are depicted in Fig. 2.13. Measurements, as shown in black, shows the air mass flow and temperature recording for the room using a simple existing control policy of the building HVAC system. RBC represents the result of the rule-based control. MPC refers to the performance of a model-based control algorithm in which no knowledge of the model uncertainty is known a-prior to the control algorithm. RMPC refers to the simulation of the control algorithm which considers the model uncertainty bound and utilizes the uncertainty feedback strategy of (2.36) in designing the control policy.

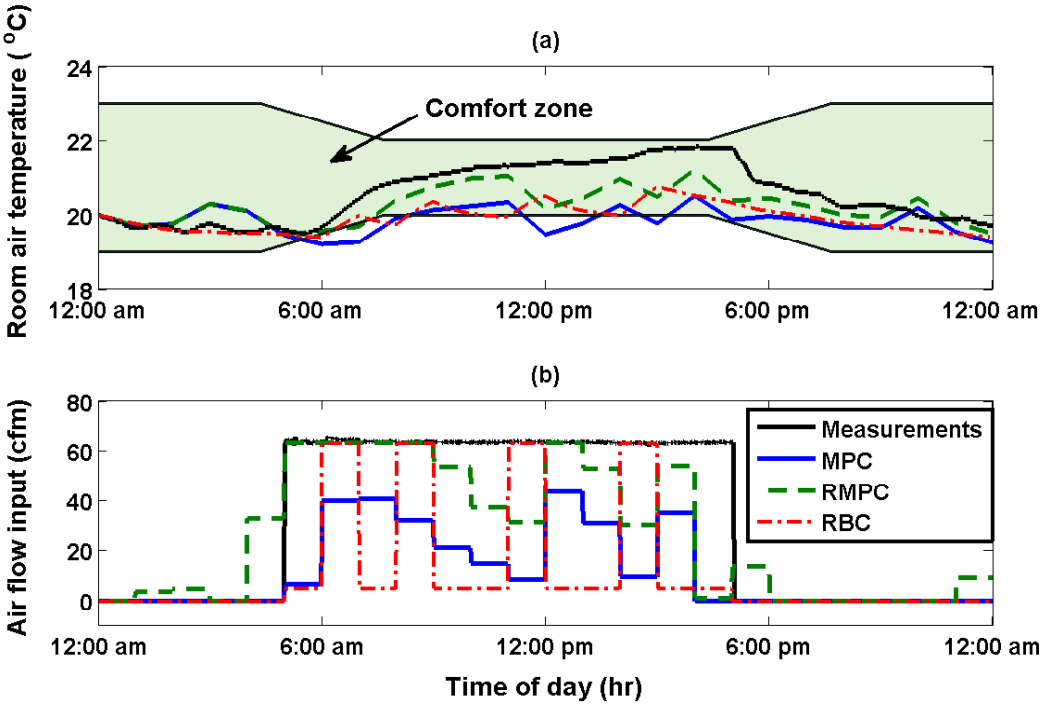

Figure 2.13: Control input and resulting temperature profile for the existing controller on the building (Measurements), RBC, MPC, and robust MPC controllers. The additive uncertainty bound is considered $\delta = 60\%$ in this case.

We consider stochastic uncertainties with different uncertainty bounds (λ) as introduced in (2.12). The MPC does not have any a-priori information regarding the additive uncertainty, and calculates the controller solely based on the deterministic system dynamics. However the RMPC integrates the uncertainty bound information in the control derivation. Controller performances are evaluated based on indices introduced in Section 2.4.5. Problem is solved using CPLEX 12.2 [69] on a 2.67 GHz machine with 4 GB RAM. Here are the discussions of the results:

Computational Aspects: Exploiting the *TLDS* structure results in the same control law that was obtained from the *LTS* structure. However, matrix $\mathbf{M}$ of *LTS* has

$l.m.r\frac{N(N-1)}{2}$ variables (quadratic in N) while matrix $\mathbf{M}$ of *TLDS* has $l.m.r(2N-3)$ variables (linear in N), and hence exhibits shorter computation time. On average, the simulation time for *TLDS* is 30% less than the *LTS* structure, as shown in Table 2.1.

Tables

Table 2.1
Comparison of LTS and TLDS uncertainty feedback parameterizations results for the case of $\delta = 60\%$.

Controller	Number of feedback decision variables	Average simulation time for $N = 24$, in (s)	I_e (kWh)	I_d (^oCh)
LTS	$l.m.r(\frac{N(N+1)}{2})$	200	16467	0
TLDS	$3l.m.r(N-1)$	138	16467	0

Comfort: It is observed from Fig. 2.13, that the RMPC is the only controller that is able to keep the temperature within the allowed comfort zone, at all times during this test simulation, meaning maintaining minimum level of discomfort ($I_d \leq I_d^*$), while RBC still does a very good job and MPC fails to do so, resulting to $I_d > I_d^*$ for all $\delta \geq 40\%$. Fig. 2.14 depicts how *discomfort index* I_d, varies with additive model uncertainty δ for MPC, and RMPC. Note that different data points for one δ value refers to simulations with different random sequences. The reason for such a wide variation of the simulation results, specially for large values of δ stems from the

fact that depending on the value of the random variable at any time, the resulting disturbance vector can either lead to temperature rise or fall with respect to the nominal disturbance value. It is shown that RMPC manages to keep the perfect comfort level ($I_d = 0$), for additive model uncertainty up to $\delta = 75\%$, while the MPC maintains the perfect comfort level for uncertainty bounds up to $\delta = 20\%$. The discomfort index for MPC goes as high as 4.61 (°Ch) while the value for RMPC reaches 1.2 (°Ch) in the worst case in the simulations corresponding to $\delta = 100\%$. Since RBC is not a model-based control technique, its performance does not depend on values of δ, hence the straight horizontal line in Fig. 2.14 ($I_d = 0.25$°Ch).

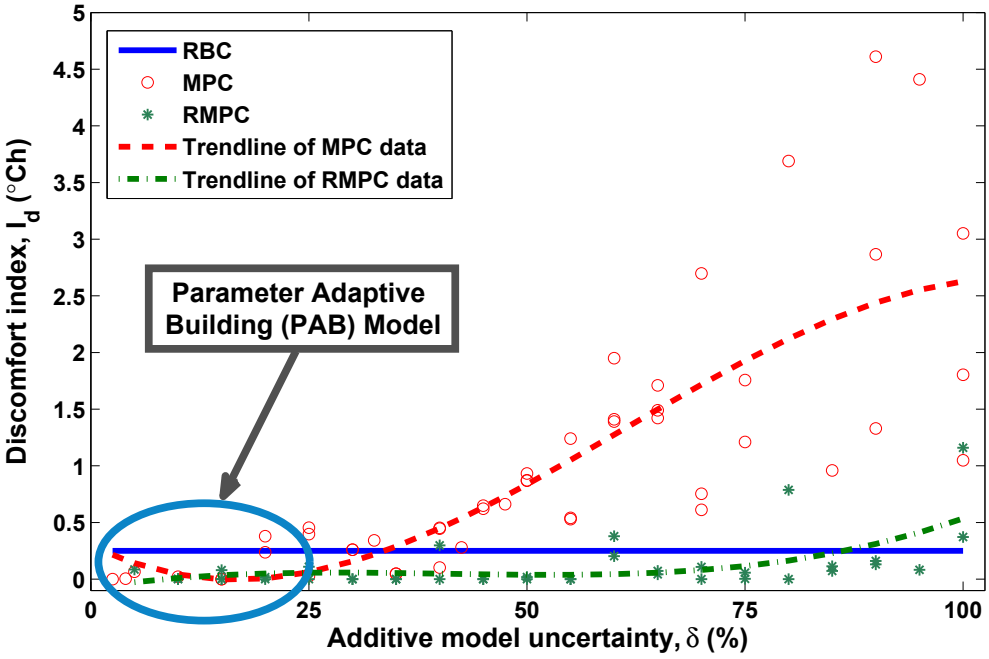

Figure 2.14: Discomfort index I_d versus additive model uncertainty (δ). We generate a uniform random sequence based on the disturbance prediction error value δ. The generated random sequence is used in the simulations for making this graph. Trendlines in this figure are calculated based on least square estimation.

Energy Consumption: Fig. 2.15 depicts the variations of *energy index* I_e, versus the uncertainty bound on the unmodeled dynamics. It is clear that the energy index for RMPC increases dramatically with δ, while the energy index for MPC only changes slightly. However, this comes with the drawback of increased discomfort index for MPC. Fig. 2.15 also shows energy consumption of RBC ($I_e = 1.43 \times 10^4$ kWh). MPC for all values of δ leads to a lower amount of energy consumption than RBC, but RMPC leads to more energy consumption than RBC soon after $\delta = 35\%$.

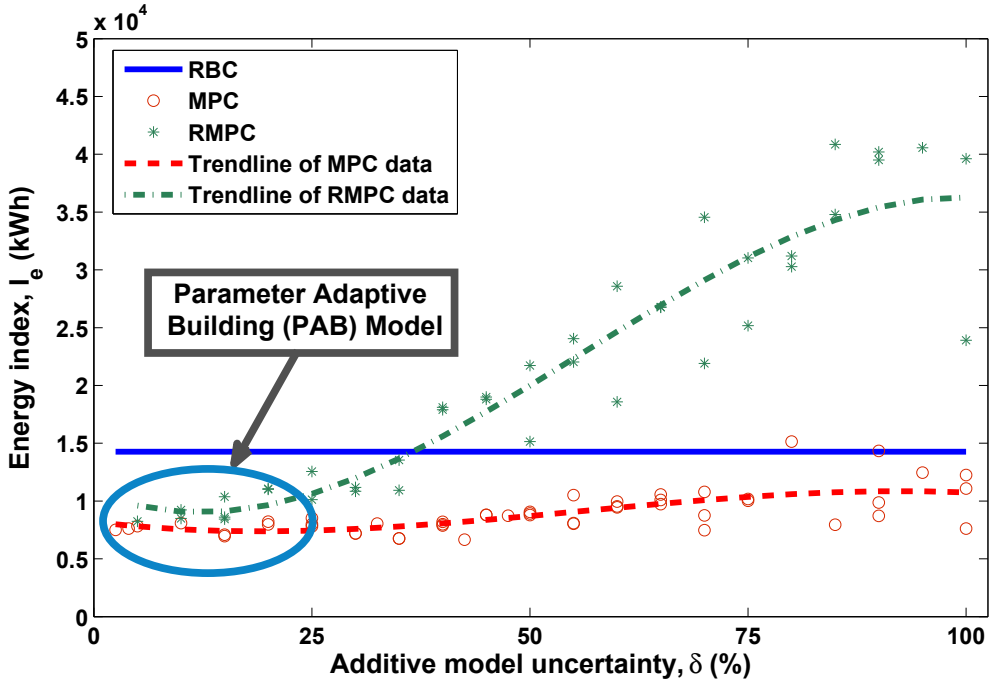

Figure 2.15: Energy index I_e versus additive model uncertainty (δ). The data points for this graph were generated using a similar technique as in Figure 2.14. Trendlines in this figure are calculated based on least square estimation.

Comfort-Energy Trade-off: An important point to notice from Fig. 2.15 is how

much more energy needs to be supplied to the HVAC system to maintain the comfort level in the presence of imperfect and faulty unmodeled dynamics predictions. Consider the case where $\delta = 75\%$. MPC will lead to a discomfort index of 1.7°Ch on average, while the RMPC is able to maintain the temperature below a discomfort index of 0.016^oCh on average. However this level of comfort provided by the RMPC comes at a cost of energy consumption of 3 times more than that of the MPC case. Note that due to the trade-off between comfort and energy consumption, the choice of which controller to use is on the building HVAC operator, and depends on various factors such as criticality of meeting the temperature constraints for the considered thermal zone in the building, and availability and price of energy at that time of the day/year.

As observed from Fig. 2.14 and 2.15 the behavior of controllers vary considerably as the model uncertainty increases. For instance, the energy required to keep the same level of comfort for RMPC in the case of $\delta = 75\%$ is almost 3 times the energy required to provide the same level of comfort when $\delta = 25\%$. Fig. 2.14 and Fig. 2.15 show the importance of a good model like PAB in minimizing the energy consumption of building HVAC systems for a desirable comfort level using model-based control techniques by accurately capturing the dynamics of the system.

MPC and RMPC versus RBC: Fig. 2.16 demonstrates savings of MPC and

RMPC versus RBC. As shown, the maximum theoretical energy saving of MPC compared to RBC is 36%, and that of RMPC is 30% for the building studied. These values decrease as model uncertainty increases. Energy saving of MPC versus RBC stays positive even for large values of model uncertainty, while energy saving of RMPC versus RBC is positive only for model uncertainty values up to about 34%, and is negative for larger model uncertainties (i.e. RMPC consumes more energy than RBC).

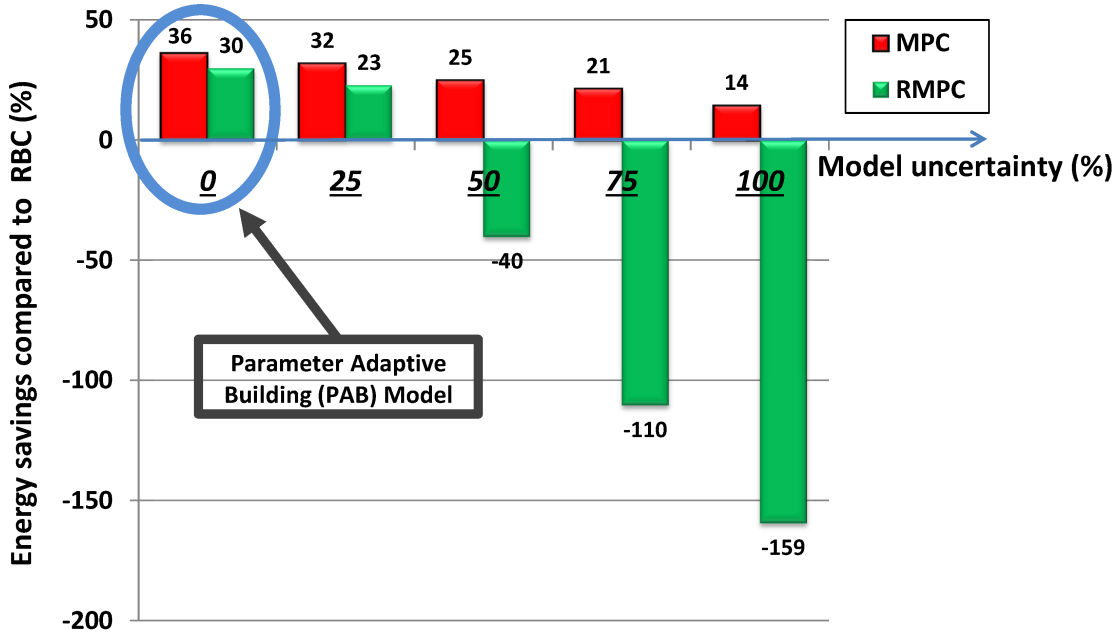

Figure 2.16: Energy saving of MPC and RMPC compared to RBC as a function of model uncertainty. The blue eclipse shows operating area of the PAB model which keeps the model uncertainty very small.

The results of an extensive study in [70] show that MPC HVAC control can potentially provide 16%-41% building energy saving compared to rule-based controllers, which is in agreement with our findings. The saving depends on various factors including climate zone, insulation level, and construction type. Stochastic MPC was shown

in [70] to be superior to the rule-based control given the uncertainties in occupancy and weather forecast. Our findings also show that the robust MPC outperforms the rule-based control in terms of energy consumption and user comfort. Although these two MPC techniques (robust and stochastic MPC) both address model uncertainty, they are formulated differently and hence can lead to different performance results. A comparative analysis of these two MPC techniques is the subject of our future work. Given the accuracy of the PAB for removing model uncertainty, designing MPC scheme based on PAB is a promising solution for building control problem.

For simulation evaluation of energy consumption and provided comfort level, we have compared the overall performance of the three controllers using I_{OP}. The results, as shown in Fig. 2.17, suggest that for model uncertainties less than 30% MPC is the best controller type. For model uncertainties above 30%, RMPC and RBC are close in performance while for δ between 30% and 67% RMPC is the best, and for model uncertainties larger than 67%, RBC leads to better overall performance than model-based control techniques. This information can be of utility for choosing a controller type for building HVAC system. As described in the chapter, proper choice of building HVAC control would depend on the accuracy of the given building model. Range of uncertainties for a given building model can be obtained by taking the difference of the temperature predictions from the building model and temperature measurements from a building. The statistics of such uncertainty can be found once such data is available. The mean and variance of the uncertainty from the statistical

analysis can be used to select the best controller type.

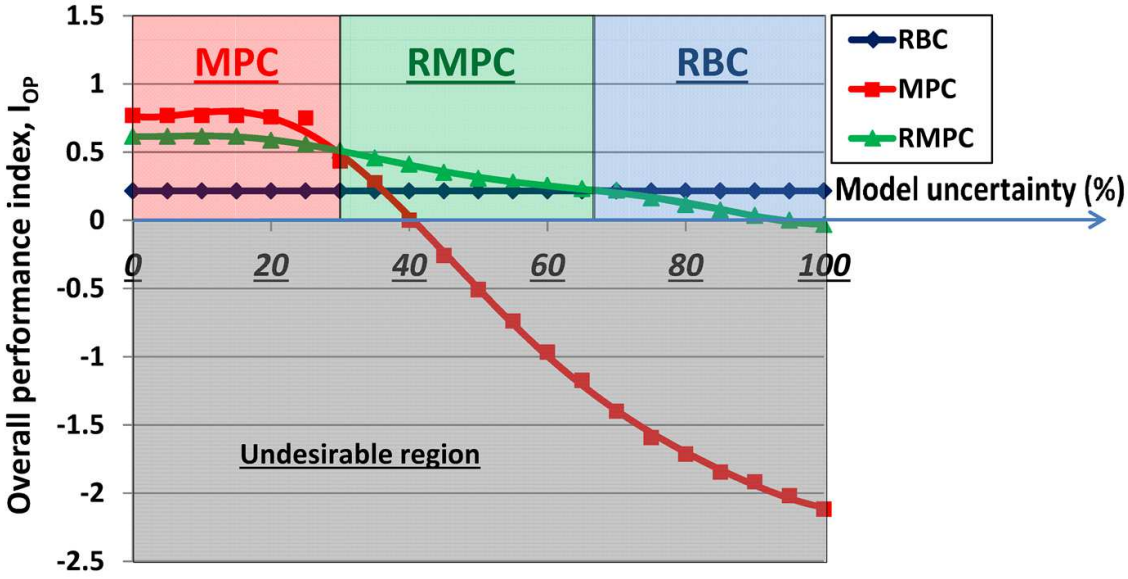

Figure 2.17: Overall performance index for RBC, MPC and RMPC as a function of model uncertainty. The red zone demonstrates the region which MPC outperforms RMPC and RBC as it yields a higher I_{OP}. The green zone represents the region that I_{OP} of RMPC is higher than that of MPC and RBC. RBC dominates in terms of I_{OP} in the blue zone. In the gray zone the resulting discomfort index is not acceptable.

2.5 Summary and Conclusion

Model uncertainty is an unavoidable challenge for modeling and model-based control of a building HVAC system. In this chapter, we characterized the impact of model uncertainty on MPC controllers and presented two approaches to minimize model uncertainty for building controls. First, we presented a new modeling framework for simultaneous state estimation and parameter identification of building predictive

models. This resulted in a Parameter-Adaptive Building (PAB) model which captures system dynamics through an *online* estimation of time-varying parameters of a building model. The PAB model aims at reducing model uncertainty and can be used for both modeling and control. Second, we presented an MPC framework that is robust against additive uncertainty. The new framework is a closed-loop Robust Model Predictive Control (RMPC) utilizing uncertainty knowledge to enhance the nominal MPC. The RMPC is capable of maintaining the temperature within the comfort zone for model uncertainties up to 75%. The specific contributions are listed below:

1. We constructed a nonlinear state space model by augmenting the parameters of the system into the state vector. We exploited the similarities in the physical properties such as wall materials and thicknesses in the building under study, and reduced the number of independent parameters in the building model. A similar approach is expected to apply to other building modeling practices.

2. We presented a PAB modeling framework that uses an unscented Kalman filter (UKF) to simultaneously estimate all the states of the dynamic model and continuously tune the parameters of the building model. The PAB was validated with the experimental HVAC data collected from a building test bed. Successful application of UKF in this work for simultaneous state and parameter estimation of a building model is promising for other building control applications which deal with model uncertainty.

3. We proposed a new uncertainty feedback parameterization of the control input, TLDS, for the closed loop RMPC which results in the same energy and discomfort indices as the previous parameterization, LTS, with a lower number of decision variables, linear in time horizon N, as opposed to quadratic, for the LTS. The new TLDS parameterization results in an average simulation time of 30% less than LTS.

4. Closed loop RMPC outperforms nominal MPC considering the provided level of comfort. However, higher comfort comes at the cost of dramatically higher energy consumption for RMPC. For uncertainty range of 30% to 67%, RMPC leads to better overall performance compared to MPC and RBC, while it fails to provide a better energy-comfort trade-off if model uncertainty is less than 30% or more than 67%. It should be noted that the model uncertainty values are relative for this case study. Selecting the controller types based on the model uncertainty may vary for different buildings.

5. We proposed a new performance index (I_{OP}) to assess buildings' energy consumption and comfort level simultaneously. The I_{OP} index is used for evaluating different building controllers. I_{OP} index can be used to generate a guideline for choosing appropriate controller type for buildings. This can be helpful for building control community for deciding on a proper controller type based on how accurate an available building model is for model-based controller design.

6. We found that the best choice for controller type changes from MPC to RMPC,

and then finally to RBC as the model uncertainty increases. A typical RBC controller outperforms model-based controllers (MPC and RMPC), if building model uncertainty is above 67%.

Chapter 3

Optimal Exergy Control of Building HVAC System[1]

Exergy or availability is an accurate metric related to quality of energy and it is used to determine sustainability of an energy system. Exergy has been extensively used to evaluate efficiency of energy systems and energy conversion processes. An exergy model for a building is presented in this chapter. In this PhD dissertation, exergy destruction, which indicates the loss of work potential, is formulated as a function of physical parameters of the building model and environment. To minimize exergy destruction in an Heating, Ventilation and Air-Conditioning (HVAC) system, we develop model predictive control (MPC) technique using the exergy model. Comparing

[1]This chapter has been published in Journal of Applied Energy [2] (doi:10.1016/j.apenergy.2015.07.051) with the permission from Elsevier as shown in Appendix E.

to a traditional onâĂŞoff controller for the building, the proposed exergy-based MPC (XMPC) reduces the exergy destruction and energy consumption up to 22% and 36%, respectively. Simulation results also indicate the advantage of XMPC over conventional energy-based MPC (EMPC). The results show that XMPC reduces exergy destruction by 4% compared to EMPC as well as saving 12% more energy.

3.1 Introduction

Exergy is described as the maximum theoretically available energy that can do work with respect to a given state via a reversible process [71]. A thermodynamic system's potential to do work increases as it moves away from its equilibrium (e.g., a higher temperature difference with the environment [72]). Conversely, there is no work potential if a system is at the thermodynamic equilibrium with its environment and the exergy of the system in that condition is zero. The First Law of Thermodynamics (FLT) is related to energy conservation. However, FLT does not provide insight about the theoretical efficiency limit due to irreversibility/deficiency in the processes and the direction of natural processes. While the Second Law of Thermodynamics (SLT) concerns entropy generation and irreversibilities which cause deficiency and energy waste in a system. SLT asserts that a spontaneous process or energy transfer occurs toward entropy increase. According to SLT, energy has quality and quantity. The Quality of energy decreases in natural processes [73]. Exergy-wise controls provide a

means to maximize the usage of energy quantity and minimize degradation of energy quality during a controlled process. Exergy is based on the First and Second Laws of Thermodynamics and unlike energy, it is not conserved. Exergy models the amount of useful energy with which a system has to work, hence, compared to energy, exergy is a more appropriate metric to analyze power systems.

Heating, ventilation, and air conditioning (HVAC) accounts for more than 50% of energy demand in buildings [12]. HVAC processes occur close to the environment temperature and therefore are considered as low quality energy demands. However, these demands are mostly granted with high quality energy (high exergy) sources such as electricity from grid which itself is mainly obtained from very high exergy sources such as fossil fuels. Thus, it is of a great importance to address low exergy demand (e.g., HVAC demands) with low exergy sources such as renewable energy sources produced by solar panels. HVAC systems can be operated in low exergy fashion by applying exergy-aware control algorithm which reduces irreversibilities in various energy subsystems such as thermal, mechanical and electrical that leads to less exergy destruction, increasing the overall exergy efficiency of the system. In other words, systems can be operated with less irreversibility and as a result, system operation will be more energy efficient and more sustainable.

There are various categories of studies on exergy analysis of energy systems. For building HVAC systems, a great number of studies have been performed for exergy

analysis [74, 75, 76, 77, 78, 79, 80, 81, 82]. For instance, in [74] a comparison between four different heating systems is provided and exergy efficiency of the systems are evaluated. In [76], authors present energy and exergy analyses of liquid natural gas (LNG) conventional boiler, LNG condensing boiler and an air source heat pump (ASHP). The energy efficiency values were found to be 8.69% for LNG condensing boiler and 80.9% for ASHP, respectively. Most concentration of these studies are on system assessment based on the First and the Second Laws of Thermodynamics and these studies do not provide control techniques to enhance the HVAC system efficiency. In recent years, use of low exergy (LowEx) system such as heat-pumps and solar collectors have spurred great interests in HVAC studies for green buildings. LowEx system and its applications have been studied before in [83, 84, 85, 86, 87, 88]. For instance, in [84] LowEx system implementation is presented. Their experimental result show that using LowEx system can drastically increase HVAC system performance. In [88], it is shown that HVAC systems are more exergy efficient if LowEx energy sources are used. Since conventional HVAC systems use high-exergy energy sources, they have not been designed or operated as exergy efficient systems. This dissertation proposes a control strategy for this problem.

As reported in [23, 26, 28, 29, 50], MPC techniques compared to the existing rule-based HVAC controllers offer potential energy saving up to 16%-41% for building HVAC. Advantages of MPC for building energy control are discussed in details in [23, 27, 28, 29, 30, 31, 32, 33, 35, 42]. Authors in [89, 90] reported results of MPC

implementation on a real building and discuss its advantages and energy savings. Thus, MPC is also used for the HVAC control framework in this study. All the previous studies [23, 27, 28, 29, 30, 31, 32, 33, 35, 42] for building HVAC controls center on incorporating energy analysis for controller design. Our study investigates and compares energy-wise and exergy-wise MPC framework for building HVAC controls.

Given the unprecedented focus on energy efficiency of built environment due to the energy crisis over the last decade, and at the same time, increasing penetration of renewable energy resources, controller design algorithms for building HVAC systems with exergy considerations is crucial. Smart control algorithms enable us to reduce exergy destruction, energy consumption and greenhouse gas emissions of buildings. For instance, exergy loss has been defined as the cost function of a supervisory control system in [14]. To minimize exergy loss, the controller makes accurate decisions based on energy source types (fossils, renewables, nuclear, and hydro-power). The authors in [14] made a comparison between exergy objective function with the *price* and the *carbon emission* objective functions. Their results show economical benefits of carefully managing exergy. In [91, 92] an optimal controller is developed to minimize exergy destruction for a vapor-compression cycle (VCC). Their experimental results in [91, 92] show that using exergy destruction as the objective function improves performance and efficiency of integrated energy systems (IES). It has been shown that exergy destruction can address irreversibilities across subsystems along with different energy forms including chemical, mechanical, thermal and electrical.

Fig. 3.1 summarizes the previous studies in building research using exergy and SLT. These studies can be divided into three main categories: (i) analysis of system performance, (ii) design optimization to increase efficiency, and (iii) exergy inspired control. In the first category, exergy and SLT principles are applied to analyze performance of building energy systems including building envelope [75], HVAC [74, 76, 79, 80, 82, 83, 84, 85, 86], boilers [74, 76, 78], renewables integration [74, 93] and energy storage systems [94, 95, 96]. The main objective of this category is to identify sources of inefficiency and irreversibility in the building energy systems. In the second category, different studies have centered on design optimization for building envelope and HVAC systems to determine the best system design to minimize irreversibilities across the system components [77, 87, 97, 98, 99, 100, 101]. In the third category, control and online optimization techniques based on exergy models are applied on building energy systems to increase system efficiency by decreasing sources of irreversible entropy generation that are affected by system control variables. While a great deal of studies have been conducted on analysis and design optimization of building systems based on exergy, only few works have been done on exergy-based control of building systems [102, 103]. Applying online optimization and control methods in buildings HVAC system increases efficiency and robustness of system to time-varying buildings loads and parameters. As shown in [102], online exergy optimization/control not only maximizes efficiency of thermal systems but also makes these systems more robust to disturbances including weather fluctuation and

varying load.

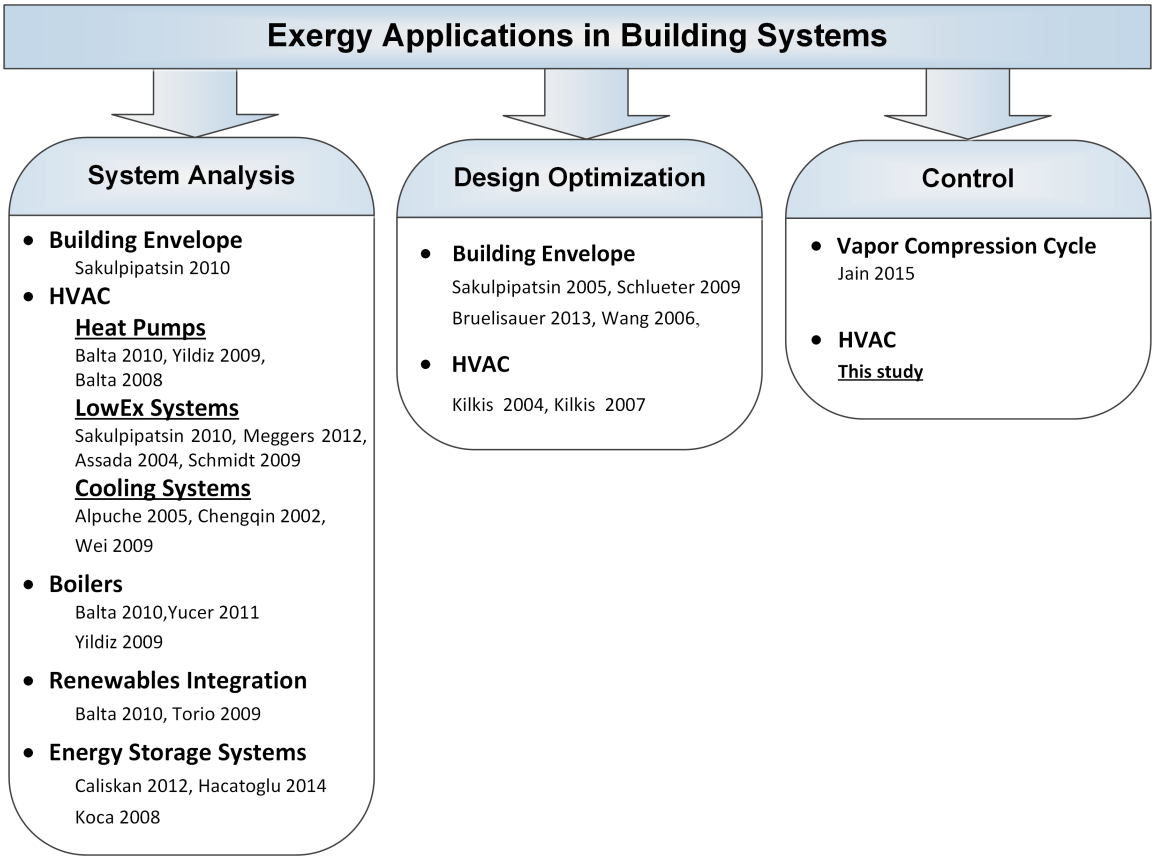

Figure 3.1: Background of exergy and SLT usage in building studies.

To evaluate efficiency of HVAC systems, energy is always used as a metric in the context of building HVAC control. In this PhD dissertation, *exergy* of the system is introduced as a more appropriate metric to assess performance of an HVAC system. We formulate an exergy model of a testbed building and develop a MPC strategy based on the minimization of exergy destruction. The optimal control problem reduces irreversible entropy generation of an HVAC system by minimizing exergy destruction, and addresses not only energy saving but also environmental concerns by saving exergy. To the best of authors' knowledge, this is the first study undertaken

to develop an HVAC model predictive control system based on minimizing exergy destruction. The results are very promising as the new MPC saves both energy and exergy and takes into the account First and the Second Laws of Thermodynamics.

This work builds upon our preliminary results in [103] and develops a new approach for exergy-based optimization in HVAC systems. This work also analyzes irreversible entropy generation for different HVAC control strategies. The Chapter is organized as follows. Section 2 explains the building testbed. In Section 3, we describe the mathematical modeling approach for the thermal model and exergy model of the building. Rule-based control, energy-based MPC and exergy-based MPC formulations are presented in Section 4. The results of three different control strategies are presented in Section 5, and conclusions are drawn in Section 6.

3.2 Test-Bed and Historical Data

The building testbed in this study is Lakeshore Center, at Michigan Technological University (MTU), Houghton, Michigan. Ground-source heat-pumps (GSHPs) provide exergy required for heating and cooling in this three-story building and each zone is equipped with a heat-pump to maintain comfort for occupants. Heat-pumps consist of four main components: compressor, expansion valve, and two heat-exchanger coils

known as evaporator and condenser. Heat-pumps work in either cooling mode and heating mode. In the cooling mode, the condenser which is the outdoor coil, dissipate heat and in the heating mode, the condenser is the indoor coil which releases heat to thermal zones. Fig. 3.2 illustrates a schematic of a heat-pump in a zone in the testbed. GSHPs exchange heat between the earth and the heating/cooling zones of the building. Average temperature of ground surface remains almost constant but differs based on the geographic location and latitude [104]. As reported by the United states environmental protection agency (EPA), GSHPs decrease energy up to 44 % compared to ASHPs [105]. Therefore, GSHPs are considered as HVAC renewable energy efficient technologies that have a high coefficient of performance (COP). The nominal COP of our testbed heat-pump is 3.2 and we assume that COP remains constant during different loads on the GSHP. GSHP units in the testbed have a multi-speed fan that supplies hot/cold air to the zone when heating or cooling is needed. The existing HVAC controller is a typical on-off controller to maintain desired temperature for each zone. The existing controller maintains the comfort level by changing supply air temperature. When zone temperature exceeds the lower limit, the compressor of heat-pump is switched on until temperature reaches the comfort level. The zone temperature is measured and logged by a combination of a temperature data-logger (shown in Fig. 3.2) and a built-in temperature sensor with the accuracy of $\pm 0.2^{\circ}$C as part of the Building Management System (BMS).

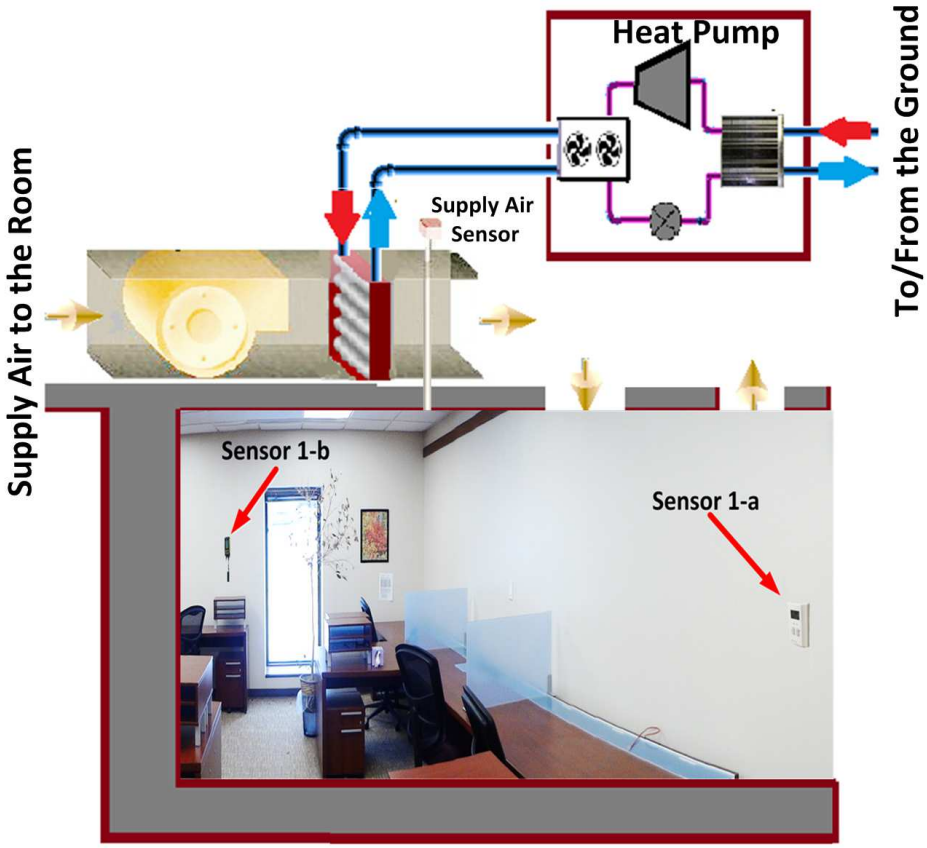

Figure 3.2: Testbed schematic with a ground-source heat-pump (GSHP). Sensor 1-a denotes the BMS temperature sensor and sensor 1-b belongs to the data-logger installed in the room.

3.3 Mathematical Modeling

3.3.1 Building Thermal Model

Conductive heat transfer via walls and ceiling, convective heat transfer due to air circulation, radiation through the windows, and solar radiation absorption are the

main heat transfer mechanisms in buildings. We use the mathematical model for heat transfer in buildings developed in [1, 61, 106].

In this section, we concisely discuss the building thermal model and nodal approach presented in [42]. In nodal approach modeling, we consider buildings as graphs containing walls and rooms as nodes. n shows number of nodes. m out of n nodes are rooms and the remaining $n-m$ nodes are walls. Fig. 3.3 shows the nodal schematic of the room studied in this chapter. We show temperature of the wall between room i and j by $T^w_{i,j}$. The following equation presents thermal heat transfer for the wall:

$$C^w_{i,j}\frac{dT^w_{i,j}}{dt} = \sum_{j\in\mathcal{N}^w_{i,j}} \frac{T^r_j - T^w_{i,j}}{R^w_{i,j}} + r_{i,j}\alpha_{i,j}A^w_{i,j}Q^{rad}_{i,j} \tag{3.1}$$

where $C^w_{i,j}$ is heat capacity of the wall between room i and j. Thermal resistance between the centerline of wall and the side of the wall is denoted with $R^w_{i,j}$. Wall identifier is shown by $r_{i,j}$ which is equal to 0 for internal walls, and equal to 1 for peripheral walls (i.e., either i or j is the outside node). $\alpha_{i,j}$ and $A^w_{i,j}$ are radiative heat absorption coefficient and area of wall between room i and j, respectively. $Q^{rad}_{i,j}$ represents the radiative heat flux density on wall (i,j) while $\mathcal{N}^w_{i,j}$ is the set of all neighboring nodes to node $w_{i,j}$. The following equation determines the temperature of the i^{th} room:

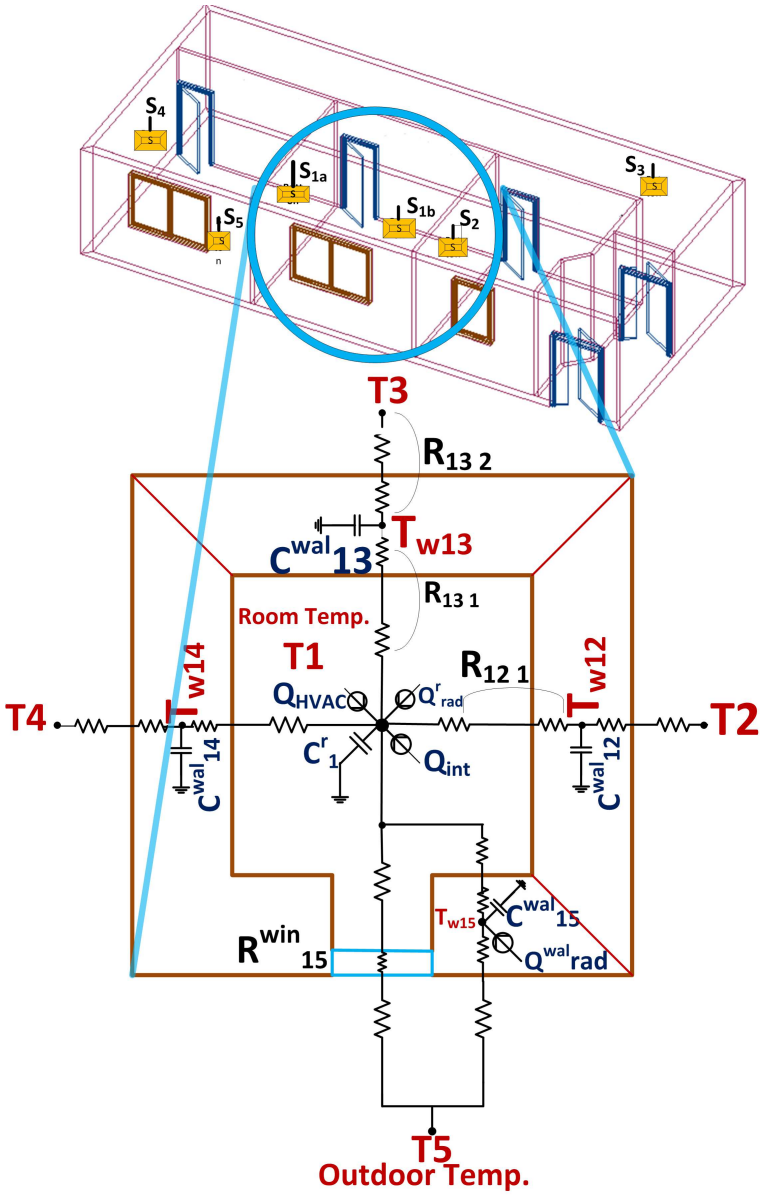

Figure 3.3: Schematic of building thermal model using nodal approach.

$$C_i^r \frac{dT_i^r}{dt} = \sum_{j \in \mathcal{N}_i^r} \frac{T_{i,j}^w - T_i^r}{R_{i,j}^w} + \pi_{i,j} \sum_{j \in \mathcal{N}_i^r} \frac{T_j^r - T_i^r}{R_{i,j}^{win}} + \dot{m}_i^r c_{p_{avg}} (T_i^s - T_i^r) + \pi_{i,j} \tau_{i,j}^w A_{i,j}^{win} Q_i^{rad} + \dot{Q}_i^{int} \tag{3.2}$$

where the temperature of i^{th} room is represented with T_i^r and C_i^r denotes the room

heat capacity. $\pi_{i,j}$ is window identifier which is equal to 0 if there is no wall between room i and j, otherwise equal to 1. Thermal resistance of the window between room i and j is denoted with $R_{i,j}^{win}$ and $\dot{m}_i^r$ shows air mass flow into or out of the room i. $c_{p_{avg}}$ denotes the average specific heat of air and T_i^s is the temperature of the supply air to room i. $A_{i,j}^{win}$ is the total area of window between room i and surrounding room j, $\tau_{i,j}^w$ is the transmissivity of glass of window between room i and j, Q_i^{rad} is the radiative heat flux density per unit area radiated to room i, and $\dot{Q}_i^{int}$ denotes the internal heat generation in room i. $\mathcal{N}_i^r$ is the set of all *nodes* surrounding room i. The thermal modeling details and estimation of the unmodelled dynamics can be found in [23, 29, 42].

The disturbance to the model is an affine function of several factors including all neighboring rooms temperature, $T_j^r(t)$, internal heat generation in rooms $\dot{Q}^{int}(t)$, and radiative heat flux density on walls, $Q_i^{rad}(t)$. Hence, the disturbance vector is given by:

$$d_t = g(T_j^r(t), Q_i^{rad}(t), \dot{Q}^{int}(t)) \tag{3.3}$$

Heat transfer of each wall and room equations and disturbance form the system dynamics of building are represented in state-space form by:

$$\dot{x}_t = f(x_t, u_t, d_t, t)$$

$$y_t = Cx_t \tag{3.4}$$

where $x_t \in \mathbb{R}^n$ is the state vector representing the temperature of the nodes in the thermal network, $u_t \in \mathbb{R}^{lm}$ is the input vector representing the air mass flow rate and its temperature for each thermal zone, and $y_t \in \mathbb{R}^m$ is the output vector of the system which represents the temperature of the thermal zones. l is the number of inputs to each thermal zone (e.g., air mass flow and supply air temperature). C is a matrix of proper dimension. Fig. 3.4 validates our model, comparing estimated and measured room temperature for four days in winter. The measured data are collected from Sensor S_{1a} shown in Fig. 3.3 and the estimated data are obtained using the same input (supply air temperature) in the building thermal model presented in equation (3.4). In the validation, we considered that the COP of the heat-pump remains constant. Thus, the power consumed by the heat-pump is the heat flow into the heating zone divided by the heat-pump COP.

Equation (3.4) describes the nonlinear time evolution of the system. The supply air temperature (i.e., input to the system) is multiplied by the air mass flow, which is the other time-varying known input to the model. Given that the air mass flow rate is constant during day and has another constant value during night, we can divide the

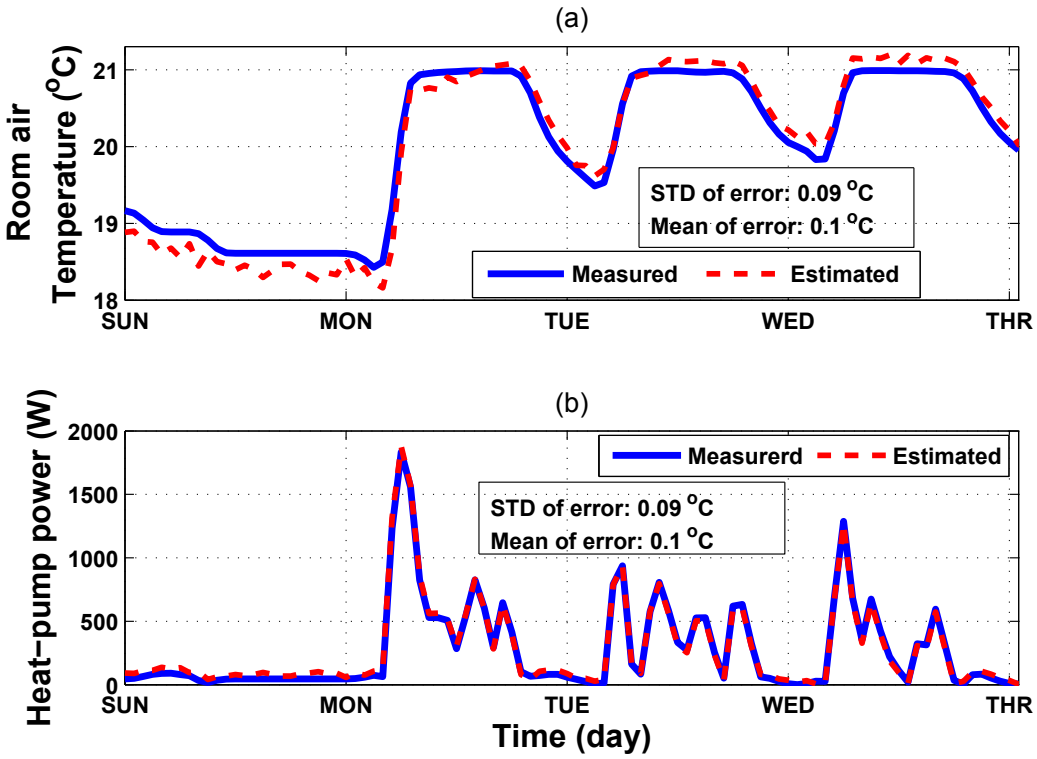

Figure 3.4: Experimental validation of building thermal model. (a) shows estimated and measured room temperature. (b) illustrates heat-pump electricity consumption based on simulation and actual data.

system into two linear subsystems with constant mass flow rates at each operating zone. In this approach, matrices A and B of the state-space model are updated at each time step t. This results in linear parameter varying (LPV) system dynamics. We use Euler's discretization method to discretize the state update equation (3.4) for controller design. The state-space model is given by:

$$x_{k+1} = \begin{cases} A_d x_k + B_d u_k + E_d d_k & k \,\epsilon\, [5, 6, \ldots, 18] \\ A_n x_k + B_n u_k + E_n d_k & k \,\epsilon\, [19, \ldots, 24, 1, 2, 3, 4] \end{cases} \tag{3.5}$$

where d_k is the disturbance vector and E is a matrix with appropriate dimension. The subscripts 'd' and 'n' refer to day and night, respectively. The procedure to derive state-space matrices from the heat transfer equations is presented in Appendix I.

3.3.2 Building Exergy Model

In exergy analysis, definition of reference environment in terms of reference temperature, pressure, and chemical composition are crucial. Ambient environment is used as a reference condition for exergy analysis in buildings for HVAC applications [107]. In our study the same definition is used while each room in a building is considered as a control volume. The following equation governs the exergy balance for a control volume with thermodynamic exergy destruction [108]:

$$\dot{X}^r_{dest_i} = \overbrace{\sum_{k\in N^r_i}(1-\frac{T_0}{T^r_i})\dot{Q}_i{}^{H.T.,k}}^{\dot{X}_i^{H.T.,r}} - \dot{W}^r_i + \sum_{in}\dot{m}^r_i\psi - \sum_{out}\dot{m}^r_i\psi - \frac{dX^r_i}{dt} \tag{3.6}$$

where the rate of exergy destruction in i^{th} room is shown by $\dot{X}^r_{dest_i}$. This term denotes the loss in work potential due to irreversibility such as air mixing and heat transfer. T_0 is the reference air temperature and $\dot{Q}_i{}^{H.T.,k}$ is the rate of heat transfer to room i. Rate of exergy transfer by work is shown by $\dot{W}^r_i$ and is equal to zero for our system since there is no associated work in room i. ψ shows the amount of exergy associated

with flow. $\frac{dX_i^r}{dt}$ represents the rate of change of exergy of the room i.

Whenever there is a temperature change, exergy destruction is inevitable. Unlike energy which is never destroyed during a process, exergy is not a conserved property [72]. Rate of exergy destruction ($\dot{X}_{dest}$) is proportional to irreversible entropy production inside the control volume. Total exergy transfer by the heat transfer is represented by $\dot{X}_i^{H.T.,r}$ in equation (3.6). This term is a function of different factors including the building type, insulation level and temperature difference between room i and surrounding zones. The third and the fourth terms of right hand side of equation (3.6) present flow exergy transfered in and out of the room, respectively. Exergy change due to heat transfer can be rewritten in the following terms:

$$\dot{X}_i^{H.T.,r} = \sum_{j \in N_i^r} (1 - \frac{T_0}{T_i^r})(\frac{T_j^r - T_i^r}{R_{i,j}^w}) \tag{3.7}$$

Total exergy of a flowing fluid in a control volume is the sum of exergies of its kinetic energy, potential energy and enthalpy. The following equation shows the unit-mass form of this equality:

$$\psi = (h - h_0) - T_0(s - s_0) + \frac{V^2}{2} + gz \tag{3.8}$$

in which h and h_0 indicate enthalpy and dead-state enthalpy of the fluid. s and s_0

show fluid entropy and dead-state entropy. Specific kinetic energy of fluid and specific gravitational potential energy are represented by $\frac{V^2}{2}$ and gz, respectively. Changes in kinetic and gravitational energy of the supply air are neglected in this study due to insignificant values. Rate of change of exergy inside room i based on change in enthalpy and entropy is demonstrated in the following equation:

$$\begin{aligned} X_i^r &= m_i^{room}[(h-h_0) - T_0(s-s_0)] \Rightarrow \\ \frac{dX_i^r}{dt} &= m_i^{room}(\frac{dh}{dt} - T_0\frac{ds}{dt}) + \frac{dm_i^{room}}{dt}[(h-h_0) - T_0(s-s_0)] \end{aligned} \tag{3.9}$$

where m_i^{room} is mass of the air inside room i. Ideal gas assumption is considered for change in enthalpy and entropy due to the compressibility factor being close to one (very low pressure of the air). We neglect change of mass of the air inside room in equation (3.9), thus we assume $\frac{dm_i^{room}}{dt}$ is equal to zero. Hence, the only remaining term of the equation (3.9) is the first term. The following equation expresses the entropy change (Δs) and the enthalpy change (Δh) of air:

$$\Delta h = \int_1^2 c_{p_{avg}} dT \Rightarrow h_2 - h_1 = c_{p_{avg}}(T_2 - T_1) \tag{3.10}$$

$$\Delta s = \int_1^2 c_{v_{avg}} \frac{dT}{T} + R \cdot ln \frac{v_2}{v_1} \Rightarrow s_2 - s_1 = c_{v_{avg}} \cdot ln \frac{T_2}{T_1} + R \cdot ln \frac{v_2}{v_1} \tag{3.11}$$

where $c_{v_{avg}}$ is average specific heat capacity at constant volume and $c_{p_{avg}}$ is average specific heat capacity at constant pressure, respectively. In equations (3.10) and (3.11), $c_{p_{avg}}$ and $c_{v_{avg}}$ values are found for the average of air temperature range studied. R and v show gas constant and specific volume, respectively. T_i^s is considered entrance temperature of supply air into room i, while T_i^r is the exit temperature in the control volume. By plugging in equations (3.7), (3.8), (3.9), (3.10), and (3.11) into equation (3.6) and discretizing the consequent equation with sampling time of T_{sample} the following equation is concluded:

$$\begin{aligned}
&\dot{X}^r_{dest_i}[k] = \\
&\sum_{j \in N_i^r} (1 - \frac{T_0[k]}{T_i^r[k]})(\frac{T_j^r[k] - T_i^r[k]}{R^w_{i,j}}) + \dot{m}_i^r[k]\{c_{p_{avg}}(T_i^s[k] - T_i^r[k]) - T_0[k] c_{v_{avg}} \ln(\frac{T_i^s[k]}{T_i^r[k]})\} \\
&+ \frac{m_i^{room}}{T_{sample}}\{c_{p_{avg}}(T_i^r[k] - T_i^r[k-1]) - T_0[k] c_{v_{avg}} \ln \frac{T_i^r[k]}{T_i^r[k-1]}\}
\end{aligned} \tag{3.12}$$

where $[k]$ indicates index of time step. Equation (3.12) expresses the exergy destruction at each time step based on the outside air temperature, mass flow rate, supply air temperature and zone temperature. In Fig. 3.5 exergy destruction for one week is

shown based on measured temperature data. The supply air temperature and exergy destruction profile show a similar pattern. At the beginning of a day, the rate of exergy destruction rises when supply air temperature increases.

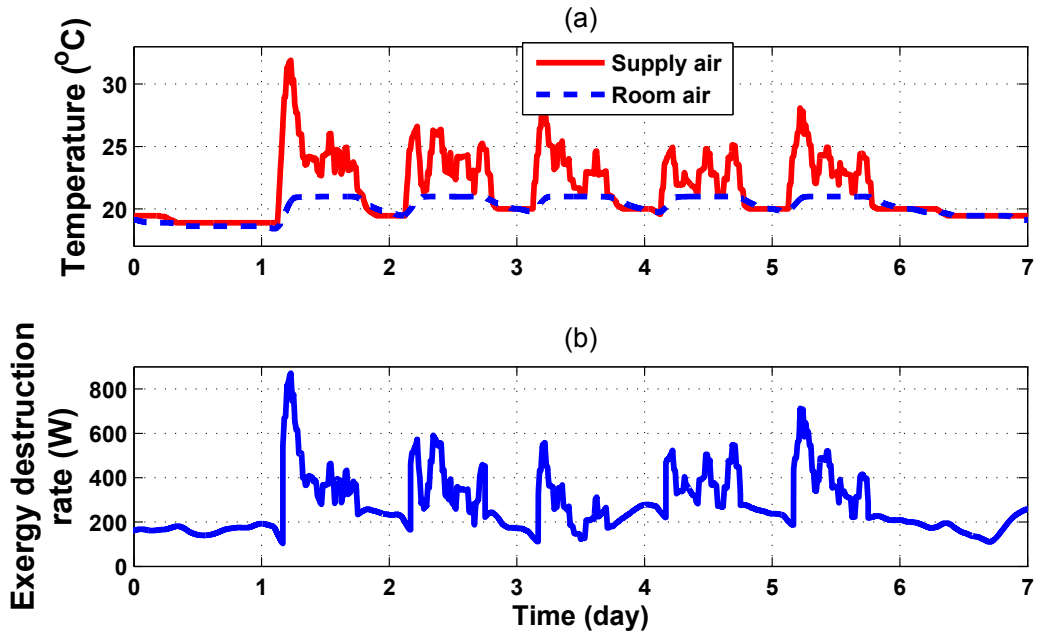

Figure 3.5: Exergy destruction over one week based on recorded data for existing HVAC control system. (a) shows room and supply air temperature and (b) shows corresponding rate of exergy destruction inside the control volume (i.e., room).

3.4 Controller Design

Two model predictive controllers based on exergy objective and energy objective are formulated. These predictive controllers are compared with a conventional rule-based

on-off controller to evaluate their performance. In order to have a fair comparison, time step is considered to be $\Delta t = 1$ hour for all controllers and the room temperature constraints are set based on ASHRAE Standard 62.1-2004 [66].

3.4.1 Rule-Based Control (RBC)

The rule-based controller in our building testbed turns off the heat-pump compressor when room temperature is within the pre-defined comfort level. When the zone temperature goes beyond lower-bound or upper-bound comfort level temperature, the controller keeps the heat-pump running for the duration of time step (Δt). Then, the controller checks the room air temperature again and determine whether the zone temperature is within the comfort level, and keeps the heat-pump on if the room air temperature is still beyond the bounds. In summer, the heat-pumps work in a reverse mode (cooling mode) and remove heat from the zones and reject it to the environment. The experimental data presented in this chapter is collected during winter only.

3.4.2 Energy-Based Model Predictive Control (EMPC)

We use the energy index, I_e, defined in [106] to minimize energy consumption in HVAC systems. I_e in (kWh) is defined as function of all HVAC loads in a building:

$$I_e = \sum_{t=1}^{24} \left[P_c(t) + P_h(t) + P_f(t) \right] \Delta t \tag{3.13}$$

where cooling power P_c, heating power P_h and fan power P_f are determined by:

$$P_c(t) = \dot{m}_i^r(t) c_{p_{avg}} [T_i^r(t) - T_c(t)] \tag{3.14a}$$

$$P_h(t) = \dot{m}_i^r(t) c_{p_{avg}} [T_h(t) - T_i^r(t)] \tag{3.14b}$$

$$P_f(t) = \kappa (\dot{m}_i^r)^3 \tag{3.14c}$$

where T_c and T_h are the supply air temperatures in the cooling mode and the heating mode, respectively. Equations (3.14a) and (3.14b) define the relationship between the supply air temperature (T_h or T_c) and the heat-pump power consumption in the heating mode and the cooling mode, respectively. κ [W.s^3.kg$^-$3] is the fan coefficient which expresses the cubic relation between power consumption and mass flow rate ($\dot{m}_i^r$). Since air mass flow has a constant value and is not a control input in the state space model, fan power (P_f) is not considered in the energy cost function. We formulate an MPC problem to minimize I_e. Hence, the controller minimizes the

required energy while keeping the room temperature within the comfort zone. We use the objective function in equation (3.15a) to minimize energy usage with low computational requirements. In addition, soft constraints denoted by ϵ in equation (3.15), are formulated to guarantee optimal problem feasibility at all times. The following optimization problem is being solved at each time step t:

$$\min_{U_t,\overline{\epsilon},\underline{\epsilon}} \{|I_e|_1 + \rho_{en}(|\overline{\epsilon}_t|_1 + |\underline{\epsilon}_t|_1)\} \tag{3.15a}$$

subject to:

$$x_{t+k+1|t} = Ax_{t+k|t} + Bu_{t+k|t} + Ed_{t+k|t} \tag{3.15b}$$

$$y_{t+k|t} = Cx_{t+k|t} \tag{3.15c}$$

$$\underline{\mathcal{U}}_{t+k|t} \leq u_{t+k|t} \leq \overline{\mathcal{U}} \tag{3.15d}$$

$$\delta\underline{\mathcal{U}} \leq u_{t+k+1|t} - u_{t+k|t} \leq \delta\overline{\mathcal{U}} \tag{3.15e}$$

$$\underline{T}_{t+k|t} - \underline{\varepsilon}_{t+k|t} \leq y_{t+k|t} \leq \overline{T}_{t+k|t} + \overline{\varepsilon}_{t+k|t} \tag{3.15f}$$

$$\underline{\epsilon}_{t+k|t}, \overline{\epsilon}_{t+k|t} \geq 0 \tag{3.15g}$$

where (3.15b) and (3.15c) is building state equation model. Input constraints on supply air temperature are shown in (3.15d) and (3.15e), and (3.15f) denotes output constraint on room air temperature and (3.15g) is the constraint on slack variables. Constraints (3.15b) and (3.15d) must hold for all $k = 0, 1, ..., N-1$ and

constraints (3.15c), (3.15e), (3.15f), and (3.15g) must hold for all $k = 1, 2, ..., N$. $U_t = [u_{t|t}, u_{t+1|t}, \cdots, u_{t+N-1|t}]$ denotes vector of control inputs, $\underline{\epsilon}_t = [\underline{\varepsilon}_{t+1|t}, \cdots, \underline{\varepsilon}_{t+N|t}]$ and $\overline{\epsilon}_t = [\overline{\varepsilon}_{t+1|t}, \cdots, \overline{\varepsilon}_{t+N|t}]$ are the slack variables vector. $y_{t+k|t}$ is thermal zone temperature vector, the output of state model. $d_{t+k|t}$ denotes the disturbance vector, and $\underline{T}_{t+k|t}$ and $\overline{T}_{t+k|t}$ for $k = 1, \cdots, N$ are the comfort bounds (lower and upper bounds) on the zone temperature, respectively. $\underline{\mathcal{U}}_{t+k|t}$ and $\overline{\mathcal{U}}$ denote the lower and upper limits on the supply air temperature provided by the heat-pump, respectively. Since physical limit on maximum supply air temperature is not time varying, therefore time invariant constraint $\overline{\mathcal{U}}$ is used. $\underline{\delta\mathcal{U}}$ and $\overline{\delta\mathcal{U}}$ are limits on rate of change of supply air temperature due to dynamics of heat-pump condenser. ρ_{en} is being used to consider penalty on the comfort constraint violations for EMPC.

At each time step, the first entry of input vector, U_t, found by the optimization problem is applied to the building model and moves the system forward to the next time step. Then, the prediction time horizon, N, is shifted to form a new optimization problem. The optimization process is repeated until covering the total time span of interest. In order to find the optimal future inputs, weather prediction for the next 24 hours, schedule of the zone (temperature bounds), and the building energy model are used. A schematic of model predictive control implementation is depicted in Fig. 3.6

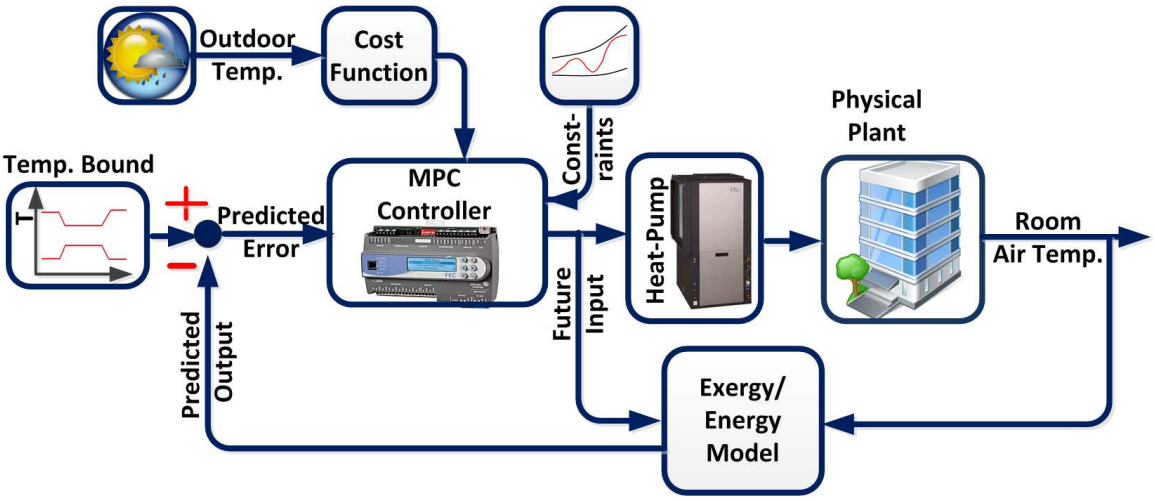

Figure 3.6: Structure of XMPC and EMPC.

3.4.3 Exergy-Based Model Predictive Control (XMPC)

An objective function based on exergy concept is constituted for XMPC problem. Exergy destruction ($\dot{X}_{dest_t}$) from equation (3.12) is selected as the objective function. In order to minimize $\dot{X}_{dest_t}$, we propose the objective function (3.16). For this purpose, XMPC algorithm finds the optimum inputs (supply air temperature) to minimize the irreversible entropy generation of the HVAC system and therefore increases the system efficiency. The following equation expresses the XMPC objective function:

$$\min_{U_t,\bar{\epsilon},\underline{\epsilon}} \{\dot{X}_{dest_t} + \rho_{ex}(|\bar{\epsilon}_t|_1 + |\underline{\epsilon}_t|_1)\} \tag{3.16}$$

The MPC problem is subjected to the same constraints on input and states as those in equation (3.15). ρ_{ex} is being used to consider penalty on the comfort constraint

violations for XMPC problem. In equation (3.16), $\dot{X}_{dest_t}$ is a nonlinear function and it leads to a nonlinear model predictive control (NMPC) problem which is computationally more expensive to solve compared to linear model predictive problem (LMPC) in equation (3.15).

sectionResults and Discussion

To set up the optimization problem in MATLAB®, YALMIP toolbox [109] is used. YALMIP toolbox provides a convenient symbolic syntax to formulate the problem, and then interfaces with an appropriate solver. Values of parameters and constants for building model are presented in Appendix II. To analyze the XMPC algorithm, we show the comparison between three controllers with respect to cumulative electrical energy consumption and the exergy destruction rate in Fig. 3.7, 3.8 and 3.9. Subplot (a) in Fig. 3.7 illustrates room air temperature profile and control input (i.e., supply air temperature) for the rule-based controller (RBC). The RBC controller fails to meet the temperature constraints at the beginning of the day (5-7 AM) since the controller is not able to detect the upcoming changes in the room's bound temperature (output constraint) in advance. Subplot (b) of Fig. 3.7 depicts exergy destruction rate as well as cumulative energy consumption. As shown in Fig. 3.7 the main exergy destruction takes place between 6-8 AM when the demand for exergy (i.e., supply air) is maximum. Having in mind that the EMPC can track the desired trajectory, it can satisfy the temperature comfort bounds (Fig. 3.8 (a)). Subplot (b) of Fig. 3.8 determines that

most of exergy destruction happens before 6 AM for EMPC. Fig. 3.9 illustrates the exergy-based MPC (XMPC) results. XMPC starts to heat the zone earlier than EMPC. Hence, maximum supply air temperature in XMPC is lower than EMPC and definitely less than RBC because supplying air with higher temperature causes more irreversiblity during heat transfer. A comparison between energy consumption and exergy destruction for the three controllers is made in Table 1. The results confirm that XMPC reduces exergy destruction of the zone, as well as decreasing the electrical energy consumption. Exergy cost function (equation (3.12)) contains more system efficiency related information compared to the energy cost function. Hence, exergy-based cost function considers energy/exergy flow from heat pump, energy/exergy loss due to heat transfer and rate of change of energy/exergy contained in the room. This information helps XMPC to reduce irreversibilities (i.e., irreversible entropy generation) which are sources of inefficiency in the HVAC operation.

Table 3.1
Performance comparison for three designed HVAC controllers.

Controller type	Cumulative exergy destruction $[kWh]$	Cumulative energy consumption $[kWh]$	Reduction in exergy destruction [%]*	Reduction in energy consumption [%]*
XMPC	2.7	4.2	22	36
EMPC	2.8	4.6	18	24
RBC	3.3	5.7	0	0

*Saving percentage is calculated by $\frac{x-x_0}{x} \times 100$, where x_0 is the energy consumption or exergy destruction of the RBC.

Fig. 3.10 represents irreversible entropy generation terms due heat transfer, mass transfer and change in stored entropy of the heating zone in the course of one day.

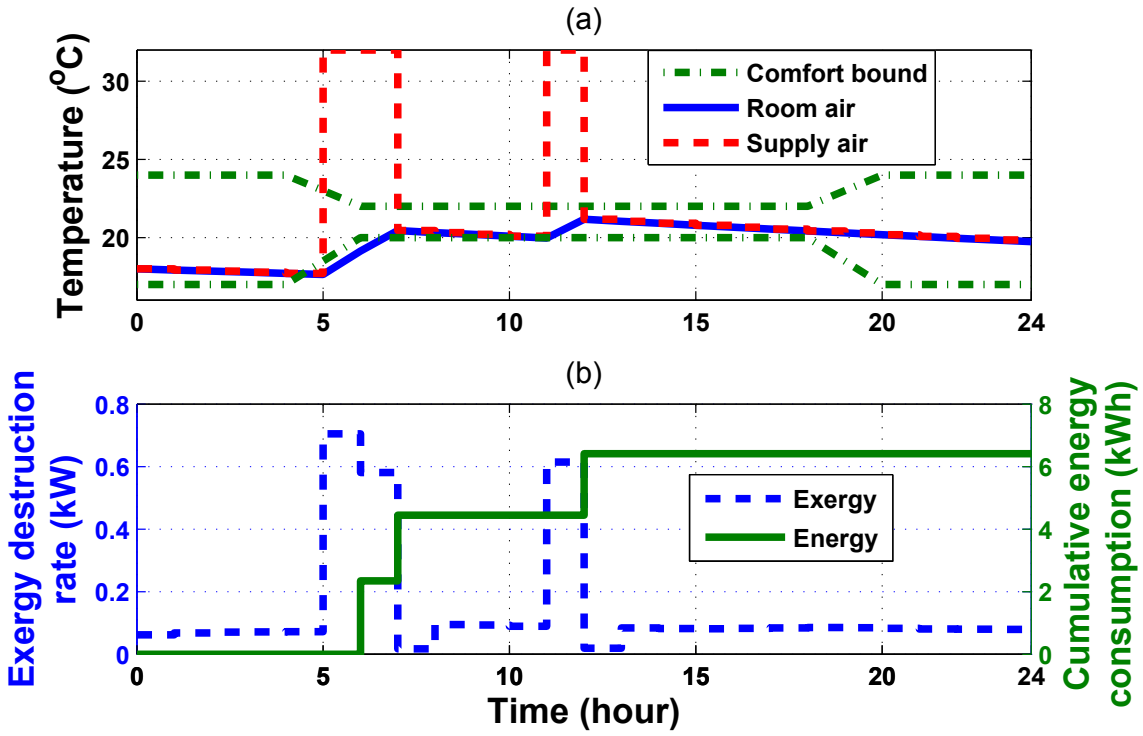

Figure 3.7: Performance of RBC with an update rate of $\Delta t = 1$ hour. (a) shows control input (i.e., supply air) and the room temperature profile, (b) illustrates exergy destruction rate and also cumulative energy consumption.

Irreversible entropy generation due to heat transfer in XMPC and EMPC are almost the same since outside temperature and the room air temperature are similar for both controllers. As shown in the second plot of Fig. 3.10, entropy generation due to mass transfer (supply air) for XMPC is less than EMPC. This happens since between hours 5-7 AM, XMPC controller supplies air with lower temperature and therefore results in less exergy destruction (Eq. (3.8)). The third plot in Fig. 3.10 illustrates change in the stored entropy of the room air. Since at the end of the day, room air temperature in XMPC is slightly lower than EMPC case (see Fig. 3.8 and 3.9), therefore the stored entropy in XMPC case is slightly less than EMPC case. Considering the

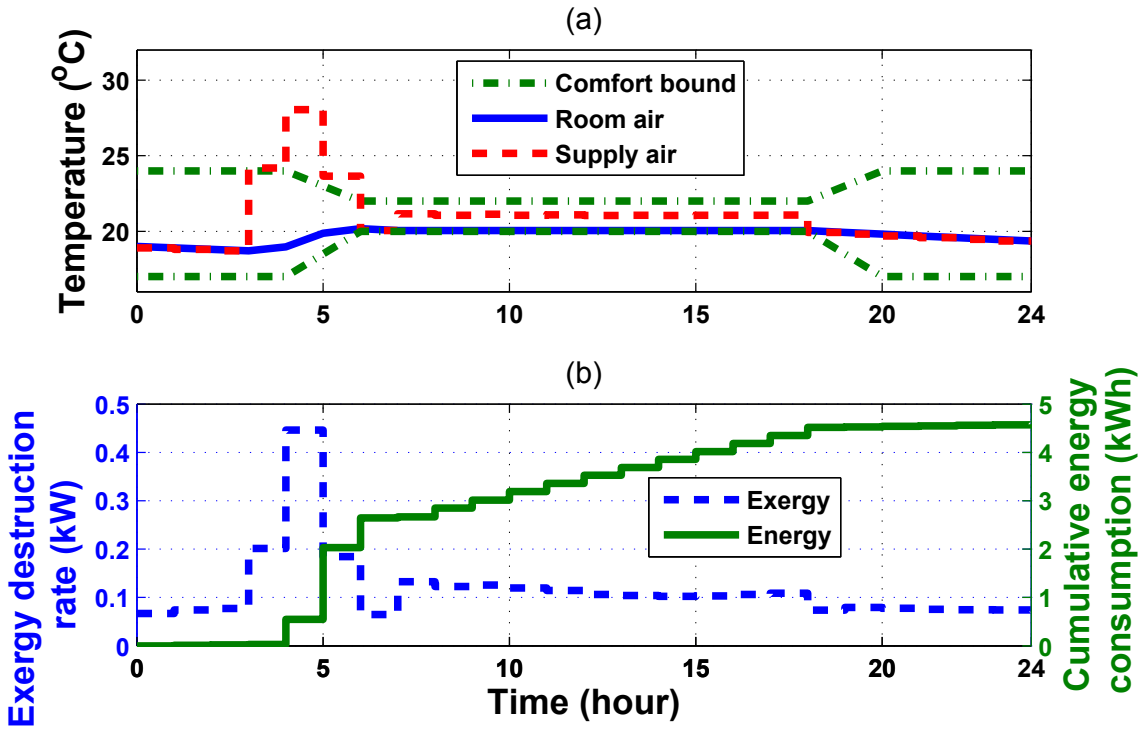

Figure 3.8: Energy-based MPC (EMPC) results.

fact that irreversible entropy generation conveys similar information with exergy destruction, we can conclude that the system efficiency in XMPC is higher than EMPC.

The benefits and drawbacks of the proposed XMPC versus the conventional EMPC and RBC can be summarized as follows:

Benefits of XMPC:

† Compared to RBC, we could achieve 22% reduction in exergy destruction and

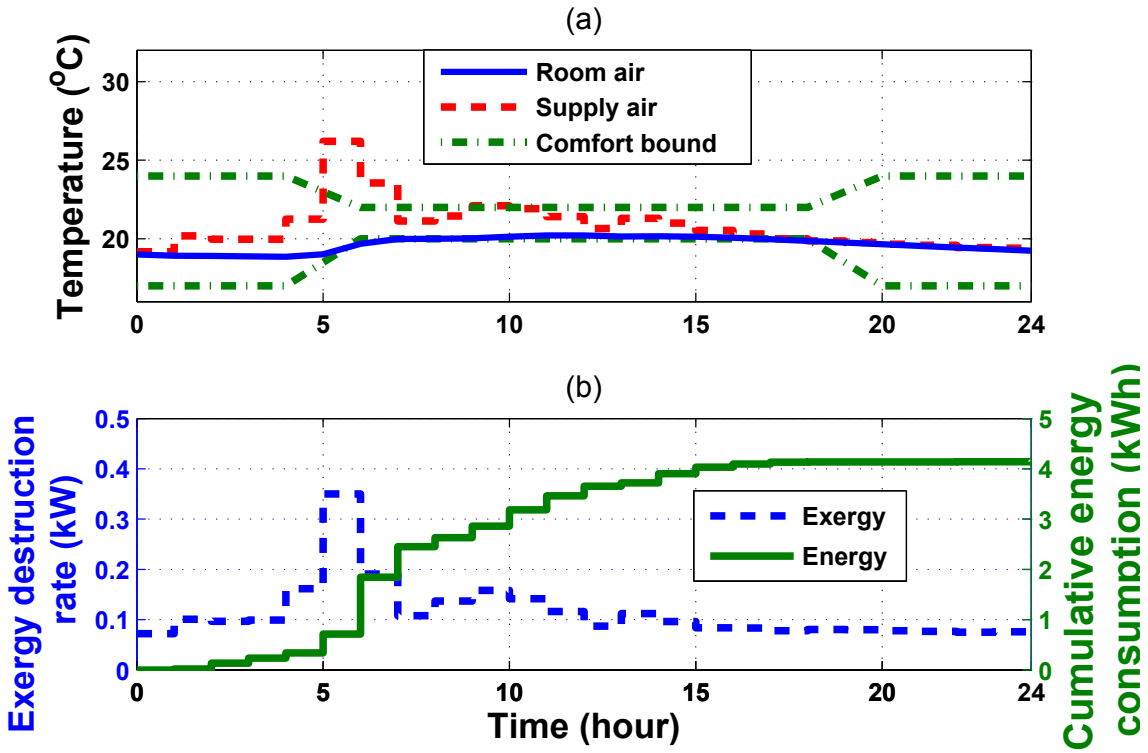

Figure 3.9: Exergy-based MPC (XMPC) results.

36% reduction in electrical energy consumption by HVAC system. XMPC optimizes the use of low quality energy (low exergy) for HVAC systems and hence decreasing irreversible entropy generation. Thus, supply air temperature needs to be close to the room temperature since large difference in supply air temperature increases entropy generation (exergy destruction).

† XMPC consumes 12% less energy and saves 4% more exergy compared to EMPC. By reducing energy loss and irreversibilities of energy/exergy flows into the zones, heat transfer of zone and rate of change of energy/exergy contained in the zone, XMPC offers more energy saving compared to conventional EMPC.

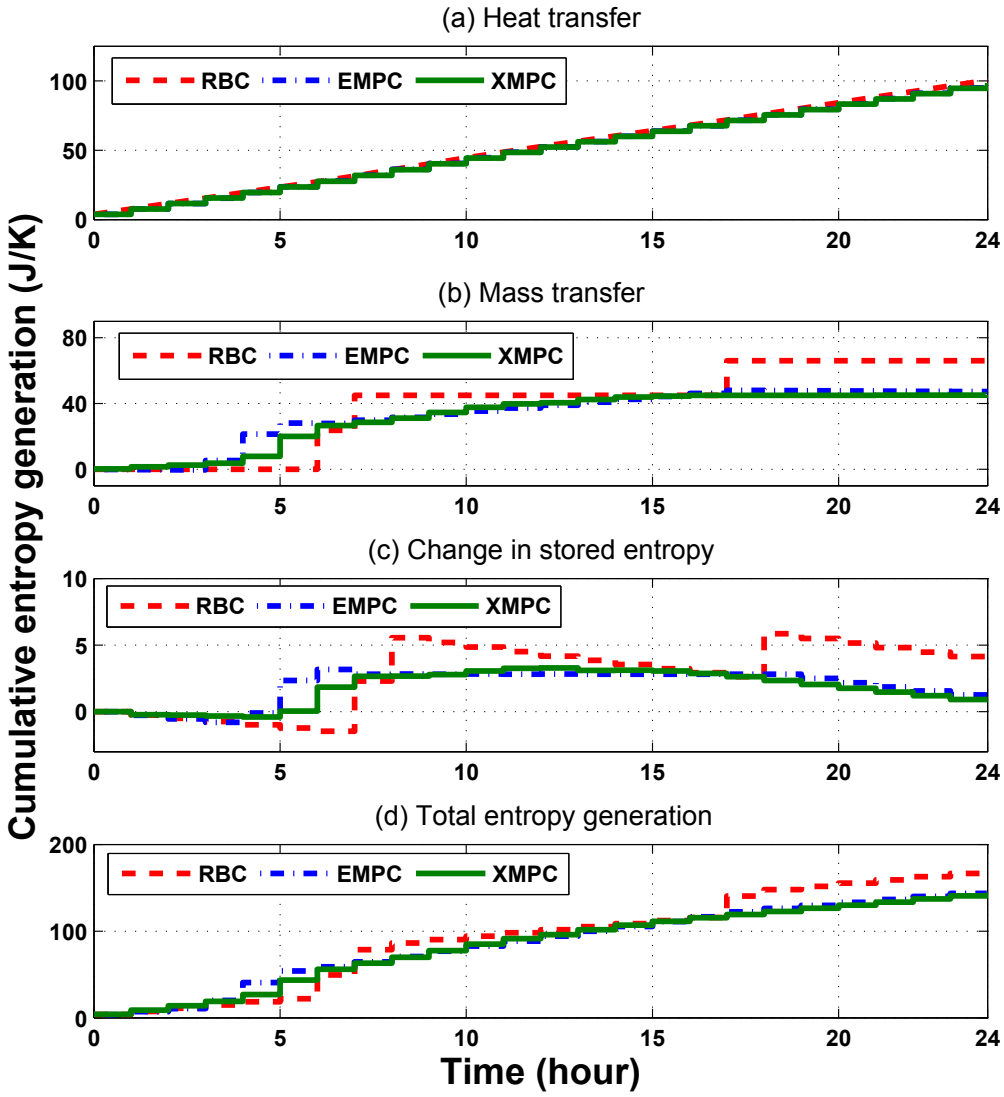

Figure 3.10: Irreversiblee entropy generation for XMPC and EMPC controllers. This figure shows three terms of entropy balance equation and corresponding entropy generation for XMPC and EMPC controllers.

Drawbacks of XMPC:

† Implementation of XMPC requires to have an accurate exergy model for HVAC system and exergy destruction model across the system components.

† In the optimization framework, solving XMPC problem is computationally expensive due to nonlinearity of the objective function. However XMPC can still run real-time (time step of 1 hour) due to slow thermal dynamics of rooms.

3.5 Summary and Conclusion

In this chapter we derived and formulated exergy destruction as a function of the physical parameters of the building. An optimal control problem is formulated to minimize exergy destruction rate. The beneficial new aspects of MPC problem based on exergy is optimizing the use of low quality energy (low exergy) for HVAC systems and hence decreasing irreversible entropy generation. Our findings show that the MPC controllers outperform the rule-based on-off controller for HVAC systems. Compared to RBC, EMPC results in 18% and 24% reduction in exergy destruction and energy consumption, respectively. XMPC enhances the results from EMPC by offering 22% reduction in exergy destruction and 36% reduction in HVAC energy consumption compared to RBC. Our results show the supremacy of XMPC compared to conventional EMPC since it consumes 12% less energy and saves 4% more exergy. The benefits from XMPC stem from reduction of sources of irreversible entropy generations by controlling the HVAC system variables that affect heat transfer, internal entropy generation rate, and exergy flows into the zones.

The implementation of the proposed XMPC is the same as conventional EMPC. The only difference is the change in the objective function. Details for implementation of conventional EMPC are extensively found in references [89, 90]. Future work includes implementation of XMPC on a real building testbed.

Chapter 4

Optimal Exergy-Based Control of Internal Combustion Engines[1]

Exergy or availability is defined as the maximum useful work during a process. This metric has been used to analyze and understand loss mechanisms of Internal Combustion Engines (ICEs). In this chapter, an optimal control method based on exergy is introduced for transient and steady state operation of ICEs. First, an exergy model is developed for a single cylinder Ricardo engine. The ICE exergy model is based on the Second Law of Thermodynamics (SLT) and characterizes irreversibilities. Such quantifications are not identified in the First Law of Thermodynamics (FLT) analysis. For steady-state operation of the ICE, a set of 175 different operating conditions is

[1]The material of this chapter has been submitted to Journal of Applied Energy [186] (APEN-D-16-04078) with the granted permission in Appendix E.

used to construct the SLT efficiency maps. Two different SLT efficiency maps are generated depending on the applications whether work, or Combined Power and Exhaust Exergy (CPEX) is the desired output. To include transient ICE operation, a model to predict exergy loss/destruction during engine transients is developed. The sources of exergy destruction/loss are identified for a Homogeneous Charge Compression Ignition (HCCI) engine. Based on the engine operating conditions (i.e., steady-state or transient) SLT efficiency contour maps or predicted exergy losses are determined at every given engine load. An optimization algorithm is proposed to find the optimum combustion phasing to maximize the SLT efficiency. Application of the optimization algorithm is illustrated for combustion phasing control. The results show that using the exergy-based optimal control strategy leads to an average of 6.7% fuel saving and 8.3% exergy saving compared to commonly used FLT based combustion control in which a fixed combustion phasing (e.g., $8°aTDC$) is used.

4.1 Introduction

The First Law of Thermodynamics (FLT) deals with energy conservation whereas the Second Law of Thermodynamics concerns about entropy production and irreversibilities in processes which cause deficiency. SLT states that energy has quality in addition to its quantity. Exergy or availability is the portion of energy that can do work in a specific environment. Exergy is based on FLT and SLT and determines the

ability of a system to do work in a specific environment [71]. Exergy can be destroyed through irreversible processes including combustion, heat transfer, friction and mixing in Internal Combustion Engines (ICEs), unlike energy which is not created nor destroyed. Irreversibilities lead to the loss of work potential during a process. For instance, exergy destruction of the combustion process in ICEs reduces the fuel potential to do mechanical work. Thus, identification of sources of exergy destruction in an ICE is crucial to enhance the engine performance and efficiency. SLT characterizes and quantifies the sources of irreversibility and exergy loss in ICEs.

FLT analysis does not recognize irreversibilities across systems' components, thus it provides limited insight for ICE optimal control. A large number of studies [7, 8, 110, 111, 112, 113, 114, 115, 116, 117, 118, 119, 120] have analyzed SLT in ICEs. Figure 4.1 illustrates a summary of the ICE studies in the literature based on the exergy and SLT. As shown in Figure 4.1, depending on the use of exergy in ICEs, studies can be categorized into three main groups: (i) system analysis, (ii) design optimization, and (iii) controls. The first group consists of exergy analysis for (a) whole engine [7, 8, 110, 111], (b) combustion phasing [112, 113], (c) closed engine cycle [114, 115, 116, 119], (d) combustion process [117, 121, 122], and (e) exhaust heat recovery [123, 124, 125]. For instance in [7], application of the SLT and its equations have been provided for different types of internal combustion engines and their subsystems (e.g., turbocharger, inlet and exhaust manifolds). Exergy analysis of a gasoline-fueled Homogeneous Charge Compression Ignition (HCCI) engine has been

studied in [112]. According to the results in [112], the main exergy loss mechanism is combustion, which accounts for 19-23% of total exergy loss. The other exergy loss mechanisms including heat loss, exhaust gases, and Unburnt Hydrocarbons (UHC) are responsible for 5-15%, 12-20%, and 1%, respectively [112].

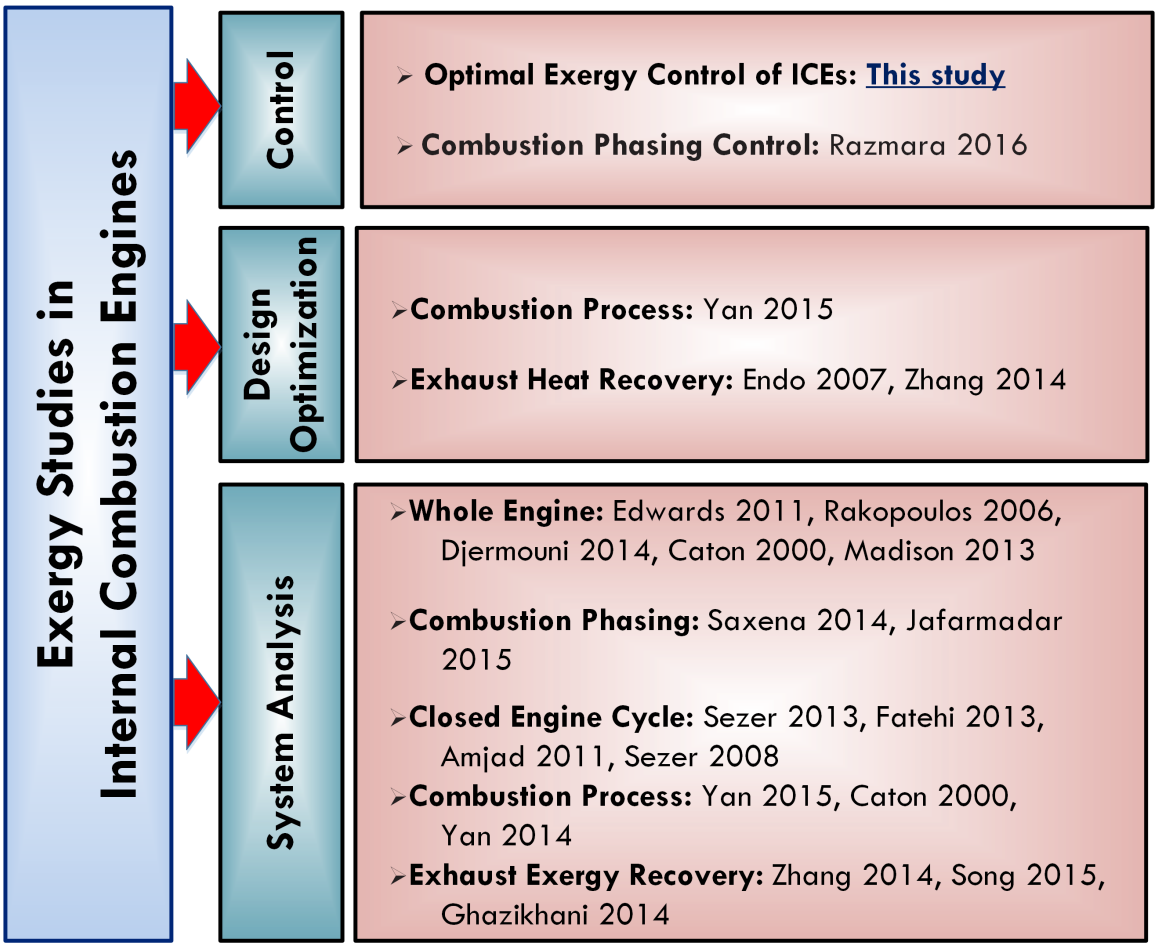

Figure 4.1: Research background of SLT and exergy studies in ICEs.

Studies in the second group (design optimization), concentrate on how to improve

the design of ICEs and related subsystems based on exergy metric [118, 121, 123]. In [121], a Reformed Molecule HCCI (RM-HCCI) method is introduced. The results in [121], show that simpler fuel molecules cause less combustion irreversibility. Thus, reforming hydrocarbon fuels into small molecules under a specific condition leads to a higher SLT efficiency.

The third group in Figure 4.1 centers on the usage of exergy and SLT for control of ICEs. While exergy-based control has been studied before for different applications [2, 102, 103] like Heating, Ventilation and Air conditioning (HVAC) with promising results by the authors of this chapter [2, 103], there are only few studies undertaken for exergy-based control of ICEs. In [3], we designed a control algorithm to find optimum combustion phasing based on exergy for steady state operation of engines. This chapter will present how to use exergy insight in control of ICEs for both steady-state and transient operations. In this chapter, experimental SLT maps and predicted exergy loss/destruction are based on physical models.

In different types of ICEs, combustion phasing is a commonly-used control variable since output power, engine-out emissions, combustion cyclic variations, and exhaust gas temperature are dependent on the combustion phasing [6]. Different control actuators have been used to adjust combustion phasing. For example, in conventional Compression Ignition (CI) engines, the fuel injection timing and number of

in-cylinder injections are used for combustion phasing control while in Spark Ignition (SI) engines, timing of spark ignition is used to control combustion phasing. In HCCI, since there is no direct means to initiate the combustion, combustion phasing is controlled by adjusting the charge properties including temperature, pressure and fuel-air concentrations [126, 127]. For HCCI combustion phasing control, different control actuators including dual fuel ratio adjustment [128, 129], intake air temperature adjustment [130] and Variable Valve Actuation (VVA) [131] have been used. In this chapter, an exergy-based optimal control method is introduced to adjust combustion phasing in ICEs.

Based on the application, the desired output of an ICE can be either power or Combined Power and Exhaust Exergy (CPEX). By minimizing exergy losses or maximizing SLT efficiency, the desired output exergy is increased. Exhaust exergy can be used in both stationary and mobile applications of energy systems. For example, turbochargers use exhaust exergy to boost the intake air pressure that leads to improve the automotive engine efficiency. Similarly, exhaust exergy is recovered in Combined Heat and Power (CHP) systems. In [124] exergy recovery for an CI engine is studied and authors experimentally showed that by recovering exhaust exergy, the Brake Specific Fuel Consumption (BSFC) decreases by 10%. In [123] exhaust exergy recovery is studied for an ICE by using a Thermo-Electric Generator (TEG). Results in [123] show 5.2% increase in the effective thermal efficiency of the ICE.

Low Temperature Combustion (LTC) mode, compared to conventional SI or CI modes, leads to higher exergy efficiency [112]. In this chapter, we focus on HCCI which is a well-recognized LTC mode for ICEs. In this study, we use SLT efficiency as an accurate metric for engine control. An exergy model for a single cylinder HCCI engine is constructed. A crank angle resolved exergy analysis for a single-zone model is first conducted. Then, the SLT efficiency contour maps are generated based on 175 experimental data points for steady-state operation. A physical model is designed to predict instantaneous in-cylinder pressure, Start of Combustion (SOC), and CA50, i.e. the crank angle where 50% of the fuel mass is burnt. The predicted pressure trace is used to calculate exergy loss/destruction of different transient operating points. An optimization algorithm is formulated based on exergy to determine the optimum combustion phasing at every given engine load for transient and steady-state modes. Then, an algorithm for Exergy-based Control of ICE (XCICE) is developed. The new exergy-based control approach is illustrated by tracking the optimum CA50. CA50 is used in this study since it is a robust feedback indicator of HCCI combustion phasing due to the steep heat release in the main stage of HCCI combustion [132].

The chapter is organized as follows. Section 2 describes the engine type and the experimental data used in this chapter. In Section 3, exergy model of the ICE is introduced. Crank-angle resolved exergy analysis is presented in Section 4. In Section 5, SLT efficiency maps are illustrated. An exergy-based optimal combustion phasing algorithm is introduced in Section 6, followed by the engine control oriented model.

XCICE is presented in Section 8 and optimization results are shown in Section 9. Finally summary and conclusion are drawn in Section 10.

4.2 Engine Experimental Data

In this section, the experimental data from [6] for a single cylinder Ricardo HCCI engine at 175 different operating conditions are used. The specifications of the HCCI engine are listed in Table 4.1. This HCCI engine is a blended fuel engine using two Primary Reference Fuels (PRFs): n-Heptane with octane number (ON) of 0 (PRF0) and iso-Octane with ON of 100 (PRF100). The fuels are injected and pre-mixed with air in the intake manifold. More details about the operation of this engine and the experimental setup used for collecting the engine data are found in [6].

Table 4.1
Specifications of the single cylinder Ricardo HCCI engine.

Parameter	**Value**
Bore	80 mm
Stroke	88.90 mm
Compression Ratio (CR)	10 : 1
Displacement volume (V_d)	447 cc
Number of valves	4
Intake valve opening (IVO)	$-175\,^\circ$ aBDC*
Intake valve closing (IVC)	$+55\,^\circ$ aBDC
Exhaust valve opening (EVO)	$-70\,^\circ$ aBDC
Exhaust valve closing (EVC)	$-175\,^\circ$ aBDC

*After bottom dead center.

Figure 4.2 shows the engine operating range in this study. As seen in Figure 4.2, the data represents a wide range of operation from naturally aspirated to boosted conditions with ultra lean or lean air-fuel mixtures.

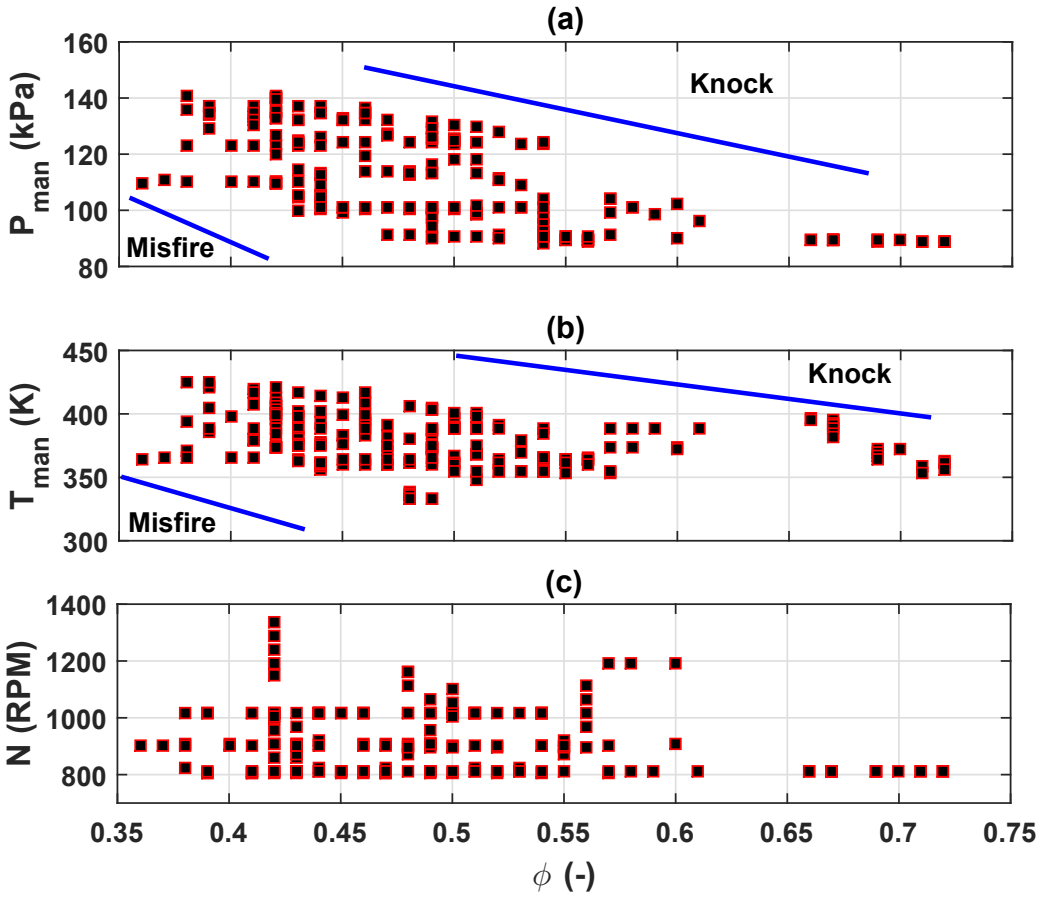

Figure 4.2: Engine operating range for 175 steady-state data-points without external Exhaust Gas Recirculation (EGR). The engine experimental data is taken from [6]. (a) Intake manifold pressure (P_{man}), (b) intake manifold temperature (T_{man}), and (c) engine speed (N).

Figure 4.3 shows the exhaust gas temperature (T_{exh}) contour map for different engine loads (Indicated Mean Effective Pressure, IMEP) for the 175 points in this study. For

these measurements the exhaust gas temperature sensor was located at the exhaust port. The data points in this contour map are the same as those in the SLT contour maps which will be shown later in the chapter. In Figure 4.3, misfire and knock limits are shown for the studied engine operating range. Too delayed combustion phasing (i.e., CA50) at low loads causes misfire while knocking occurs at higher loads with too early CA50s. The top right region in Figure 4.3 shows the region that higher engine loads can be obtained once dilution is used, e.g., by using Exhaust Gas Recirculation (EGR). No EGR is used in this study.

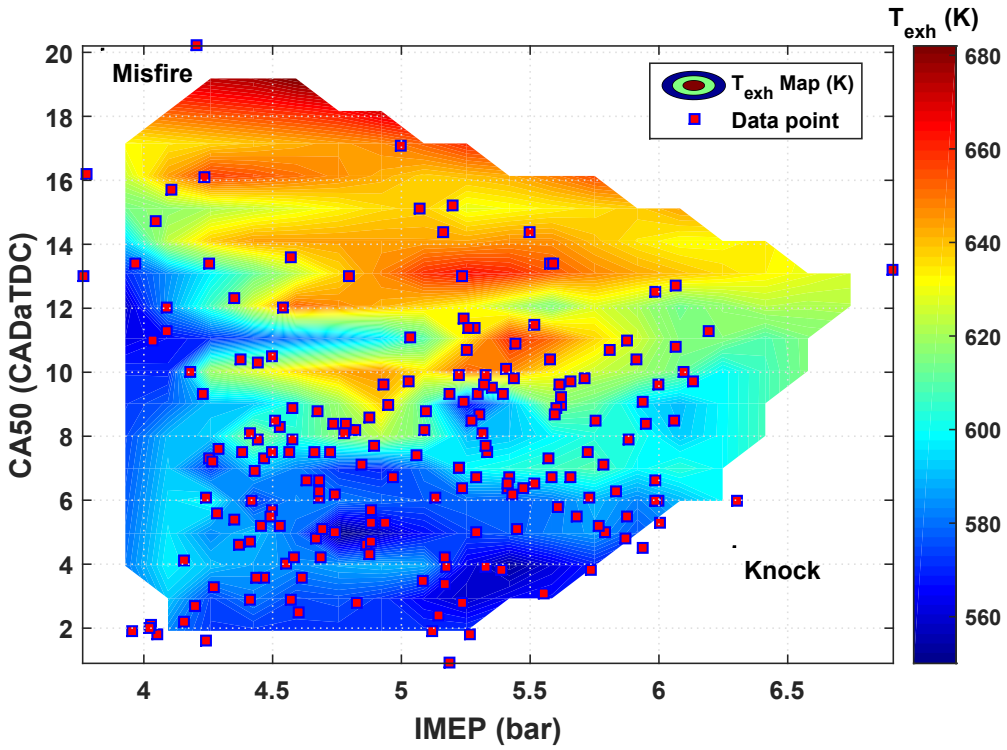

Figure 4.3: Exhaust gas temperature (T_{exh}) contour map with the distribution of the experimental data points in this study.

4.3 Engine Exergy Model

4.3.1 Dead-State Condition

The potential of a system to deliver work is defined with respect to a reference point that is called dead-state condition. In this study, restricted dead-state is used and denoted by asterisk subscript ('$*$'). The restricted dead-state is defined as the condition when a system is at the same temperature and pressure with its reference environment (i.e., $T_0 = 298.15\ K$ and $P_0 = 101.325\ kPa$) [7]; However, in the restricted dead-state, the chemical composition (e.g., molar mass of substances) may differ from the environment. Actual dead-state (or true dead-state) condition is the condition in which the system or mixture is in thermo-mechanical equilibrium and has chemical composition similar to that of the reference point (i.e., 75.67% N_2, 20.35% O_2, 3.03% H_2O, 0.03% CO_2, and 0.92% for other substances) [7]. In this chapter, to calculate the exergy flow of the processes during the engine operation, P_0, T_0 and dead-state air chemical molecular composition are used.

4.3.2 Exergy Balance

The following equation governs the exergy balance for an ICE cylinder:

$$X_{Fuel} + X_{Phys,in} =$$
$$X_{Work} + X_{Exh} + \underbrace{(X_{d,Comb} + X_{HT} + X_{d,Fric})}_{X_d} + \underbrace{X_{UHC} + X_{Blow-by} + X_{d,Mix}}_{X_{Others}} \tag{4.1}$$

where X_{Fuel} is fuel exergy at Intake Valve Closing (IVC) moment. Physical exergy of the mixture at IVC is denoted with $X_{Phys,in}$ and is calculated by using Eq. (4.2a) by knowing temperature and pressure at IVC moment. X_{Work} is the exergy transferred by work and the exhaust physical exergy is shown by X_{Exh}. $X_{d,Comb}$, X_{HT} and $X_{d,Fric}$ are exergy destruction due to combustion, exergy loss due to heat transfer, and exergy destruction due to friction, respectively. Exergy loss corresponding to UHC is shown with X_{UHC}. To calculate X_{UHC}, the measured UHC data from emission analyzer is used in this chapter [6]. $X_{Blow-by}$ denotes exergy losses due to blow-by gases. $X_{d,Mix}$ is the exergy destruction due to mixing. When two or more streams with different thermodynamic properties and chemical compositions mix, irreversible entropy is produced and exergy is destructed. The summation of other irrevrsibilities, $X_{d,Mix}$ and exergy losses including X_{UHC}, and $X_{Blow-by}$ is denoted by X_{Others} term in this chapter.

Flow of exergy in an engine is divided into two parts: physical and chemical. Physical exergy is related to the mixture's pressure and temperature. The difference in chemical composition of species with the reference environment compositions results in chemical exergy. Physical and chemical exergies of a system are determined by the

following equation [112]:

$$x_{Phys} = (u - u_*) + P_0(v - v_*) - T_0(s - s_*) \tag{4.2a}$$

$$x_{Chem} = \mu_* - \mu_0 \tag{4.2b}$$

where x_{Phys} and x_{Chem} denote physical and chemical exergies of a system, respectively. Specific internal energy, the specific volume and specific entropy are denoted by u, v and s, respectively. μ is the specific chemical potential in (4.2b), and is calculated by using Eq. (4.3):

$$\mu_* = h_* - T_0\ s_* \tag{4.3a}$$

$$\mu_0 = h_0 - T_0\ s_0 \tag{4.3b}$$

where specific enthalpy of the in-cylinder mixture is shown by h. Total specific exergy of a system (x_{total}) is defined as the summation of specific physical and chemical exergies [7]:

$$x_{total} = x_{Phys} + x_{Chem} \tag{4.4}$$

The thermodynamic properties (in Eq. (4.2) and Eq. (4.3)) for mixture species are dependent on in-cylinder gas temperature. Ideal gas law is used to calculate in-cylinder gas temperature. In order to calculate the thermodynamic properties in various conditions, NASA Polynomials [133] are used. NASA Polynomials include seven coefficients for species with temperatures less than 1000 K and seven constant coefficients for gases with the temperatures between 1000 K and 6000 K [133].

$$\frac{c_p}{R_u} = a_1 + a_2 T + a_3 T^2 + a_4 T^3 + a_5 T^4 \tag{4.5a}$$

$$\frac{H}{R_u T} = a_1 + a_2 \frac{T}{2} + a_3 \frac{T^2}{3} + a_4 \frac{T^3}{4} + a_5 \frac{T^4}{5} + \frac{a_6}{T} \tag{4.5b}$$

$$\frac{S}{R_u} = a_1 lnT + a_2 T + a_3 \frac{T^2}{2} + a_4 \frac{T^3}{3} + a_5 \frac{T^4}{4} + a_7 \tag{4.5c}$$

where $a_1, a_2, a_3, a_4, a_5, a_6, a_7$ are the polynomial coefficients [133]. c_p and R_u are the specific heat at constant pressure and the universal gas constant, respectively. H and S are enthalpy and entropy of in-cylinder species, respectively.

4.3.2.1 Indicated Work Exergy

Eq. (4.6) is used to calculate the rate of exergy transfer by work in the ICE. X_{Work} in Eq. (4.1) is gross indicated work which is calculated by taking integral of Eq. (4.6)

between IVC to EVO moments.

$$\frac{dX_W}{d\theta} = (P - P_0)\frac{dV}{d\theta} \tag{4.6}$$

where P is the in-cylinder pressure and θ is the crank angle degree (CAD). V is the instantaneous volume of cylinder. The crank-slider mechanism formulation from [134] is used to calculate V.

4.3.2.2 Exhaust Exergy

Eq. (4.2a) is used to calculate exhaust exergy between EVO and EVC moments. The exhaust exergy, X_{Exh}, is calculated by knowing the specific internal energy, volume and entropy of exhaust gas. For steady-state operation of ICE, experimentally measured pressure and temperature are used to find the thermodynamic properties of exhaust gases. For transient operation of ICE, pressure and Temperature at EVO are estimated using the in-cylinder pressure model explained in Section 4.3.5.

4.3.2.3 Combustion Irreversibility

Any process in an ICE that involves temperature change, destructs exergy (i.e., work potential loss). Up to 25% of the fuel exergy is wasted during combustion process [112] which is the largest portion of exergy loss/destruction in a conventional ICE. The factors that affect combustion irreversibilities include: (1) fuel-air equivalence ratio, ϕ, (2) EGR rate, (3) fuel molecule complexity, and (4) inlet oxygen concentration [121, 135]. For instance, by increasing ϕ values, the exergy destruction of combustion process decreases due to higher mixture temperature [112]. The following equation is used to calculate combustion irreversibility [7]:

$$dX_{d,Comb} = -\frac{T_0}{T}\sum_i(\mu_i dm_i) \tag{4.7}$$

where the differential of the exergy destruction due to combustion is denoted by $dX_{d,Comb}$. μ_i in Eq. (4.7) for fuel is equal to x_{Fuel} and for other mixture species is considered to be specific Gibbs free enthalpy. As seen in Eq. (4.7), the combustion irreversibility depends on the in-cylinder mixture temperature, species type and changes in species mass (dm_i) that is controlled by the chemical reaction rates.

4.3.2.4 Exergy loss due to heat transfer

In engine operation, exergy is lost due to heat transfer between in-cylinder mixture and cylinder wall. X_{HT} in Eq. (4.1) is calculated by:

$$\frac{dX_{HT}}{d\theta} = (1 - \frac{T_o}{T})\frac{dQ_L}{d\theta} \tag{4.8}$$

where $\frac{dX_{HT}}{d\theta}$ denotes the rate of exergy loss due to heat transfer and $(1 - \frac{T_o}{T})$ is the Carnot cycle efficiency. To calculate the heat transfer rate (denoted by $\frac{dQ_L}{d\theta}$) in Eq. (4.8), modified Woschni correlation from [136] is used for the HCCI engine.

4.3.2.5 Friction

Chen & Flynn correlation [134] is used to estimate Friction Mean Effective Pressure (FMEP) for the engine in this chapter. Eq. (4.9) governs the exergy destruction due to friction [134].

$$FMEP = c_1 + c_2 P_{max} + c_3 U_p + c_4 U_p^2 \tag{4.9a}$$

$$X_{d,Fric} = FMEP \times V_d \tag{4.9b}$$

Where P_{max} is the maximum cylinder pressure. V_d and U_p denote the engine displacement volume and the mean piston speed, respectively. The constants in (4.9a) (c_1, c_2, c_3 and c_4) are determined based on engine experimental data. In this study, the experimental data of whole engine $FMEP$ from [137] was used.

The contour map of X_d (i.e., combined exergy destruction and exergy loss) with respect to the engine load (IMEP) and the combustion phasing (CA50) is shown in Fig. 4.4. As expected, more exergy destruction is observed during high engine load operations, since more fuel is burnt, compared to fuel burnt at lower loads. A proper selection of CA50 can reduce the amount of exergy X_d at each engine load. As seen in Figure 4.4, too early combustion (e.g., $CA50 \leq 4\ CADaTDC$) have higher X_d.

4.3.2.6 Fuel Exergy

Liquid hydrocarbon fuels for ICEs have a general structure of C_cH_h. Eq. (4.10) determines the approximate chemical exergy of hydrocarbon fuels based on the fuel Lower Heating Value (LHV) [138].

$$x_{Fuel} = (1.04224 + 0.011925\frac{h}{c} - \frac{0.042}{c}) \times LHV \tag{4.10}$$

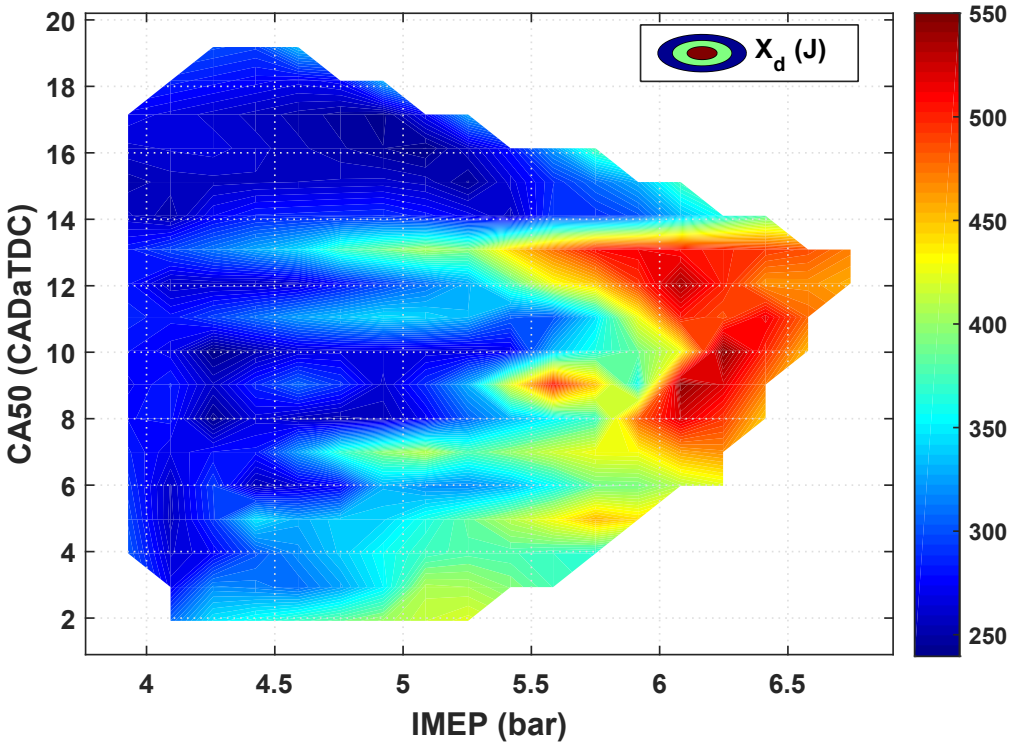

Figure 4.4: Combined exergy destruction and exergy loss (X_d) contour map. This map is generated using the data points from Fig. 4.2 and Fig. 4.3 and the exergy model in this study.

Where x_{Fuel} denotes the specific chemical exergy of the fuel. The ratio of fuel exergy to LHV ($\frac{x_{Fuel}}{LHV}$) which indicates the value of chemical exergy to chemical energy depends on the hydrocarbon type. This ratio for n-Heptane (C_7H_{16}) and iso-Octane (C_8H_{18}) are 1.06350 and 1.06382, respectively.

4.3.3 Chemical Reaction

A single-zone combustion model is used in this work which is intended for control applications. The global chemical reaction for burning the blends of n-Heptane and iso-Octane is:

$$\begin{aligned}(1-\frac{ON}{100})C_7H_{16} + (\frac{ON}{100})C_8H_{18} + (11 + \frac{3}{2}\frac{ON}{100})(O_2 + 3.76N_2) \Rightarrow \\ (\frac{ON}{100} + 7)CO_2 + (\frac{ON}{100} + 8)H_2O + 3.76(\frac{3}{2}\frac{ON}{100} + 11)N_2\end{aligned} \tag{4.11}$$

Stoichiometric air to fuel ratio (AFR) is denoted by $AFR_{Stoich.}$ and is determined by Eq. (4.12):

$$AFR_{Stoich.} = \frac{(11 + \frac{3}{2}\frac{ON}{100}) \times 4.76 \times MW_a}{(1 - \frac{ON}{100}) \times MW_{n-Hep} + (\frac{ON}{100}) \times MW_{iso-Oct}} \tag{4.12}$$

where MW_a, MW_{n-Hep} and $MW_{iso-Oct}$ are the molecular weights of air, n-Heptane and iso-Octane, respectively.

4.3.4 Second Law of Thermodynamics Efficiency

The SLT efficiency is the ratio of the desired output exergy to the consumed exergy. For each application, the desired output is defined. If the resulting shaft work from in-cylinder mixture combustion is the desired output, the SLT efficiency is defined as [7]:

$$\eta_{II,W} = \frac{X_W}{X_{Fuel} + X_{Phys,in}} \tag{4.13}$$

where $\eta_{II,W}$ is the SLT efficiency when work is the desired output. Physical exergy of in-cylinder mixture at IVC, $X_{Phys,in}$, is very small compared to X_{Fuel}; thus, $X_{Phys,in}$ is neglected in some studies [7]. Since $X_{Phys,in}$ is negligible compared to X_{Fuel}, value of $\eta_{II,W}$ is close to gross indicated thermal efficiency of the engine cycle (η_I).

In other applications, Combined Power and Exhaust Exergy (CPEX) is the desired output. For instance, in boosted engines, the exhaust exergy is used in turbochargers in order to increase the intake manifold pressure. Using exergy of exhaust gas in a turbocharger leads to a higher indicated engine work [134]. Another example includes Combined Heat and Power (CHP) systems in which exhaust exergy of ICE is used for heating applications. In addition, Thermoelectric Generator (TEG) uses the exhaust exergy to generate electricity; however, one should never sacrifice in-cylinder exergy

work for increasing the exhaust exergy, when work exergy is the desired output since efficiency of exhaust recovery systems are low.

Eq. (4.14) determines the SLT efficiency of CPEX systems [7]:

$$\eta_{II,CPEX} = \frac{X_W + X_{Exh}}{X_{Fuel} + X_{Phys,in}} \tag{4.14}$$

where X_{Exh} is the average of the physical exergy of exhaust gases.

4.3.5 In-cylinder Pressure Model

There are many factors that affect in-cylinder pressure trace in an ICE. These factors include engine geometrical parameters, heat-release rate, intake manifold pressure and temperature (P_{man} and T_{man}), EGR, ϕ, etc. In this chapter, an experimentally validated physics-based model is used to predict Start of Combustion (SOC) and End of Combustion (EOC) [128]. By knowing P_{SOC} and P_{EOC}, we are able to predict the closed-cycle in-cylinder pressure trace. The closed-cycle pressure can be divided into three parts: (1) IVC to SOC, (2) SOC to EOC, and (3) EOC to EVO. A polytropic compression process is assumed to estimate the pressure trace between IVC to SOC [134]. To estimate pressure during combustion (SOC to EOC) heat-release which is determined based on fuel mass fraction burned (MFB) is used. To this end,

the modified Wiebe function is used to calculate MFB [126]:

$$MFB(\theta) = 1 - exp\left(- a \left[\frac{\theta - SOC}{\theta_d} \right]^b \right) \tag{4.15}$$

where a and b are the parameters of the Wiebe function, and θ_d denotes the combustion duration as a function of EGR rate and ϕ. Combustion duration is calculated by using the following equation [126]:

$$\theta_d = c(1 + EGR)^d \phi^e \tag{4.16}$$

where c, d and e are constant values. CA50 is the crank-angle by which 50% of the fuel mass is burnt (i.e., $MFB = 0.5$).

To estimate the pressure between EOC and EVO a polytropic assumption is used [134]. The predicted pressure trace will be used to calculate exergy losses/destructions during an engine cycle. Fig. 4.5 demonstrates pressure trace validation for four different ICE conditions. The results show a good agreement between predicted and measured pressure trace.

The predicted in-cylinder pressure model can be used to predict exergy destruction/losses for different engine conditions. If in-cylinder pressure sensors are available in the engine, the predicted pressure trace values can be replaced by real in-cylinder

pressure measurements. In this study, measured in-cylinder pressure (P_{Cyl}) data is used for exergy analysis of 175 steady-state experimental data. The in-cylinder pressure model is used for predicting P_{Cyl} for the conditions that measured data is not available to us, particularly during engine transients.

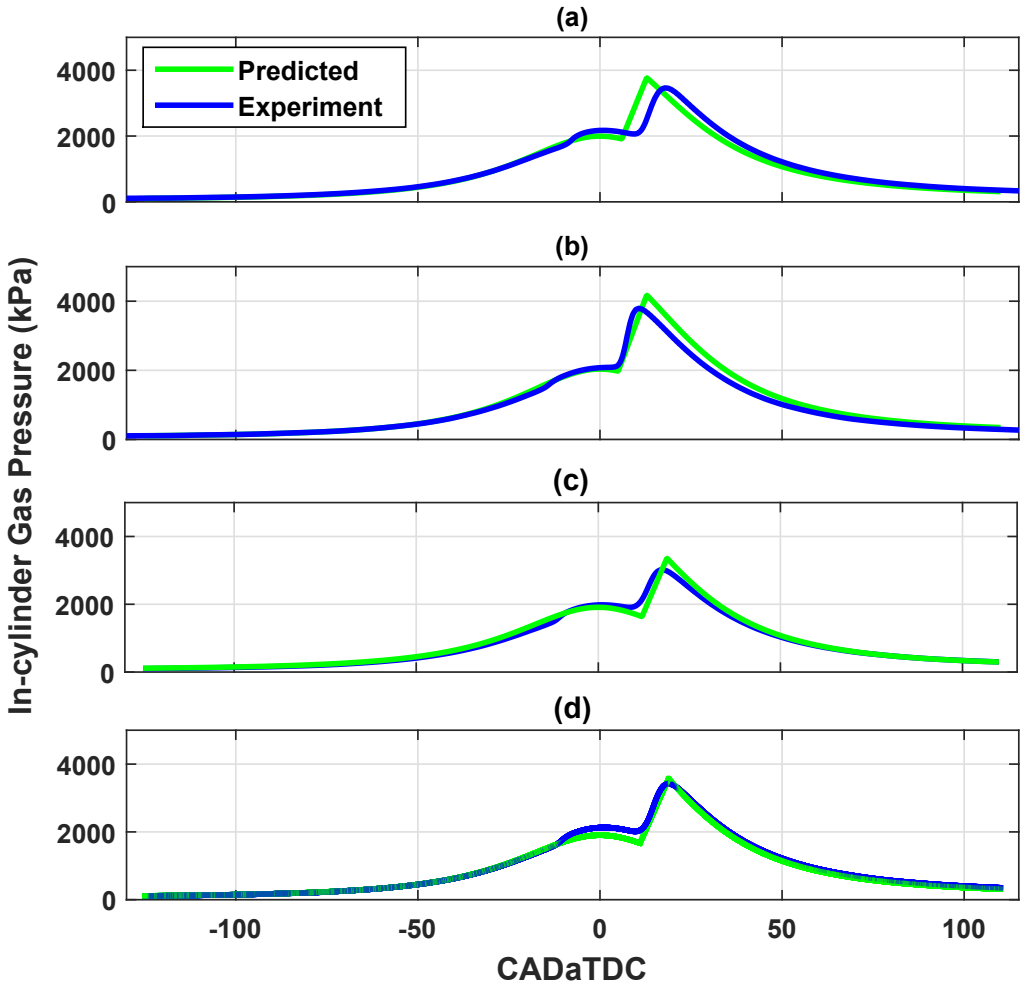

Figure 4.5: Experimental validation of predicted in-cylinder gas pressure for four different engine operating conditions. (a) ϕ=0.40, N=1016 RPM, P_{man}=100 kPa, T_{man}=393 K, (b) ϕ=0.50, N=1016 RPM, P_{man}=100 kPa, T_{man}=393 K, (c) ϕ=0.36, N=900 RPM, P_{man}=110 kPa, T_{man}=364 K, (d) ϕ=0.41, N=900 RPM, P_{man}=110 kPa, T_{man}=366 K.

4.4 Crank-Angle Resolved Exergy Analysis

Measured in-cylinder pressure data [6] with 0.1 CAD resolution is used to analyze exergy change from IVC to EVO. The pressure trace data is used to calculate the engine exergy loss/destruction and exergy transfer by work for the engine conditions shown in Figures 4.2 and 4.3. Ideal gas assumption is used to calculate the in-cylinder mixture temperature. Fig. 4.6 shows a crank-angle resolved exergy analysis of the cylinder for an arbitrary operating point using engine cylinder as the control volume. Negative values in Fig. 4.6 show that the exergy of cylinder is lost or destructed. Fig. 4.6 (a) shows the rate of indicated work using Eq. (4.6). Fig. 4.6 (b) demonstrates combustion irreversibility rate using Eq. (4.7) and the rate of exergy loss due to heat-transfer using Eq. (4.8). As seen in Fig. 4.6 (b), heat-loss rate increases during compression which results in mixture temperature rise. After SOC moment, combustion irreversibility rate and heat-loss rate increase considerably. At the end of combustion phase, EOC moment, the rate of combustion irreversibility becomes zero and the rate of exergy loss due to heat-transfer slowly decreases since mixture temperature decreases gradually. Fig. 4.6 (c) shows the cumulation of Fig. 4.6 (a) and (b) which shows the exergy destruction/loss and exergy transfer during the closed cycle (i.e., IVC to EVO). Air and fuel mass flow rates are obtained from the experimental measurements in [6]. Eq. (4.10) is used to calculate fuel exergy (X_{Fuel}) which is converted to X_W, X_{Exh} and X_d during the four strokes of the ICE.

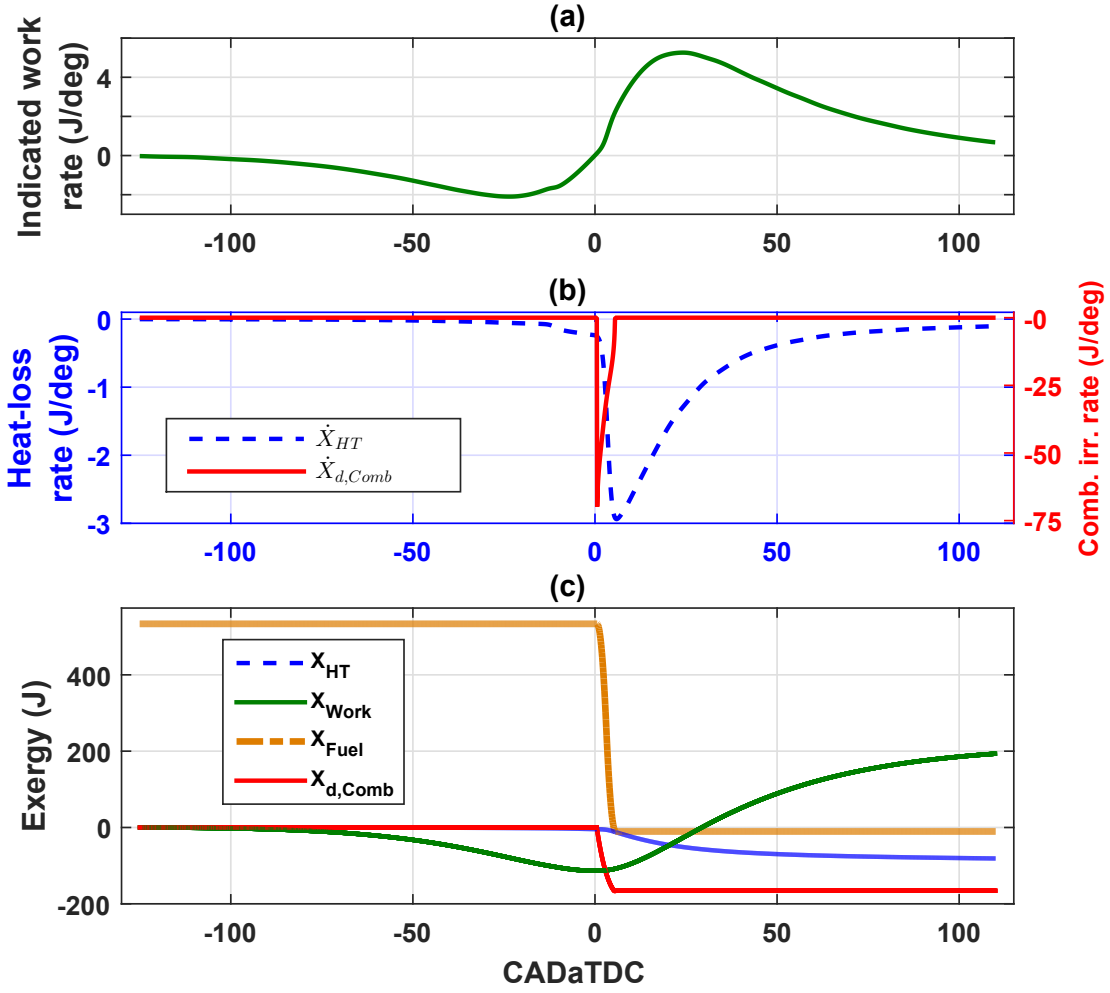

Figure 4.6: Crank-angle resolved exergy flow for an arbitrary engine cycle. (a) exergy work rate in the engine cycle, (b) exergy destruction rate due to combustion and exergy loss rate due to heat transfer through the cylinder walls, (c) cumulative exergy flow for the closed engine cycle. [Operating condition: $\phi = 0.45,\ N = 810\ RPM,\ ON = 0,\ P_{man} = 101\ kPa,\ T_{man} = 365\ K,\ EGR = 0\%$]

Fig. 4.7 shows the breakdown of energy and exergy distribution for the same operating point shown in Fig. 4.6. The percentages of indicated work, heat loss, and exhaust gas energy and exergy are shown in Fig. 4.7. In addition to these terms, for the exergy distribution, friction, combustion irreversibility, and other exergy losses including

blow-by gases, UHC, and mixing are shown. Due to 6.4% difference between fuel LHV and specific exergy (see Eq. (4.10)), the values of work in exergy and energy breakdown are not equal [7, 8]. As seen in Fig. 4.7, there is a difference between heat loss values in energy and exergy breakdown. The reason for this difference is that only 70% of the transferred heat (i.e., energy) can do work (i.e., exergy) and the rest of energy which is 30% of the transferred energy by heat, does not have potential to do work. In the same way, exhaust gases account for 43% of the fuel energy but only 16% of fuel exergy.

As seen in Fig. 4.7, the exergy destruction due to combustion is the main source of exergy loss accounting for more than 40% of the total exergy loss. In this operating point, 5% of fuel exergy is destroyed due to friction. Exergy losses due to blow-by, and, UHC and exergy destruction due to mixing of air-fuel charge and residual gases are shown in a category shown by 'Other irreversibilities' in Fig. 4.7 that account for 9% of fuel exergy loss. η_{II_W} and $\eta_{II_{CPEX}}$ are 38% and 55%, respectively for the operating point shown in Fig. 4.7.

4.5 SLT Contour Maps

Based on Equations (4.13) and (4.14) and using the ICE experimental data shown in Figs. 4.2 and 4.3, two different SLT efficiency contour maps are generated. These

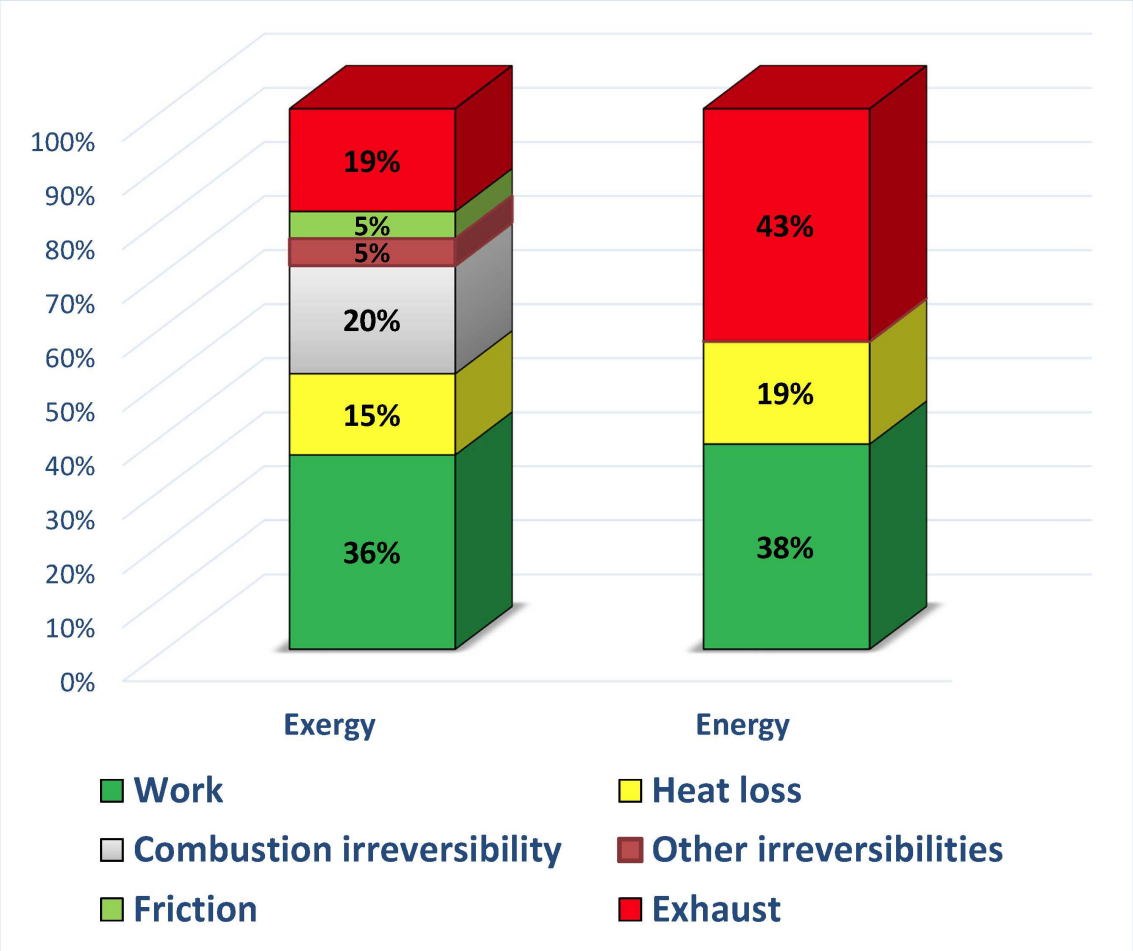

Figure 4.7: Energy and exergy breakdown for the engine cycle in Fig. 4.6. Note: Since exergy of n-Heptane fuel is 6.4% more than its LHV [7, 8], the work percentages are different; however, in both energy and exergy breakdowns, the values of indicated work are identical.

maps are used to find the optimum combustion phasing for steady-state operation of the engine.

Fig. 4.8 shows the SLT contour map ($\eta_{II,W}$) as a function of combustion phasing (CA50) and engine load (IMEP). Fig. 4.9 shows the SLT efficiency ($\eta_{II,CPEX}$) map for CPEX based on Eq. (4.14).

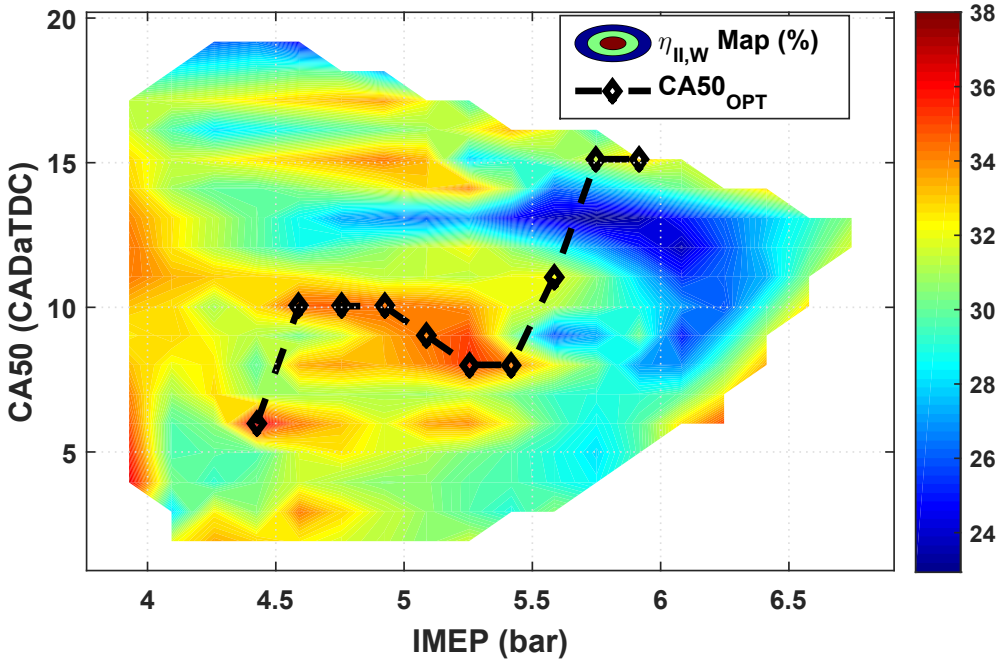

Figure 4.8: The SLT efficiency map (η_{II_W}) with respect to the engine load (IMEP) and combustion phasing (CA50) along with the optimal CA50 trajectory.

4.6 Exergy-Based Optimal Combustion Phasing (XOCP)

In this section, an optimization algorithm is introduced to determine optimum combustion phasing trajectories for given engine load sweeps. This algorithm is based on the SLT maps and will be used for steady-state operation of the ICE in this chapter. $CA50_{OPT}$ trajectories are based on the contour maps of $\eta_{II,W}$ and $\eta_{II,CPEX}$ (Figs. 4.8 and 4.9). Fig. 4.10 demonstrates the details of the proposed Exergy-based Optimal

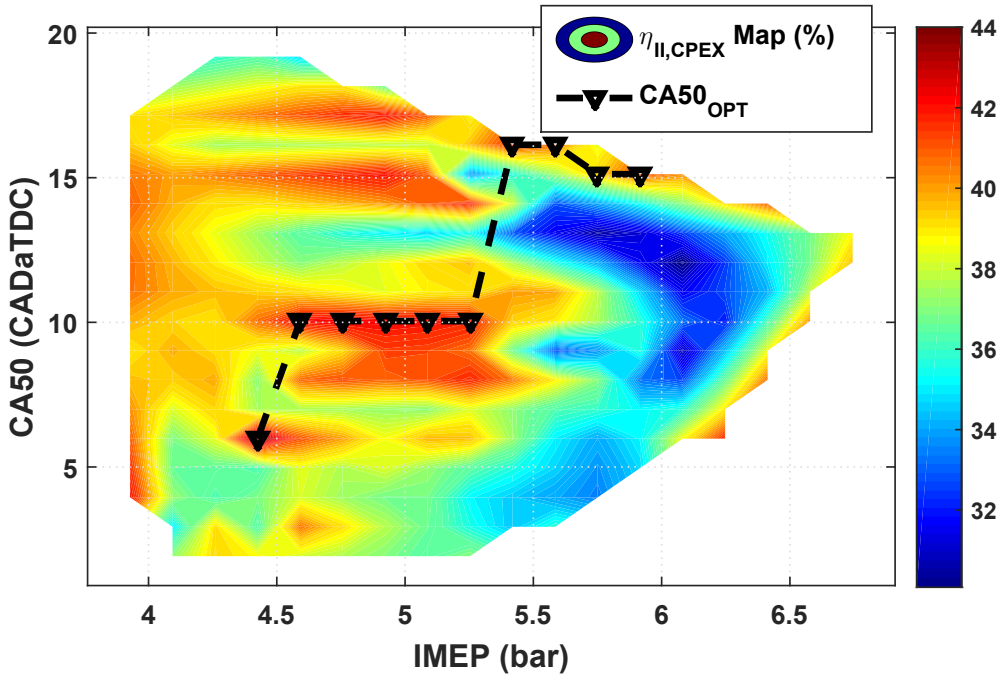

Figure 4.9: The SLT efficiency map for CPEX ($\eta_{II_{CPEX}}$) with respect to IMEP and CA50 along with the optimal CA50 trajectory.

Combustion Phasing (XOCP) algorithm. Desired IMEP is an input to the XOCP algorithm. At every given IMEP, the corresponding CA50 is determined such that $\eta_{II,W}$ or $\eta_{II,CPEX}$ is maximized. When the required engine load is changed, XOCP finds the $CA50_{OPT}$ according to the maps in Figs. 4.8 and 4.9.

The $CA50_{OPT}$ at different engine loads based on the proposed XOCP algorithm are shown in Figs. 4.8 and 4.9. $CA50_{OPT}$ trajectory, shown in Fig. 4.8, is the optimum CA50 that maximizes the SLT efficiency ($\eta_{II,W}$) at every given engine load. As seen in Fig. 4.8, in low load engine operation, the mid-range CA50 values result in the maximum $\eta_{II,W}$. At higher engine loads, a delayed combustion phasing results in

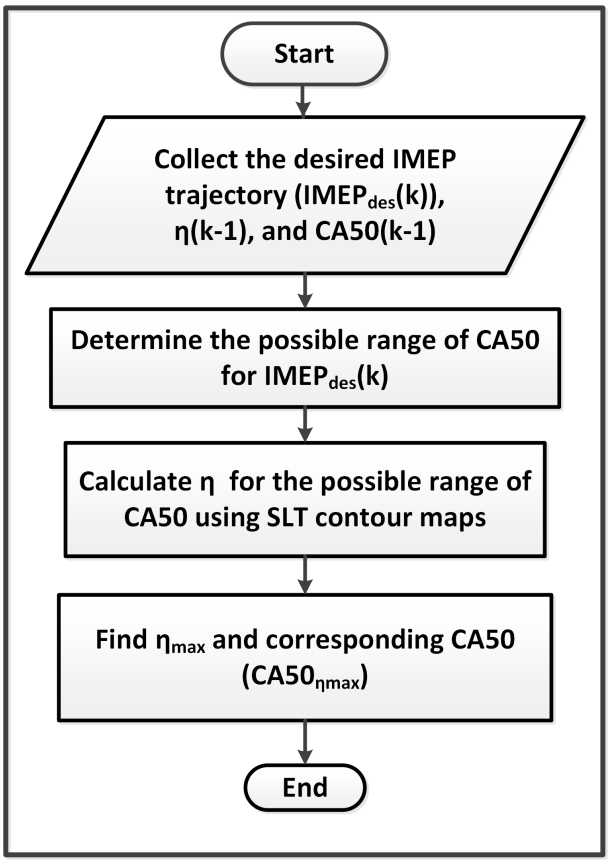

Figure 4.10: Proposed Exergy-based Optimal Combustion Phasing (XOCP) algorithm. XOCP is used to determine $CA50_{OPT}$ at every given engine load. η in the algorithm can be either $\eta_{II,W}$ or $\eta_{II,CPEX}$ based on the desired output.

higher $\eta_{II,W}$. Similar to Fig. 4.8, at every given engine load, the corresponding CA50 of the maximum value of $\eta_{II,CPEX}$ is selected. Comparing $CA50_{OPT}$ trajectories in Figs. 4.8 and 4.9 shows that the maximum $\eta_{II,CPEX}$ occurs at higher CA50 values compared to $\eta_{II,W}$. This can be explained by the fact that higher CA50 values (i.e., delayed combustion) lead to higher T_{exh} which increases X_{Exh}. Considering X_{Exh} as the useful output exergy in CPEX systems leads to greater values of efficiency for $\eta_{II,CPEX}$ compared to $\eta_{II,W}$.

As seen in Figs. 4.8 and 4.9, the obtained trajectories are affected by the existence of efficiency islands in Figs. 4.8 and 4.9. These islands depends on the experimental data points used. Thus, it is important that enough engine data points are collected to generate the η_{II} efficiency maps. The focus of this chapter is more on proposing a methodology for optimum engine operation rather than absolute η_{II} values.

4.7 Control Oriented Engine Model

In this chapter, we introduce a control method for ICEs based on exergy. This control method consists of steady-state and transient operation modes. In the steady-state operation of the engine, SLT maps (Figs. 4.8 and 4.9) are used to find $CA50_{OPT}$. For the transient operation of the ICE, in-cylinder pressure is predicted using the model introduced in Sec. 4.3.5. Then the model is used along with exergy Equations (4.1) to (4.16). Next, the resulting model is combined with the model in [128] for estimating residual gas and capturing thermal coupling dynamics that are caused by residual gases from one cycle to the next engine cycle. The final model is able to predict cycle-to-cycle combustion phasing, IMEP and exergy destruction/loss in transient operation. The final nonlinear model is represented by the following state

equations:

$$\mathcal{X}_{k+1} = f(\mathcal{X}_k, \mathcal{U}_k, \mathcal{V}_k) \tag{4.17a}$$

$$\mathcal{Y} = \mathcal{C}\mathcal{X}_k \tag{4.17b}$$

where $\mathcal{X}$ is the vector of states, $\mathcal{U}$ is the vector of inputs and $\mathcal{V}$ is the vector of disturbances. The control inputs and states of the ICE model are as following:

$$\mathcal{X} = [CA50, T_{SOC}, P_{SOC}, T_{rg}, m_{evc}]^T \tag{4.18}$$

where T_{SOC} and P_{SOC} are the temperature and pressure of in-cylinder mixture at SOC, respectively. T_{rg} denotes residual gas temperature and m_{evc} shows mass of residual gases at EVC moment.

The control inputs vector consists of ON and ϕ as shown in Eq. (4.19):

$$u = [ON, \phi]^T \tag{4.19}$$

4.8 Exergy-based Control of Internal Combustion Engines (XCICE)

Structure of the proposed XCICE controller is shown in Fig. 4.11. The XCICE controls combustion phasing (CA50) and engine load (IMEP). Depending on the required IMEP, a map-based feedforward integral controller adjusts the engine load by manipulating the amount of injected fuel (i.e., fuel equivalence ratio, ϕ). Details of the IMEP controller are found in [139]. The reference optimum CA50, shown as $\tilde{y}_{2,ref}$ in Fig. 4.11 is determined by $IMEP - CA50 - \eta_{II}$ map (Figs. 4.8 and 4.9) for steady-state operation. For transient operation, $\tilde{y}_{2,ref}$ is found using exergy model along with an optimal controller to choose CA50 such that exergy loss/destruction (X_d) is minimized.

Eq. (4.20) defines the control problem to find $CA50_{OPT}$ for transient engine operation. We use X_d in Eq. (4.1) as the objective function. The following optimization problem is solved at each engine cycle k.

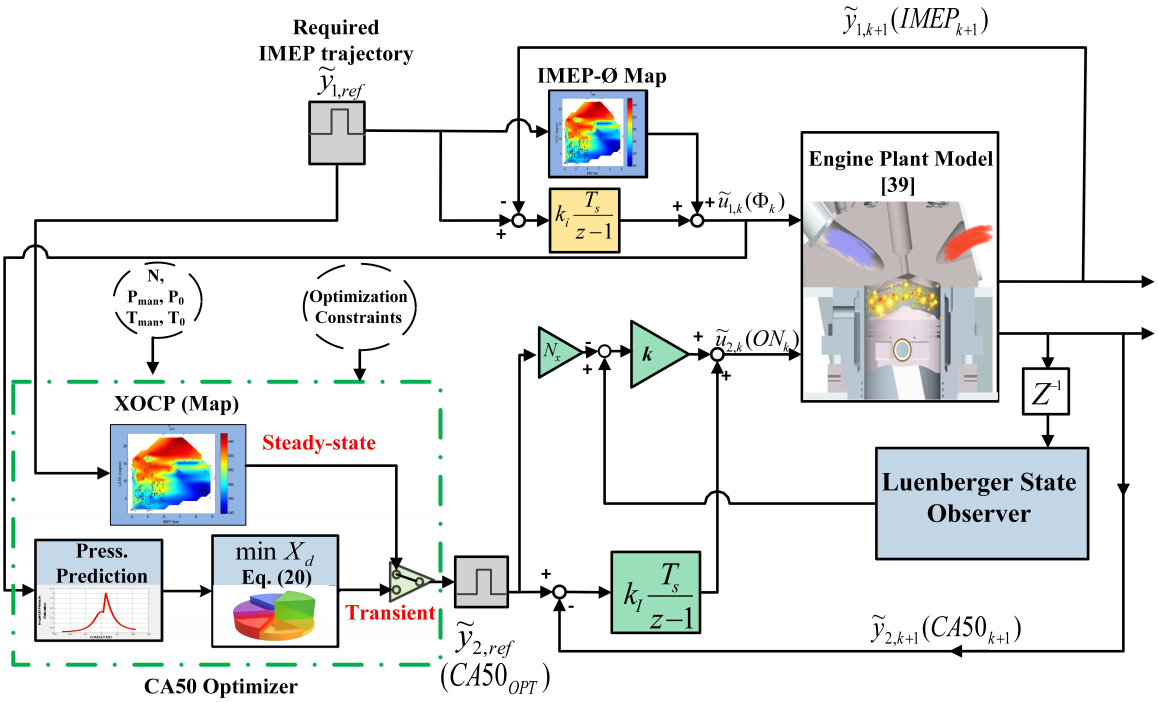

Figure 4.11: Structure of proposed Exergy-based Control of the IC engine (XCICE).

$$\min_{CA50}\{X_d\} \tag{4.20a}$$

subject to:

$$\mathcal{X}_{k+1} = f(\mathcal{X}_k, \mathcal{U}_k, \mathcal{V}_k) \tag{4.20b}$$

$$\mathcal{Y} = \mathcal{C}\mathcal{X}_k \tag{4.20c}$$

$$0 \leq ON_k \leq 100 \tag{4.20d}$$

$$\underline{CA50} \leq CA50_k \leq \overline{CA50} \tag{4.20e}$$

$$\underline{\delta}^\circ \leq CA50_{k+1} - CA50_k \leq \overline{\delta}^\circ \tag{4.20f}$$

(4.20g)

where Eq. (4.20d) shows the constraint on ON as the control input. Eq. (4.20e) is the output constraint on CA50 based on knock and misfire data [6] in which $\underline{CA50}$ and $\overline{CA50}$ are the lower and upper limits of combustion phasing. Due to the actuator limitations, Eq. (4.20f) is defined to impose constraints on the rate of changes in combustion phasing at lower and upper limits denoted with $\underline{\delta}^{\circ}$ and $\overline{\delta}^{\circ}$.

Once the desired CA50 is determined, the ON (i.e., blending ratio of two PRF fuels) is adjusted using an integral state feedback controller described in [129]. This feedback controller tracks the desired CA50 values. The integrator in the controller helps to track the desired combustion phasing trajectory with no steady-state error. A Luenburger state observer is used in the control structure since most of the control states cannot be measured in practice. This controller is tested on a detailed experimentally validated ICE plant model [140]. The tracking results of the proposed exergy-based controller for transient engine operation are shown in Fig. 4.12. An IMEP trajectory (4.43 $\rightarrow$ 4.56 $\rightarrow$ 4.62 bar) in Fig. 4.12 (c) is used as the reference load trajectory to test the proposed transient controller. The IMEP trajectory is similar to the loads shown in Fig. 4.8. The controller tracks the $CA50_{OPT}$ using exergy model in optimization framework shown in Eq. (4.20). Fig. 4.12 (a) shows the CA50 tracking performance with a settling time of one engine cycles. Fig. 4.12 (b) shows the actuated ON as the control input for tracking the desired CA50. Fig. 4.12 (c) shows the required IMEP, and Fig. 4.12 (d) shows the actuated input, ϕ to obtain the required IMEP. Fig. 4.12 (e) demonstrates X_d for optimum CA50 trajectory and

unoptimized case (i.e., $CA50 = 8\ CADaTDC$). As shown in Fig. 4.12 (e), the optimization algorithm introduced in Eq.(4.20) keeps X_d minimum for all transient cycles compared to the unoptimized case.

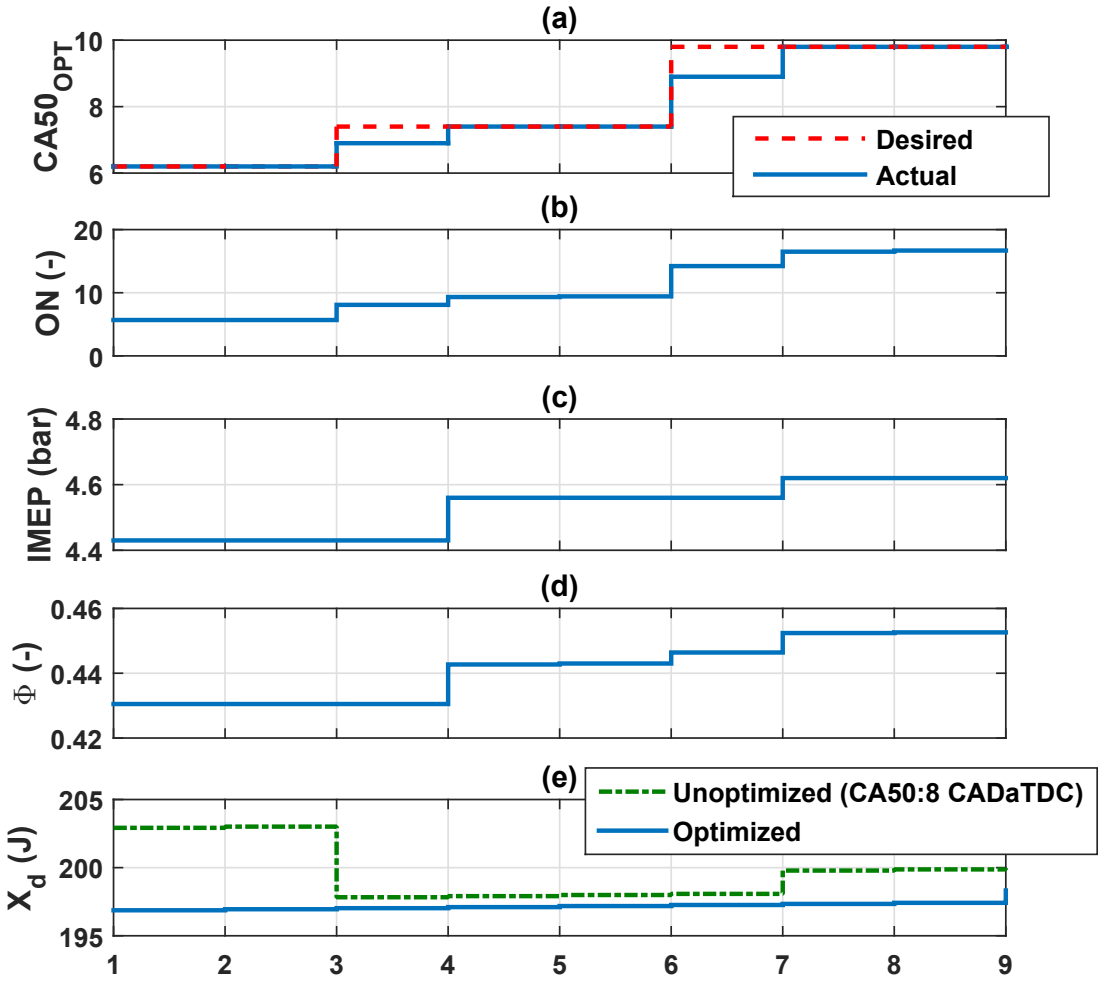

Figure 4.12: Results of the XCICE for tracking engine load (IMEP) and combustion phasing during transient engine operation ($N = 800\ RPM,\ EGR = 0\%,\ P_{man} = 100\ kPa$).

4.9 Optimization Results

Depending on the application of an ICE, the desired output and the SLT efficiency are defined. For ICE applications in which output work is of primary interest, the $CA50_{OPT}$ trajectory of $\eta_{II,W}$ is used to increase the SLT efficiency and improve the fuel economy. If CPEX is desired, then $\eta_{II,CPEX}$ map is used to determine optimum combustion phasing to maximize output exergy ($X_{Work} + X_{Exh}$).

The $CA50_{OPT}$ trajectories based on $\eta_{II,W}$ and $\eta_{II,CPEX}$ maps are used to show the effects of the proposed XCICE in fuel saving and output exergy saving in Fig. 4.13. Experimentally calculated $\eta_{II,W}$ map (shown in Fig. 4.8) is used to compare fuel consumption. The baseline for comparison is a conventional practice where CA50 is maintained constant (i.e., 8 $CADaTDC$). The fuel consumption for the optimization modes of $\eta_{II,W}$ and $\eta_{II,CPEX}$ is compared with that of the baseline.

As shown in Fig. 4.13 (a), $CA50_{OPT}$ shown in $\eta_{II,W}$ map leads to the best fuel saving at every given IMEP. Fig. 4.13 (b) demonstrates the increase in total output exergy (CPEX) when CA50 is selected based on $\eta_{II,CPEX}$ map (i.e., Fig. 4.9).

Table 4.2 summarizes the fuel and exergy savings using the optimum combustion phasing values derived from the trajectories illustrated on $\eta_{II,W}$ and $\eta_{II,CPEX}$ maps. Compared to the unoptimized case, the average achieved fuel saving and exergy saving

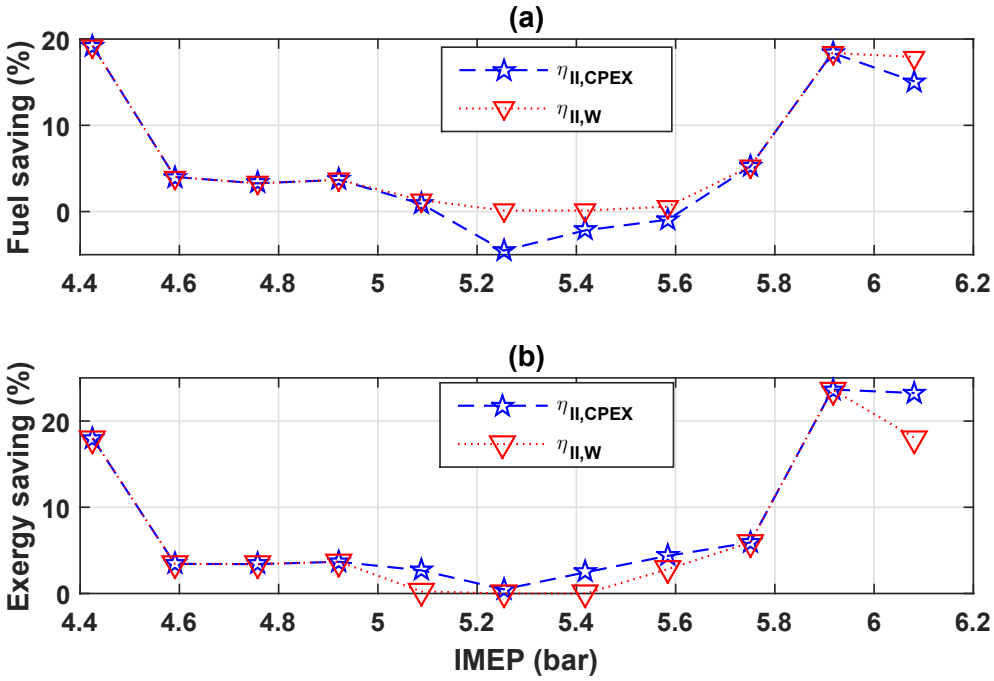

Figure 4.13: Fuel and exergy saving percentages compared to the unoptimized case (i.e., $8^o aTDC$) for the operating conditions in Fig. 4.8 and 4.9. (a) fuel saving when the trajectories on $\eta_{II,W}$ and $\eta_{II,CPEX}$ maps are used, (b) exergy saving ($X_{Work} + X_{Exh}$) by using the trajectory shown on $\eta_{II,W}$ and $\eta_{II,CPEX}$ maps. To calculate the saving percentage, $\frac{x-x_0}{x_0} \times 100$ is used, where x_0 is the corresponding value for the unoptimized case.

based on the $\eta_{II,W}$ optimization mode are 6.7% and 7.2%, respectively. However, if maximizing CPEX is of interest, by using the $\eta_{II,CPEX}$ optimization mode, the average output exergy saving ($X_{Work} + X_{Exh}$) is 8.3% while 5.7% fuel saving is achieved. As mentioned in Section 4.3.4, value of $\eta_{II,W}$ is close to thermal efficiency of the engine cycle, η_I. Thus, exergy and fuel savings can be compared to the commonly used thermal efficiency by using $\eta_{II,W}$ values.

Table 4.2
Comparison of the fuel and exergy savings for different optimization modes.

Optimization Mode	**Combustion Phasing**	**Avg. Energy Saving (%)**	**Avg. Exergy Saving (%)**
$\eta_{II,W}$	Variable CA50	6.7	7.2
$\eta_{II,CPEX}$	Variable CA50	5.7	8.3
Unoptimized*	$CA50 = 8°aTDC$	-	-

*'Unoptimized' case is considered the baseline for savings calculation.

4.10 Summary and Conclusion

In this chapter, exergy is introduced as an effective metric to control the performance of ICEs. We present a novel approach for Exergy-based Control of ICEs (XCICE) for steady-state and transient engine operations. First, an exergy model for a single-cylinder HCCI engine was developed. Then, an exergy analysis carried out using the exergy model along with the experimental engine data. The main sources of exergy loss/destruction including combustion irreversibility, heat-loss, and friction are identified based on the exergy analysis results. Depending on the ICE applications, two different SLT efficiency maps were generated. The first SLT map was to maximize the output work, while the second SLT map aimed for maximizing Combined Power and Exhaust Exergy (CPEX). The optimal combustion phasing (i.e., $CA50_{OPT}$) at every given IMEP was determined (i) using SLT maps for steady-state engine operation and (ii) using exergy model within Model Predictive Control (MPC) framework

for engine transient ICE. A control method to track $CA50_{OPT}$ and IMEP was developed for both transient and steady-state engine operations. Here is the list of major findings from this work for the studied engine:

† Exergy destruction due to combustion ($X_{d,Comb.}$) is the main source of exergy loss in the ICE. Combustion irreversibility accounts for more than 40% of total in-cylinder exergy destruction/losses for the 175 experimental data points in this study. Heat-transfer, X_{HT}, causes $12 \pm 3\%$ of the fuel exergy loss. In addition, $9 \pm 4\%$ of the fuel exergy is lost/destroyed due to mixing irreversibility, unburnt hydrocarbons, and blow-by gases. Finally, in-cylinder friction, $X_{d,Fric}$, destroys $4 \pm 0.5\%$ of the total exergy.

† Based on the application, two optimization objectives including (i) maximum $\eta_{II,W}$, and (ii) maximum $\eta_{II,CPEX}$ were defined for steady-state engine operation. $CA50_{OPT}$ is determined based on the SLT analysis. The results of the proposed optimization method were compared to those from a conventional approach in which a constant ($CA50 = 8\ CADaTDC$) is used. The results show that on average, the proposed method can reduce the fuel consumption by 6.7% when the output work is of interest. For cases in which CPEX is desired, such as CHP systems, the proposed method can increase the desired output exergy by 8.3% on average.

† Transient control of the engine via exergy-based MPC framework can minimize

X_d while meeting required IMEP. The simulation results showed up to 5% reduction in X_d by using the proposed transient control for the engine load sweep in this study.

† Results from this study illustrated that $\eta_{II,W}$ map along with exergy breakdown of engine cycle can be used to determine the maximum available work (exergy). Exhaust exergy can be utilized in a turbocharger or a TEG system in order to increase the engine output work. Typical efficiency of TEG systems for ICEs is around 5-8% [141]. Depending on the exhaust gas temperature and pressure, the FLT and SLT efficiencies of the overall energy recovery system could be as low as 8% and 24%, respectively [142]. Thus, when indicated work is the desired output, one should never sacrifice work exergy for increasing the exhaust exergy.

The key outcome from this study is to show how the knowledge from an exergy analysis can be used for ICE controls. The proposed XCICE method is generic and can be applied to a wide range of ICEs. We presented the results for a specific type of LTC engine known as HCCI with ON and ϕ as the control variables, yet the same XCICE method can be applied to other ICEs with different combustion modes and control inputs.

Chapter 5

Bilevel Optimization Framework for Smart Building-to-Grid Systems[1]

This chapter proposes a novel framework suitable for bilevel optimization in a system of commercial buildings integrated to smart distribution grid. The proposed optimization framework consists of comprehensive mathematical models of commercial

[1]This chapter has been published in IEEE Transactions on Smart Grid [5] (doi:10.1109/TSG.2016.2557334) with the granted permission in Appendix E.

buildings and underlying distribution grid, their operational constraints, and a bilevel solution approach which is based on the information exchange between the two levels. The proposed framework benefits both entities involved in the building-to-grid (B2G) system, i.e., the operations of the buildings and the distribution grid. The framework achieves two distinct objectives: increased load penetration by maximizing the distribution system load factor and reduced energy cost for the buildings. This chapter also proposes a novel B2G index, which is based on buildingâĂŹs energy cost and nodal load factor, and represents a metric of combined optimal operations of the commercial buildings and distribution grid. The usefulness of the proposed framework is demonstrated in a B2G system that consists of several commercial buildings connected to a 33-node distribution test feeder, where the building parameters are obtained from actual measurements at an office building at Michigan Technological University.

5.1 INTRODUCTION

Building sector in the United States accounts for about 70% of electricity energy consumption [12], in which 41.4% of energy consumption is directly related to the space heating, ventilation, and air conditioning (HVAC). Thus, HVAC systems have a great potential to reduce the energy usage/cost in buildings. As reported in [1, 28], smart control techniques, such as model predictive control (MPC), can provide

significant energy saving. Development of MPC for optimal control of HVAC systems has been a focus in [143, 144], which yields benefits to the operations of buildings and electric power grid.

Smart grid technologies, such as smart appliances and home area network (HAN), render the electrical loads more manageable and controllable at customersâĂŹ premise, and facilitates advanced demand side management (DSM) activities [145]. However, existing mathematical models developed for customer side DSM mainly consider minimization of electricity cost [146, 147], which results in increased load at hours with low electricity price. Increased load at those hours may impact voltage performance in the distribution grid. In [148], it is demonstrated that uncontrolled penetration of electric vehicle loads violates the voltage standards set by the ANSI. Thus, it is advisable that DSM should be employed considering the operational requirements of customers as well as the electric power grid. In DSM activities, distribution utilities are more concerned about feeder loss minimization, load factor improvement, reactive power optimization, etc., as part of their operational objectives [149, 150, 151, 152, 153, 154]. On the other hand, the objectives of DSM activities at customer level are mainly focused on comfort maximization and cost minimization. This illustrates that the objective set by the grid and customers in DSM activities could often be conflicting.

In [155, 156], promising results are obtained from DSM in reducing customer's energy price. In [155], pre-cooling and pre-floating is performed to reduce total electricity

cost. In [156], optimization is performed with a trade-off between cost and user comfort. In [147], HAN is employed to reshape the demand profile based on the impact on distribution transformer. In DSM models proposed in [147, 155, 156], customers obtain benefits by shifting the loads. The mathematical models used in [147, 155, 156] consider peak power information from distribution grid as one of the constraints of optimization but detailed modeling and operational constraints of distribution system have not been considered. Thus, for advanced DSM activities in Smart Grids, detailed mathematical modeling considering objectives and operational requirements of customers and the distribution system with real-time information exchange between customer and the grid is crucial; which is a major focus of the proposed work.

Fig. 5.1 summarizes past studies related to three research categories: building, grid, and integrated building-grid optimization. In the first category, optimal and model predictive unidirectional building optimization are studied [1, 2, 27, 28, 30, 33, 35, 103, 143, 144, 157, 158, 159, 160]. In this category, building's HVAC performance or operational cost is optimized using optimal or model predictive control technique. The second category include studies in which distribution grid operation is optimized for various operational objectives considering aggregated loads [149, 150, 151, 152, 153, 154]. The third category includes building-to-grid (B2G) integration in which performance of buildings including comfort level and energy cost is optimized considering grid side information [146, 155, 161, 162, 163, 164, 165, 166], and demonstrates its usefulness

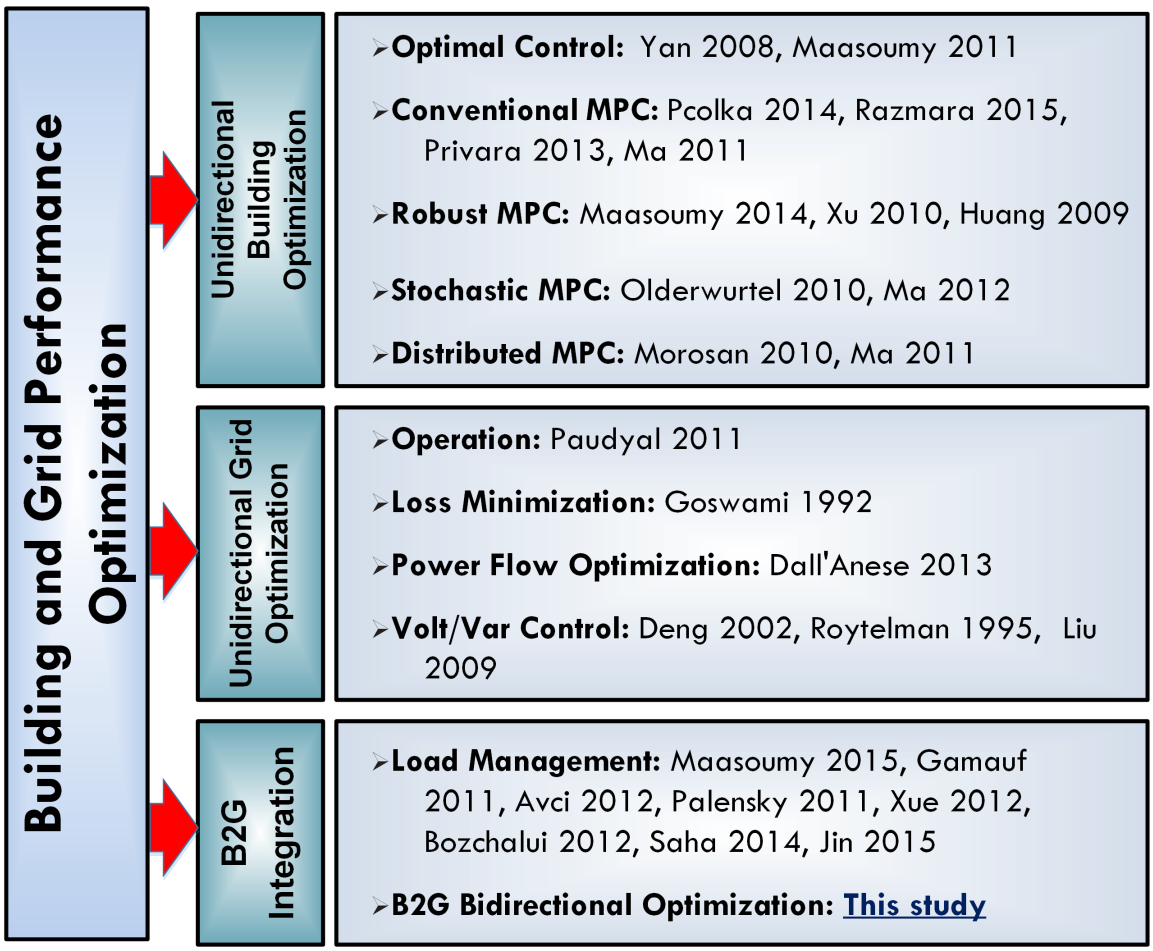

Figure 5.1: Summary of past studies on building, grid, and B2G optimization.

for grid services. However, in the modeling in [146, 155, 161, 162, 163, 164, 165, 166] distribution grid is simplified or completely ignored. Survey results in Fig. 5.1 reveal that there are extensive works accomplished in the area of control/optimization of distribution grid and buildingâĂŹs HVAC systems independently. However, there is little work done in the area of bi-directional B2G, including mathematical modeling required for the B2G integration. This work proposes a bi-directional B2G optimization framework based on detailed mathematical modeling of a B2G system.

The proposed B2G framework is based on information exchange between the two levels, i.e, the BEMS and distribution system operation (DSO) control center. The predicted and optimized load profile of buildings are provided to the DSO by the BEMSs. Similarly, maximum allowable load penetration information, that ensures feasible grid operations, are provided to the BEMSs by the DSO.

For the demand response applications discussed in this work, a bidirectional communication infrastructure is required, as shown in Fig. 5.2, between the BEMSs and the DSO. Also, unidirectional communication links are required between the BEMSs and the market operator (MO), BEMSs and local weather station, DSO and control equipment at distribution level. The required communication infrastructure must be secure, reliable, and low-cost for autonomous interactions [167, 168]. In this proposed work, the interaction between the two levels, i.e., the building and grid, are kept at the minimum; thus, the communication bandwidth usage is sporadic. The information that building receives from the grid control center is the maximum demand limit, which can be sent once every 15-30 minutes for next couple hours to next day. Building receives information from utility or MO about energy price once per day (i.e., the day ahead energy price) and/or every 5 minutes to one hour (i.e., the real-time energy price), depending on which energy rate is applied to the building customers. Building receives weather forecast on daily basis and/or the hourly weather update. It should be noted that the information flow depends on the variation of the parameters in the building and grid models during the course of operation, and the type of services

the building loads provide to the grid (such as demand response, regulation). The communication infrastructure must be flexible to interact with the existing and future BEMSs and communication protocols such as Modbus, RS-484, BACnet, etc. [167]. To manage real-time and bidirectional information exchange cloud computing can be deployed [168]. VOLTTRON, OpenADR, BEMOSS are some of the open source platforms that can be utilized for the implementation of the proposed models at the customer and grid levels [169, 170, 171].

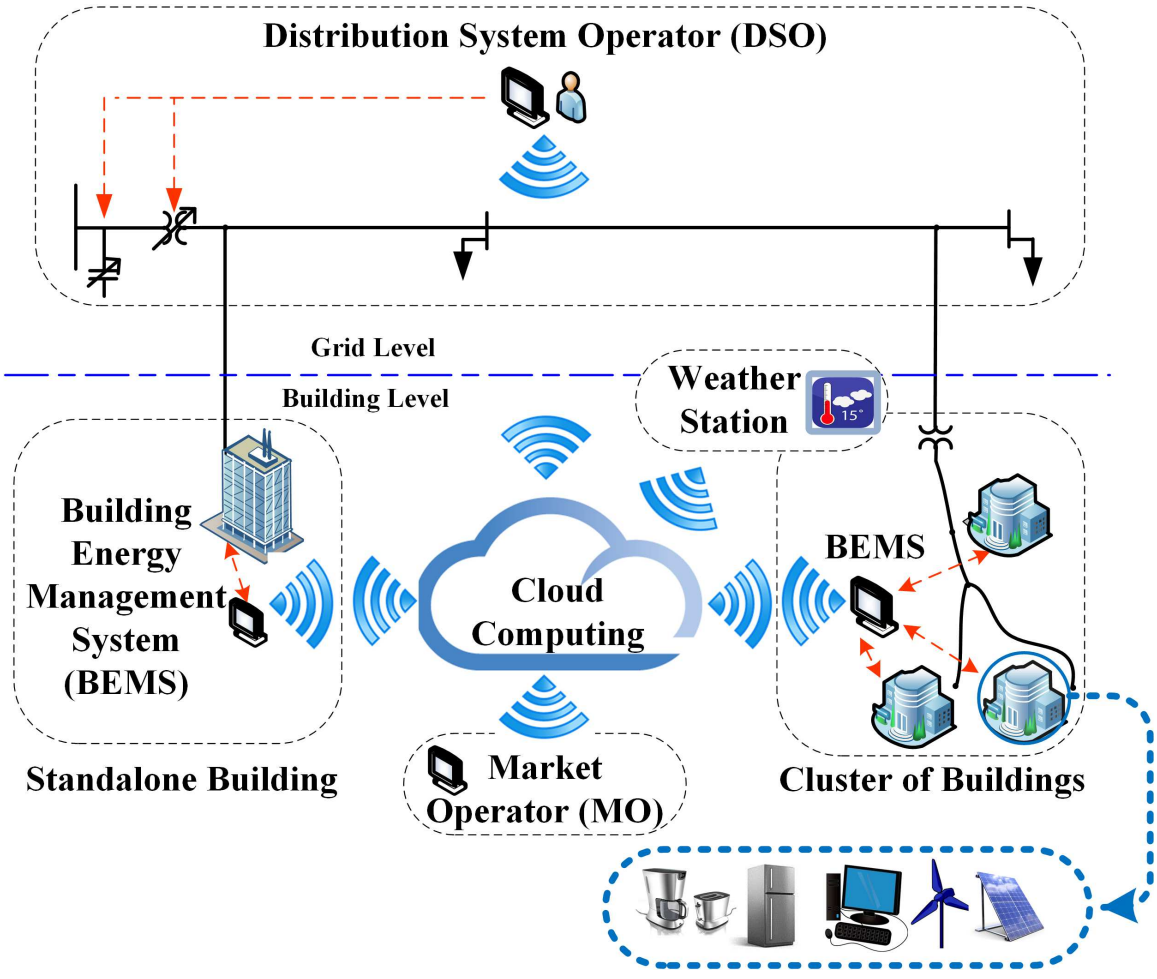

Figure 5.2: Conceptual building to grid communication framework.

This study improves previous single level optimization of buildings by considering the grid model and builds upon preliminary results in [172] by the authors. To our knowledge, it is the first study that proposes a bilevel optimization framework in B2G interaction, which benefits both building and grid operations. The contribution of this chapter is on the development of generic hierarchical optimization framework for B2G system, which is essential for coordinated control of multiple BEMSs connected to distribution grid for large scale demand response and other grid level services. More specifically, to reach this goal this dissertation:

1. develops a physics-based comprehensive mathematical model of HVAC system and model predictive controller (MPC) with the aim of minimizing buildingâĂŹs electricity costs. The MPC controller works in grid friendly manner, i.e, it communicates with distribution grid control center and incorporates the constraints set by the grid controller required for the feasibility of grid operation.

2. develops a detailed and generic mathematical model of distribution grid that coordinates with several building controllers to optimize the operation of the power grid.

This PhD dissertation proposes a novel B2G index that ensures the benefits at the grid level from the building side optimization, and develops a coordination algorithm to solve the hierarchical B2G framework.

Rest of this chapter is organized as follows. Section II presents mathematical models of building and distribution system, MPC based optimization model at building level, and distribution grid optimization model. Section III discusses methodology for bidirectional optimization and the proposed B2G index. Section IV describes the building testbed and distribution test feeder. The results of case studies are presented in Section V, and the main conclusions from this work are included in Section VI.

5.2 Mathematical Modeling

5.2.1 Building Components Thermal Modeling

Convection, radiation and conduction are the main heat transfer ways in buildings which are time varying. We use a common building modeling approach known as nodal approach to model building's construction and materials with electrical components such as resistors, capacitors, and current sources [1, 106]. For this purpose, buildings are considered as graphs containing walls and rooms as nodes. p represents number of nodes, q out of p nodes are rooms, and the remaining $p-q$ nodes are walls. $i = 1, \ldots, q$ numbers are assigned to each room. The following equation determines

the heat transfer of the walls [106]:

$$\frac{dT^w_{i,j}}{dt} = \frac{1}{C^w_{i,j}}\Big(\sum_{k\in\mathcal{N}^w_{i,j}} \frac{T^r_k - T^w_{i,j}}{R^{w_{i,j}}_k} + r_{i,j}\gamma_{i,j}A^w_{i,j}Q^{rad}_{i,j}\Big) \tag{5.1}$$

where $T^w_{i,j}$ is the temperature of the wall between room i and room j, $C^w_{i,j}$ is the heat capacity of the wall between room i and j, T^r_k is the temperature of adjacent rooms to wall $w_{i,j}$. Thermal resistance between the center-line of wall (node $w_{i,j}$) and the neighboring node k is denoted with $R^{w_{i,j}}_k$. $\gamma_{i,j}$ and $A^w_{i,j}$ are radiation heat absorption coefficient and area of wall between room i and j, respectively. Wall identifier is shown by $r_{i,j}$ which is equal to 0 for internal walls, and equal to 1 for peripheral walls. $Q^{rad}_{i,j}$ represents the radiative heat flux density on wall (i,j) while $\mathcal{N}^w_{i,j}$ is the set of all neighboring nodes to node $w_{i,j}$.

The following equation governs the temperature of the i^{th} room [106]:

$$\begin{aligned}\frac{dT^r_i}{dt} =& \frac{1}{C^r_i}\Big(\sum_{k\in\mathcal{N}^r_i}\Big[\frac{T_k - T^r_i}{R_{i,k}} + \pi_{i,k}\tau^w_k A^{win}_{i,k}Q^{rad}_i\Big] \\ &+ \dot{m}^r_i c_{p_{avg}}(T^s_i - T^r_i) + \dot{Q}^{int}_i\Big)\end{aligned} \tag{5.2}$$

where C^r_i and $\dot{m}^r_i$ denote the heat capacity and air mass flow into or out of the room i, respectively. T_k is the temperature of surrounding node k to room i. $c_{p_{avg}}$ denotes the average specific heat capacity of air and T^s_i is the temperature of the supply air to room i. $\pi_{i,j}$ is window identifier which is equal to 0 if there is no wall between room

i and j, otherwise equal to 1. $A_{i,j}^{win}$ is the total area of window between room i and surrounding room j, $\tau_{i,j}^{w}$ is the transmissivity of glass of window between room i and j, Q_i^{rad} is the radiative heat flux density per unit area radiated to room i, and $\dot{Q}_i^{int}$ denotes the internal heat generation in room i. $\mathcal{N}_i^r$ is the set of all nodes surrounding room i.

The disturbance to the model, $w(t)$, is function of neighboring room temperature, $T_k^r(t)$, internal heat generation in rooms $\dot{Q}_i^{int}(t)$, and radiative heat flux density on walls, $Q_i^{rad}(t)$. The disturbance is given by [106]:

$$w(t) = g(T_k^r(t), Q_i^{rad}(t), \dot{Q}_i^{int}(t)) \tag{5.3}$$

Function g is approximated as a linear function of $T_k^r(t)$, $Q_i^{rad}(t)$ and $\dot{Q}_i^{int}(t)$. Thus, the disturbance is $w = aT_k^r(t) + bQ_i^{rad}(t) + c\dot{Q}_i^{int}(t)$.

Heat transfer of each wall and room equations and disturbance form the system dynamics of building are represented in state-space form by:

$$\begin{aligned} \dot{x}(t) &= f(x(t), u(t), w(t), t) \\ y(t) &= Cx(t) \end{aligned} \tag{5.4}$$

where $x(t) \in \mathbb{R}^n$ is the state vector. State vector includes nodes' temperature in

the nodal network. $y(t) \in \mathbb{R}^m$ is the output vector of the system presenting thermal zones' temperature. Thermal zone is a section of a building that is required to meet certain comfort level. In this chapter, each room is considered as a thermal zone. The input vector which is the air mass flow rate and its temperature for each zone is shown with $u(t) \in \mathbb{R}^{l \times m}$. l is the number of inputs to each thermal zone (i.e., air mass flow and supply air temperature). C is the output matrix with proper dimension to return output, $y(t)$, from states.

In our testbed, HVAC air mass flow rate is directly measured using a vent mass flow meter. Density, heat capacity, trasnsmissivity and etc. are determined using standard engineering thermodynamics tables. There are unknown (e.g., wall heat capacitance and outside air convection coefficient) that are determined for the testbed using Unscented Kalman Filter (UKF) techniques presented in [1].

Equation (5.4) describes the nonlinear time evolution of the system. The supply air temperature (i.e., input to the system) is multiplied by the air mass flow, which is the other time-varying known input to the model. Given that the air mass flow rate is constant during day, we can consider the linearized form of the system. We use Euler's discretization method to discretize the state update equation (5.4) for controller design. The state-space model is given by:

$$x_{k+1} = Ax_k + Bu_k + Ew_k \tag{5.5}$$

where w_k is the disturbance vector at instant k and E is the disturbance coefficient matrix with appropriate dimension.

Fig. 5.3 represents the experimental validation of the building thermal model for few days in winter. Fig. 5.3(a) compares the simulated and measured room temperature, and Fig. 5.3(b) illustrates the heat-pump power based on the difference between the room temperature and the measured supply air temperature. Details of HVAC heat-pump system are discussed in Section 4.2.

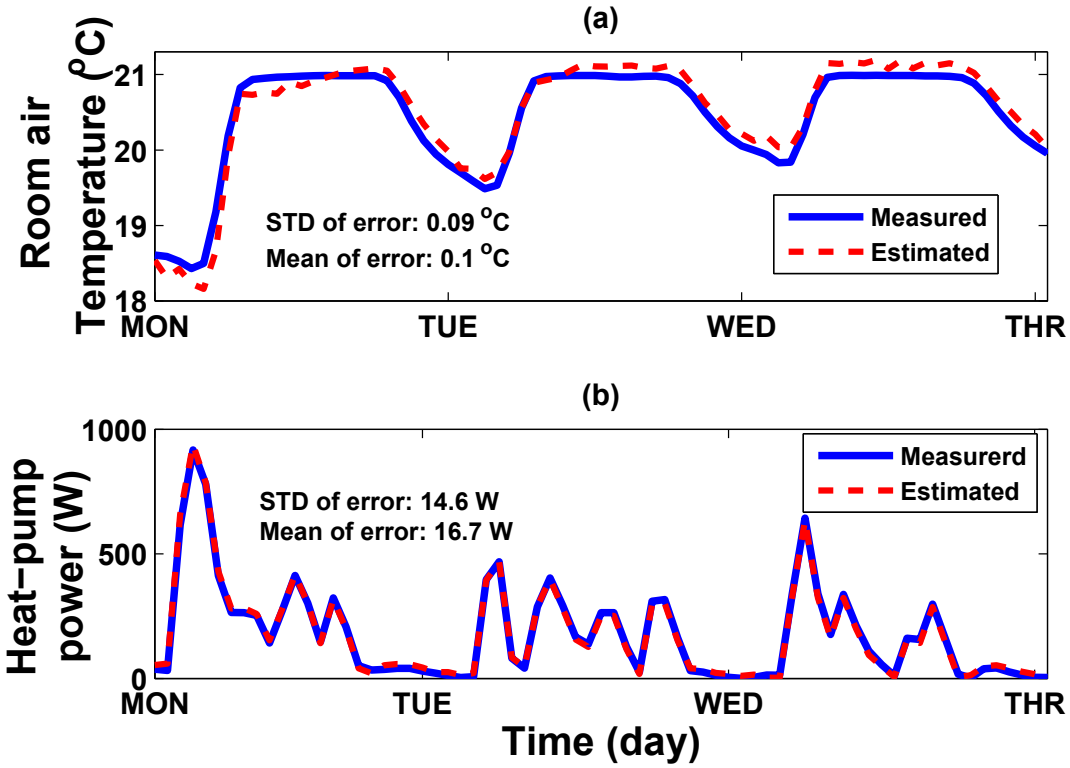

Figure 5.3: Experimental validation of the building thermal model for a sample room/zone.

5.2.2 Building Optimization Model-I

The main goal of optimization is to minimize energy cost by the building's HVAC system. For this purpose, both HVAC energy usage and time varying electricity price are taken into account. Energy usage is characterized by the energy index I_e which is defined as [1]:

$$I_t^e = \sum_{t=1}^{24} P_t^B \Delta t \tag{5.6a}$$

$$P_t^B = P_t^h + P_t^c + P_t^f + P_t^o \tag{5.6b}$$

where P_t^B is the active power consumption of building. P^h is heating power, P^c, and P^f are cooling power and fan power, respectively. We denote all buildings' other loads with P^o which includes lighting and appliances loads. Heating, cooling and fan power consumption are determined by [1]:

$$P_t^h = \dot{m}_i^r(t) c_{p,air} [T_t^h - T_{i,t}^r] \tag{5.7a}$$

$$P_t^c = \dot{m}_i^r(t) c_{p,air} [T_{i,t}^r - T_t^c] \tag{5.7b}$$

$$P_t^f = \lambda (\dot{m}_i^r)^3 \tag{5.7c}$$

where T^h and T^c are the supply air temperatures in the heating mode and the cooling mode, respectively and these variables are the system control inputs. Equations (5.7a) and (5.7b) represent the relationship between the HVAC heat-pump power consumption and the temperature difference. λ [W.s^3.kg^{-3}] is the coefficient of fan which defines the cubic relation between power required and mass flow rate. Since air mass flow rate is not a control input in the state model, and it is constant during the daytime, fan power, P^f, does not affect optimization result.

The temperature difference between supply air and the room air is proportional to electrical energy consumption. Hence, the building controller keeps the room temperature within the comfort levels such that energy cost is minimized. We use the proposed objective function in equation (5.8a) to minimize energy cost. In addition, soft constraints (i.e., ϵ) are implemented to guarantee feasibility of optimal solution at all times. The following optimization problem is being solved at each time step t, and cumulative cost is calculated from t to t_{max}:

$$\min_{U_t,\overline{\epsilon},\underline{\epsilon}}\{(\sum_{t}^{t_{max}} I_t^e\ \Omega^T) + \rho(|\overline{\epsilon}_t|_1 + |\underline{\epsilon}_t|_1)\} \tag{5.8a}$$

subject to:

$$x_{t+k+1|t} = Ax_{t+k|t} + Bu_{t+k|t} + Ed_{t+k|t} \tag{5.8b}$$

$$y_{t+k|t} = Cx_{t+k|t} \tag{5.8c}$$

$$\underline{\mathcal{U}}_{t+k|t} \leq u_{t+k|t} \leq \overline{\mathcal{U}} \tag{5.8d}$$

$$\underline{\delta\mathcal{U}} \leq u_{t+k+1|t} - u_{t+k|t} \leq \delta\overline{\mathcal{U}} \tag{5.8e}$$

$$\underline{T}_{t+k|t} - \underline{\varepsilon}_{t+k|t} \leq y_{t+k|t} \leq \overline{T}_{t+k|t} + \overline{\varepsilon}_{t+k|t} \tag{5.8f}$$

$$\underline{\varepsilon}_{t+k|t}, \overline{\varepsilon}_{t+k|t} \geq 0 \tag{5.8g}$$

where (5.8b) and (5.8c) form building's state model, (5.8d) and (5.8e) are constraints on input i.e. supply air temperature, (5.8f) is output constraint on temperature of room and (5.8g) represents the constraint on slack variables. Constraints (5.8b) and (5.8d) should hold for all $k = 0, 1, ..., N-1$, and N is the prediction horizon. In section 5.5.6, effect of N on simulation results will be discussed. (5.8c), (5.8e), (5.8f), and (5.8g) should hold for all $k = 1, 2, ..., N$. $U_t = [u_{t|t}, u_{t+1|t}, \cdots, u_{t+N-1|t}]$ represents control inputs vector and $u_{t+1|t}$ is the estimated value of u_{t+1} at time t, $\underline{\epsilon}_t = [\underline{\varepsilon}_{t+1|t}, \cdots, \underline{\varepsilon}_{t+N|t}]$ and $\overline{\epsilon}_t = [\overline{\varepsilon}_{t+1|t}, \cdots, \overline{\varepsilon}_{t+N|t}]$ are the slack variables. Slack variables are added to ensure feasibility of optimal control problem. In equation (5.8a) there is penalty (ρ) for slack variables. Therefore, by choosing large values for ρ, the

optimizer enforces the slack variables to take small values and does not violate the temperature constraints. ρ characterizes the flexibility of a building to provide services at the grid level. ϵ is not a pre-determined value in the optimization; however, by choosing large enough values for ρ, deviation from comfort bound (i.e., ϵ) is guaranteed to be minimum. In Equation (5.8a), lower values for ρ leads to higher flexibility for grid level services; however, this results in occupants' discomfort [1]. Equation (5.8f) defines the relationship between the room temperature and the slack variable value. Ω is dynamic pricing of electricity which is considered to be independent of power consumption by the building loads. $y_{t+k|t}$ is the vector of thermal zone temperature, $d_{t+k|t}$ is the disturbance load, and $\underline{T}_{t+k|t}$ and $\overline{T}_{t+k|t}$ for $k = 1, \cdots, N$ are the lower and upper bounds on the zone comfort level, respectively. $\underline{\mathcal{U}}_{t+k|t}$ and $\overline{\mathcal{U}}$ are the lower and upper limits on the supply air temperature delivered by the heat-pump of the HVAC system, respectively. Operational limit on maximum supply air temperature is not time varying, therefore time invariant constraint $\overline{\mathcal{U}}$ is used. $\underline{\delta\mathcal{U}}$ and $\overline{\delta\mathcal{U}}$ are limitation on rate of change of supply air temperature according to dynamics of heat-pump condenser.

5.2.3 Building Optimization Model-II

Objective of this optimization model is the same as (5.8). However, an additional constraint is used as a feedback from distribution grid, which is given as:

$$P_t^B \leq P_t^{var} \tag{5.9}$$

where P_t^{var} is the maximum allowable building active power penetration in the distribution grid, which will be discussed in Section 5.2.4. Equations (5.6), (5.7a)-(5.7c), (5.8b)-(5.8g), and (5.9) define equality and inequality constraints of the optimization model.

5.2.4 Distribution Grid Optimization Model-I

Objective of this optimization model is to determine maximum additional building loads that can be connected at different nodes of the distribution system. This information is used as a feedback to the building optimization model-II described in Section 5.2.3, which represents information exchange between the two levels of the bilevel optimization framework. Mathematically, objective function can be written

as:

$$max \left\{ \sum_{t=1}^{t_{max}} \sum_{nb \in n} P_t^{var,nb} \right\} \tag{5.10}$$

where n represents nodes and nb represents nodes where buildings are connected.

Equality constraints of the grid optimization model include component modeling and voltage/current balance equations. Distribution feeders, transformers, and voltage regulators with load tap changers (LTCs) are modeled using ABCD parameters as described in [173]. Constant power, constant current, and constant impedance loads are considered at each node. Mathematically, these equality constraints can be represented as:

$$\begin{bmatrix} V_t^n \\ I_t^{sen,m} \end{bmatrix} = \begin{bmatrix} a^m & b^m \\ c^m & d^m \end{bmatrix} \begin{bmatrix} V_t^{n+1} \\ I_t^{res,m} \end{bmatrix} \tag{5.11a}$$

$$\begin{aligned} I_t^{res,m-1} = I_t^{sen,m} + I_t^{Z,n} + I_t^{I,n} \\ + I_t^{P,n} + I_t^{C,n} + I_t^{var,n} \end{aligned} \tag{5.11b}$$

$$Z^n \; I_t^{C,n} = V_t^n \; Ctap_t^n \tag{5.11c}$$

where m represents feeder branches, $I_t^{res,m-1}$ and $I_t^{sen,m}$ are receiving and sending end currents on branch $m-1$ and m, respectively. For branches with LTC, $a^m = \frac{1}{1+\Delta s \cdot Ttap_t^m}$, $b_j = c_j = 0$ and $d_j = a_j^{-1}$ where Δs represents voltage change (p.u.) with one step change of transformer tap position and $Ttap_t^m$ represents LTC tap positions,

Z^n is the impedance of single capacitor in a bank at nominal power and voltage. $I_t^{P,n}, I_t^{I,n}, I_t^{Z,n}$, and $I_t^{C,n}$ are the currents from the constant power, constant current, constant impedance loads, and capacitor banks connected at node n, respectively. V_t^n represents nodal voltage and $Ctap_t^n$ represents number of capacitor banks switched on.

Base loads in the distribution feeder are modeled using sum of constant power, constant current, and constant impedance loads. Building loads are additional power to the grid and modeled as *constant power load*. Building load current in terms of building power can be calculated using:

$$V_t^{nb} \left(I_t^{var,nb}\right)^* = \frac{P_t^{var,nb}}{cos\phi} \angle \phi \tag{5.12}$$

where ϕ is the power factor angle of the building load. An additional equation is needed to ensure that building load penetration is allowed fairly in the distribution grid. Thus, a fairness index (I_t^F) is defined to ensure fair distribution of building loads as:

$$I_t^F = \frac{P_t^{var,nb}}{P_t^{E,nb}} \tag{5.13}$$

where, $P_t^{E,nb}$ is the base load in nodes nb.

Inequality constraints of the distribution grid optimization model include limits of

voltage as per ANSI standards, limits on capacitor and LTC positions, limits on I_t^F, and other limits such as feeder capacity, transformer capacity, etc. Mathematically, the inequality constraints can be written as,

$$\underline{V} \leq V_t^n \leq \overline{V} \tag{5.14a}$$

$$0 \leq Ctap_t^n \leq \overline{Ctap}^n, \forall\ Ctap_t^n \in \mathbb{I} \tag{5.14b}$$

$$\underline{Ttap} \leq Ttap_t^m \leq \overline{Ttap}, \forall\ Ttap_t^m \in \mathbb{I} \tag{5.14c}$$

$$0 \leq I_t^F \leq \overline{I}^F \tag{5.14d}$$

In Equations (5.14a, 5.14b, 5.14c, & 5.14d) overbar and underbar denote the maximum and minimum value for variable, respectively. Equation (5.14a) ensures that the voltage limits are within the standard set by ANSI. Equations (5.14b) and (5.14c) are the limits on tap positions in transformer and capacitor banks, which take integer numbers only.

5.2.5 Distribution Grid Optimization Model-II

Objective in this optimization model is to maximize the system load factor. Mathematically, this objective function is written as [174, 175]:

$$max \left\{ \frac{\sum_{t=1}^{t_{max}} P_t}{t_{max} \left| P_t \right|_\infty} \right\} \tag{5.15}$$

where, P_t total active power load connected to the distribution grid at hour t is calculated as:

$$P_t = \sum_n \Re \left\{ V_t^n \left(I_t^{Z,n} + I_t^{I,n} + I_t^{P,n} \right)^* \right\} + \sum_{nb} P_t^{var,nb} \tag{5.16}$$

Equations (5.11), (5.12), and (5.14) represent the equality and inequality constraints. Load factor in (5.15) is improved by controlling LTC and switched capacitor banks. For grid power flow analysis and distribution grid optimization model-II, $P_t^{var,nb} = P_t^{B,nb}$, which is obtained from (5.6).

5.2.6 B2G Index

In the hierarchical approach to solve the proposed optimization models, the lower level is concerned about the electricity costs in buildings, while the upper level is concerned in maximizing the system load factor. A worthwhile B2G optimization should maintain an appropriate compromise between low electricity cost in buildings and high load factor in the distribution system. To account for this, we define a new B2G index (I_{B2G}) to assess the performance of the proposed B2G optimization framework, which allows reduction in the electricity costs and improvement of system load factor starting at the building level with the use of nodal load factor. The B2G

index is defined as:

$$I_{B2G} = \alpha \left(I_t^e \Omega^T\right) + \beta \overbrace{\frac{t_{max} \left|P_t^{B,nb}\right|_\infty}{\sum_{t=1}^{t_{max}} P_t^{B,nb}}}^{L_f^{-1}} \tag{5.17}$$

where α and β are the weight factors for energy price ($I_e\Omega^T$) and nodal load factor (L_f), respectively. The smaller the I_{B2G} index, the better the performance for the B2G optimization. The ratio of weight factors, α to β, determines the importance of energy cost compared to the system load factor. α and β are the design parameters in the B2G optimization problem and can be adjusted by the building and grid operators, depending on whether the benefits from the building side or the benefits from the grid side are more desirable. Thus, selection of proper values of α and β for optimal operation system requires sensitivity analysis of the building-grid system under consideration.

In the case studies, I_{B2G} is used as an alternative objective function to (5.8a) in building optimization models. Note that (5.8a) does not account for grid's objective; while the proposed B2G index considers the grid's objective in the building optimization model with consideration of the nodal load factor.

5.3 Solution Method

A solution method, shown in Fig. 5.4, is proposed for the bilevel B2G optimization framework. The proposed solution method consists of information exchange between the two levels, i.e., the commercial buildings and the grid control center; thus, it is bidirectional in nature. The B2G optimization framework consists of two optimization models for the demand side (i.e., building systems) and two optimization models for the supply side (i.e., distribution grid). These optimization procedures include:

- † Building Optimization Model-I: Building energy cost minimization;
- † Distribution Grid Optimization Model-I: Maximizing penetration of building loads in the distribution grid;
- † Building Optimization Model-II: Minimizing building electricity cost considering constraints from grid side (5.9);
- † Distribution Grid Optimization Model-II: Maximizing load factor of distribution grid.

The solution procedure begins with the demand side optimization with an objective to reduce electricity cost for the next day (label A in Fig. 5.4). At this stage, the optimized load profiles of each of the commercial buildings are made available to the

distribution grid control center. A distribution grid power flow analysis is carried out to confirm the feasibility of building load profiles. The feasibility test checks various operational constraints of the distribution grid including voltage limits as per ANSI standards defined by (5.14a)-(5.14c). Violation of operational constraints makes the building loads in-feasible for grid operation. In case the building loads are feasible for the grid (label B in Fig. 5.4), tap positions of capacitor banks and transformers are calculated using distribution grid optimization model-II, which maximizes the system load factor.

In case of in-feasibility of the building loads from grid side, the maximum allowable load, $\overline{P}_t^{B,ib}$, is obtained from the distribution grid optimization model-I. $\overline{P}_t^{B,ib}$ is used as a feedback to the BMS system (label D in Fig. 5.4) to solve the building optimization model-II. If the updated optimization is feasible, then the optimized load profile is sent back to the distribution optimization model-II to maximize load factor (label F in Fig. 5.4). Otherwise, other options like changing building's temperature requirements (label E in Fig. 5.4) becomes necessary. Next, building optimization model-II is solved by considering the feedback from the grid as additional constraint. Then, the resulting building load profile information is sent to the distribution grid control center, which is used to solve distribution optimization model-II.

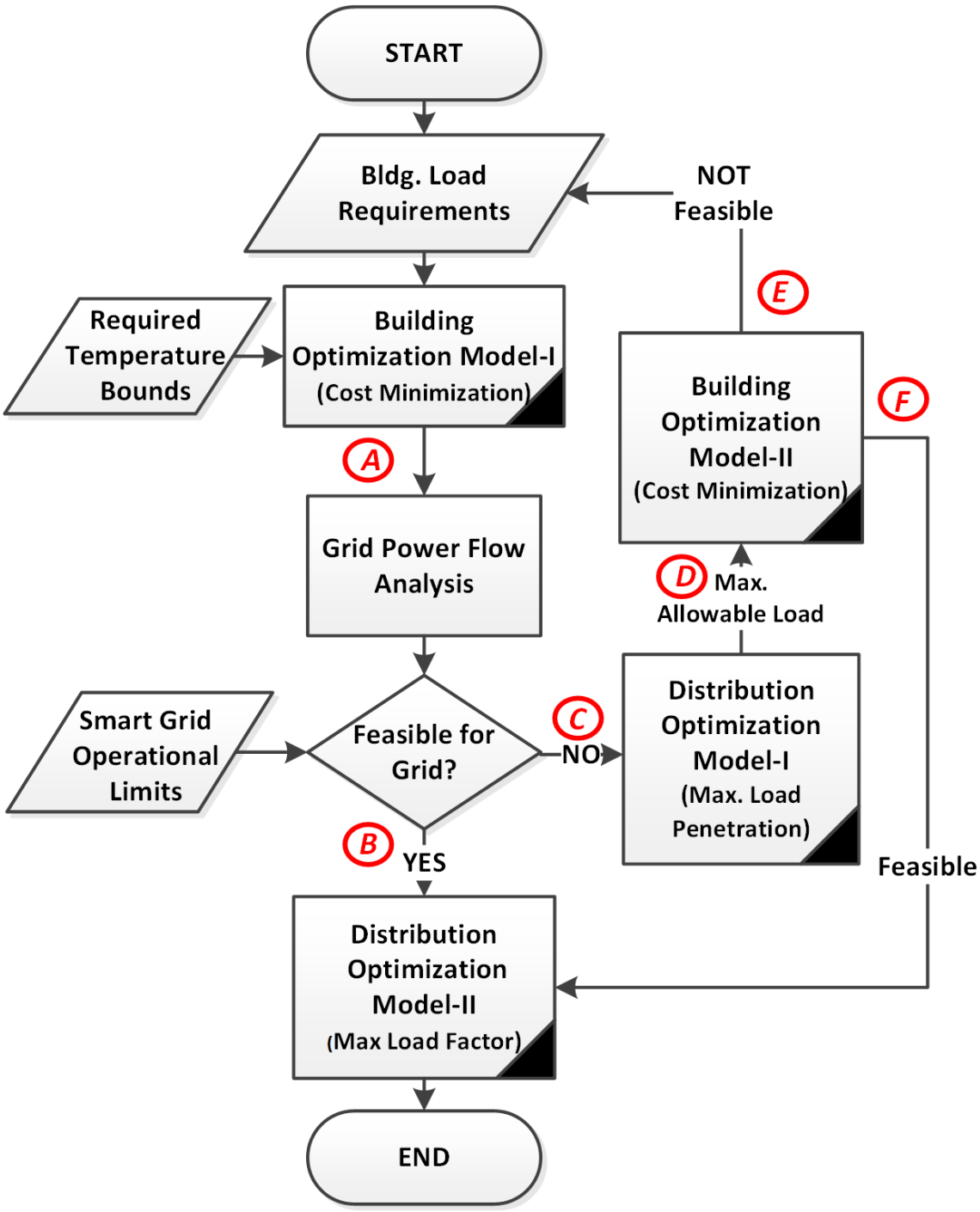

Figure 5.4: Proposed bidirectional B2G optimization flowchart.

Change of the control variables, i.e., LTC and capacitor banks may result in different node voltages from the two distribution grid optimization models, which in turn can impact the voltage dependent loads and make the grid optimization problems in-feasible. Thus, depending on the types of load used in the distribution grid optimization model, the whole solution process may need to reiterate. An alternate approach to handle this issue is to consider a small unused margin of power in the maximum allowable loads in (5.10) that can accommodate change in power consumption of loads due to the voltage change. However, this change will not affect the feasibility of HVAC system since they can be considered as constant power load [176].

5.4 Test Systems

5.4.1 Building Testbed

A commercial three story Lakeshore Center building with an area of $61,500 ft^2$ at Michigan Technological University (MTU), Houghton, Michigan, is considered as the testbed. The testbed is equipped with ground-source heat-pumps (GSHP) to provide required energy for heating and cooling. GSHPs transfer geothermal energy from the ground to rooms. GSHPs are HVAC energy efficient technologies with high coefficient of performance (COP). The GSHPs in this study have a nominal COP of 3.2.

Each room is equipped with a GSHP to maintain comfort of occupants. Fig. 5.5 shows the schematic of the building with GSHPs connected to the distribution grid at node #10. Temperature of each zone in Lakeshore Center building is measured using a temperature sensor from the BMS with accuracy of ±0.2°C. HVAC system in the testbed consumes up to 44% of electricity in winter, while the rest of electricity consumption is attributed to lighting, computers, and office appliances. Historical data of energy consumption of an office building at MTU is used to compute the share of energy consumption of major loads in the testbed.

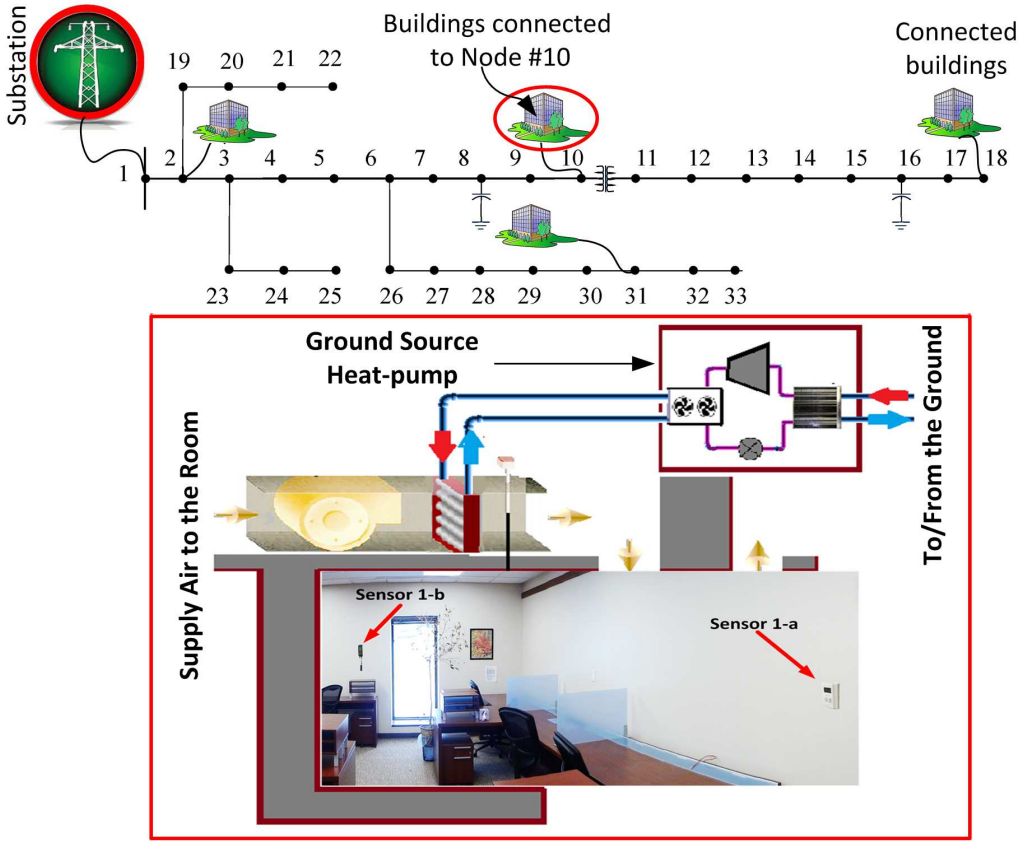

Figure 5.5: Schematic of the testbed with a ground-source heat-pump. Two temperature sensors are used to measure the average room air temperature.

5.4.2 Distribution Test Feeder

A standard single phase 12.66 kV, 33-node distribution feeder [150] is considered for the case studies. The standard test system is modified by adding a regulator and capacitor banks to account for the control equipment available in distribution grids.

As shown in Fig. 5.5, a transformer is equipped with voltage regulator (connected between 10^{th} and 11^{th} nodes in the test systems), which maintains the voltage at node 11 within $\pm 10\%$ of the nominal value. A 32-step regulator is considered, and a single tap change represents voltage of 0.00625 p.u. Capacitor banks are connected at 8^{th} and 16^{th} nodes of the feeder and are modeled as constant impedance load capable of delivering reactive power to the grid. Identical five units of capacitors with 10 kVAr each are considered, which are represented as switched capacitors with tap positions from 0 to 5.

It is assumed that smart buildings are connected at four arbitrary nodes, i.e., nodes 2, 10, 18, and 31. Each building is considered to have twenty identical zones with similar load profiles and with the same temperature requirements.

5.5 Results

The building model is implemented in MATLAB® and YALMIP [109] toolbox is used to provide a symbolic syntax to formulate the problem and interfaces with the optimization solver. Distribution system optimization model is developed in GAMS [177]. The accuracy of the building model is validated using actual measurements collected from an office building at Michigan Tech [1]. The distribution grid model is validated using the results in [150].

This work considers the weather forecast and energy price as the inputs required for the building and grid optimization models. Thus, electricity dynamic pricing available from Midcontinent Independent System Operator (MISO) is used [9]. Weather forecast information available from a local weather station is used. The constraints on the room temperature are set based on ASHRAE standards [66]. Other building and grid parameters used in the simulation can be found in [2] and [150], respectively.

The optimization results are compared with the non-optimized rule-based controller (RBC). We use same $\Delta t = 1$ hour time step to have a fair comparison among B2G optimizers in this study. Given the slow thermal behavior of the testbed building and the type of demand response applications, one hour time step is sufficient to capture the dynamics. Depending on building type, a shorter time step may be required.

For the case study, five buildings each having twenty zones are connected at node 2 of the distribution grid, similar three buildings are connected at node 10, four buildings are connected at node 18, and seven buildings are connected at node 31. In this chapter, the optimization results are only presented for the buildings at node #10 (see Fig. 5.5). The nodal load factor is presented for the node #10 as a node representing B2G system. In addition, system level load factors are also determined for the distribution grid system to compare the operation of different B2G optimizers.

As mentioned in the Section I, HVAC systems account for a large amount of load in buildings. Therefore, in this study, we focus on controlling the HVAC load of the buildings which is considered to be *dispatchable*. Other loads in buildings including lighting, appliances, and base loads in the distribution grid are considered to be non-dispatchable. For MPC simulation, a prediction horizon of $N = 24$ is used with time step of 1 hour. Here, we introduce three different optimization methods and compare them with the RBC.

5.5.1 Unoptimized Rule Based Control

In this approach, when temperature goes below the lower-bound temperature, the HVAC RBC keeps the heat-pump compressor on for the duration of Δt. In the next time step, the RBC checks the room temperature again and determines whether

Table 5.1
Performance of four different B2G optimization techniques, compared to the unoptimized (RBC) case study.

Optimization type	Monthly Bldg. elec. cost [$]	Monthly Bldg. elec. consumption [kWh]	Node #10 load factor [-]	System (grid) load factor [-]	I_{B2G} index [-]	Bldg. cost saving* [%]	Bldg. energy saving* [%]
	One day ahead prediction (including weather, dynamic pricing, comfort bounds, etc.)						
Unoptimized (Base case)	935	368.1	0.41	0.72	10.50	0	0
Optimized (Bldg Unidirectional)	693	310.6	0.44	0.81	9.2	26	16
Optimized (Grid Unidirectional)	909	341.4	0.84	0.86	8.7	3	7
Optimized (Bidirectional)	698	310.1	0.46	0.84	8.8	25	17
Optimized (Using I_{B2G})	707	305.2	0.67	0.84	6.9	24	17

*Percentage saving is calculated by $\frac{x-x_0}{x_0} \times 100$, where x_0 is the energy consumption/cost for the unoptimized (base) case.

Table 5.2
Performance of two different B2G real-time optimization techniques, compared to the unoptimized (RBC) case study.

Optimization type	Monthly Bldg. elec. cost [$]	Monthly Bldg. elec. consumption [kWh]	Node #10 load factor [-]	System (grid) load factor [-]	I_{B2G} index [-]	Bldg. cost saving* [%]	Bldg. energy saving* [%]
	Real-time prediction (including weather, dynamic pricing, comfort bounds, etc.)						
Optimized (Bidirectional)	752	308.9	0.47	0.81	9.8	20	16
Optimized (Using I_{B2G})	758	308.6	0.59	0.83	7.9	19	16

*Percentage saving is calculated by $\frac{x-x_0}{x_0} \times 100$, where x_0 is the energy consumption/cost for the unoptimized (base) case.

the room temperature is within the comfort bounds. The monthly electricity cost of the building and energy consumption along with other B2G metrics are listed in TABLE 5.1.

5.5.2 Building/Grid side Optimizations

The results of uncoordinated building side and grid side optimization are presented here. Fig. 5.6 shows the results of a building MPC controller using building optimization model-I. The main objective in the building-side optimization is to minimize

building electricity costs. Fig. 5.6 (a) demonstrates the temperature profile of the room, and Fig. 5.6 (b) shows load distribution of buildings connected to node #10 including lighting load, appliances (computers, elevators, refrigerators, etc.) and buildings' HVAC load. Building load distribution is based on simulation results carried out for Lakeshore Center building at Michigan Tech using Carrier HAP software. Fig. 5.6(c) shows load distribution on node #10. Fig. 5.6(d) illustrates the building electricity load and the maximum feasible load for node #10 which is obtained from distribution optimization model-I block shown in Fig. 5.4. In Fig. 5.6(d), the importance of grid-wise optimization for buildings is emphasized since the optimized building loads violate the maximum allowable loads by the grid. Note that in Fig. 5.6, the power and supply temperature peaks at unusual time is due to the pre-heating of the HVAC system when the electricity price is cheaper. The dynamic pricing and result HVAC cost are shown in Fig. 5.7. The monthly building electricity cost is listed in TABLE 5.1. Compared to the RBC, building-side optimization results in 26% cost saving and 16% energy saving.

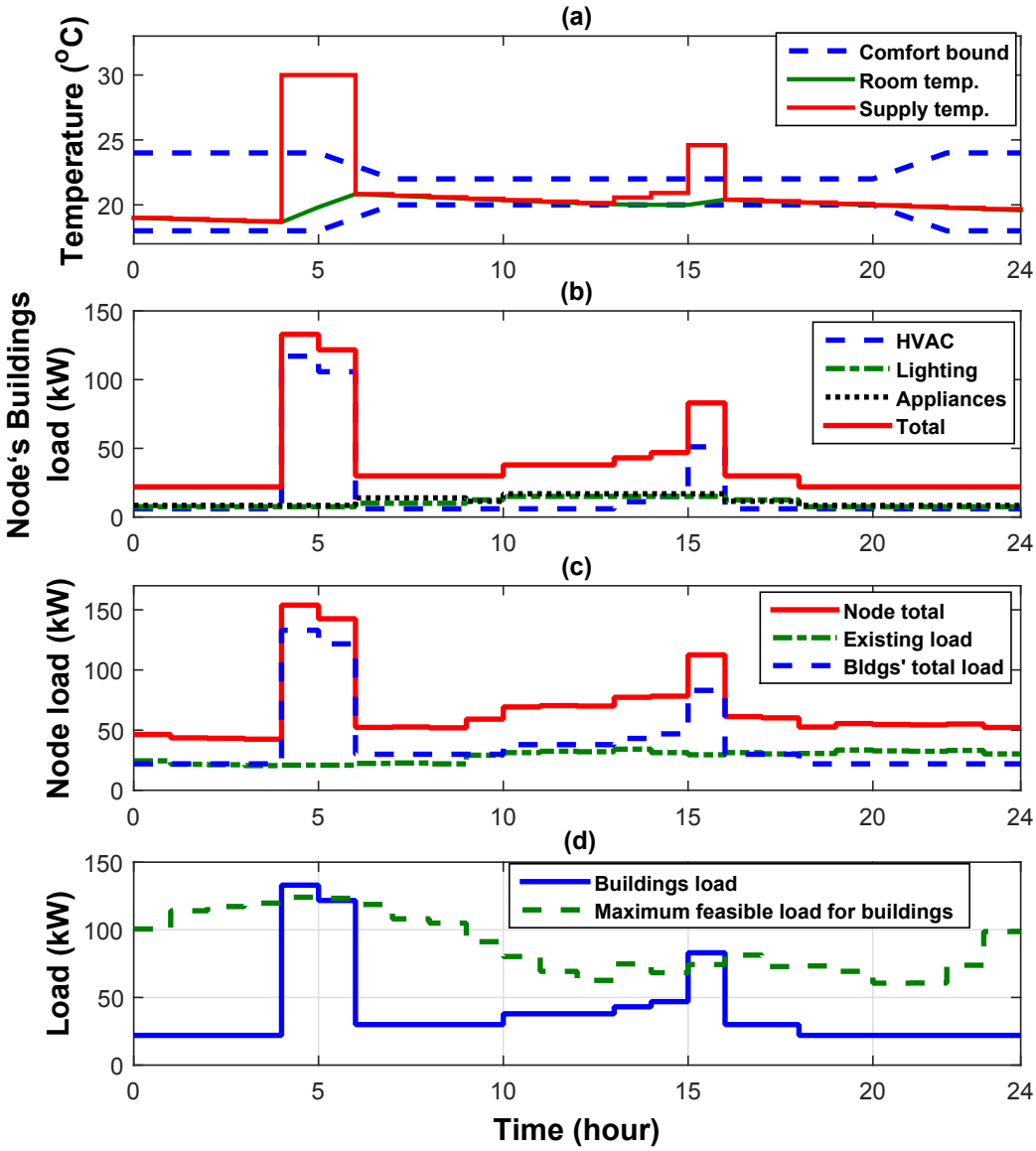

Figure 5.6: Building-side optimization: (a) Control input and resulting temperature profile for the building MPC controller, (b) Buildings' load profile including HVAC load, lighting load and appliances load, (c) Buildings' total load at node #10 and base load, (d) Buildings' electricity load versus maximum feasible load for node #10.

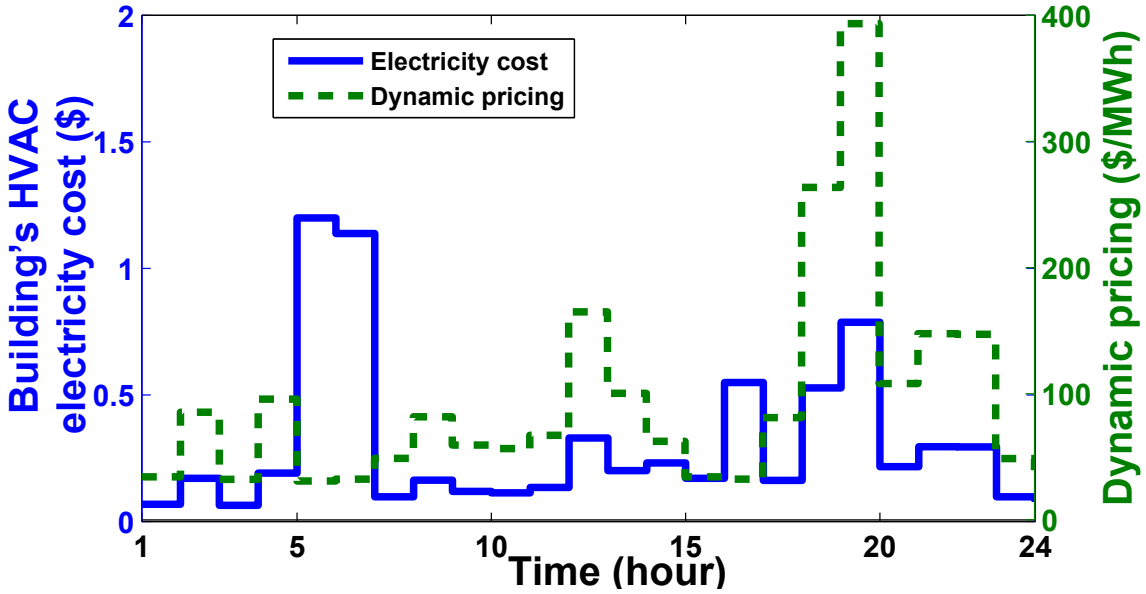

Figure 5.7: Building-side Optimization: dynamic pricing versus hourly cost for the building.

If the objective is to maximize load factor in the distribution grid (i.e, the grid-side optimization), the nodal load factor is significantly increased to 0.84 , while the building's energy cost increases.

5.5.3 Bidirectional Optimization

The proposed B2G methodology in Section 5.3 is applied for the case study similar to that in subsection 5.5.2. Building optimization results are illustrated in Fig. 5.8 and summarized in TABLE 5.1. The results show the B2G optimizer satisfies the building comfort levels, while keeping the building load under the maximum load allowed by

the distribution grid. In addition, compared to the unidirectional (demand side) optimization, the system level load factor is increased from 0.81 to 0.84. I_{B2G} index also depicts a significant improvement as seen in TABLE 5.1. Bidirectional optimizer offers 25% cost saving compared to the unoptimized case while energy cost saving is only dropped by 1% compared to unidirectional (building side). Thus, this case study demonstrates that with the grid constraints, the cost of operation of buildings increases, but it ensures a feasible operation of the grid.

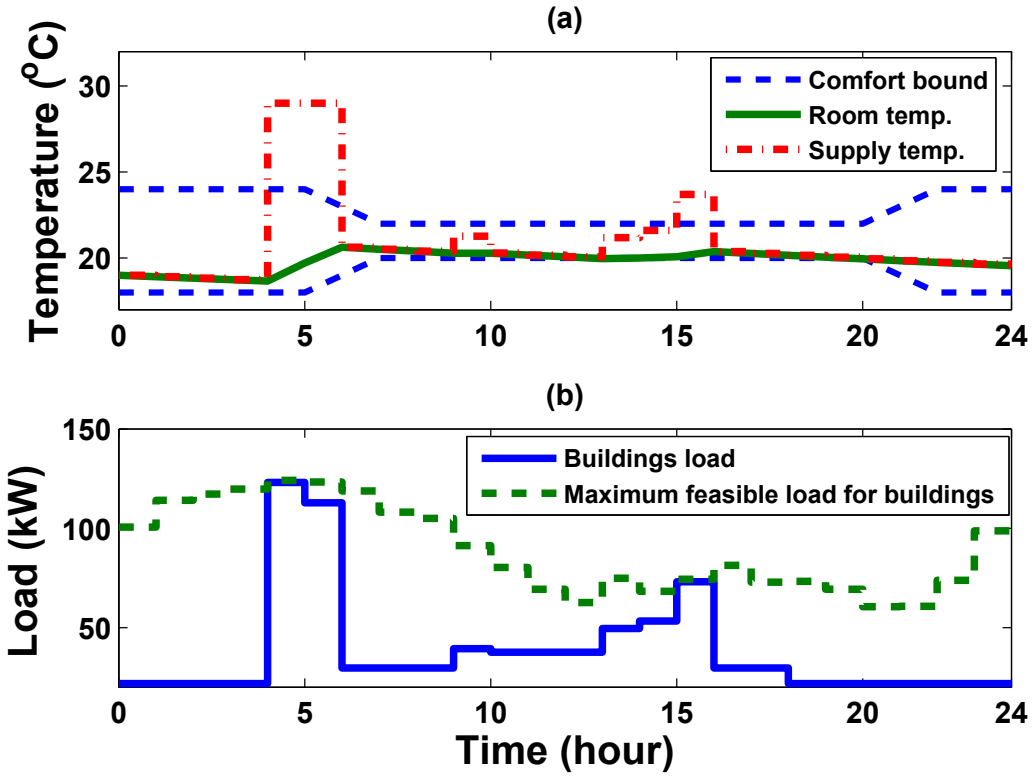

Figure 5.8: Bidirectional optimization: (a) Control input and room temperature profile for the MPC controller, (b) Building load vs maximum feasible load.

5.5.4 Bidirectional Optimization Using I_{B2G} Index

I_{B2G} index provides a way to control/formulate the importance of building benefits versus grid benefits. The results of bidirectional optimization using I_{B2G} index are shown in Fig. 5.9 and summarized in the TABLE 5.1. As expected, the new optimization approach leads to the best result in terms of I_{B2G}. The smaller value for I_{B2G}, the better performance for the B2G system. Using I_{B2G} in the building objective function helps to improve building/nodal load factor and consequently better system level load factor, while minimizing the building energy costs. As a result, I_{B2G} is better in the new bidirectional optimization, compared to the bidirectional optimization with objective 5.8a. 0.5 and 0.54 are chosen for α and β, respectively, to provide comparable weight to building and grid. Selection of α and β can be another optimization problem which is outside the scope of this work. In this case study, the cost of electricity is decreased by 24% with respect to the base case and both nodal and system load factors are significantly improved compared to the base case.

If α in I_{B2G} in the bidirectional optimization is chosen to be zero, the bidirectional optimization becomes unidirectional which mainly satisfies the grid benefits (Grid unidirectional in TABLE 5.1). As expected, this leads to the best load factor compared to other four cases in TABLE 5.1. But, the buildings' electricity cost is increased by 21% compared to the bidirectional I_{B2G} case. Overall, bidirectional optimization

using I_{B2G} provides an optimization platform in which an operator can easily decide the desirable compromise for the benefits of customers and the grid. By using the proposed I_{B2G} index as the optimization cost function, the temperature boundaries are met based on the ASHRAE standards.

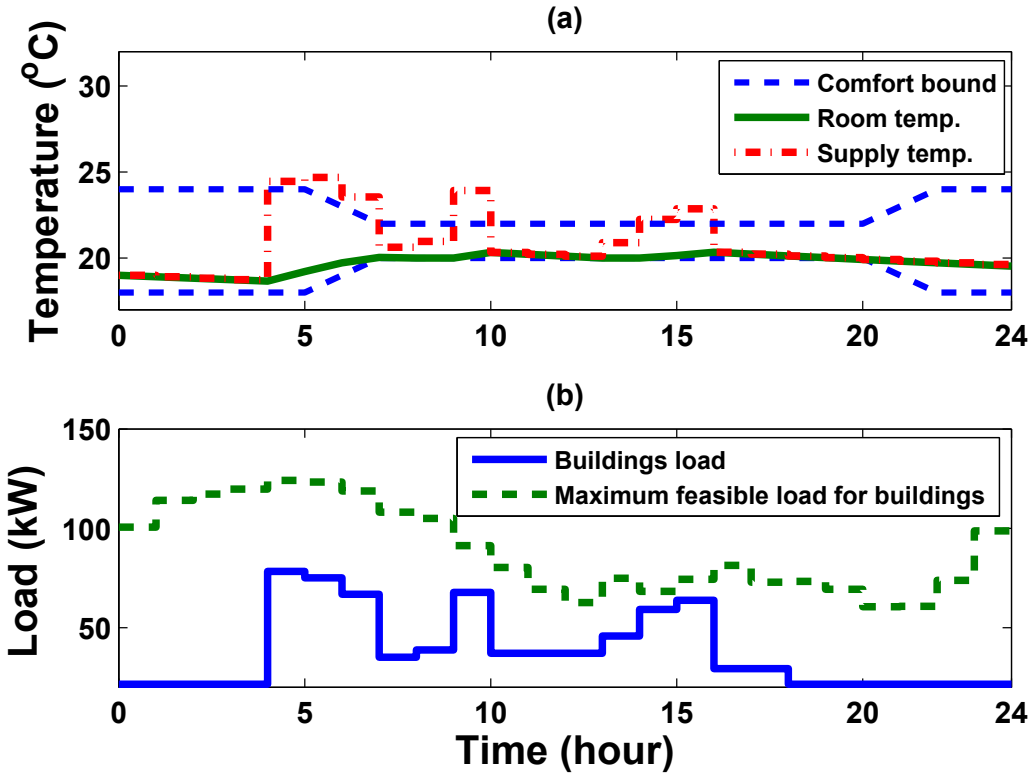

Figure 5.9: Bidirectional optimization based on I_{B2G} index: (a) Control input and resulting temperature profile, (b) Building load versus maximum feasible load.

5.5.5 Impact on Voltage Performance

Permissible voltage range, as specified in ANSI C84.1, is one of the standards to maintain power quality in distribution feeders. Fig. 5.10(a) shows the voltage at few selected nodes for unidirectional optimization (building-side) which are violated in certain hours, and (b) illustrates that the optimization model with I_{B2G} index where voltages are maintained within the limits.

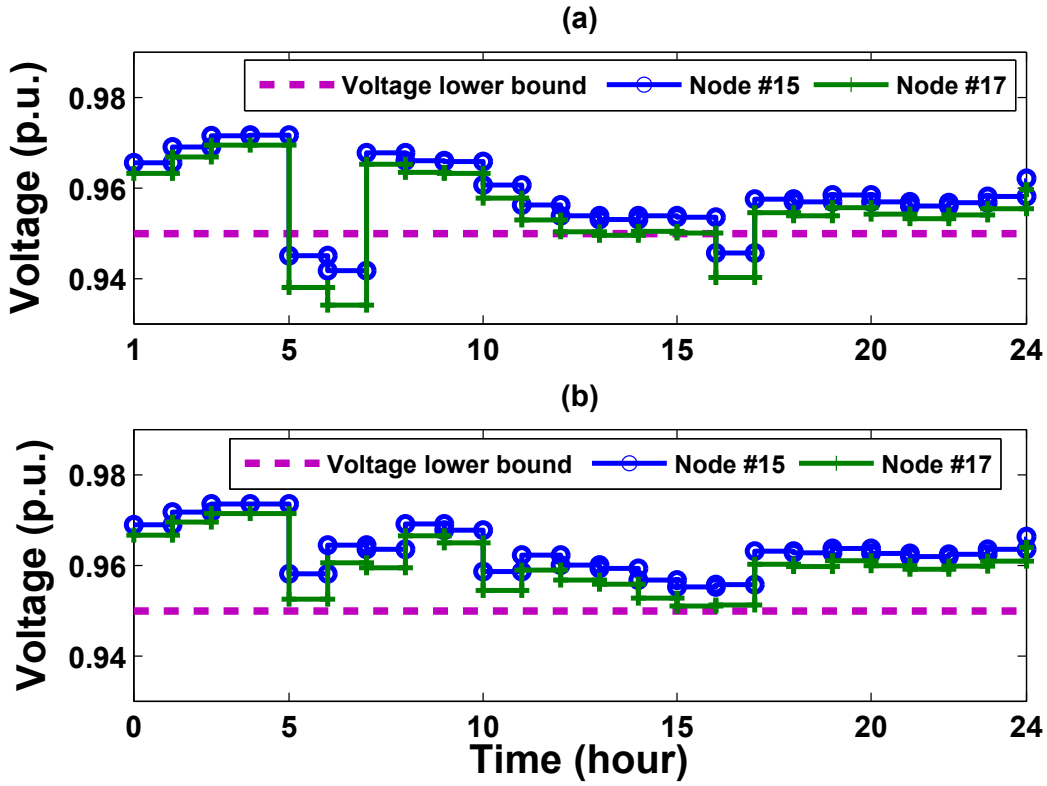

Figure 5.10: Voltage at selective nodes. Fig. (a) shows the voltage profile of unidirectional optimization and Fig. (b) illustrates the voltage profile of bidirectional optimization (using I_{B2G} index).

5.5.6 Hour-ahead vs Day-ahead Optimization

In the case studies in TABLE 5.1, the prediction horizon N is considered to be 24. It means that the optimization algorithm has prediction of weather forecast and dynamic pricing for the next 24 hours. If the weather forecast or prediction of electricity cost (dynamic pricing) is not available or not accurate for that period, the MPC algorithm cannot find the optimal solution for the next 24 hours. Here, we show two examples that the dynamic pricing and the weather forecast are available for the next hour in TABLE 5.2. Simulations for two proposed methods, bidirectional using (5.8a) and bidirectional using I_{B2G}, are carried out to demonstrate the effect of prediction horizon on the cost saving and I_{B2G} index. Results show that B2G metrics deteriorate by reducing the prediction horizon but the proposed algorithm still offers benefits for both grid and buildings. Using the real-time B2G optimization, building electricity cost drops up to 20% and building load factor increases over 0.1 compared to the baseline unoptimized case.

5.5.7 Impact of Dynamic Pricing and Seasonal Weather

The savings on electricity price and improvement on system load factor greatly depend on various factors including dynamic pricing, weather, flexibility of commercial

building's loads, building's temperature set-points, available control equipment in the building and distribution grid, and accuracy/availability of the forecasts. The impact of dynamic pricing and weather variations on the customer's cost savings and system load factor are also studied.

Fig. 5.11 (a) shows the weather condition for three sample days in Fall, Winter, and Spring in our testbed. Fig. 5.11 (b) illustrates three different dynamic energy prices at nodes in Michigan, Illinois and Minnesota. Based on the weather and energy price data, two sets of simulations are carried out. Fig. 5.12 (a) shows the effect of weather on the building's electricity cost and system load factor for the three seasons by keeping the dynamic energy price same (Michigan node). Fig. 5.12 (b) demonstrates the effect of dynamic pricing on the electricity cost saving and the system load factor improvement using same weather forecast (Fall). During the Winter, 33% saving in electricity cost and 8% improvement on system load factor. However, as weather gets warmer, the cost saving decreases. For instance, in Spring, only 6% decrease in electricity bill compared to RBC is observed. The reason for less saving in Spring compared to Winter is that the cold outside weather in Winter makes HVAC running more often which provides more opportunities to save energy costs by shifting the load. Less constraints (i.e., heating requirement) on the HVAC controller in Spring/Fall compared to Winter provides more flexibility for load factor optimization. Thus the percentage of increase in the B2G system's LF is more in Fall/Spring compared to that in the Winter. Finally, the results in Fig. 5.12 (b) show that the proposed B2G

optimization provides cost saving and system LF increase for all the three dynamic pricing profiles studied.

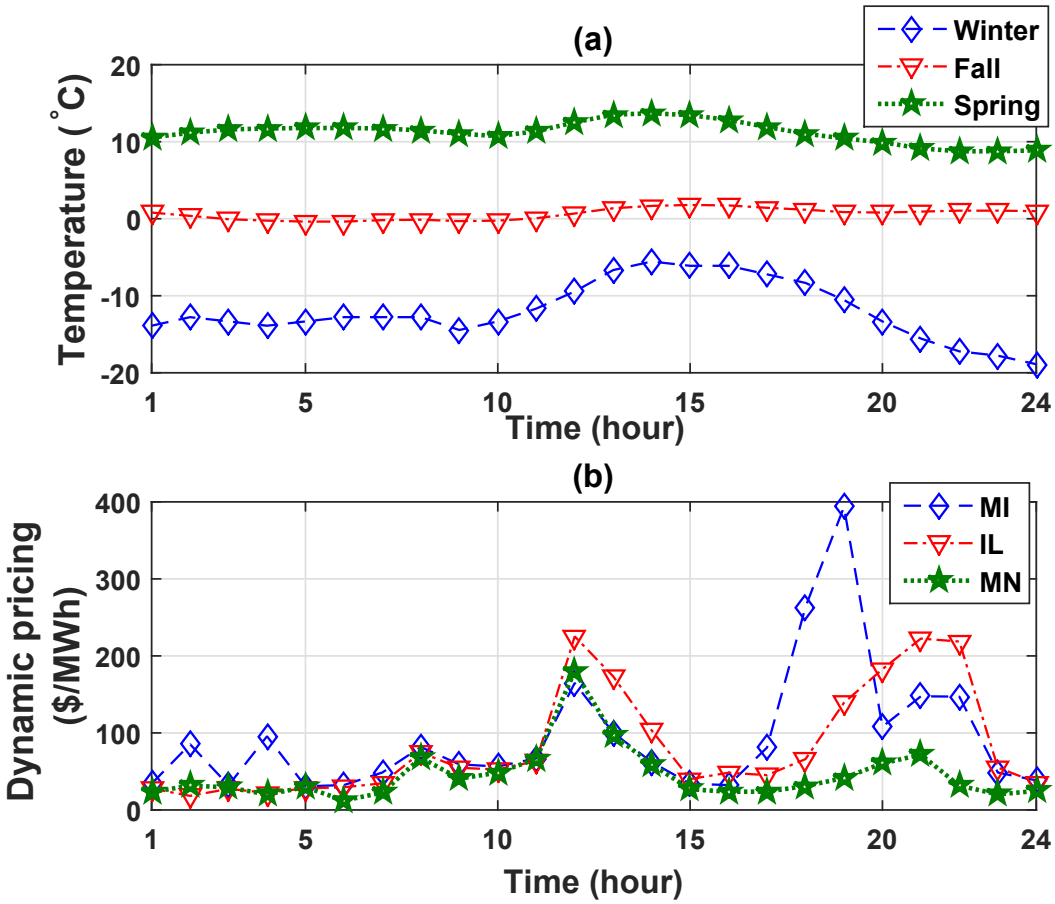

Figure 5.11: (a) weather forecast of three sample days in Fall, Winter, and Spring using measured data at Michigan Tech testbed and (b) Dynamic pricing for Michigan, Illinois, and Minnesota obtained from [9].

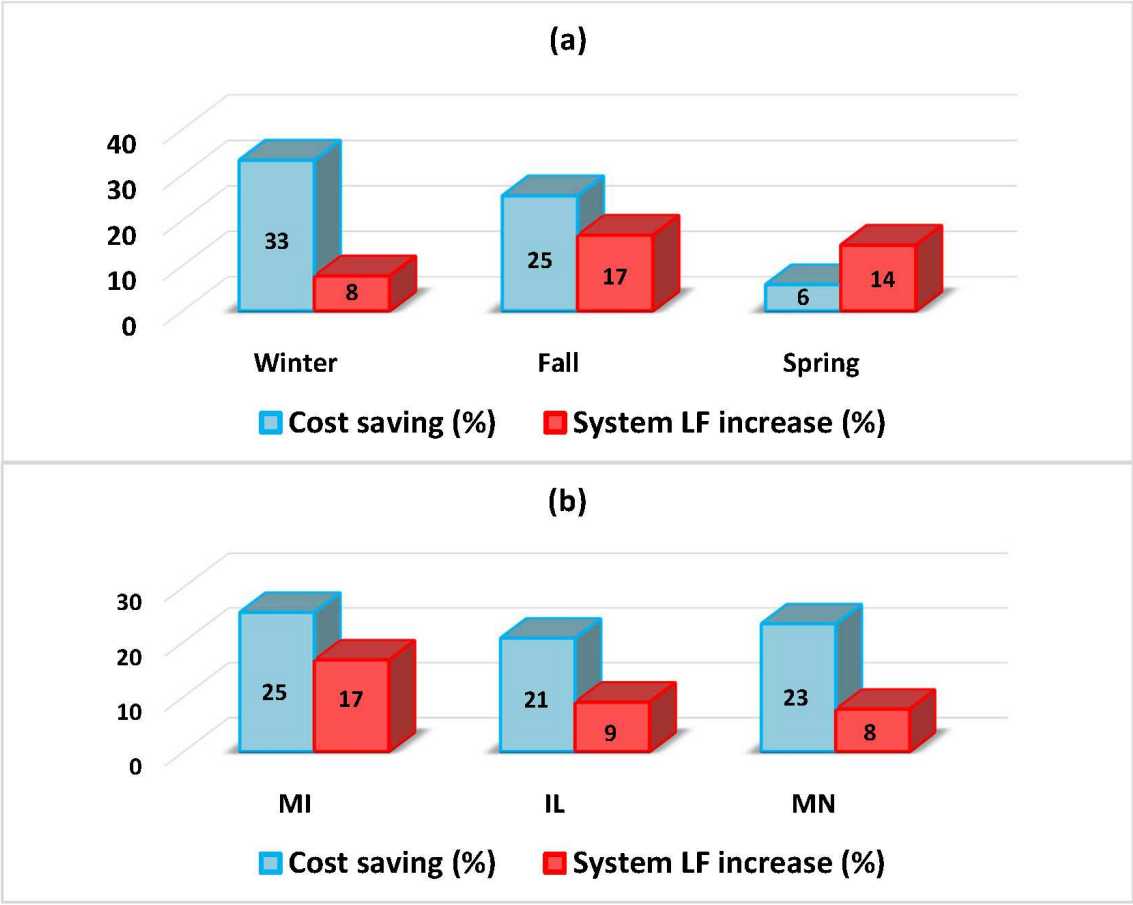

Figure 5.12: (a) shows the weather effect on the building's electricity bill and system load factor, and (b) illustrates the effect of dynamic pricing on the electricity bill and system load factor for the conditions shown in Fig. 5.11. An RBC structure similar to that in TABLE 5.1 is used as a baseline to calculate saving percentages.

5.5.8 Computational Cost

The problem formulation is hierarchical in nature, which allows each BEMS to solve its own building optimization model. The developed building optimization model

in Section II is linear programming in nature, thus the computational tasks at the building level are not challenging for the demand response applications discussed in this work. At the grid level, the nature of the problem is non-linear and LTCs and cap banks add integer variables in the model. This poses inherent computational challenges associated with the large scale non-convex optimization of distribution grid [178]. However, for the size of the system considered in this chapter, computational complexity was not an issue. Simulation time for bidirectional optimization discussed in this chapter on an INTEL Core i5, 3.2 GHz CPU desktop computer is less than one minute for building's unidirectional optimization and around 5 minutes for optimization of both building and grid models. The entire hierarchical optimization problem takes maximum of two iterations to solve. First, optimal load profiles at each interval (i.e., each hour in this work) from the buildings are sent to grid control center to determine feasibility of the grid operation. In case of infeasibility, maximum feasible load profiles are sent to each building controllers.

Computational challenges associated with large practical size grid can be reduced by using methods of convexification [179], distributed approaches [153], and heuristic approaches [149]. The solution time desired for the proposed models depend on the B2G applications sought. For example, voltage regulation needs to be tackle in a few minutes, and load shifting in the order of hours [180]. For the type of B2G applications proposed in this work, solution time of 5 minutes and a coarse time interval of one hour suffice.

5.5.9 Benefits, Challenges, and Limitations

This work provides a generic mathematical framework to optimally coordinate building loads and grid level assets, which is useful for near-term energy usage planning and/or near-real time dispatch of building loads. This opens up opportunities to deploy multiple distributed building loads for grid level applications such as demand response, load following, and regulation services. The framework ensures that, in the demand dispatch process, the operational constraints and interests of the grid level and customer level energy management activities are honored; thus providing benefits to both the entities involved.

The case studies clearly demonstrated the benefits of the proposed framework to the building and grid operations. However, the major challenges in large scale deployment of B2G integration are: (1) infrastructural challenges including interoperability of tools at building and customer levels, bandwidth limitation, compatibility of system to handle different data with different resolution and with different communication standards, and (2) mechanism barriers including lack of financial models for costumer motivation, accurate predication of weather and energy price, computational issues for grid optimization for real-time applications in practical-sized systems, and scalability of the control and optimization algorithms [180].

Use of dynamic pricing (day ahead or real-time) at small residential and commercial buildings has already begun [181, 182]. With the widespread implementation of dynamic pricing for small customers, and with energy management systems at customer's premise, the power peak in distribution systems will shift to the hours with least expensive energy prices. Thus, the utility needs to devise demand limits for the customers for the feasible grid operation. However, with the demand limits, energy savings of the customer will reduce. An appropriate incentive/compensation mechanism need to take place [183], where utilities may compensate the customers for the reduction in the savings. However, the compensation may not be necessary for all cases, since the case studies demonstrated that the optimized energy costs of the buildings are reduced compared to the RBC even with the grid constraints. Utilities need to devise subscription plans where the customers agree that the BEMSs honor the demand limits sent by the DSO and penalties for noncompliance. The another approach to solve this issue is the use of distribution location marginal price (DLMP) [184]. If appropriate method for setting DLMP can be designed, which considers the customer's expected response for the low energy prices, the impact of low energy price on peak demand can be eliminated to a certain extent.

5.6 Conclusion

This study develops a bidirectional B2G optimization framework using an experimentally validated building thermal model and a mathematical model for the distribution grid. The building optimization model is based on disturbance and heat transfer phenomena, and its model parameters are obtained from actual measurements collected from an office building at Michigan Technological University. The distribution grid model is comprised of modeling of typical distribution system components including feeders, transformers, and control equipment such as capacitor banks and transformer load tap changers. In the proposed bidirectional optimization model, the objective is to minimize energy cost for the demand side and to maximize load factor for the grid. To account for conflicting interests of the BEMS and distribution operators in the bidirectional optimization, a novel B2G index is developed based on building energy cost and nodal load factor. Based on the provided case studies, it can be concluded that the developed bidirectional optimization framework can reduce commercial buildings' monthly electricity costs by 25% in Winter, compared to the unoptimized rule-based control of the building loads, while improving the system load factor. However, the savings obtained in energy price and improvement on system load factor greatly depend on various factors including energy price, flexibility of commercial building loads, customers' preferences, available control equipment in a distribution grid, accuracy/availability of weather forecast and dynamic pricing

prediction, etc. Nevertheless, the developed bidirectional optimization framework certainly offers benefits to the customers and the utilities in B2G integration.

Chapter 6

Conclusion and Future Work

Summary of the results and contributions of this dissertation are outlined in this Chapter.

6.1 Summary and Conclusion

Model uncertainty is a crucial challenge for model-based control of a building's HVAC system. First, a Parameter Adaptive Building (PAB) technique is presented in this dissertation. The PAB model learns and updates building time-varying parameters. Then, an MPC framework that is robust against model uncertainty is proposed. The

new framework is Robust Model Predictive Control (RMPC) which utilizes uncertainty knowledge to enhance the nominal MPC. The specific contributions are listed below:

1. A PAB modeling framework was developed using an unscented Kalman filter (UKF) to simultaneously estimate all the states of the dynamic model and continuously tune the parameters of the building model.

2. Closed loop RMPC outperformed nominal MPC considering the provided level of comfort. However, higher comfort comes at the cost of higher energy consumption for RMPC. For uncertainty range of 30% to 67%, RMPC leads to better overall performance compared to MPC and RBC, while it fails to provide a better energy-comfort trade-off if model uncertainty is less than 30% or more than 67%.

3. This dissertation proposed a new performance index (I_{OP}) to assess buildings' energy consumption and comfort level simultaneously. The I_{OP} index is used for evaluating different building controllers. I_{OP} index can be used to generate a guideline for choosing appropriate controller type for buildings.

4. It is found that the best choice for controller type changes from MPC to RMPC, and then finally to RBC as the model uncertainty increases. A typical RBC controller outperforms model-based controllers (MPC and RMPC), if building model uncertainty is above 67%.

Next, SLT is applied to study entropy production and irreversibilities in thermodynamic processes of heat-pump which cause deficiency and energy waste. HVAC systems can be operated in low exergy fashion by applying exergy-aware control algorithm which reduces irreversibilities and as a result, operation of HVAC will be more energy efficient. In this dissertation, we derived and formulated exergy destruction as a function of the physical parameters of the building and it is used as the cost function of the optimal control problem to minimize exergy destruction rate. The beneficial new aspects of MPC problem based on exergy is decreasing irreversible entropy generation. The findings from exergy-based control of HVAC systems show that:

1. Compared to RBC, XMPC achieves 22% reduction in exergy destruction and 36% reduction in electrical energy consumption by HVAC system. XMPC optimizes the use of low quality energy (low exergy) for HVAC systems and hence decreasing irreversible entropy generation. Thus, supply air temperature needs to be close to the room temperature since large difference in supply air temperature increases entropy generation (exergy destruction).

2. XMPC consumes 12% less energy and saves 4% more exergy compared to EMPC. By reducing energy loss and irreversibilities of energy/exergy flows into the zones, heat transfer of zone and rate of change of energy/exergy contained in the zone, XMPC offers more energy saving compared to conventional EMPC.

3. Implementation of XMPC requires to have an accurate exergy model for HVAC system and exergy destruction model across the system components.

4. In the optimization framework, solving XMPC problem is computationally expensive due to nonlinearity of the objective function. However XMPC can still run real-time (time step of 1 hour) due to slow thermal dynamics of rooms.

In this dissertation, the same exergy-wise approach was used for control of ICEs. Exergy was introduced as an effective metric to control of steady-state and transient engine operations. Depending on the ICE applications, two different SLT efficiency maps were generated. The first SLT map was to maximize the output work, while the second SLT map aimed for maximizing Combined Power and Exhaust Exergy (CPEX). This method is applicable to efficient operation of CHP systems in buildings to provide required heat and electric power of commercial and residential buildings. The followings are the main findings of this dissertation:

1. Exergy destruction due to combustion is the main source of exergy loss in the ICE. Heat-transfer causes $12 \pm 3\%$ of the fuel exergy to be lost. By optimal control of combustion phasing, a portion of exergy loss/destruction can be prevented.

2. Based on the application, two optimization objectives including (i) maximum

$\eta_{II,W}$, and (ii) maximum $\eta_{II,CPEX}$ were defined for steady-state engine operation. The results show that on average, the proposed XCICE can reduce the fuel consumption by 6.7% when the output work is of interest. For cases in which CPEX is desired, such as CHP system, the proposed method can increase the desired output exergy by 8.3% on average.

3. Transient control of the ICE using predictive exergy-based approach can minimize exergy loss/destruction while meeting required IMEP. The simulation results showed up to 5% reduction in exergy loss/destruction by using the proposed transient control for the engine load sweep in this study.

By optimizing energy usage, smart buildings can provide occupants' comfort in a cost effective way, and ancillary service for power grids. For this purpose, this thesis develops a bidirectional B2G optimization framework using a building thermal model and a mathematical model for the distribution grid. The building model is based on heat transfer phenomena. The distribution grid model is comprised of modeling of typical distribution system components including feeders, transformers, and control equipment such as capacitor banks and transformer load tap changers. In the proposed bidirectional optimization model, the objective is to minimize energy cost for the demand side and to maximize load factor and load penetration for the grid side.

1. To account for conflicting interests of the BEMS and distribution operators in the bidirectional optimization, a novel B2G index was developed based on

building energy cost and nodal load factor.

2. Compared to the unoptimized rule-based control of the building loads, the proposed bilevel optimization framework can reduce commercial buildings' monthly electricity costs by 25% while increasing the system load factor by 17%.

3. The savings obtained in energy price and improvement on system load factor greatly depend on various factors including energy price, flexibility of commercial building loads, customers' preferences, available control equipment in a distribution grid, accuracy/availability of weather forecast and dynamic pricing prediction, etc.

6.2 Suggestions for Future Work

Despite the promising results of the proposed methodology presented in chapters of this dissertation, there is always room for improvement and expanding the study. Here is the list of some research areas worthy of further investigation:

1. The proposed exergy-based optimal control of ICE can be studied for other types of engines including SI, diesel, Premixed Charge Compression Ignition (PCCI) and Reactivity Controlled Compression Ignition (RCCI). In addition, modeling is a crucial part of model-based control. Thus, using detailed and

more accurate exergy models is anticipated to lead to more reliable advanced control methods for ICEs.

2. In this dissertation, effects of exergy-based control of ICE on noise and emission have not been investigated. Noise and emissions can be included in the optimization problem as constraints.

3. In Chapter 5, a framework for bilevel optimization was proposed. However, effect of ESS (e.g., TES, CAES and EES) and DG (e.g., Solar panels, and wind turbines) on the operation of B2G systems could be further studied.

4. Electrical energy is pure exergy. Therefore, all models used in the power generation and distribution grid sides are exergy models. A possible area of research could be integrating building's exergy model into distribution grid model (i.e., inherent exergy model). This procedure can define the optimum efficiency that can be obtained from a B2G exergy system.

5. Real-time implementation of exergy-based controllers on an engine test-cell and a building test-bed represents the next steps to realize the designed controllers from this PhD dissertation.

References

[1] M. Maasoumy, M. Razmara, M. Shahbakhti, and A. Sangiovanni Vincentelli. "Handling model uncertainty in model predictive control for energy efficient buildings". *Energy and Buildings*, 77, 2014.

[2] M. Razmara, M. Maasoumy, M. Shahbakhti, and R. D. Robinett III. "Optimal exergy control of building HVAC system". *Applied Energy*, 156:555–565, 2015.

[3] M. Razmara, M. Bidarvatan, M. Shahbakhti, and R. D. Robinett III. "Innovative Exergy-Based Combustion Phasing Control of IC Engines". SAE Paper 2016-01-0815, 2016.

[4] M. Razmara, M. Bidarvatan, M. Shahbakhti, and R.D. Robinett. "Novel Exergy-Wise Predictive Control of Internal Combustion Engines". In *American Control Conference (ACC)*, pages 1–6, 2016.

[5] M. Razmara, G. R. Bharati, M. Shahbakhti, S. Paudyal, and R. D. Robinett III.

"Bilevel Optimization Framework for Smart Building-to-Grid Systems". *IEEE Transactions on Smart Grid*, PP(99):1–12, 2016.

[6] M. Shahbakhti and C.R. Koch. "Characterizing the cyclic variability of ignition timing in a homogeneous charge compression ignition engine fuelled with n-heptane/iso-octane blend fuels". *International Journal of Engine Research*, 9(5):361–397, 2008.

[7] C.D. Rakopoulos and E.G. Giakoumis. "Second-law analyses applied to internal combustion engines operation". *Progress in Energy and Combustion Science*, 32(1):2–47, 2006.

[8] J.A. Caton. "A Review of Investigations Using the Second Law of Thermodynamics to Study Internal-Combustion Engines". SAE Paper 2000-01-1081, 2000.

[9] MISO. (Accesseed on Sep 3rd, 2014). "Midcontinent Independent System Operator".

[10] GB EPA. "Buildings and the Environment: A Statistical Summary Compiled by: US Environmental Protection Agency GB Workgroup". *Environmental Protection Agency Green Building, Washington, DC. Available at: www.epa.gov/greenbuilding/pubs/gbstats.pdf (accessed 22 May 2016)*, 2004.

[11] US DOE. "EIA. Emissions of Greenhouse Gases in the United States 2006". Technical report, DOE/EIA-0573, 2006.

[12] 2014) DOE. (Accessed on 10th Dec. "2011 building energy data book".

[13] Energy Efficiency & Renewable Energy DOE. "Building Technologies Office (BTO) Multi-Year Program Plan". Technical report, Available at: http://energy.gov/sites/prod/files/2016/02/f29/BTO%20Multi-Year%20Program%20Plan%20-%20Final.pdf, (Accessed on May 22nd, 2016), 2016.

[14] P.J. Boait, R.M. Rylatt, and A. Wright. "Exergy-based control of electricity demand and microgeneration". *Applied Energy*, 84(3):239–253, 2007.

[15] US Energy Information Administration. "US Energy Flow". Technical report, Available at: http://www.eia.gov/totalenergy/data/monthly/pdf/flow/total_energy.pdf (accessed 17 July 2015), 2014.

[16] United States Environmental Protection Agency (EPA). "Inventory of US greenhouse gas emissions and sinks: 1990-2009". Technical report, 2011.

[17] D. Mendoza, K.R. Gurney, I. Razlivanov, S. Geethakumar, V. Chandrasekaran, and Y. Zhou. "US Onroad Transportation CO2 Emissions Analysis Comparing Highly-Resolved CO2 Emissions and a National Average Approach: Mitigation Options and Uncertainty Reductions". In *AGU Fall Meeting*, volume 1, 2011.

[18] U.S. Environmental Protection Agency(EPA). "EPA and NHTSA Propose to Extend the National Program to Reduce Greenhouse Gases and Improve Fuel Economy for Cars and Trucks". *U.S. Environmental Protection Agency,*

Washington, D.C.; Available at: ***http://www.epa.gov/otaq/climate/documents/420f11038.pdf*** *(accessed 22 May 2016)*, 2011.

[19] T.F. Stocker. *"Climate change 2013: the physical science basis: Working Group I contribution to the Fifth assessment report of the Intergovernmental Panel on Climate Change"*. Cambridge University Press, 2014.

[20] Global Anthropogenic Non-CO2 Greenhouse Gas Emissions: 1990 - 2030. " *http://www.epa.gov/climatechange/Downloads/EPAactivities*". 2012.

[21] P. Piagi and R.H. Lasseter. "Autonomous Control of Microgrids". In *PES GM*, pages 8–pp. IEEE, 2006.

[22] ASHRAE Standard. 90.1. *"American Society of Heating, Refrigerating, and Air-Conditioning Engineers"*, 1989.

[23] M. Maasoumy and A. Sangiovanni-Vincentelli. "Total and Peak Energy Consumption Minimization of Building HVAC Systems Using Model Predictive Control". *IEEE Design and Test of Computers*, 2012.

[24] F. Oldewurtel, C.N. Jones, and M. Morari. "A Tractable Approximation of Chance Constrained Stochastic MPC Based on Affine Disturbance Feedback". In 47^{th} *IEEE Conference on Decision and Control (CDC)*, pp. 4731-4736, 2008.

[25] Y. Ma, F. Borrelli, B. Hencey, A.w Packard, and S. Bortoff. "Model predictive control of thermal energy storage in building cooling systems". In *Joint* 48^{th}

IEEE Conference on Decision and Control and 28th Chinese Control Conference, Shanghai, P.R. China, 2009.

[26] Y. Ma, F. Borrelli, B. Hencey, B. Coffey, S. Bengea, and P. Haves. "Model predictive control for the operation of building cooling systems". In *IEEE Transactions on Control Systems Technology*, vol. 20, no. 3, pp. 796-803, 2012.

[27] F. Oldewurtel, A. Parisio, C.N. Jones, M. Morari, D. Gyalistras, M. Gwerder, V. Stauch, B. Lehmann, and K. Wirth. "Energy Efficient Building Climate Control Using Stochastic Model Predictive Control and Weather Predictions". In *American Control Conference (ACC)*, pp. 5100-5105, 2010.

[28] S. Privara, J. Cigler, Z. Váňa, F. Oldewurtel, C. Sagerschnig, and E. Žáčeková. "Building modeling as a crucial part for building predictive control". *Energy and Buildings*, 56:8–22, 2013.

[29] M. Maasoumy. "Modeling and Optimal Control Algorithm Design for HVAC Systems in Energy Efficient Buildings". MS Thesis, Dept. Mechanical Engineering, University of California at Berkeley, 2011.

[30] X. Xu, S. Wang, and G. Huang. "Robust MPC for temperature control of air-conditioning systems concerning on constraints and multitype uncertainties". *Building Services Engineering Research and Technology*, 31(1):39–55, 2010.

[31] J. Širokỳ, F. Oldewurtel, J. Cigler, and S. Prívara. "Experimental analysis

of model predictive control for an energy efficient building heating system". *Applied Energy*, 88(9), 2011.

[32] J. Ma, S.J. Qin, B. Li, and T. Salsbury. "Economic Model Predictive Control for Building Energy Systems". In *Innovative Smart Grid Technologies (ISGT)*, Los Angeles, CA, 2011.

[33] P. D. Moroşan, R. Bourdais, D. Dumur, and J. Buisson. "Building temperature regulation using a distributed model predictive control". *Energy and Buildings*, 42(9):1445–1452, 2010.

[34] D. Bertsimas and M. Sim. "Tractable Approximations to Robust Conic Optimization Problems". *Mathematical Programming*, vol. 107, no. 1-2, pp. 5-36, 2006.

[35] Y. Ma, G. Anderson, and F. Borrelli. "A Distributed Predictive Control Approach to Building Temperature Regulation". In *American Control Conference (ACC)*, pages 2089–2094, 2011.

[36] M. Maasoumy and A. Sangiovanni-Vincentelli. "Optimal Control of HVAC Systems in the Presence of Imperfect Predictions". In *ASME, Dynamic System Control Conference (DSCC)*, 2012.

[37] J. Cigler, S. Prívara, Z. Váňa, E. Žáčeková, and L. Ferkl. "Optimization of predicted mean vote index within model predictive control framework: Computationally tractable solution". *Energy and Buildings*, vol. 52, pp. 39-49, 2012.

[38] S. Cheng, Y. Chen, C. HK Chan, T. Lee, H. L. Chan, J. Qin, Q. Zhou, A. Cheung, and K. Yu. "A Robust Control Strategy for VAV AHU Systems and Its Application". In *Frontiers in Computer Education*. pp. 635-642, 2012.

[39] G. Huang and F. Jordán. "Model-Based Robust Temperature Control for VAV Air-Conditioning System". *HVAC&R Research, Taylor & Francis*, vol. 18, no. 3, pp. 432-445, 2012.

[40] H. Moradi, F. Bakhtiari-Nejad, and M. Saffar-Avval. "Multivariable robust control of an air-handling unit: A comparison between pole-placement and H_∞ controllers. *Energy Conversion and Management*, vol. 55, pp. 136-148, 2012.

[41] H. Moradi, M. Saffar-Avval, and A. Alasty. "Nonlinear dynamics, bifurcation and performance analysis of an air-handling unit: Disturbance rejection via feedback linearization". *Energy and Buildings*, 2012.

[42] Maasoumy, M. and Pinto, A. and Sangiovanni-Vincentelli, A. "Model-Based Hierarchical Optimal Control Design For HVAC Systems". In *ASME Dynamic Systems and Control Conference (DSCC)*, pages 271–278, 2011.

[43] C. Agbi, Z. Song, and B. Krogh. "Parameter Identifiability for Multi-Zone Building Models". In *IEEE,* 51^{st} *Annual Conference on Decision and Control (CDC)*, pp. 6951-6956, 2012.

[44] K. Deng, P. Barooah, P.G. Mehta, and S.P. Meyn. "Building thermal model

reduction via aggregation of states". In *American Control Conference (ACC)*, pp. 5118-5123, 2010.

[45] G.L. Plett. "Sigma-point Kalman filtering for battery management systems of LiPB-based HEV battery packs: Part 2: Simultaneous state and parameter estimation". In *Journal of Power Sources*, vol. 161, no. 2, pp. 1369-1384, 2006.

[46] H. Moradkhani, S. Sorooshian, H.V. Gupta, and P.R. Houser. "Dual state-parameter estimation of hydrological models using ensemble Kalman filter". In *Advances in Water Resources*, vol. 28, no. 2, pp. 135-147, 2005.

[47] M. Rafiee, A. Tinka, J. Thai, and A.M. Bayen. "Combined state-parameter estimation for shallow water equations". In *American Control Conference (ACC)*, pp. 1333-1339, San Francisco, CA, 2011.

[48] P. May-Ostendorp, G.P. Henze, C.D. Corbin, B. Rajagopalan, and C. Felsmann. "Model-predictive control of mixed-mode buildings with rule extraction". *Building and Environment*, vol. 46, no. 2, pp. 428-437, 2011.

[49] D.B. Crawley, J.W. Hand, M. Kummert, and B.T. Griffith. "Contrasting the capabilities of building energy performance simulation programs". *Building and Environment*, vol. 43, no. 4, pp. 661-673, 2008.

[50] F. Oldewurtel, A. Parisio, C.N. Jones, D. Gyalistras, M. Gwerder, V. Stauch, B. Lehmann, and M. Morari. "Use of model predictive control and weather

forecasts for energy efficient building climate control". *Energy and Buildings*, vol. 45, pp. 15-27, 2012.

[51] Y. Agarwal, B. Balaji, R. Gupta, J. Lyles, M. Wei, and T. Weng. "Occupancy-Driven Energy Management for Smart Building Automation". In *Proceedings of the 2nd ACM Workshop on Embedded Sensing Systems for Energy-Efficiency in Building*, pp. 1-6, 2010.

[52] B. Dong and B. Andrews. "Sensor-Based Occupancy Behavioral Pattern Recognition for Energy and Comfort Management in Intelligent Buildings". In *Proc. of International Building Performance Simulation Association (IBPSA) Conference*, 2009.

[53] M. Maasoumy, Q. Zhu, C. Li, F. Meggers, and A. Sangiovanni-Vincentelli. "Co-Design of Control Algorithm and Embedded Platform for HVAC Systems". In *The 4th ACM/IEEE International Conference on Cyber-Physical Systems (ICCPS)*, 2013.

[54] F. P. Incropera, A. S. Lavine, and D.P. DeWitt. *"Fundamentals of heat and mass transfer"*. John Wiley & Sons Incorporated, 2011.

[55] M. Maasoumy. "Controlling Energy-Efficient Buildings in the Context of Smart Grid: A Cyber Physical System Approach". Number UCB/EECS-2013-244, Dec 2013.

[56] C.C. Federspiel. "Estimating the inputs of gas transport processes in buildings".

IEEE Transactions on Control Systems Technology, vol. 5, no. 5, pp. 480-489, 1997.

[57] M.A. Goforth, G.W. Gilcrest, and J.D. Sirianni. "Cloud Effect on Thermal Downwelling Sky Radiance". *Proc. SPIE, Society of Photo-Optical Instrumentation Engineers*, vol. 4710, no. 1, pp. 203-213, 2002.

[58] "National Renewable Energy Laboratory (NREL)"`http://www.nrel.gov/`. 2013.

[59] S.J. Julier and J.K. Uhlmann. "New Extension of the Kalman Filter to Nonlinear Systems". In *International Society for Optics and Photonics, AeroSense'97*, pp. 182-193, 1997.

[60] S.J. Julier, J.K. Uhlmann, and H.F. Durrant-Whyte. "A New Approach for Filtering Nonlinear Systems". In *American Control Conference (ACC)*, vol. 3, pp. 1628-1632, 1995.

[61] M. Maasoumy, B. Moridian, M. Razmara, M. Shahbakhti, and A. Sangiovanni-Vincentelli. "Online Simultaneous State Estimation and Parameter Adaptation for Building Predictive Control". In *ASME Dynamic System and Control Conference (DSCC)*, 2013.

[62] ASHRAE Standard. "Standard 55-2004". *Thermal Environmental Conditions for Human Occupancy*, 2004.

[63] R. de Dear and G. S. Brager. "Thermal comfort in naturally ventilated buildings: revisions to ASHRAE Standard 55 ". *Energy and Buildings*, vol. 34, no. 6, pp. 549 - 561, 2002.

[64] R. de Dear and G. S. Brager. "The adaptive model of thermal comfort and energy conservation in the built environment". *International Journal of Biometeorology*, vol. 45, no. 2, pp. 100-108, 2001.

[65] V. Bradshaw. *"The building environment: Active and passive control systems"*. `www.Wiley.com`, 2010.

[66] ASHRAE. "Standard 62.1-2004". *Ventilation for Acceptable Indoor Air Quality*, 2004.

[67] J. Löfberg. "YALMIP : A toolbox for modeling and optimization in MATLAB". In *Proceedings of the CACSD Conference, http://users.isy.liu.se/johanl/yalmip*, Taipei, Taiwan, 2004.

[68] J. Löfberg. "Minimax approaches to robust model predictive control". *Department of Electrical Engineering LinkÂĺoping University*, 2003.

[69] ILOG CPLEX. "High-Performance Software for Mathematical Programming and Optimization", 2005.

[70] D. Gyalistras and M. Gwerder. "Use of weather and occupancy forecasts for optimal building climate control (OptiControl): Two years progress report". In

Terrestrial Systems Ecology ETH Zurich, Switzerland and Building Technologies Division, Siemens Switzerland Ltd, 2010.

[71] R.D. Robinett III and D.G. Wilson. *"Nonlinear Power Flow Control Design: Utilizing Exergy, Entropy, Static and Dynamic Stability, and Lyapunov Analysis"*. Springer, 2011.

[72] I. Dincer and M.A. Rosen. *"Exergy: energy, environment and sustainable development"*. 2^{nd} Edition, Elsevier Science, 2012.

[73] I. Dincer and Y.A. Cengel. "Energy, Entropy and Exergy Concepts and Their Roles in Thermal Engineering". *Entropy*, 3(3):116–149, 2001.

[74] M.T. Balta, I. Dincer, and A. Hepbasli. "Performance and sustainability assessment of energy options for building HVAC applications". *Energy and Buildings*, 42(8):1320–1328, 2010.

[75] P. Sakulpipatsin, L.C.M. Itard, H.J. Van Der Kooi, E.C. Boelman, and P.G. Luscuere. "An exergy application for analysis of buildings and HVAC systems". *Energy and Buildings*, 42(1):90–99, 2010.

[76] A. Yildiz and A. Güngör. "Energy and exergy analyses of space heating in buildings". *Applied Energy*, 86(10):1939–1948, 2009.

[77] A. Schlueter and F. Thesseling. "Building information model based energy/exergy performance assessment in early design stages". *Automation in Construction*, 18(2):153–163, 2009.

[78] C. Tahsin Yucer and A. Hepbasli. "Thermodynamic analysis of a building using exergy analysis method". *Energy and Buildings*, 43(2):536–542, 2011.

[79] M. Guadalupe Alpuche, C. Heard, R. Best, and J. Rojas. "Exergy analysis of air cooling systems in buildings in hot humid climates". *J. Applied Thermal Engineering*, 25(4):507–517, 2005.

[80] R. Chengqin, L. Nianping, and T. Guangfa. "Principles of exergy analysis in HVAC and evaluation of evaporative cooling schemes". *Building and environment*, 37(11):1045–1055, 2002.

[81] L. Ozgener, A. Hepbasli, and I. Dincer. "Energy and exergy analysis of geothermal district heating systems: an application". *Building and Environment*, 40(10):1309–1322, 2005.

[82] Z. Wei and R. Zmeureanu. "Exergy analysis of variable air volume systems for an office building". *Energy Conversion and Management*, 50(2):387–392, 2009.

[83] M. Tolga Balta, Y. Kalinci, and A. Hepbasli. "Evaluating a low exergy heating system from the power plant through the heat pump to the building envelope". *Energy and Buildings*, 40(10):1799–1804, 2008.

[84] F. Meggers, V. Ritter, P. Goffin, M. Baetschmann, and H. Leibundgut. "Low exergy building systems implementation". *Energy*, 41(1):48–55, 2012.

[85] H. Asada and E.C. Boelman. "Exergy analysis of a low temperature radiant heating system". *Building Services Engineering Research and Technology*, 25(3):197–209, 2004.

[86] D. Schmidt. "Low exergy systems for high-performance buildings and communities". *Energy and Buildings*, 41(3):331–336, 2009.

[87] D. Schmidt and M. Ala-Juusela. "Low exergy systems for heating and cooling of buildings". In *Proceedings of the* 21^{st} *conference on Passive and Low Energy Architecture, Eindhoven, The Netherlands*, pages 19–22, 2004.

[88] B.I. Kilkis. "From Floor Heating to Hybrid HVAC Panel: A Trail of Exergy-Efficient Innovations". *ASHRAE transactions*, pages 343–349, 2006.

[89] S.C. Bengea, A.D. Kelman, F. Borrelli, R. Taylor, and S. Narayanan. "Implementation of model predictive control for an HVAC system in a mid-size commercial building". *HVAC&R Research*, 20(1):121–135, 2014.

[90] E. Žáčeková, Z. Váňa, and J. Cigler. "Towards the real-life implementation of MPC for an office building: Identification issues". *Applied Energy*, 135:53–62, 2014.

[91] N. Jain. "Thermodynamics-Based Optimization and Control of Integrated Energy Systems". In *PhD Thesis, University of Illinois at Urbana-Champaign*, 2013.

[92] N. Jain and A.G. Alleyne. "A framework for the optimization of integrated energy systems". *Applied Thermal Engineering*, 48:495–505, 2012.

[93] H. Torio, A. Angelotti, and D. Schmidt. "Exergy analysis of renewable energy-based climatisation systems for buildings: a critical view". *Energy and Buildings*, 41(3):248–271, 2009.

[94] H. Caliskan, I. Dincer, and A. Hepbasli. "Energy and exergy analyses of combined thermochemical and sensible thermal energy storage systems for building heating applications". *Energy and Buildings*, 48:103–111, 2012.

[95] K. Hacatoglu, I. Dincer, and M.A. Rosen. "Exergy Analysis of a Hybrid Solar–Wind–Biomass System with Thermal and Electrical Energy Storage for a Community". In *Progress in Exergy, Energy, and the Environment*, pages 3–14. Springer, 2014.

[96] A. Koca, H.F. Oztop, T. Koyun, and Y. Varol. "Energy and exergy analysis of a latent heat storage system with phase change material for a solar collector". *Renewable Energy*, 33(4):567–574, 2008.

[97] P. Sakulpipatsin, E. Boelman, and D. Schmidt. "Exergy analysis applied to building design". In 7^{th} *Nordic Symposium on Building Physics*. Citeseer, 2005.

[98] M. Bruelisauer, K.W. Chen, R. Iyengar, H. Leibundgut, C. Li, M. Li, M. Mast, F. Meggers, C. Miller, D. Rossi, et al. "BubbleZERODesign, Construction and Operation of a Transportable Research Laboratory for Low Exergy Building System Evaluation in the Tropics". *Energies*, 6(9):4551–4571, 2013.

[99] W. Wang, H. Rivard, and R. Zmeureanu. "Floor shape optimization for green building design". *Advanced Engineering Informatics*, 20(4):363–378, 2006.

[100] B.I. Kilkis and S. Kilkis. "Exergetic Optimization of Generated Electric Power Split in a Heat Pump Coupled Poly-Generation System". In *Energy Sustainability Conference*, pages 211–218, 2007.

[101] B.I. Kilkis. "An exergy aware optimization and control algorithm for sustainable buildings". *International journal of green energy*, 1(1):65–77, 2004.

[102] N. Jain and A. Alleyne. "Exergy-based optimal control of a vapor compression system". *Energy Conversion and Management*, 92:353–365, 2015.

[103] M. Razmara, M. Maasoumy, M. Shahbakhti, and R. D. Robinett III. "Exergy-based Model Predictive Control for Building HVAC systems". In *American Control Conference (ACC)*, 2015.

[104] F.C. McQuiston, J.D. Parker, and J.D. Spitler. *"Heating, Ventilating, and Air Conditioning: Analysis and Design"*. Wiley, 6th Edition, 2010.

[105] R. Lowe. "Combined heat and power considered as a virtual steam cycle heat pump". *Energy Policy*, 39(9):5528–5534, 2011.

[106] M. Maasoumy, M. Razmara, M. Shahbakhti, and A. Sangiovanni-Vincentelli. "Selecting Building Predictive Control Based on Model Uncertainty". In *American Control Conference (ACC)*, 2014.

[107] F. Meggers and H. Leibundgut. "The reference environment: utilising exergy and anergy for buildings". *Exergy*, 11(4):423–438, 2012.

[108] Y.A. Cengel, M.A. Boles, and M. Kanoğlu. *"Thermodynamics: an Engineering Approach"*. 8^{th} Edition, Chapter 8, McGraw-Hill, New York, 2015.

[109] J. Lofberg. "YALMIP: A toolbox for modeling and optimization in MATLAB". In *IEEE International Symposium on Computer Aided Control Systems Design*, pages 284–289, 2004.

[110] K.D. Edwards, R.M. Wagner, T.E. Briggs, and T.J. Theiss. "Defining Engine Efficiency Limits". In 17^{th} *DEER Conference, Detroit, MI, October*, pages 3–6, 2011.

[111] M. Djermouni and A. Ouadha. "Thermodynamic analysis of an HCCI engine based system running on natural gas". *Energy Conversion and Management*, 88:723–731, 2014.

[112] S. Saxena, N. Shah, I. Bedoya, and A. Phadke. "Understanding optimal engine

operating strategies for gasoline-fueled HCCI engines using crank-angle resolved exergy analysis". *Applied Energy*, 114:155–163, 2014.

[113] S. Jafarmadar, P. Nemati, and R. Khodaie. "Multidimensional modeling of the effect of Exhaust Gas Recirculation (EGR) on exergy terms in an HCCI engine fueled with a mixture of natural gas and diesel". *Energy Conversion and Management*, 105:498–508, 2015.

[114] I. Sezer and A. Bilgin. "Exergy analysis of SI engines". *International Journal of Exergy*, 5(2):204–217, 2008.

[115] I. Sezer and A. Bilgin. "Effects of Charge Properties on Exergy Balance in Spark Ignition Engines". *Fuel*, 112:523–530, 2013.

[116] R. Ghahfarokhi Fatehi, S. Khalilarya, and R. Ebrahimi. "Energy and exergy analyses of homogeneous charge compressin ignition (HCCI) engine". *Thermal Science*, 17(1):107–117, 2013.

[117] J.A. Caton. "On the destruction of availability (exergy) due to combustion processesâĂŤwith specific application to internal-combustion engines". *Energy*, 25(11):1097–1117, 2000.

[118] T. Endo, S. Kawajiri, Y. Kojima, K. Takahashi, T. Baba, S. Ibaraki, T. Takahashi, and M. Shinohara. "Study on Maximizing Eexergy in Automotive Engines". SAE Paper 2007-01-0257, 2007.

[119] A.K. Amjad, R. Khoshbakhti Saray, S.M.S. Mahmoudi, and A. Rahimi. "Availability analysis of n-heptane and natural gas blends combustion in HCCI engines". volume 36, pages 6900–6909, 2011.

[120] Daniel P Madison. *"Thermal Characterization of a Gasoline Turbocharged Direct Imjection (GTDI) Engine Utilization Lean Operation and Exhaust Gas Recirculation (EGR)"*. PhD thesis, 2013.

[121] F. Yan and W. Su. "A Promising High Efficiency RM-HCCI Combustion Proposed by Detail Kinetics Analysis of Exergy Losses". SAE Paper 2015-01-1751, 2015.

[122] F. Yan and W. Su. "Numerical Study on Exergy Losses of n-Heptane Constant-Volume Combustion by Detailed Chemical Kinetics". *Energy & Fuels*, 28(10):6635–6643, 2014.

[123] C. Zhang, G. Shu, H. Tian, H. Wei, G. Yu, and Y. Liang. "Theoretical Analysis of a Combined Thermoelectric Generator (TEG) and Dual-loop Organic Rankine Cycle (DORC) System Using for Engines' Exhaust Waste Heat Recovery". SAE Paper 2014-01-0670, 2014.

[124] M. Ghazikhani, M. Hatami, D. Domiri Ganji, M. Gorji-Bandpy, A. Behravan, and G. Shahi. "Exergy recovery from the exhaust cooling in a DI diesel engine for BSFC reduction purposes". *Energy*, 65:44–51, 2014.

[125] Songsong Song, Hongguang Zhang, Zongyong Lou, Fubin Yang, Kai Yang,

Hongjin Wang, Chen Bei, Ying Chang, and Baofeng Yao. "Performance analysis of exhaust waste heat recovery system for stationary CNG engine based on organic Rankine cycle". *Applied Thermal Engineering*, 76:301–309, 2015.

[126] M. Shahbakhti. *"Modeling and Experimental Study of an HCCI Engine for Combustion Timing Control"*. PhD thesis, Department of Mechanical Engineering, University of Alberta, 2009.

[127] M. Shahbakhti, R. Lupul, and C. R. Koch. "Sensitivity analysis and modeling of HCCI auto-ignition timing". In *Advances in Automotive Control*, volume 5, pages 303–310, 2007.

[128] M. Bidarvatan, M. Shahbakhti, S.A. Jazayeri, and C.R. Koch. "Cycle-to-cycle modeling and sliding mode control of blended fuel HCCI engine". *Control Engineering Practice*, 24:79–91, 2014.

[129] M. Bidarvatan, M. Shahbakhti, and S.A. Jazayeri. "Model-based Control of Combustion Phasing in an HCCI Engine". *SAE International Journal of Engines*, 5(3):1163–1176, 2012.

[130] S. Saxena, J.-Y. Chen, and R. Dibble. "Maximizing Power Output in an Automotive Scale Multi-Cylinder Homogeneous Charge Compression Ignition (HCCI) Engine". SAE Paper 2011-01-0907, 2011.

[131] G.M. Shaver, J.C. Gerdes, and M.J. Roelle. "Physics-based modeling and control of residual-affected HCCI engines". *Journal of Dynamic Systems, Measurement, and Control*, 131(2), 2009.

[132] J. Bengtsson, P. Strandh, R. Johansson, P. Tunestål, and B. Johansson. "Hybrid control of homogeneous charge compression ignition (HCCI) engine dynamics". *International Journal of Control*, 79(05):422–448, 2006.

[133] A. Burcat. "Thermochemical data for combustion calculations". In *Combustion Chemistry*, pages 455–473. Springer, 1984.

[134] J.B. Heywood. "Internal Combustion Engine Fundamentals". Chapter 5, McGraw-Hill New York, 1998.

[135] J. A. Caton. "Exergy destruction during the combustion process as functions of operating and design parameters for a spark-ignition engine". *International Journal of Energy Research*, 36(3):368–384, 2012.

[136] J. Chang, O. Güralp, Z. Filipi, D.N. Assanis, T.W. Kuo, P. Najt, and R. Rask. "New Heat Transfer Correlation for an HCCI Engine Derived from Measurements of Instantaneous Surface Heat Flux". SAE Paper 2004-01-2996, 2004.

[137] R. A. W. Lupul. "Steady State and Transient Characterization of a HCCI Engine with Varying Octane Fuel". Master's thesis, Department of Mechanical Engineering, University of Alberta, 2008.

[138] M.J. Moran. *"Availability analysis: a guide to efficient energy use"*. New Jersey: Prentice-Hall Inc., Oxford, 1982.

[139] M. Bidarvatan and M. Shahbakhti. "Two-input two-output control of blended fuel HCCI engines". SAE Paper 2013-01-1663, 2013.

[140] M. Shahbakhti and C.R. Koch. "Physics Based Control Oriented Model for HCCI Combustion Timing". *Journal of Dynamic Systems, Measurement, and Control*, 132(2), 2010.

[141] Wikipedia: The Free Encyclopedia. "Thermoelectric Generator", available from: *https://en.wikipedia.org/wiki/thermoelectric_generator*, retrieved, 10 october, 2015.

[142] C.W. Chan, J. Ling-Chin, and A.P. Roskilly. "A review of chemical heat pumps, thermodynamic cycles and thermal energy storage technologies for low grade heat utilisation". *Applied Thermal Engineering*, 50(1):1257–1273, 2013.

[143] J. Ma, S. J. Qin, B. Li, and T. Salsbury. "Economic Model Predictive Control for Building Energy Systems". In *Proceeding IEEE PES Innovative Smart Grid Technologies*, 2011.

[144] M. Pcolka, E. Zacekova, R. Robinett, S. Celikovsky, and M. Sebek. "Economical Nonlinear Model Predictive Control for Building Climate Control". In *Proceeding of American Control Conference (ACC)*, 2014.

[145] A. Brooks, E. Lu, D. Reicher, C. Spirakis, and B. Weihl. "Demand dispatch". *Power and Energy Magazine*, 8(3):20–29, 2010.

[146] M. C. Bozchalui, S. A. Hashmi, H. Hassen, C. A. Cañizares, and K. Bhattacharya. "Optimal Operation of Residential Energy Hubs in Smart Grids". *IEEE Transactions on Smart Grid*, 3(4):1755–1766, 2012.

[147] Shengnan Shao, M. Pipattanasomporn, and S. Rahman. "Demand Response as a Load Shaping Tool in an Intelligent Grid With Electric Vehicles". *IEEE Transactions on Smart Grid*, 2(4):624–631, Dec. 2011.

[148] J. Taylor, A. Maitra, M. Alexander, D. Brooks, and M. Duvall. "Evaluations of Plug-in Electric Vehicle Distribution System Impacts". In *Proc. IEEE Power and Energy Society General Meeting*, 2010.

[149] S. Paudyal, C. A. Cañizares, and K. Bhattacharya. "Optimal Operation of Distribution Feeders in Smart Grids". *IEEE Transactions on Industrial Electronics*, 58(10):4495–4503, Oct. 2011.

[150] S. K. Goswami and S. K. Basu. "A New Algorithm for the Reconfiguration of Distribution Feeders for Loss Minimization". *IEEE Transactions on Power Delivery*, 7(3):1484–1491, Jul. 1992.

[151] Y. Deng, X. Ren, C. Zhao, and D. Zhao. "A Heuristic and Algorithmic Combined Approach for Reactive Power Optimization with Time-Varying Load

Demand in Distribution Systems". *IEEE Transactions on Power Systems*, 17(4):1068–1072, Oct. 2002.

[152] I. Roytelman, B. K. Wee, and R. L. Lugtu. "Volt/var control algorithm for modern distribution management system". *IEEE Transactions Power Systems*, 10(3):1454–1460, 1995.

[153] E. Dall'Anese, H. Zhu, and G. Giannakis. "Distributed Optimal power flow for smart microgrids". *IEEE Transactions on Smart Grid*, 4(3):1464–1475, 2013.

[154] M.B. Liu, C.A. Cañizares, and W. Huang. "Reactive Power and Voltage Control in Distribution Systems With Limited Switching Operations". *IEEE Transactions Power Syst.*, 24(2):889–899, 2009.

[155] M. Avci, M. Erkoc, and S. S. Asfour. "Residential HVAC load control strategy in real-time electricity pricing environment". In *Proc. Energytech*, May 2012.

[156] D. T. Nguyen and Long Bao Le. "Joint Optimization of Electric Vehicle and Home Energy Scheduling Considering User Comfort Preference". *IEEE Transactions on Smart Grid*, 5(1):188–199, Jan. 2014.

[157] Y. Yan, J. Zhou, Y. Lin, W. Yang, P. Wang, and G. Zhang. "Adaptive optimal control model for building cooling and heating sources". *J. Energy and Buildings*, 40(8):1394–1401, 2008.

[158] M. Maasoumy, A. Pinto, and A. Sangiovanni-Vincentelli. "Model-based Hierarchical Optimal Control Design for HVAC Systems". In *ASME Dynamic Systems and Control Conference (DSCC)*, pages 271–278, 2011.

[159] G. Huang, S. Wang, and X. Xu. "A robust model predictive control strategy for improving the control performance of air-conditioning systems". *J. Energy Conversion and Management*, 50(10):2650–2658, 2009.

[160] Y. Ma, S. Vichik, and F. Borrelli. "Fast Stochastic MPC with Optimal Risk Allocation Applied to Building Control Systems". In *IEEE 51st Annual Conference on Decision and Control*, pages 7559–7564, Dec. 2012.

[161] M. Maasoumy and A. Sangiovanni-Vincentelli. "Buildings to Grid Integration: A Dynamic Contract Approach". In *Proc. IEEE/ACM International Conference on Computer-Aided Design*, pages 473–478, 2015.

[162] T. Gamauf, T. Leber, K. Pollhammer, and F. Kupzog. "A Generalized Load Management Gateway Coupling Smart Buildings to the Grid". In *Proc. AFRICON Conf.*, 2011.

[163] P. Palensky and D. Dietrich. "Demand Side Management: Demand Response, Intelligent Energy Systems, and Smart Loads". *IEEE Transactions on Industrial Informatics*, 7(3):381–388, Aug. 2011.

[164] X. Xue and W. Shengwei. "Interactive Building Load Management for Smart

Grid". In *Proceeding of IEEE Power Engineering and Automation Conference*, pages 1–5, 2012.

[165] A. Saha, M. Kuzlu, W. Khamphanchai, M. Pipattanasomporn, S. Rahman, O. Elma, U. S. Selamogullari, M. Uzunoglu, and B. Yagcitekin. "A Home Energy Management Algorithm in a Smart House Integrated with Renewable Energy". In *Proceeding of IEEE Innovative Smart Grid Technologies Conference Europe*, pages 1–6, 2014.

[166] B. Jin, P. Nuzzo, M. Maasoumy, Y. Zhou, and A. Sangiovanni-Vincentelli. "A Contract-based Framework for Integrated Demand Response Management in Smart Grids". In *Proc. 2nd ACM International Conference on Embedded Systems for Energy-Efficient Built Environments*, pages 167–176, 2015.

[167] J. Hagerman, G. Hernandez, A. Nicholls, and N. Foster. "Buildings-to-Grid Technical Opportunities: Introduction and Vision". Technical report, US Department of Energy, Energy Efficient and Renewable Energy (EERE), 2014.

[168] S. Bera, S. Misra, and J.J.P.C. Rodrigues. "Cloud Computing Applications for Smart Grid: A Survey". *IEEE Transactions Parallel Distribution Systems*, 26(5):1477–1494, May 2015.

[169] "VOLTTRON: An Intelligent Agent Platform for the Smart Grid". Pacific Northwest National Laboratory (PNNL).

[170] W. Khamphanchai, A. Saha, K. Rathinavel, M. Kuzlu, M. Pipattanasomporn,

S. Rahman, B. Akyol, and J. Haack. "Conceptual architecture of building energy management open source software (BEMOSS)". In *Innovative Smart Grid Technologies Conference Europe*, pages 1–6, 2014.

[171] G. Ghatikar and R. Bienert. "Smart grid standards and systems interoperability: a precedent with OpenADR". In *Grid Interop Forum*, 2011.

[172] M. Razmara, G. Bharati, M. Shahbakhti, S. Paudyal, and R. D. Robinett III. "Bidirectional Optimal Operation of Smart Building-to-Grid Systems". In *American Control Conference (ACC)*, pages 288–293, 2015.

[173] W. H. Kersting. *"Distribution System Modeling and Analysis"*. Chapters 3-6, Boca Raton, FL: CRC press, 2012.

[174] E. Sortomme, M. M. Hindi, S. D. J. MacPherson, and S. S. Venkata. "Coordinated Charging of Plug-In Hybrid Electric Vehicles to Minimize Distribution System Losses". *IEEE Transactions on Smart Grid*, 2(1):198–205, Mar. 2011.

[175] R. F. Chang and C. N. Lu. "Feeder reconfiguration for load factor improvement". In *Proc. Power Engineering Society Winter Meeting*, volume 2, pages 980–984, 2002.

[176] A. Bokhari, A. Alkan, R. Dogan, M. Diaz-Aguilo, F. de Leon, D. Czarkowski, Z. Zabar, L. Birenbaum, A. Noel, and R.E. Uosef. "Experimental Determination of the ZIP Coefficients for Modern Residential, Commercial, and Industrial Loads". *IEEE Transactions Power Delivery*, 29(3):1372–1381, Jun. 2014.

[177] GAMS Development Corporation. (Accessed on Dec 10th, 2014). "General Algebric Modeling System, Release 24.2.1".

[178] S. Paudyal, C.A. Cañizares, and K. Bhattacharya. "Three-phase Distribution OPF in Smart Grids: Optimality versus Computational Burden". In *Proc. Innovative Smart Grid Technologies Europe*, pages 1–7, Dec. 2011.

[179] S.H. Low. "Convex Relaxation of Optimal Power Flow –Part I: Formulations and Equivalence". *IEEE Transactions on Control of Network Systems*, 1(1):15–27, Mar. 2014.

[180] T. Kuruganti and M. Brambley. "Building-to-Grid Technical Opportunity: From the Information and Communications Technology Perspective". *DOE Energy Efficiency & Renewable Energy, Accessed on Feb 18, 2016.*

[181] Ameren. "Power Smart Pricing; A Smart Electricity Rate From Ameren Illinois" (Accessed on May 3rd, 2016).

[182] The COMED Residential Real-time Pricing Program Guide. "*Commonwealth Edison (ComEd)".*

[183] Z. Wang. "Compensation Methods for Demand Response". Master's thesis, University of Kentucky, 2015.

[184] Ruoyang Li, Qiuwei Wu, and S.S. Oren. "Distribution Locational Marginal Pricing for Optimal Electric Vehicle Charging Management". *IEEE Transactions on Power Systems*, 29(1):203–211, Jan. 2014.

[185] E.A. Wan and R. Van Der Merwe. "The Unscented Kalman Filter. *kalman filtering and neural networks*". pp. 221-280, 2001.

[186] M. Razmara, M. Bidarvatan, M. Shahbakhti, and R. D. Robinett III. "Optimal exergy-based contol of internal combustion engines". *Applied Energy*, Submitted, 2016.

[187] G. R. Bharati, M. Razmara, S. Paudyal, M. Shahbakhti, and R. D. Robinett III. "Hierarchical Framework for Demand Dispatch in Building-Grid Systems". In *PES GM*, pages 1–6. IEEE, 2016.

[188] J. Dobbs, M. Razmara, M. Shahbakhti, and S. Paudyal. "Selecting Control Input Type for a Building Predictive Controller Integrated in a Power Grid". In *American Control Conference (ACC)*, 2014.

Appendix A

Unscented Kalman Filter

To perform UKF, we conduct the following initialization:

$$\hat{x}_0 = \mathbb{E}[x_0] \tag{A.1}$$

$$P_0 = \mathbb{E}[(x_0 - \hat{x}_0)(x_0 - \hat{x}_0)^T] \tag{A.2}$$

Each step of the UKF can be summarized as follows:

Unscented Kalman Filter Algorithm

Prediction:

Calculate sigma points:

$$\mathcal{X}_{k-1} = [\hat{x}_{k-1} \quad \hat{x}_{k-1} + \gamma\sqrt{P_{k-1}} \quad \hat{x}_{k-1} - \gamma\sqrt{P_{k-1}}]$$

Propagate each column of $\mathcal{X}_{k-1}$ through time:

$$(\mathcal{X}_k)_i = f((\mathcal{X}_{k-1})_i) \qquad i = 0, 1, ..., 2L$$

A-priori state estimate: $\hat{x}_k^- = \sum_{i=0}^{2L} W_i^{(m)} (\mathcal{X}_k)_i$

A-priori error covariance: $P_k^- = \sum_{i=0}^{2L} W_i^{(c)} [(\mathcal{X}_k)_i - \hat{x}_k^-][(\mathcal{X}_k)_i - \hat{x}_k^-]^T + Q_k$

Update:

Measurement estimate: $(\mathcal{Z}_k)_i = h((\mathcal{X}_k)_i) \quad i = 0, .., 2L$

$\hat{z}_k^- = \sum_{i=0}^{2L} W_i^{(m)} (\mathcal{Z}_k)_i$

A-posteriori state estimate: $\hat{x}_k = \hat{x}_k^- + K_k(z_k - \hat{z}_k^-)$

where: $K_k = P_{\hat{x}_k \hat{z}_k} P_{\hat{z}_k \hat{z}_k}^{-1}$

A-posteriori estimate of error covariance: $P_k = P_k^- - K_k P_{\hat{z}_k \hat{z}_k} K_k^T$

where:

$$P_{\hat{x}_k \hat{z}_k} = W_i^{(c)} [(\mathcal{X}_k)_i - \hat{x}_k^-][(\mathcal{Z}_k)_i - \hat{z}_k^-]^T$$

$$P_{\hat{z}_k \hat{z}_k} = \sum_{i=0}^{2L} W_i^{(c)} [(\mathcal{Z}_k)_i - \hat{z}_k^-][(\mathcal{Z}_k)_i - \hat{z}_k^-]^T + R_k$$

where $\hat{x}^-$ denotes a-priori estimate of state x. $\gamma = \sqrt{(L+\lambda)}$, and $\lambda = \alpha^2(L+\delta) - L$ are the composite scaling parameters. α is a scaling parameter that determines the spread of the sigma points around $\hat{x}$, and is usually set to a small positive value (e.g. $1e-4 \leq \alpha \leq 1$). δ is a secondary scaling parameter which is usually set to 0 or $3-L$ [60]. Q_k is the process error covariance matrix and R_k is the measurement noise covariance matrix. $W_i^{(m)}$ and $W_i^{(c)}$ weights are defined by:

$$W_i^{(m)} = \begin{cases} \frac{\lambda}{(L+\lambda)}, & \text{if } i = 0 \\ \frac{1}{2(L+\lambda)}, & \text{if } i = 1, 2, ..., 2L \end{cases} \tag{A.3}$$

and

$$W_i^{(c)} = \begin{cases} \frac{\lambda}{L+\lambda} + (1 - \alpha^2 + \beta), & \text{if } i = 0 \\ \frac{1}{2(L+\lambda)}, & \text{if } i = 1, 2, ..., 2L \end{cases} \tag{A.4}$$

where β is a parameter used to incorporate the prior knowledge of the distribution of x. We use $\beta = 2$ which is optimal for Gaussian distributions [185].

Appendix B

State-space building model

Equations (B.1a)-(B.1d) represent the governing heat transfer equations which constitute 5 states of the system.

$$\frac{dT_1^r}{dt} = \frac{1}{C_1^r}(\sum_{j=1}^{4} \frac{T_{1,j}^w - T_1^r}{R_{1,j}^w} + \frac{T_5^r - T_1^r}{R_{1,5}^{win}} + \dot{m}_1^r c_{p_{avg}}(T_1^s - T_1^r) + \tau^w A_{1,5}^{win} Q_1^{rad} + \dot{Q}_1^{int}) \tag{B.1a}$$

$$\frac{dT_{1,2}^w}{dt} = \frac{1}{C_{1,2}^w}(\frac{T_1^r - T_{1,2}^w}{R_{1,2}^w} + \frac{T_2^r - T_{1,2}^w}{R_{1,2}^w} + r_{1,2}\alpha_{1,2}A_{1,2}^w Q_{1,2}^{rad}) \tag{B.1b}$$

$$\frac{dT_{1,3}^w}{dt} = \frac{1}{C_{1,3}^w}(\frac{T_1^r - T_{1,3}^w}{R_{1,3}^w} + \frac{T_3^r - T_{1,3}^w}{R_{1,3}^w} + r_{1,3}\alpha_{1,3}A_{1,3}^w Q_{1,3}^{rad}) \tag{B.1c}$$

$$\frac{dT_{1,4}^w}{dt} = \frac{1}{C_{1,4}^w}(\frac{T_1^r - T_{1,4}^w}{R_{1,4}^w} + \frac{T_4^r - T_{1,4}^w}{R_{1,4}^w} + r_{1,4}\alpha_{1,4}A_{1,4}^w Q_{1,4}^{rad}) \tag{B.1d}$$

$$\frac{dT_{1,5}^w}{dt} = \frac{1}{C_{1,5}^w}(\frac{T_1^r - T_{1,5}^w}{R_{1,5}^w} + \frac{T_5^r - T_{1,5}^w}{R_{1,5}^w} + r_{1,5}\alpha_{1,5}A_{1,5}^w Q_{1,5}^{rad}) \tag{B.1e}$$

The model states are presented in equation (B.2) and the first state which is the room air temperature is considered as the system output.

$$x = [T_1^r, T_{1,2}^w, T_{1,3}^w, T_{1,4}^w, T_{1,5}^w]^T \tag{B.2}$$

Values of elements of the linear model matrices are shown in equations (B.3) and

(B.4).

$$
A_d = \begin{bmatrix} 0.8715 & 0.0033 & 0.0028 & 0.0033 & 0.0062 \\ 0.0012 & 0.9976 & 0 & 0 & 0 \\ 0.0012 & 0 & 0.9976 & 0 & 0 \\ 0.0012 & 0 & 0 & 0.9976 & 0 \\ 0.0001 & 0 & 0 & 0 & 0.9998 \end{bmatrix}
$$

$$
A_n = \begin{bmatrix} 0.9183 & 0.0033 & 0.0028 & 0.0033 & 0.0062 \\ 0.0012 & 0.9976 & 0 & 0 & 0 \\ 0.0012 & 0 & 0.9976 & 0 & 0 \\ 0.0012 & 0 & 0 & 0.9976 & 0 \\ 0.0001 & 0 & 0 & 0 & 0.9998 \end{bmatrix} \tag{B.3}
$$

$$
B_d = \begin{bmatrix} 0.1106 \\ 0 \\ 0 \\ 0 \\ 0 \end{bmatrix}
$$

$$
\begin{aligned}
B_n &= \begin{bmatrix} 0.0638 \\ 0 \\ 0 \\ 0 \\ 0 \end{bmatrix} \\
E_d = E_n &= \begin{bmatrix} 0 & 0 & 0 & 0.0023 \\ 0.0012 & 0 & 0 & 0 \\ 0 & 0.0012 & 0 & 0 \\ 0 & 0 & 0.0012 & 0 \\ 0 & 0 & 0 & 0.0001 \end{bmatrix} \\
C &= \begin{bmatrix} 1 & 0 & 0 & 0 & 0 \end{bmatrix} \\
D &= \begin{bmatrix} 0 \end{bmatrix}
\end{aligned}
\tag{B.4}
$$

Table B.1
Building model parameters.

Parameter/constant	Value
$\dot{m}^r_{day}$	0.52 kg/s
$\dot{m}^r_{night}$	0.3 kg/s
$c_{p_{avg}}$	1005 $J/kg.K$
$c_{v_{avg}}$	718 $J/kg.K$
R	287 $J/kg.K$
$A^w_{1,2}$	27.5 m^2
$A^w_{1,3}$	23.0 m^2
$A^w_{1,4}$	27.5 m^2
$A^w_{1,5}$	20.2 m^2
$A^{win}_{1,5}$	2.8 m^2
T_{sample}	1 $hour$
N	24
τ^w	0.9
κ	711 W.s^3/kg^3
$\delta\underline{\mathcal{U}}$	6 K
$\alpha_{i,j}$	0.4
$\delta\overline{\mathcal{U}}$	6 K
$C^w_{1,2}$	7.9 $e+5$ J/K
$C^w_{1,3}$	6.6 $e+5$ J/K
$C^w_{1,4}$	7.9 $e+5$ J/K
$C^w_{1,5}$	2.6 $e+7$ J/K
C^r_1	2.8 $e+5$ J/K
$R^w_{1,2}$	0.0640 K/W
$R^w_{1,3}$	0.0768 K/W
$R^w_{1,4}$	0.0640 K/W
$R^w_{1,5}$	0.0299 K/W
$R^{win}_{1,5}$	0.0868 K/W
$\overline{\mathcal{U}}$	32 K
ρ_{en}	50 $kW.h/K$
ρ_{ex}	3.8 $e+8$ $kW.h/K$
h_0	298.6 $e+3$ J/kg
s_0	6.86 $e+3$ $J/kg.K$

Appendix C

PhD Publications

C.1 Peer Reviewed Journal Papers

C.1.1 Published Journal Papers

1. M. Razmara, G. Bharati, M. Shahbakhti, S. Paudyal, and R. D. Robinett III, "Bilevel Optimization Framework for Smart Building-to-Grid Systems", IEEE Transaction on Smart Grid, 12 pages, Issue 99, 2016. (Ref. [5])

2. M. Razmara, M. Maasoumy, M. Shahbakhti, R.D. Robinett III, "Optimal exergy control of building HVAC system," Journal of Applied Energy, Vol. 156, Pages 555–565, October 2015. (Ref. [2])

3. M. Maasoumy, M. Razmara, M. Shabakhti, and A. Sangiovanni-Vincentelli, "Handling model uncertainty in model predictive control for energy efficient buildings," Journal of Energy and Buildings., Pages 377âĂŞ392, Vol. 77, July 2014. (Ref. [1])

C.1.2 Submitted Journal Papers

1. M. Razmara, M. Bidarvatan, M. Shahbakhti, and R. D. Robinett III, "Optimal exergy-based contol of internal combustion engines," Journal of Applied Energy, 38 pages, June 2016.(Ref. [186])

C.2 Refereed Conference Papers

1. M. Razmara, M. Bidarvatan, M. Shahbakhti, R. D. Robinett, "Innovative Exergy-based Control of Combustion Phasing in ICEs," Society of Automotive Engineers (SAE) Technical Paper 2016-01-0815, 13 pages, Detroit, MI, 2016. (Ref. [3])

2. M. Razmara, M. Bidarvatan, M. Shahbakhti, R. D. Robinett, "Novel Exergy-Wise Predictive Control of Internal Combustion Engines," American Control Conference (ACC), 6 pages, Boston, MA, 2016. (Ref. [4])

3. G. Bharati, M. Razmara, S. Paudyal, M. Shahbakhti, and R. D. Robinett, "Hierarchical Framework for Demand Dispatch in Building-Grid Systems," IEEE PES General Meeting, 5 pages, Boston, MA, 2016. (Ref. [187])

4. J. Dobbs, M. Razmara, M. Shahbakhti, and S. Paudyal, "Selecting Control Input Type for a Building Predictive Controller Integrated in a Power Grid," American Control Conference (ACC), 6 pages, Boston, MA, 2016. (Ref. [188])

5. M. Razmara, G. Bharati, M. Shahbakhti, S. Paudyal, and R. D. Robinett III, "Bidirectional Optimal Operation of Smart Building-to-Grid Systems," American Control Conference (ACC), 6 pages, Chicago, IL, 2015. (Ref. [172])

6. M. Razmara, M. Maasoumy, M. Shahbakhti, and R. D. Robinett III, "Exergy-Based Model Predictive Control for Building HVAC System," American Control Conference (ACC), 6 pages, Chicago, IL, 2015. (Ref. [103])

7. M. Maasoumy, M. Razmara, M. Shahbakhti, and A. Sangiovanni-Vincentelli, "Selecting Building Predictive Control Based on Model Uncertainty," American Control Conference (ACC), 6 pages, Portland, OR, 2014. (Ref. [106])

8. M. Maasoumy, B. Moridian, M. Razmara, M. Shahbakhti and A. Sangiovanni-Vincentelli, "Online Simultaneous State Estimation and Parameter Adaptation for Building Predictive Control," Dynamic System and Control Conference (DSCC), 10 pages, Best Paper Award Finalist, Palo Alto, CA, 2013. (Ref. [61])

Appendix D

Program and Data File Summary

Following files were used for this dissertation arranged in the tables.

D.1 Chapter 1

Table D.1
Chapter 1 Figure files.

File name	File description
Thesis_Concept_Figure_v2.vsdx	Figure 1.1
Thesis_organization.vsdx	Figure 1.2

D.2 Chapter 2

Table D.2
Chapter 2 Figure files.

File name	File description
testbed.vsd	Figure 2.1
Datalogger.fig	Figure 2.2
Architect final PAB.vsd	Figure 2.3
PersCircuit-Final.vsd	Figure 2.4
Dist.fig	Figure 2.5
inputs.fig	Figure 2.6
calib.fig	Figure 2.7
UKFTroom.fig	Figure 2.8
UKFwalls.fig	Figure 2.9
UKFparams.fig	Figure 2.10
justUKF-new.fig	Figure 2.11
RMPC_Schematic - new.vsd	Figure 2.12
RMPC_OL-CL_edited_Final.fig	Figure 2.13
Discomfort-new.fig	Figure 2.14
Energy-new.fig	Figure 2.15
EnergySavingComparedToRBC.xlsx	Figure 2.16
EnergySavingComparedToRBC.xlsx	Figure 2.17

Table D.3
Experimental data files.

File name	File description
SI-Datasheet_OLD.xls	Experimental temperature data

Table D.4
MATLAB script and SIMULINK files.

File name	File description
HVACModel_RealData_EKF_final.m	Extended Kalman Filter function and plotting
myfun.m	State Space Function
myfun_noise.m	Noise Function function
pathdef.m	Search path function
HVACModel_RealData_UKF_final.m	Unscented Kalman Filter function and plotting
CA50DynamicModeling_VO.m	Physical model
Sliding_lqr_physicmodel.mdl	Control Simulink model

D.3 Chapter 3

Table D.5
Chapter 3 figure files.

File name	File description
ExergyLitSurveyFigure_v4.vsd	Figure 3.1
testbed_new.vsd	Figure 3.2
PersCircuit-Finalist.vsd	Figure 3.3
TempPower_Valid.fig	Figure 3.4
Weekly_exergy.fig	Figure 3.5
MPC Structure.vsd	Figure 3.6
RBC_newest.fig	Figure 3.7
EMPC_newest.fig	Figure 3.8
XMPC_newest.fig	Figure 3.9
entropy_v2.fig	Figure 3.10

Table D.6
Required data files.

File name	File description
SI-Datasheet_OLD.xls	Experimental temperature data

Table D.7
MATLAB script and Simulink files.

File name	File description
LPV_EMPC.m	Script to call energy based LPV MPC
LPV_RBC.m	Script to run RBC
LPV_XMPC.m	Script to run exergy based LPV MPC
Model_validation.m	Script for model validation
Validation2.mdl	Simulink model used for model validation
MPTinstall.m	Script to call Multi Parametric Toolbox of Matlab
opti_Install.m	Script to run OPTI Toolbox of Matlab

D.4 Chapter 4

Table D.8
Chapter 4 figure files.

File name	File description
LitReview_APEN_XCICE.vsd	Figure 4.1
Datapoints.fig	Figure 4.2
Texh_new.fig	Figure 4.3
Destruction.fig	Figure 4.4
PressValidation4_new.fig	Figure 4.5
CrankAngleResolved.fig	Figure 4.6
BarCharts_APEN.xlsx	Figure 4.7
Map_2nd_Work.fig	Figure 4.8
Map_2nd_CPEX.fig	Figure 4.9
Algorithm_new.vsdx	Figure 4.10
XCIC - MPC.vsd	Figure 4.11
Tracking_APEN_new.fig	Figure 4.12
SavingsCA50.fig	Figure 4.13

Table D.9
Experimental data files.

File name	File description
EngineExergyData_WithoutEGR.mat	Exp. data w/o EGR
DataLimitedNOxEfficiency50_limitedIMEP.mat	Exp. data w/o NOX
Vol_cyl.mat	Instantaneous cylinder volume
species.mat	Species datafile
reactions.mat	Reactions datafile

Table D.10
MATLAB script and Simulink files.

File name	File description
ExperimentalExergyMap_General.m	Call XCICE for steady operation
XCIC_fnc2.m	Func. to calc. exergies for each cycle
Fuel_Estimator.m	Script for fuel estimation
ExperimentalExergyMap_2ndLaw_brake.m	$\eta_{II,W}$ map generator
ExperimentalExergyMap_2ndLaw.m	$\eta_{II,CPEX}$ map generator
ExperimentalExergyMap_1stLaw.m	1^{st} map generator
ExperimentalExergyMap_Dest	Exergy destruction map
ExperimentalExergyMap_Texh.m	Generates exhaust temperature map
Comparison_Plot2.m	Optimized and unoptimized plots

D.5 Chapter 5

Table D.11
Chapter 5 figure files.

File name	File description
Ch5_ControllerBackground.vsd	Figure 5.1
Concept.vsd	Figure 5.2
TempPower_Valid.fig	Figure 5.3
B2G_Flowchart4.vsd	Figure 5.4
TestSystem.vsd	Figure 5.5
Subplots.fig	Figure 5.6
DynPricing.fig	Figure 5.7
Bidirectional_Temp.fig	Figure 5.8
B2G_Temp.fig	Figure 5.9
Voltage_Profile.fig	Figure 5.10
WeatherPrice.fig	Figure 5.11
Heterogeneity.xlsx	Figure 5.12

Table D.12
Required data files.

File name	File description
SI-Datasheet_OLD.xls	Experimental Temperature data data
Dyn_Pricing.xls	Dynamic pricing data for MI hub
Base_Load_for33nodes.xls	Existing loads in 33 nodes
Base_Load.xls	Existing loads for 4 studied nodes
Power.xls	Maximum allowable load

Table D.13
MATLAB script and Simulink files.

File name	File description
B2G.m	Script to run bilevel optimization using B2G index
BangBang.m	Script to run On-OFF controller
Bidirectional.m	Script to run bilevel optimization
Bidirectional_5minInterval.m	Script for B2G with 5 min intervals

Appendix E

Letters of Permission

E.1 Letter of Permission for [1, 2] (Chapter 2 and Chapter 3)

Type your question

(http://service.elsevier.com/app/overview/session/L2F2LzEvdGltZS8xNDYzNjY4Mjc1L3NpZC90ZF9kZlVRbQ%3D%3D)

Home (http://service.elsevier.com/app/overview/session/L2F2LzEvdGltZS8xNDYzNjY4Mjc1L3NpZC90ZF9kZlVRbQ%3

Publishing a Book
(http://service.elsevier.com/app/answers/list/c/10550/session/L2F2LzEvdGltZS8xNDYzNjY4Mjc1L3NpZC90ZF9kZlVRbQ%3D%3D)

WHAT RIGHTS DO I RETAIN AS AN AUTHOR?

Last updated on 07/11/2013 03.43 PM

As an author, you retain rights for a large number of author uses, including use by your employing institute or company. These rights are retained and permitted without the need to obtain specific permission from Elsevier. These include:

- The right to make copies of the article for your own personal use, including for your own classroom teaching use.
- The right to make copies and distribute copies (including through e-mail) of the article to research colleagues, for the personal use by such colleagues (but not commercially or systematically, e.g. via an e-mail list or list serve).
- The right to post a pre-print version of the article on Internet web sites including electronic pre-print servers, and to retain indefinitely such version on such servers or sites (see also our information on **electronic preprints** **(http://www.elsevier.com/wps/find/supportfaq.cws_home/electronicpreprints)** for a more detailed discussion on these points.).
- The right to post a revised personal version of the text of the final article (to reflect changes made in the peer review process) on the author's personal or institutional web site or server, with a link to the journal home page (on **elsevier.com** **(http://www.elsevier.com/wps/find/homepage.cws_home)**).

Figure E.1

- The right to present the article at a meeting or conference and to distribute copies of such paper or article to the delegates attending the meeting.
- For the author's employer, if the article is a 'work for hire', made within the scope of the author's employment, the right to use all or part of the information in (any version of) the article for other intra-company use (e.g. training).
- Patent and trademark rights and rights to any process or procedure described in the article.
- The right to include the article in full or in part in a thesis or dissertation (provided that this is not to be published commercially).
- The right to use the article or any part there of in a printed compilation of works of the author, such as collected writings or lecture notes (subsequent to publication of the article in the journal).
- The right to prepare other derivative works, to extend the article into book-length form, or to otherwise re-use portions or excerpts in other works, with full acknowledgement of its original publication in the journal.

Other uses by authors should be authorized by Elsevier through the **Global Rights Department** (for addresses see **Obtaining Permissions (http://www.elsevier.com/wps/find/supportfaq.cws_home/permissionusematerial)**) and authors are encouraged to let Elsevier know of any particular needs or requirements.

(http://service.elsevier.com/app/contact/supporthub/elsevier/session/L2F2LzEvdGltZS8xNDYzNjY4Mjc1L3NpZC90ZF9kZlVRbQ%3D%3D)

We will answer within 48 hours

Email

(http://service.elsevier.com/app/contact/supporthub/elsevier/session/L2F2LzEvdGltZS8xNDYzNjY4Mjc1L3NpZC90ZF9kZlVRbQ%3D%3D)

Back to top

Figure E.2

(/app/answers/detail/a_id/565/track/AvMregrjDv8Q~fM6GmQa~yKgDG0qRS75Mv~K~zj~PP8D#)

Figure E.3

E.2 Letter of Permission for [186] (Chapter 4)

Meysam Razmara <mrazmara@mtu.edu>

Embargo of my thesis for submitted paper

Permissions Helpdesk <permissionshelpdesk@elsevier.com> Thu, Jul 21, 2016 at 11:41 AM
To: Meysam Razmara <mrazmara@mtu.edu>

Dear Meysam,

As an Elsevier journal author, you retain the right to Include the article in a thesis or dissertation (provided that this is not to be published commercially) whether in part or *in toto*, subject to proper acknowledgment; see http://www.elsevier.com/about/company-information/policies/copyright/personal-use for more information. As this is a retained right, no written permission from Elsevier is necessary.

As outlined in our permissions licenses, this extends to the posting to your university's digital repository of the thesis provided that if you include the published journal article (PJA) version, it is embedded in your thesis only and not separately downloadable:

19. Thesis/Dissertation: If your license is for use in a thesis/dissertation your thesis may be submitted to your institution in either print or electronic form. Should your thesis be published commercially, please reapply for permission. These requirements include permission for the Library and Archives of Canada to supply single copies, on demand, of the complete thesis and include permission for Proquest/UMI to supply single copies, on demand, of the complete thesis. Should your thesis be published commercially, please reapply for permission. Theses and dissertations which contain embedded PJAs as part of the formal submission can be posted publicly by the awarding institution with DOI links back to the formal publications on ScienceDirect.

Best of luck with your dissertation and best regards,
Laura

Laura Stingelin
Permissions Helpdesk Associate
Elsevier
1600 John F. Kennedy Boulevard
Suite 1800
Philadelphia, PA 19103-2899
T: (215) 239-3867
F: (215) 239-3805
E: l.stingelin@elsevier.com
Questions about obtaining permission: whom to contact? What rights to request? When is permission required? Contact the Permissions Helpdesk at:
+1-800-523-4069 x 3808 *permissionshelpdesk@elsevier.com*

From: Meysam Razmara [mailto:mrazmara@mtu.edu]
Sent: Wednesday, July 20, 2016 3:47 PM
To: Permissions Helpdesk

Figure E.4

E.3 Letter of Permission for [5] (Chapter 5)

Title: Bilevel Optimization Framework for Smart Building-to-Grid Systems

Author: Meysam Razmara; Guna R. Bharati; Mahdi Shahbakhti; Sumit Paudyal; Rush D. Robinett III

Publication: Smart Grid, IEEE Transactions on

Publisher: IEEE

LOGIN

If you're a copyright.com user, you can login to RightsLink using your copyright.com credentials. Already **a RightsLink user** or want to learn more?

Thesis / Dissertation Reuse

The IEEE does not require individuals working on a thesis to obtain a formal reuse license, however, you may print out this statement to be used as a permission grant:

Requirements to be followed when using any portion (e.g., figure, graph, table, or textual material) of an IEEE copyrighted paper in a thesis:

1) In the case of textual material (e.g., using short quotes or referring to the work within these papers) users must give full credit to the original source (author, paper, publication) followed by the IEEE copyright line © 2011 IEEE.
2) In the case of illustrations or tabular material, we require that the copyright line © [Year of original publication] IEEE appear prominently with each reprinted figure and/or table.
3) If a substantial portion of the original paper is to be used, and if you are not the senior author, also obtain the senior author's approval.

Requirements to be followed when using an entire IEEE copyrighted paper in a thesis:

1) The following IEEE copyright/ credit notice should be placed prominently in the references: © [year of original publication] IEEE. Reprinted, with permission, from [author names, paper title, IEEE publication title, and month/year of publication]
2) Only the accepted version of an IEEE copyrighted paper can be used when posting the paper or your thesis on-line.
3) In placing the thesis on the author's university website, please display the following message in a prominent place on the website: In reference to IEEE copyrighted material which is used with permission in this thesis, the IEEE does not endorse any of [university/educational entity's name goes here]'s products or services. Internal or personal use of this material is permitted. If interested in reprinting/republishing IEEE copyrighted material for advertising or promotional purposes or for creating new collective works for resale or redistribution, please go to http://www.ieee.org/publications_standards/publications/rights/rights_link.html to learn how to obtain a License from RightsLink.

If applicable, University Microfilms and/or ProQuest Library, or the Archives of Canada may supply single copies of the dissertation.

BACK CLOSE WINDOW

Figure E.5